The Consolidation and Strength of Rafted Sea Ice.

A thesis submitted to University College London for the degree of Doctor of Philosophy

Eleanor Bailey

Rock & Ice Physics Laboratory
Department of Earth Sciences
University College London
London WC1E 6BT

March, 2011

I, Eleanor Bailey confirm that the work presented in this thesis is my own. Where information has been derived from other sources, I confirm that these have been correctly referenced.

Signed _____ Date _____

Abstract

The research presented in this thesis is an investigation into the consolidation and strength of rafted sea ice. A model for the consolidation of rafted sea ice has been developed that predicts how long it will take for the layers in a rafted section of sea ice to bond effectively into a coherent ice sheet. The rafted ice is assumed to be composed of layers of sea ice of equal thickness, separated by thin layers of ocean water. Heat transport within the sea ice is described using the mushy layer equations and the rate of freezing is given by the Stefan condition. Concurrent laboratory experiments were conducted in the Rock and Ice Physics Laboratory at UCL. To simulate a section of rafted sea ice, layers of laboratory grown saline ice were stacked on top of one another with spacers between adjacent ice sheets allowing water from the tank below to flood in. The rate of consolidation was then monitored using a combination of temperature readings recorded in the ice and liquid layer, salinity measurements of the liquid layer, and cores taken using a manual core auger. Once consolidated, cores were taken and sheared using the four-point asymmetrical bending method to measure the strength of the bond between two-rafted ice sheets. These were then compared to the shear strength of level ice. Results showed that the rafted ice had consolidated in less than a day, however it took many more days (6 to 30 depending on the conditions) for the blocks to reach maximum strength. Increasing the thickness of the ice, the salinity of the solution and the gap size all increased the consolidation time. The shear strength of the bond between rafted ice sheets was found to be ~30% weaker than that of level ice.

Acknowledgements

First and foremost I would like to thank my supervisors Peter Sammonds and Daniel Feltham for their guidance, support and understanding throughout the project, which never faltered even when the going was tough. Their wisdom and experience was a constant source of inspiration.

In designing and constructing the laboratory apparatus I am grateful to the laboratory support staff Steve Boon, John Bowles and Neil Hughes for their technical expertise and innovation to get around any problem that arose. Their bonhomie also deserves a mention.

I am indebted to the British Antarctic Survey (through Ted Maksym) and the Hamburgische Schiffbau-Versuchsanstalt (through Karl Evers) for kindly loaning me their core augers which were an essential tool in my laboratory work.

A big thank you Liz Gaunt for her willingness and enthusiasm through the many hours spent coring at subzero temperatures, not forgetting the hot chocolates afterwards.

I would also like to thank Derek Mayne and the ice team at AgipKCO who provided the background expertise of the project in the field.

Many thanks to my flatmate and boyfriend John who lived for many months with a monothematic partner!

None of this would have been possible without the financial support of the National Environmental Research Council and the UCL Graduate School, who provided further funding toward the end. Their support is gratefully acknowledged.

Last but by no means least, I thank my parents, Jill and Roger. They raised me, supported me, taught me, and loved me. To them I dedicate this thesis.

Table of Contents

List of Figures

List of Tables

1 Introduction

Despite efforts to move to more climate-friendly energy sources, global demand for oil and gas is still on the rise and there is anxiety that global "Peak Oil" production has been reached (BP, 2010). This has meant that the search for hydrocarbons has had to venture into harsher and more challenging environments, which has led to a boom in oil exploration in the sea ice infested waters of the Arctic and sub-Arctic. The Arctic is currently estimated to hold about 90 billion barrels (1.4×10^{10} m^3) of undiscovered, technically recoverable oil and 44 billion barrels of natural gas (USGS, 2008). The Arctic environment is severe: low temperatures, ice and its remoteness all pose tremendous technological challenges to offshore hydrocarbon activity. Oil companies have therefore invested considerable resources in cold-regions research in order to gain a greater understanding of ice problems and be able to quantify ice hazards and risks associated with offshore exploration (POAC, 2009; Sanderson, 1988). Presently, offshore activity in ice-infested waters is ongoing in the European Arctic (Barents, Pechora and Kara Seas), North American Arctic (Beaufort Sea and Canadian Arctic Archipelago), offshore Sakhalin, the Bohai Sea and the north Caspian Sea. There are no internationally agreed engineering design codes for dealing with sea ice loads on offshore structures, which is a reflection not only of uncertainty in calculating ice loads but also of the different ice conditions prevalent in different regions; although an international Arctic Offshore Structures Standard (ISO/FDIS 19906) is currently under preparation.

The Caspian Sea is located at the southerly limit of sea ice formation and has become of particular interest due to the recently discovered oil and gas reserves. In the north Caspian Sea is located the giant Kashagan oil field, which extends over an area of approximately 75km by 45 km. It is currently estimated that the field holds up to 38 billion barrels of oil, of which 9 billion barrels are potentially recoverable, rising to 11 billion barrels with the use of gas re-injection (AgipKCO, 2010). This makes it the largest discovery in over 30 years. The proposed Trans-Caspian Oil Transport System and Gas Pipeline would provide important routes for export, bypassing Russia, and making the north Caspian Sea of particular importance for European energy security. The Kashagan field is situated offshore and is subject to a harsh environment, with temperature extremes that vary between +40°C

and –30°C. The low winter temperatures combined with the low salinity (6 – 8 ppt) of the north Caspian Sea causes the sea surface to readily freeze over for 3-5 months of the year. This has major effects on offshore operations and influences the design of offshore facilities such as platforms, ships and pipelines.

Sea ice is a hazard to offshore operations as, when driven by wind, sea ice features such as ridges or rafted sea ice have the potential to exert huge forces on drilling rigs or artificial islands. Ridges are elongated piles of rubble and rafting is the simple overriding of one sheet by another. Multiple rafting is also known to occur in some regions, where ice floes override one another multiple times to produce thick sea ice features (Babko et al., 2002). This process is particularly common in the north Caspian Sea where rafted sections of up to 13 layers have been observed, giving a total ice thickness of up to 4 m (D. Mayne, personal communication, 2007). Lateral dimensions extending for several hundreds of metres have also been observed. Rafting is also common in areas such as the Southern Ocean, the Sea of Okhotsk and Norton Sound, Alaska, where the sea ice thickness is usually less than a meter. For example, Worby et al. (1996) analyzed 62 ice cores retrieved from 50 ice floes in the Bellingshausen and Amundsen Seas and found that the floes with an average thickness of 0.9 m contained around eight distinct layers. Toyota et al. (2007) collected ice cores from 27 different locations chosen at random in the Sea of Okhotsk and found that all the ice samples consisted of multiple layers of rafted sea ice roughly 10-12 cm thick. Wang et al. (1994) investigated the ice regime in Norton Sound and found rafting to be a common feature with average rafted ice thicknesses of 9.2 m and lateral dimensions of a few kilometres.

To date rafting has not received as much attention as ridging in the literature. This is perhaps because ridges have been a greater concern for engineers as in most regions they determine the design load for offshore structures and ridge keels may scour the seabed endangering pipelines and wellheads. From a geophysical point of view, ridges account for a large percentage of the ice volume and are therefore important for the parameterisation of energy and mass exchange processes in climatic problems (Hoyland, 2002). Ridges are also easily identifiable in aerial photos, laser altimetry and underwater sonar records. Rafted ice, however, can only be easily identified in aerial imagery up to a thickness of 0.15-0.2 m

(Babko et al., 2002) and by coring and sampling the ice, which is both time consuming and costly.

In the north Caspian Sea the shallow waters (1-5 m) constrain the size to which pressure ridges can grow. In addition, the lack of significant snow cover, and the low salinity of Caspian ice, seems to favour rafting over ridging. Therefore it is likely that rafted sea ice is the governing design ice feature for ice load calculations in the Caspian Sea. It is not clear what load rafted ice would exert on a given structure or how it would deform. In a rafted section, the layers of sea ice are initially separated by thin layers of water. The bonds between the layers are at first weak but may strengthen with time to produce a coherent ice sheet. At present most design loads assume that the strength of rafted ice is 10-20% less than that of level ice of the same thickness (Jizu et al., 1991). This is because it is believed that the bonds between layers in a rafted section may be weaker than solid ice. However, there is very little experimental or theoretical data to back this theory. Poplin and Wang (1994) carried out extensive uniaxial compression tests on rafted ice samples collected in Norton Sound. Their results showed that on ice samples cut horizontal to the crystal growth direction, at strain rates of 10^{-4} and 10^{-5} s^{-1}, the mean strengths of consolidated rafted ice were actually larger (1.55 and 1.06 MPa) than the corresponding landfast samples (1.25 and 0.64 MPa). Since rafted ice loads are usually applied horizontally to offshore structures, this result implies that once consolidated, rafted ice may be a significant ice hazard. Increased knowledge of the physical and mechanical properties of rafted sea ice is necessary to improve these load estimates. An understanding of these concepts is of particular interest to offshore operations in the Caspian, however the research has broader implications for understanding rafted sea ice in other areas.

In addition to its engineering interests, rafting has also been shown to play an important part in the mechanical re-distribution of the sea ice thickness (Babko et al., 2002; Toyota et al., 2004). This is particularly apparent in the autumn in the Arctic, when the sea ice is thin or in the Sea of Okhotsk where the sea ice is typically made up of several layers 5-10 cm thick. Given that with the effects of global warming there is expected to be an overall thinning of sea ice in the Arctic (Johannessen et al., 2004), rafting events are likely to increase. Therefore, I believe that in the years to come rafting is going to be of importance

not only for better estimation of ice loads on offshore structures but also for modelling of sea ice dynamics.

The research presented in this thesis aims to gain a greater insight into rafting by investigating the consolidation and strength of rafted sea ice. This has been achieved by:

1. Developing a model for the consolidation of rafted sea ice that predicts how long it will take the layers in a section of rafted sea ice to effectively bond into a coherent ice sheet. This has been published in the Journal of Geophysical Research-Ocean (Bailey et al., 2010).
2. Testing the consolidation model though controlled laboratory experiments in the UCL Ice Physics Laboratory.
3. Measuring the strength of the bond between two layers of rafted sea ice by performing shear experiments under increasing states of consolidation.

The motivation for this research came from AgipKCO, a subsidiary of Eni, who is operating the north Caspian Sea Project on behalf of a consortium of oil companies: Eni, KazMunayGaz, ExxonMobile, Shell, Total, ConocoPhillips and INPEX. I participated in two AgipKCO field expeditions that are run on an annual basis to understand the Caspian Sea ice regime. I spent a total of 2 months in offices in Atyrau, Kazakhstan, collecting and analysing helicopter borne ground penetrating radar and familiarising myself with the Caspian Sea ice conditions. Initially the plan was that I perform large scale consolidation experiments in the field to test how representative the laboratory experiments are at simulating natural conditions. However due to insufficient ice cover in the winter of 2006-07 and inadequate helicopter time in 2007-08 I was unable to do so. Fortunately, I was able to incorporate a couple of experiments into a larger project that was investigating sea ice friction and rheology in the Arctic Environmental Test Basin at the Hamburgische Schiffbau-Versuchsanstalt (HSVA) in Germany (Lishman et al., 2009). These are presented in Appendix F and shall be referred to throughout the thesis.

The plan of this thesis is as follows:

In Chapter 2, I describe the formation, growth and structure of first year sea ice, and the salinity evolution in sea ice. After this I highlight the types of sea ice predominant in the Arctic, Antarctic and the north Caspian Sea, which I later use as the three case studies in our modelling and experimental studies.

In Chapter 3, I describe the different types of rafted sea ice, followed by a synopsis on previous work that has been carried out on rafted sea ice. I then describe the mechanics of rafting, discuss the provenance of the liquid layer between rafted layers and outline complementary studies on consolidation and strength of rafted sea ice.

In Chapter 4, I give a brief description of previous sea ice models and how they have developed over the past century. I then present the mushy layer equations that are used to describe heat transport within the sea ice and their application to sea ice modelling. After this, I present a thermodynamic model of sea ice growth that I later develop into a consolidation model for rafted sea ice (Chapter 6).

In Chapter 5, I describe how natural sea ice growth was simulated in the Ice Physics Laboratory at UCL. The thermodynamic model of sea ice growth is then tested against laboratory data using the temperatures recorded during ice growth. The physical and mechanical properties of the laboratory grown saline ice are then presented.

In Chapter 6, the consolidation model for rafted sea ice is presented.

In Chapter 7, the consolidation experiments that were carried out in the ice physics laboratory at UCL are presented.

In Chapter 8, the rafted ice consolidation model is tested against laboratory data by imposing parameters that force the model according to the observations made.

In Chapter 9, I investigate the strength of the bond between two rafted ice sheets by shearing cores under increasing states of consolidation.

In Chapter 10 the main conclusions of this research are presented and recommendations for further work are given.

2 Sea Ice

2.1 Introduction

Sea ice is formed from the freezing of sea water. This distinguishes it from terrestrial ice such as glaciers, ice sheets and lake and river ice, in that it contains significant amounts of salt, which greatly influences its formation, growth, structure and properties. The extent and thickness of sea ice varies depending on the thermal and physical processes to which it has been subjected. Thermodynamic effects cause the sea ice to grow or melt due to variations in atmospheric and oceanic forcing. Winds, ocean currents and the thermal expansion and contraction of the ice can cause the ice to fracture forming open-water leads and the subsequent deformation of the ice cover. The thermodynamic and dynamic forcing varies both spatially and temporally leading to considerable diversity in sea ice characteristics from one region to the next.

The majority of sea ice is found at high latitudes in the Arctic and Southern Oceans, however seasonal sea ice can also be found in lower latitudes in areas such as the north Caspian Sea, the Baltic Sea, the Sea of Okhotsk and the Bohai Sea (see Figure 2.1). At its maximum extent sea ice can cover up to 10 % of our planet's oceans and as a result plays a significant role in the global climate system, due to its radiative and thermal properties. In addition, sea ice presents a major obstacle to marine navigation and offshore oil and gas operations.

In this chapter, I describe the formation, growth, structure and properties of first year sea ice, and describe the salt content in sea ice. After this I describe the strength of first year ice, with emphasis on the compressive strength and shear strength of sea ice as these are the two types of strength tests that have been conducted in this thesis. I then highlight the types of sea ice predominant in the Arctic, Antarctic and the north Caspian Sea, which I later use as the three case studies in our modelling and experimental studies. This is not a comprehensive review but focuses on the properties and processes important for the consolidation and strength of rafted sea ice. Further details on sea ice properties and processes can be found in Eicken (2003), Wadhams (2000) and Weeks and Ackley (1986).

Figure 2.1. The extent of Arctic sea ice along with global snow cover from 1/10/2002 through 23/6/2003 (courtesy of the NASA/Goddard Space Flight Centre Scientific Visualization Studio).

2.2 Formation and growth of sea ice

The formation of ice on the surface of water is strongly affected by the water salinity. For instance, consider a freshwater lake of zero salinity being cooled from above. As the surface water is cooled it will increase in density causing it to sink and be replaced by warmer less dense water from below. Convective overturning will continue until the entire water column has reached its maximum density, which for fresh water is at a temperature of +4°C (Pounder, 1965). After this, further cooling will cause the surface waters to stratify, with ice forming as soon as it has reached its freezing temperature, while most of the underlying water column is still well above freezing.

The addition of salt to water lowers both the freezing temperature of the water and the temperature of the maximum density. In Figure 2.2, both these temperatures are plotted against salinity. This shows there is a crossover point at 24.7 ppt (parts per thousand or grams of salt per kilogram of water) and that for salinities above this, the freezing point is higher than the temperature of maximum density. Therefore surface cooling creates an unstable vertical density distribution resulting in convective mixing, which will continue until the water column reaches the freezing point. In the Polar Oceans, there exists a strong vertical density gradient known as the pynocline which stratifies the ocean, limiting convection to the upper few tens of metres of the ocean (Eicken, 2003; Wadhams, 2000). For this reason 24.7 ppt is defined as a critical value which distinguishes brackish water from true sea water. Most of the Polar Oceans have salinities that exceed 24.7 ppt. However, there are a number of key areas where water salinity falls below this value, in particular the north Caspian Sea has a salinity of 6-8 ppt and the northern Baltic Sea 3.5-5.5 ppt. These low salinities allow these seas to freeze readily at the onset of winter, as well as influencing the sea ice physical and mechanical properties.

Once the surface water has cooled to the freezing point (-0.36ºC at 6 ppt and -1.8ºC at 35 ppt), further cooling results in the formation of disc-shaped ice crystals, 2-3 mm in diameter, that float flat with their crystallographic c-axes oriented vertically. These crystals soon take on a hexagonal, star-shaped form, with long fragile dendritic arms stretching out over the surface. Any kind of turbulence causes these arms to break off, leaving a suspension of discs and arm fragments, known as frazil ice. In calm conditions, frazil

freezes together to form a thin smooth sheet of ice referred to as nilas (Weeks and Ackley, 1986). The open ocean is rarely calm and wave-induced turbulence causes the frazil ice to mix allowing crystals to increase in numbers until the surface of the ocean resembles a soupy layer (Weeks and Ackley, 1986). As this dense suspension of frazil ice undergoes further compaction, crystals start to freeze together and form small coherent cakes of slush a few centimetres in diameter, which grow larger and solidify as more crystals accrete. These are known as ice pancakes (see Figure 2.3), which, with time, will coalesce to form a continuous ice sheet. The crystals in this top layer of ice are typically 1 mm in diameter, frozen together more or less randomly, and are referred to as granular ice.

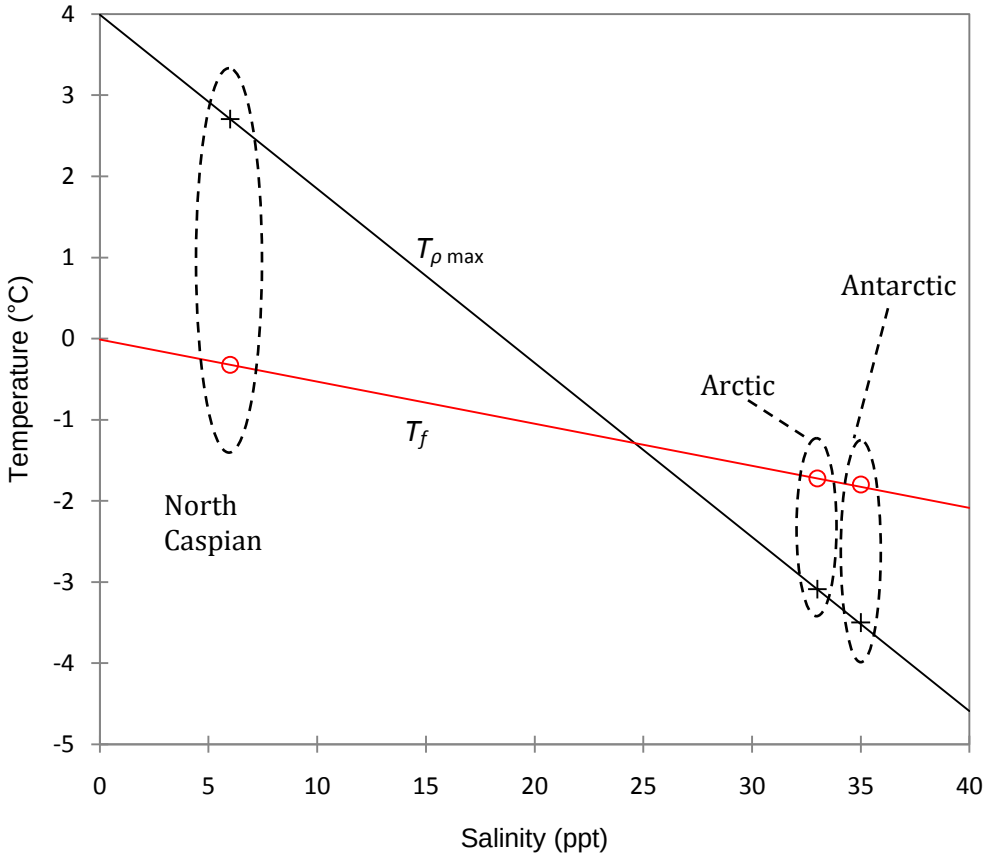

Figure 2.2. The temperature of maximum density ($T_{\rho\ max}$) and the freezing point of sea water (T_f) for different sea water salinities. Note how these lines crossover at 24.7 ppt. (after Ono, 1965).

Figure 2.3. Pancake ice in the Weddell Sea at the onset of winter. Note the raised rims caused by continued abrasion with neighbouring cakes (photo courtesy of NASA).

Once a continuous skim of nilas or consolidated pancake ice has formed, the ice creates a barrier insulating the ocean water from the cold temperatures of the atmosphere. This reduces the growth rate of the ice, as the removal of latent heat is now only by vertical conduction through the ice sheet. This prevents crystals from growing laterally and grains compete for survival during the subsequent downward growth. This creates a transition zone where crystals with unfavourable orientations are eliminated (Perey and Pounder, 1958). Below this, the ice crystals elongate downwards creating a columnar structure with their c-axes oriented in the horizontal plane and are either randomly oriented within this plane or aligned with the ocean current. Columnar grains can be up to centimetres in diameter and span the thickness of the ice sheet. This is known as columnar or congelation ice. Figure 2.4 shows a schematic of a cross section through a typical sample of first year sea ice.

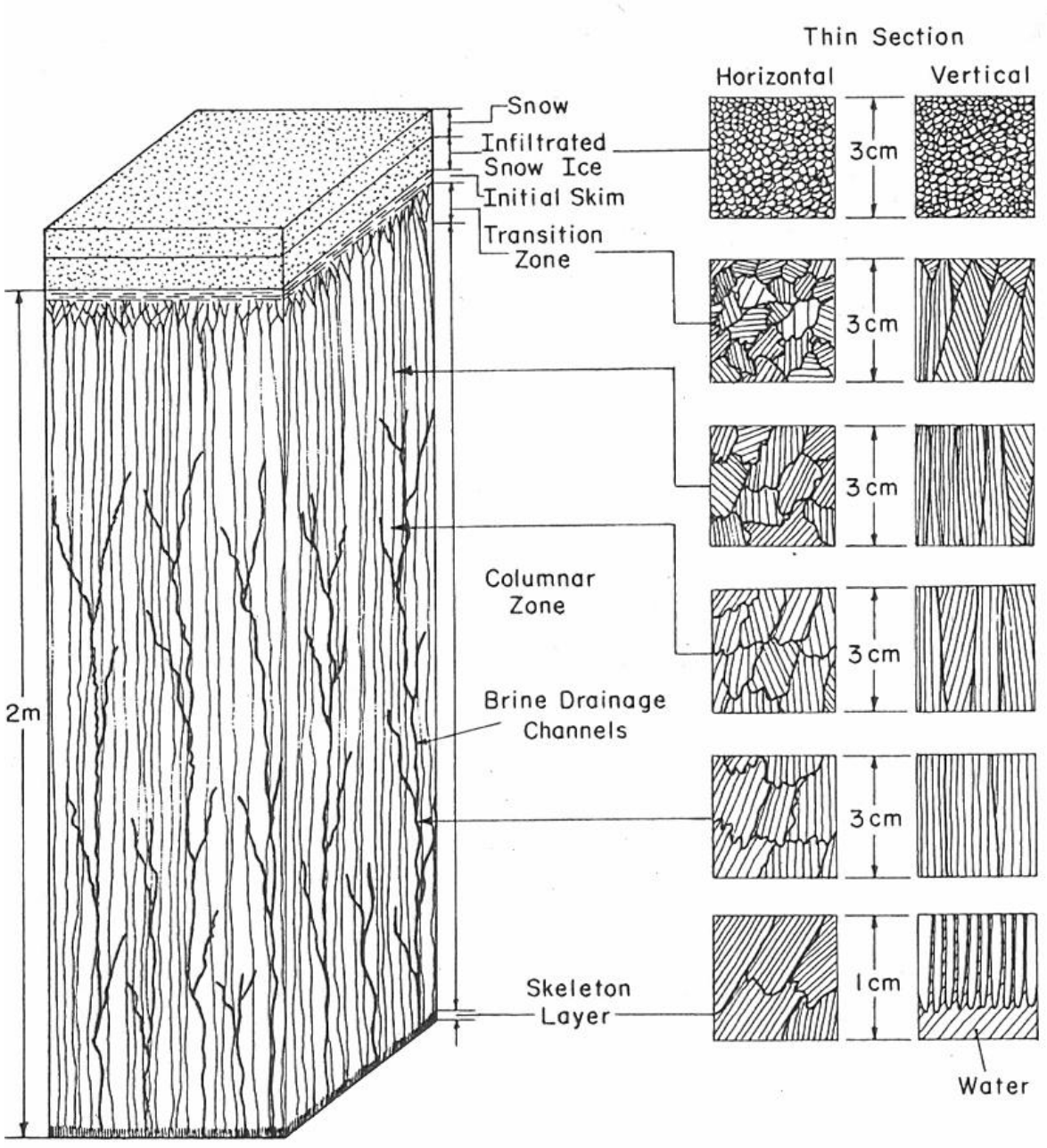

Figure 2.4. The structure of first year sea ice (taken from Schwartz and Weeks, 1977).

2.3 Salt in Sea Ice

As sea ice grows the solid ice phase is practically pure because very few ions have the correct size and charge to be incorporated into the ice crystal lattice. The major ions in seawater (Cl^-, Na^+, K^+, Ca^{2+}, Mg^{2+}, SO_4^{2-}, CO_3^{2-}) are rather retained as liquid inclusions of brine that have been physically trapped in the ice on formation or are rejected into the water column below. This has important consequences for the properties and macroscopic structure of sea ice.

Brine Entrapment

At the growing ice-water interface, most of the salt ions are rejected and a thin layer of salt solution builds up ahead of the advancing interface. The condition for thermodynamic equilibrium requires that at the growing interface the solution should always remain at its liquidus (melting/freezing) point, such that an increase in salt concentration would cause a reduction in temperature. Since the salt ions diffuse away from the growing ice-water interface more slowly than the rate at which heat conducts to the interface there exists a region directly ahead of the interface where the local temperature is below the equilibrium freezing temperature and the liquid in this layer is said to be constitutionally supercooled. The solidification front advancing into the supercooled solution is unstable. Any small perturbation that protrudes into the supercooled solution finds itself at a growth advantage, whereby the local supercooling provides a heat sink for the latent heat released on freezing. This process causes the ice to advance in an ordered pattern of lamellar bulges known as dendrites, separated by narrow layers of brine (see Figure 2.5) (Eicken, 2003). As the dendrites advance, they thicken causing ice bridges to develop between adjacent dendrites, isolating pockets of brine. A similar mechanism is responsible for trapping of air bubbles.

Once trapped, the brine pockets exist in a state of thermodynamic equilibrium with the surrounding ice. For example, at -1.8ºC the salinity of brine is 35 ppt but at lower temperatures, pure ice crystallises out of solution onto the walls of the brine pockets causing the brine concentration to increase. The relationship between the ice, liquid brine and solid salts for standard sea ice can be shown in the phase diagram for sea ice (see Figure 2.6). Here we see that as temperature decreases, seawater salts start to precipitate out of solution. The first major constituent in seawater to precipitate is sodium sulphate

($Na_2SO_4 \cdot 10H_2O$) at -8.2ºC, followed, more importantly, by sodium chloride ($NaCl \cdot 2H_2O$) at -22.9ºC, which alone accounts for ~85% of the mass of dissolved salts in sea water.

Sea ice therefore forms what is referred to by metallurgists as a 'mushy layer', a region of mixed phase composed of solid matrix with concentrated liquid trapped within the interstices (pores) of the solid (Feltham et al., 2006). Mushy layers shall be discussed in greater detail in the next chapter.

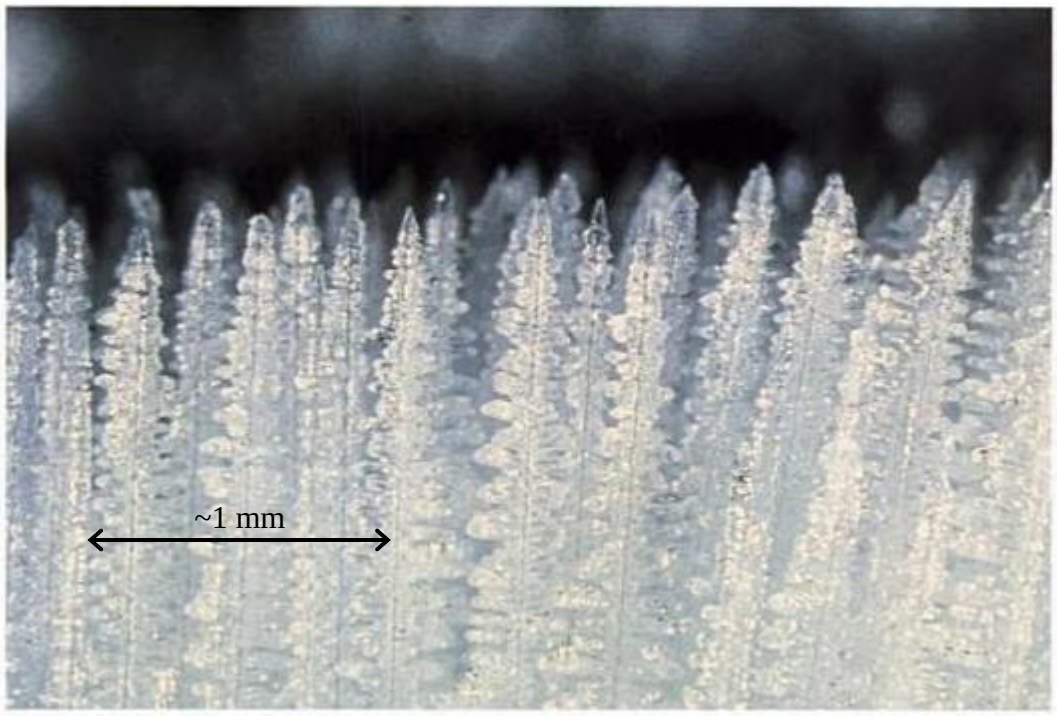

Figure 2.5. Dendritic ice growth of a mushy layer. In this case the solid phase is ammonium chloride (taken from Worster, 2000).

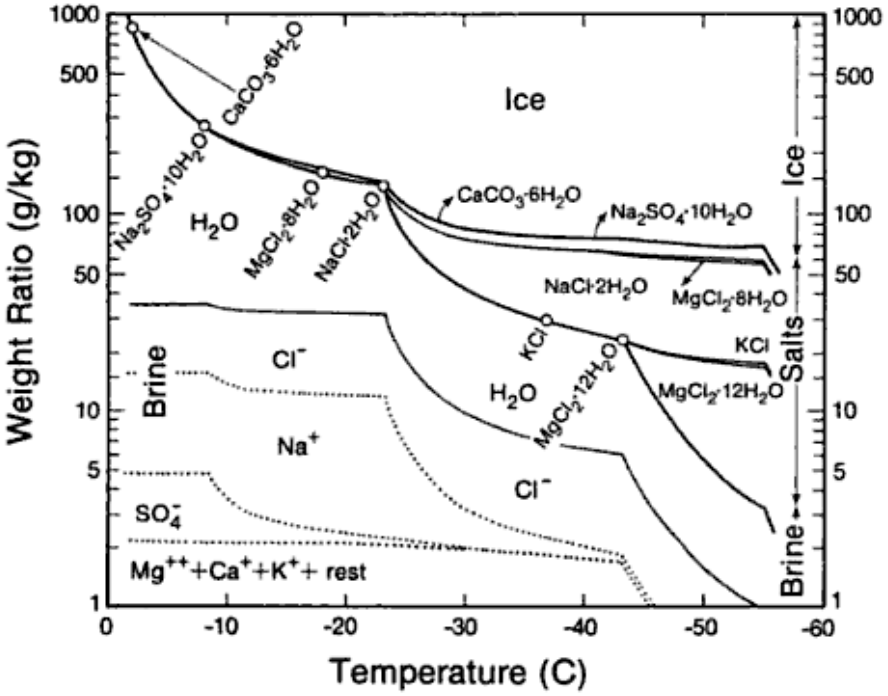

Figure 2.6. Phase relations for standard sea ice. The different curves indicate the mass fraction of liquid brine (bottom), salts (middle) and solid ice (top) present in a closed volume of sea water as a function of temperature, where the circles indicate the temperatures at which solid salts precipitate (after Assur, 1958).

Brine and air volumes

The volume of brine and air in sea ice is dependent on many factors, including the growth conditions, the thermal history of the ice, the salinity of the water from which it was formed and the temperature of the ice sheet. The porosity (brine plus air volume) of sea ice is an important parameter in controlling the physical, mechanical and electrical properties of sea ice. This is because brine and air pockets influence the heat capacity and conductivity of ice, have negligible strength and so act as weak points in an ice sheet, and alter the permittivity of the ice causing scattering of electromagnetic waves.

Assur (1958) showed the brine volume to be a function of ice temperature, and that it increases rapidly when the ice reaches near melting temperatures. Frankenstein and Garner (1967) formulated a set of empirical equations that calculate brine volume from the temperature θ (in °C) and bulk salinity S of the ice (in ppt). They found that between the temperatures -0.5°C and -22.9°C the brine volume could be approximated by

$$v_b = S\left(\frac{49.185}{|\theta|} + 0.532\right). \quad (2.1)$$

Both these works assume a constant density of 0.926 Mgm^{-3} for sea ice. In their review of sea ice density, Timco and Frederking (1996) quote density variations in first year sea ice ranging from 0.84-0.94 Mgm^{-3}. Therefore it is more accurate to include density as a variable when calculating the total porosity of the ice. Cox and Weeks (1983) later developed equations for calculating brine and air volumes using the measured density, temperature and salinity. They found that the brine and air content can be determined from

$$v_b = \frac{\rho_{si} S_{si}}{F_1(\theta)} \quad (2.2)$$

$$v_a = 1 - \frac{\rho_{si}}{\rho_i} + \rho_{si} S_{si} \frac{F_2(\theta)}{F_1(\theta)} \quad (2.3)$$

where ρ_{si} and S_{si} are the density (in Mgm^{-3}) and salinity (in ppt) of the sea ice, ρ_i is the density of pure ice and $F_1(\theta)$ and $F_2(\theta)$ are temperature dependent functions that describe the temperature dependence of the density and salinity of the brine and solid salt content. Cox and Weeks (1983) determined the values for $F_1(\theta)$ and $F_2(\theta)$ using Assur's (1958) phase equilibrium table and fit a cubic polynomial of the form,

$$F(\theta) = \alpha_0 + \alpha_1\theta + \alpha_2\theta^2 + \alpha_3\theta^3, \quad (2.4)$$

to the data. In this thesis, the polynomial coefficients for sodium chloride ice defined by Häusler (1989) (see Table 2.1) will be used along with the equations (2.2) and (2.3) to determine the brine and air content of ice samples.

Table 2.1. Regression coefficients of the polynomial functions $F_1(\theta)$ and $F_2(\theta)$ for NaCl solutions.

Function	α_0	α_1	α_2	α_3
$F_1(\theta)$	0	$-1.7914 \cdot 10^{1}$	$-2.543 \cdot 10^{-1}$	$-8.07 \cdot 10^{-4}$
$F_2(\theta)$	$8.85 \cdot 10^{-2}$	$-1.3548 \cdot 10^{-2}$	$-2.758 \cdot 10^{-4}$	$-2.65 \cdot 10^{-6}$

Desalination mechanisms in sea ice

The liquid brine retained in sea ice can result in bulk salinities as high as 25 ppt for ice 5 cm thick. However, with time brine drains out of the ice sheet via a network of brine drainage channels, gradually reducing the concentration of the sea ice. Figure 2.7 shows the evolution of salinity profile during thickening of a typical Arctic sea ice sheet. Initially, the profile is C-shaped, with high salinities near the top and bottom of the ice sheet. With time, ice thickens and the bulk salinity decreases until an almost constant salinity of 5-6 ppt is reached. Desalination processes play a vital role in the consolidation and strength of rafted sea ice and are described below.

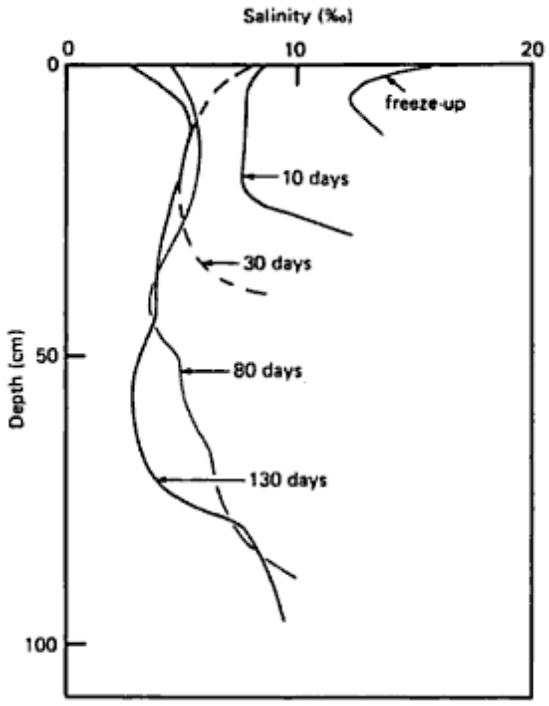

Figure 2.7. The salinity profiles (in ppt) of typical Arctic sea ice plotted as a function of depth. Note the characteristic C-shaped profiles of the young sea ice and the gradual desalination as the ice thickens (taken from Vincent, 1988).

Four mechanisms have been suggested to contribute to the loss of salt from sea ice: the migration of brine pockets through the ice sheet, brine expulsion, gravity drainage and flushing.

Brine cell migration was one of the first mechanisms suggested to explain the desalination of sea ice after its formation. Whitman (1926) pointed out that in the winter brine pockets

are subject to a vertical temperature gradient, where the top of the brine pocket is colder than the bottom. For phase equilibrium to be maintained, a concurrent salinity gradient must exist, with high salinities towards the top of the brine pocket. This causes the salt to diffuse downwards resulting in freezing at the top of the brine pocket and dissolution at the base. The brine pocket therefore gradually 'migrates' downwards, towards the warm end of the ice sheet and may eventually drain out through the bottom of the ice sheet. This process has been shown experimentally and theoretically to be very slow, of the order of ~ 1 cm per month (Weeks and Ackley, 1986), and therefore is generally thought to have little or no significance on the salinity evolution of sea ice (Hoekstra et al., 1965; Kingery and Goodnow, 1963; Untersteiner, 1968).

Brine expulsion was first described by Bennington (1963), who noted that when ice was cooled the thermal contraction of the ice produced a high internal pressure within the brine pocket. This pressure can at times be sufficient to cause the surrounding ice to fail, preferentially along the basal crystallographic planes, allowing the brine to be expelled through the cracks surrounding the brine pocket. While most of the expelled brine would be expected to drain downwards to the base of the ice sheet, in thin ice brine is also expelled upward toward the surface of the ice. This process is believed to contribute to the high surface salinities observed in young sea ice (Martin, 1979). Untersteiner (1968) and Cox and Weeks (1975) used models to investigate the contribution that brine expulsion has in the desalination of sea ice. They found that brine expulsion alone could not explain the observed changes in salinity profiles of first-year sea ice and therefore concluded that brine expulsion only plays a minor role in the desalination of sea ice.

Gravity drainage refers to the convective overturning of the brine caused by density gradients in the ice sheet (Cox and weeks, 1975; Notz and Worster, 2008; 2009). During the winter, the upper part of the ice sheet is colder than the lower part, producing an unstable density profile. This can, depending on the permeability of the ice, result in convective overturning of the brine where the high salinity brine in the upper part of the sheet is replaced with less saline sea water or brine from the lower layers of the ice sheet. Cox and Weeks (1975) conducted a series of experiments that estimated the amount of gravity drainage from measurements of the bulk salinity. They found gravity drainage to be a function of the temperature gradient in the ice sheet and the brine volume fraction. They

also found that for brine volumes below a critical value of ~5%, the ice is effectively impermeable to fluid transport and brine drainage stops altogether. Golden at al. (1998) noting that this brine volume corresponded to a critical temperature $T_c = -5$°C and bulk salinity of $S = 5$ ppt, named this the "law of fives".

Wettlaufer et al. (1997a; 1997b) later conducted laboratory experiments that simulated the initial growth of sea ice by cooling sodium-chloride solutions from above. They found that the brine initially remains trapped in the ice but once the thickness of the ice sheet exceeds a critical value convective overturning (gravity drainage) initiates. They explained this behaviour using the porous-medium Rayleigh number,

$$Ra = \frac{g\rho_l \beta \Delta S \Pi(\phi_v) h}{\kappa \mu}, \tag{2.5}$$

which must exceed a critical value before convective overturning can begin (Worster, 1992; 1997; 2000). In this equation, g is the acceleration due to gravity, $\rho_l \beta \Delta S = \rho_l \beta (S_{ocean} - S_{brine})$ is difference in density across the ice sheet, where S_{ocean} is the salinity of the underlying ocean and S_{brine} is the brine salinity determined by the surface temperature, $\Pi(\phi) = 10^{-17}[10^3(1-\phi_v)]^{3.1}$ m^2 (Freitag, 1999) is the permeability of the ice as a function of solid volume fraction ϕ_v, h is the thickness of the mushy layer and κ and μ are the thermal diffusivity and the dynamic viscosity of the liquid. Initially, in their experiments, the available potential energy $g\rho_l \beta \Delta S h$ is too small to overcome the dissipative effects of thermal diffusion and viscosity. But once the ice has reached a critical thickness, the potential energy caused by the gradient in brine density becomes large enough to trigger the onset of convection thus allowing high salinity brine to drain out of the ice sheet. This leads to a decrease in the overall bulk salinity of the ice and thus an increase in the solid fraction, which in turn lowers the value of *Ra*. Theoretical and experimental studies on the convection of mushy layers have shown that for convective overturning or gravity drainage to occur in sea ice the local Rayleigh number must exceed a critical value $Ra_c \sim 10$ (Notz and Worster, 2008; Wettlaufer et al., 1997b; Worster, 1992; 2000).

Flushing is usually thought of as a desalination mechanism that takes place during the melt season, whereby the fresh melt water on the surface of the ice produces a pressure head driving the high salinity brine out of the ice and replacing it with the fresher melt water (Untersteiner, 1968). However in this thesis I refer to "flushing" as all processes where the weight of fluid above sea level, whether due to the presence of a pond, the natural height of the ice above sea level (to maintain hydrostatic equilibrium), or because the ice sheet has been lifted out of the water due to rafting/ridging processes, produces a positive hydraulic head that causes brine to be 'flushed' out of the porous matrix. For flushing to take place the whole ice sheet has to be sufficiently permeable (i.e. have a brine volume $\gtrsim 5$ %). This is usually the case in the melt season when the ice is warm, however when the ice is thin it will also have a high salinity and hence permeability. The amount and rate of fluid displacement can then be calculated from Darcy's law (e.g. Eicken et al., 2004).

Notz (2005) and Notz and Worster (2008; 2009) recently re-examined the effects of brine pocket migration, brine expulsion, gravity drainage and flushing on the salinity evolution in sea ice through a series of analytical and numerical studies, laboratory experiments and field work. They found gravity drainage and flushing to be the only mechanisms through which significant amounts of salt are lost from first-year sea ice, with only minor internal re-distribution of salt caused by brine expulsion. In this thesis, I will only consider brine drainage and flushing to be of importance in the desalination of sea ice.

2.4 Strength of sea ice

Strength is the mechanical property of ice that is perhaps of most interest to engineers when dealing with problems such as specifying the ice forces acting on a structure or the load bearing capacity of an ice cover. Strength is defined as the maximum stress that a test specimen can support. The reference to test specimen is of importance since strength is not a fundamental material property, in the way that the fracture toughness is, as it is also scale dependent. This is because the ice is extremely brittle and contains natural cracks and flaws. The larger the sample or the failure zone, the higher the probability of a larger number of natural flaws and for the failure process to be non-simultaneous across the zone of failure. These processes lead to large scale ice strengths being lower than those measured on small samples (Sanderson, 1988). Nevertheless, small-scale strength tests are of interest

for inter-comparison between ice types from one region to another. Strength is further qualified by the type of failure mode. Ice may fail on a structure by crushing, bending, shearing or some combination of these failure modes (Timco and Frederking, 1990). Vastly different strengths are associated with each mode of failure. Crushing is the best measure of the force exerted on a structure by moving ice forces; bending is of interest for interactions with inclined structures; shear is of importance when considering the load carrying capacity on an ice sheet (Freitag and McFadden, 1997). In this section I present a brief review of the compressive and shear strength of sea ice as these are the two types of tests that have been carried out for this research. Additional information on the strength of sea ice can be found in Sanderson (1988), Tskiner (1994), Ashton (1986) and Timco and Weeks (2010).

Compressive strength

The compressive strength of sea ice is of fundamental importance in ice mechanics. This is because observations show that ice often fails in compression either by the formation of pressure ridges or by crushing against an offshore structure (Timco and Weeks, 2010). To date there is no well accepted method for measuring the compressive strength of ice, especially in the field. Unconfined uniaxial tests are the most common test carried out to define the ice properties where axial force is applied to a specimen that is unstrained laterally and free to deform. Samples are typically prismatic or cylindrical , 7-10 cm in diameter and have a length to diameter ratio of 2-3:1 (Schwartz et al., 1981).

Many investigators (Butkovitch, 1959; Frederking and Timco, 1983; 1984b; Moslet, 2007; Peyton, 1966; Sinha, 1983a; Sinha, 1983b; Wang, 1979) have measured the uniaxial compressive strength of small samples of sea ice. It has been found that values of the uniaxial compressive strength for ice range from 0.5 to 15 MPa and that several factors influence the measured strength of sea ice. These factors are either related to the physical properties of the ice (temperature, ice salinity, porosity, ice type, the grain size and orientation) or the test conditions (the loading rate, the loading direction, sample size, stiffness of test machine and sample preparation techniques).

Temperature has a significant effect on the compressive strength of ice. This is attributed principally to the exponential increase in the plastic flow stress with decreasing temperature (Goodman et al., 1981). This also causes ice to become more brittle with decreasing

temperature. However for sea ice there is also a contribution from the effect temperature has on brine volume. As temperature decreases the pure ice content increases and as a result the sea ice becomes stronger and harder. Ice salinity and porosity affect the strength of sea ice in a similar fashion in that as the salinity and porosity increase so does the volume of brine and air inclusions thus decreasing the number of ice-to-ice contacts. Sanderson (1988) proposed that the strength of sea ice conforms to the strength of freshwater ice if allowance is made for the effect of brine by considering a net section stress. Uniaxial compression tests conducted by Zhijun et al. (1995) on ice samples that were taken from the Liaodong Gulf show that the strength of ice decreased by ~50% when the porosity increased from around 2 % to 16 %. Tests were performed in the laboratory at temperatures that ranged from -2 to -5°C.

Grain size and orientation also influence the strength of the ice. Granular ice is typically isotropic as it is a conglomerate of randomly oriented frazil crystals. Columnar ice however, with its strong c-axis alignment in the horizontal is transversely isotropic (orthotropic). There is a strong contrast in the mechanical behaviour of columnar ice when deformed along (vertically) or across (horizontally) the columnar grains. Indeed many experimentalists (Butkovitch, 1959; Frederking and Timco, 1984b; Peyton, 1966; Sinha, 1983b) have found that the compressive strength of vertically loaded ice is about 3 times higher that ice loaded horizontally. This is principally due to the fact that for horizontal loading ice grains will be favourably oriented for easy glide on the basal plane, whereas in vertical loading all grains have their basal planes aligned in, or close to, the loading direction, making basal glide difficult. For sea ice there is also an effect due to the morphology of columnar ice in which brine channels are naturally vertical, so presenting a smaller net section to the loading direction.

Strain rate has a marked influence on the strength of ice. Analyses of compressive strength measurements show that the strength of sea ice increases with strain rate up until about 10^{-3} s^{-1} (see Figure 2.8). This is the ductile failure zone, where deformation is controlled by the number of mobile dislocations occurring along the basal planes in the ice crystals (Goodman et al., 1981). At higher strain rates, plasticity requires higher stresses than is required for cracking to initiate which causes abrupt brittle failure of the ice. However the strength of ice in the range of brittle failure is controversial as experiments are difficult to

control at these high strain rates. For example Peyton (1966) found a decrease in the compressive strength at high strain rates, whereas, Jones (1997) data suggest that uniaxial strength continues to increase up until strain rates of 10^{1} s^{-1}. Sammonds et al. (1998) also found that the compressive strength of multi-year sea ice increased with strain-rate. They argued that the discrepancy can be explained because two failure modes are present: failure by axial splitting at lower stresses, caused by the opening of vertically oriented tension cracks, and shear failure at higher stresses.

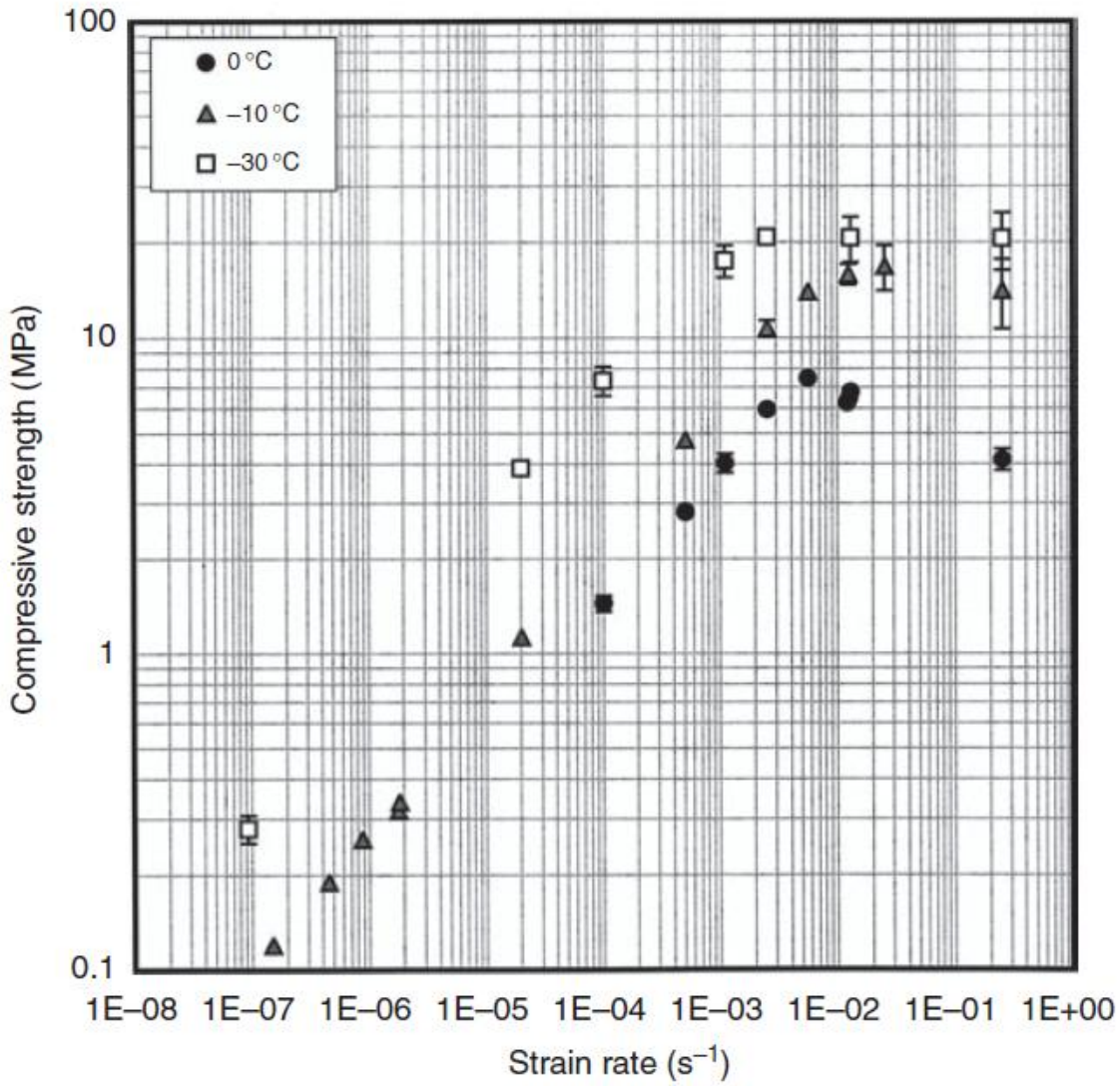

Figure 2.8. Compressive strength of single crystals of ice vs strain rate. The ductile-brittle transition occurs at a strain rate between 10^{-3} s^{-1} and 10^{-2} s^{-1} (taken from Schulson and Duval, 2009).

Shear strength

In many ice interaction problems, ice can be subject to biaxial stress conditions involving tensile stresses and compressive stresses, causing ice to fail in shear. Measurements of shear strength are therefore important for the analysis of ice loads where this type of failure is taking place. In addition, shear strength data are also useful in determining the failure envelope of ice under multiaxial stress conditions (Frederking and Timco, 1984a). Shear is a difficult property to measure, both in terms of performing experiments and interpreting results. This is because in most cases it is assumed that pure shear is generated, whereas in many cases undefined normal stresses are also created in the plane of failure. Previous methods include torsion, direct shear, punching and asymmetric four-point bending.

To date there have been relatively few direct measurements on the shear strength of sea ice. Early work by Butkovich (1956) measured the shear strength of first year sea ice by using the double shear technique. Cylindrical specimens (7.6 cm in diameter and 30 cm long) cut parallel to the growth direction were fixed at both ends to a cylindrical support. The central area of the specimen was loaded perpendicular to its long axis causing shear to occur on two circular surfaces. The total area of both surfaces was then used to calculate shear strength. Results showed that average shear strength was 1600 kPa between the temperature range of -5.5 to -7.3°C and 2380 kPa in the range of -9.9 to -12.8°C. The average salinity of the cores was about 6 ppt. Paige and Lee (1967) and Dykins (1971) carried out single shear tests on cylindrical specimens that were 7.6 cm in diameter and length. Specimens were loaded over opposing semi-circular areas at each end so that failure was generated along the length of the sample. A hole was also drilled into the centre of the specimen to reduce confinement effects. Samples were oriented so that failure was parallel to the growth direction. Paige and Lee (1967) found shear strengths that ranged from 500 to 1200 kPa for naturally grown sea ice. Dykins (1971) obtained values in the range of 100 to 250 MPa for laboratory grown sea ice.

Frederking and Timco (1984a; 1986) employed the asymmetric four-point bending (AFPB) as a method of performing improved shear tests on ice. Originally developed by Stepetz et al. (1978) to evaluate shear properties of large metallic specimens and polymer composites, the AFPB provides a nearly pure stress state by applying a load to four points on a beam.

Beams of dimensions 40 cm long, 50 cm wide and 10 cm thick were loaded between two aluminium plates each with a bar and a ball (12 mm in diameter) positioned asymmetrically about the loading axis (see Figure 2.9). Load was applied by a test machine to the upper plate and transferred to the specimen via the bars and balls producing a region of high shear and low bending in the centre of the specimen. Assuming the shear stress distribution at the centre plane to be parabolic, they found the maximum shear stress at mid height of the beam to be given by

$$\tau = \frac{3}{2}\frac{(1-\alpha)}{(1+\alpha)}\frac{P}{bh} \tag{2.6}$$

where P is the total applied load, b and h are the specimen thickness and height, and α relates to the loading geometry. For granular sea ice collected in the Beaufort Sea, they found the average shear strength to be 550 ±120 kPa for an average test temperature of -13°C and salinity of 4.2 ppt. Their data also showed that there was no functional dependence of strength on loading rate or orientation of the sample, which they attributed to the isotropic natural of granular ice. They did note however that at lower loading rates of 1 mm min^{-1} some indentation was caused by the bars. Frederking and Timco (1986) measured the shear strength of columnar grained ice from Labrador and found that at -12°C the average horizontal shear strength (760 kPa) was greater than the vertical shear strength (645 kPa) for ice with a salinity of 1.9 ppt. As already mentioned, such a difference is expected as this is the easy fail direction for a shear test. Counter-intuitively, at a temperature of -2°C the average vertical shear strength (715 kPa) was greater than the horizontal shear strength (560 kPa). They gave no explanation for this anomalous behaviour, although Barnes et al. (1971) proposed that grain boundary sliding is promoted at temperatures close to the melting point, which would be more effective for this orientation. At lower temperatures, they noted that failure always extended between the inner loading pins and was always abrupt with an instantaneous drop off load, whereas at higher temperatures the deformation was typically ductile and in some cases the specimen did not fail but reached an upper yield stress combined with indentation of the inner loading bars into the specimen.

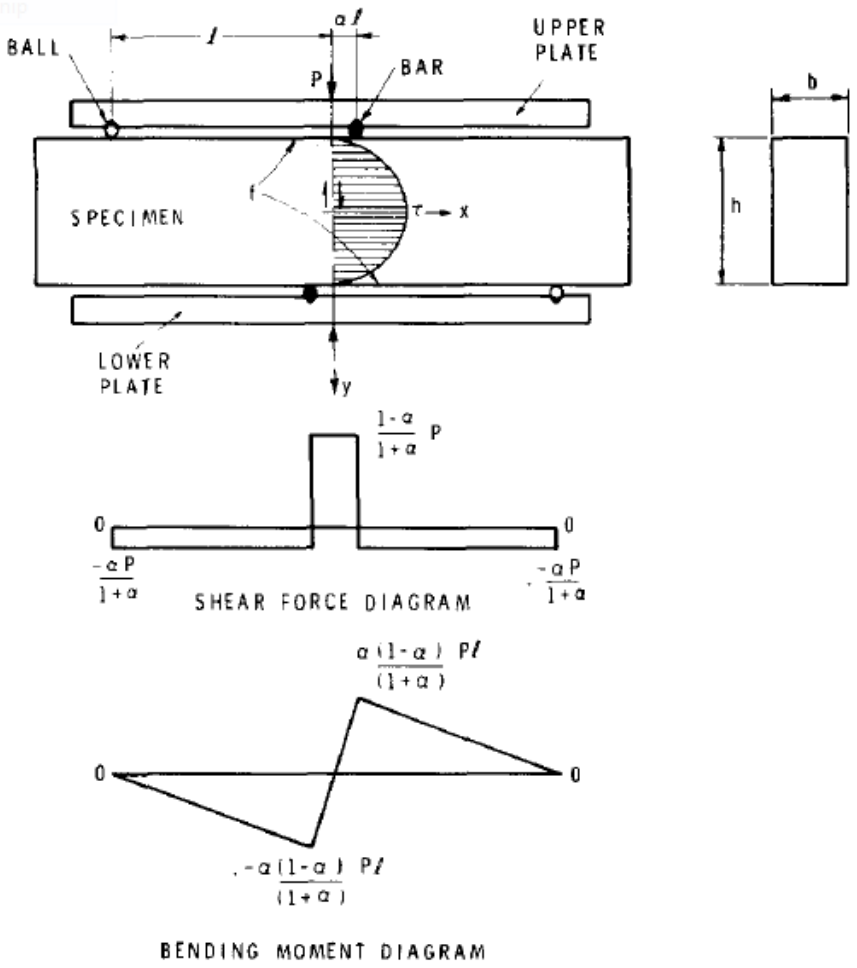

Figure 2.9. Asymmetric four-point bending (AFPB) apparatus and shear force and bending moment diagrams (from Frederking and Timco, 1984a).

Frederking et al. (1988) later carried out a finite element analysis on beams subjected to AFPB to calculate the internal stress fields for different specimen and loading geometries. Their simulations showed that the shear stresses determined from these stress fields were considerably different from the parabolic distribution calculated in simple beam theory (Eq. 2.5). They then conducted laboratory experiments on samples of fresh water columnar ice and found that consistent values of shear strength could be obtained provided specimen and loading geometries did not vary beyond a particular range. Based on this experience, they recommended the following test conditions:

- beams of dimensions 35 cm long, 50 cm wide and 10 cm thick

- a loading position $\alpha = 0.1$ (for this set-up the outer and inner loading pins are located 15 cm, i.e. L=15 cm, and 1.5 cm from the centre line)
- use stress relief material under loading pins (e.g. bakerlite or cardboard)

Using these conditions they found that the average shear strength of fresh water columnar-grained ice was 600 kPa at an average temperature of -10°C. All ice samples were loaded with the long axis of columnar grains normal to the loading axis at a nominal actuator rate of 30 mm min^{-1}.

Overall, there is substantial spread in the measured shear strength of sea ice. This is because many of the test methods impose unrealistic and unknown normal stresses in the plane of failure making it difficult the compare the results from various investigators. The AFPB method, with its better-defined loading condition produces greater consistency in shear strength results. Therefore in this thesis, the AFPB shall be used to determine the shear strength of the bond between two rafted ice blocks.

2.5 Ice conditions

Geographic location plays an important role in the different ice conditions prevalent in different regions. In this section the types of sea ice predominant in the Arctic, Antarctic and the north Caspian Sea are described, which are later used as case studies in our modelling and experimental studies. Table 2.2 shows a summary of the major differences between the Arctic, Antarctic and north Caspian Sea.

Table 2.2. Major differences between the Arctic Ocean, Antarctic Southern Ocean and north Caspian Sea.

Variable	Arctic	Antarctic	North Caspian Sea
Latitude range	90-44°N	55-75°S	47- 43°N
Maximum extent (km^2)	$15.7 \cdot 10^6$ (Mar.) (Comiso, 2003)	$18.8 \cdot 10^6$ (Sept.) (Comiso, 2003)	$7.1 \cdot 10^4$ (Feb.)
Minimum extent (km^2)	$9.3 \cdot 10^6$ (Sept.) (Comiso, 2003)	$3.6 \cdot 10^6$ (Feb.) (Comiso, 2003)	0
Seawater salinity (ppt)	30-32 (Wadhams, 2000)	33-35 (Wadhams, 2000)	6-8
First year sea ice salinity (ppt)	4-10 (Wadhams, 2000)	5-14 (Wadhams, 2000)	1-2
Mean ice thickness (m)	3 (Wadhams, 2000)	0.5-0.6 (Wadhams, 2000)	0.35-0.5
Texture	5-20 % frazil (Tucker et al., 1987)	50-60 % frazil (Lange et al., 1989)	-
Drift velocity (ms^{-1})	0.02 (Gow and Tucker, 1990)	>0.2 (Ackley, 1981)	0.3
Snow cover (m)	0.3 (Warren et al., 1999)	0.5 (Massom et al., 2001)	0-0.1
Mean ocean heat flux (Wm^{-2})	4 (Haas, 2003)	40 (Haas, 2003)	10

Arctic

Sea ice in the Arctic Ocean is at its maximum extent in February/March, covering an area of $15.7 \cdot 10^6$ km^2, and is at its minimum in September (Comiso, 2003). At maximum extent, sea ice covers the entire Arctic Basin reaching its lowest latitude (44°N) in the northern Sea

of Japan. Most of the Arctic Ocean is surrounded by land, with its only major deep outlet through the Fram Strait. Ice motion is therefore confined by coasts where the ice converges and thickens by deformation. Ice can drift for 3-6 years (Colony and Thorndike, 1984) thickening through dynamic and thermodynamic processes until it reaches an equilibrium thickness, where it can survive the summer to become multiyear ice. There is little snow cover in the Arctic, which acts to accelerate ice growth. The Arctic Ocean has a comparably low surface salinity (30-32 ppt) due to the large influx of fresh water supplied by rivers draining into the Arctic Basin. This gives rise to a strong pynocline preventing any significant heat flux from warmer underlying Atlantic waters. The average oceanic heat flux for the Arctic Ocean is 4 Wm^{-2} (Haas, 2003). Recent estimates of Arctic sea ice thickness from satellite altimetry show an overall thinning of ~0.6 m in multiyear ice thickness between 2004 and 2008 (Kwok et al., 2009). In contrast, the average thickness of the seasonal first-year ice in mid-winter (~2 m) has not changed. The total area covered by multiyear ice in the winter shrank by 42% in since 2005 while the first year ice cover gained volume due to increased overall coverage of the Arctic Ocean. These changes have resulted in seasonal ice becoming the dominant Arctic sea ice type for the first time on record (Giles et al., 2008b; Kwok and Rothrock, 2009).

Antarctic

The sea ice conditions in the Antarctic are very different from those found in the Arctic principally due to the unconfined nature of the Southern Ocean. The Southern Ocean is circumpolar and is connected to the Indian, Atlantic and Pacific Oceans. This causes the ice to drift northwards towards the open oceans forming new leads and subsequent new ice growth. There is also no fresh water run-off into the Southern Ocean resulting in a saltier (33-35 ppt), less stratified mixed layer allowing for greater vertical mixing and heat transfer with the warmer underlying ocean. The average oceanic heat flux for the Antarctic Southern Ocean is 40 Wm^{-2} (Haas, 2003). The open ocean also provides a permanent source of moisture, allowing for heavy snow fall. On perennial ice in the Weddell Sea the snow depth can exceed 0.5 m (Massom et al., 2001), which acts to limit the thermodynamic growth of the sea ice [and also inhibits satellite altimeter measurements of ice thickness (Giles et al., 2008a)]. The resultant ice cover is predominately thin, 0.5-0.6 m, first year ice (Wadhams, 2000). With the seasons reversed, the maximum ice extent in the Antarctic

occurs in August/September ($18.8 \cdot 10^6$ km^2) and is at its minimum in February ($3.6 \cdot 10^6$ km^2) (Comiso, 2003). The winter ice extent also exceeds that of the Arctic winter stretching north to about 55°S.

North Caspian Sea

Sea ice conditions in the Caspian Sea are different to those found anywhere else in the world owing to some of the unique characteristics of the Caspian Sea. The Caspian Sea is located at the southerly limit of sea ice formation (see Figure 2.1) and as a result ice conditions can vary considerably from one season to the next depending on the severity of the winter. In mild winters, the level ice thickness can be limited to 35 cm and extend only to near shore areas east of the Volga Delta and along the east coast north of Arman. In harsh winters, the level ice can reach up to 90 cm thick and extend as far south as Baku on the west coast and as far as Aktau on the east coast (see Figure 2.10). The salinity of the north Caspian Sea is considerably lower than the open ocean, ranging from as low as 1-2 ppt near the Volga delta to 8-10 ppt near Aktau. This causes the ice to form readily at the onset of winter as the whole water column need not be cooled to the freezing point (c.f. section 2.2). In addition, the Caspian Sea ice has comparably lower bulk salinity (1-2 ppt) and consequently higher strength than sea ice in the Polar Oceans. There is little snow in the Caspian Sea, which results in faster ice growth rates and lower ice-ice friction (D. Mayne, personal communication, 2007). Ice formation typically begins in late November from the shallow coastal areas in the northeast and descends south along the shoreline forming the landfast ice zone. The ice then grows further seaward reaching its maximum ice extent in February, covering most of the north Caspian Sea (see Figure 2.11). In March, the ice front begins to retreat and the Caspian Sea is ice free by early to mid April. Winds in the region are strong resulting in fracturing and deformation of the ice cover (Terziev et al., 1992). Rafting is particularly common in the north Caspian, where ice sheets override each other multiple times to produce thick sea ice features. Rafted sections have been observed to contain up to 13 layers, all of roughly equal thickness, producing structures that are greater than 4 m in thickness (see Figure 2.12). The horizontal extent of rafted features has also been observed to extend for several hundred metres (D. Mayne, personal communication, 2007). Ice pressure ridges (elongated piles of ice rubble) and hummocks (piles of ice rubble above the ice surface), which form during compressive deformation of

the ice cover, are also common. In most regions pressure ridges produce the greatest loads on offshore structures. In the north Caspian Sea the shallow waters (1-5 m) constrain the size to which pressure ridges can grow. In addition, the lack of significant snow cover, and the low salinity of Caspian ice, seems to favour rafting over ridging. Therefore it is likely that rafted sea ice is the governing design ice feature for ice load calculations in the Caspian Sea. Rafting shall be discussed in greater detail in Chapter 3.

Figure 2.10. Ice conditions in the north Caspian Sea showing the ice extent in a 1) mild, 2) moderate and 3) severe winter. The circles show the average length of the ice period in days (top) and the maximum ice thickness in cm (bottom) in each location and the contours the show the depth in meters (after Atlas, 1997).

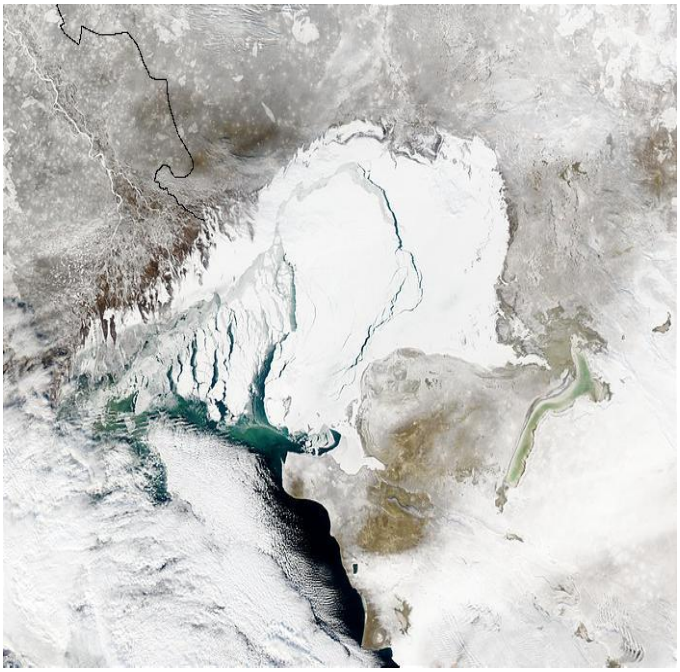

Figure 2.11. Sea ice in the north Caspian Sea. Image taken from the Aqua satellite on 18th Dec. 2002 (taken from http://rapidfire.sci.gsfc.nasa.gov/gallery/index.cgi?20023451211/Kazakhstan.A20023450925.1km.jpg).

Figure 2.12. A section of multiply rafted sea ice in the Caspian Sea (courtesy of D. Mayne).

2.6 Summary

In this chapter, the formation, growth, structure and salt content of first year sea ice have been described. It was explained that sea ice is composed of a solid matrix of essentially pure ice with brine trapped at the sub-grain boundaries within the ice lattice, referred to as a mushy layer. The ratio of liquid brine to solid ice is important as it determines many of the thermodynamic, optical, mechanical and electrical properties of sea ice. With time the salinity of sea ice gradually reduces as brine drains out of the ice and into the ocean below through a network of brine drainage channels. The physical processes responsible for this desalination (brine diffusion, brine expulsion, gravity drainage and flushing) have been summarised. Gravity drainage and flushing have been shown to be the only mechanisms through which considerable amounts of brine is lost from sea ice.

A brief summary of previous research on the compressive and shear strength of sea ice has been presented. Values for the compressive strength of first-year sea ice range from 0.5 to 15 MPa and depend on many factors relating to the physical properties of the ice and the test conditions. There is considerable scatter in the shear strengths measured for sea ice which is principally due to difficulties in performing experiments that produce a zone of pure shear. Frederking and Timco (1984a; 1986) suggested asymmetric four-point bending (AFPB) as a method of performing improved shear tests on ice. They found greater consistency in results with average shear strengths of 550 ±120 kPa for granular sea ice and 550 to 900 kPa for columnar sea ice.

The predominant sea ice types in the Arctic, Antarctic and the north Caspian Sea were then described with emphasis on parameters that are needed for my modelling and experimental studies. The Arctic Ocean has a lower surface salinity (30-33ppt) and hence sea ice salinity (4-10 ppt) in comparison to the Southern Ocean (33-35 ppt; 5-14 ppt) which is due to the large influx of fresh water which drains into the Arctic basin. This induces a strong pynocline, which causes the oceanic heat flux to be markedly lower in the Arctic (4 Wm^{-2}) than the Antarctic (40 Wm^{-2}). In the north Caspian Sea, the salinity is considerably lower (6-8 ppt), which in turn lowers the bulk salinity of the ice (1-2 ppt) and alters its physical and mechanical properties. The thin ice cover and strong winds causes ice to readily raft producing thick structures which pose a threat to offshore structures in the region.

3 Rafting

3.1 Introduction

The sea ice cover is rarely stable: winds and ocean currents exert shear on the surfaces of the ice causing it to drift. If internal stresses in the ice cover are high enough, ice will fracture and open-water leads will form. Leads are then either quickly refrozen or further motion causes the ice to collide or shear past other ice forming sea ice features such as ridges or rafted sea ice. Ridges are elongated piles of rubble and rafting is the simple overriding of one sheet by another. Understanding these processes is important because the energy expended in deformation determines the large scale strength of the pack ice and because the strength and thickness of ridges and rafted sea ice are important in the design and operation of offshore structures (Sanderson, 1988). In addition, rafting and ridging play an important role in the mechanical re-distribution of the sea ice thickness (Babko et al., 2002; Toyota et al., 2004).

Since the main focus of this thesis is rafted sea ice, in this chapter I will describe the different types of rafted sea ice. This will be followed by a synopsis on previous work that has been carried out on rafted sea ice. I then describe the mechanics of rafting, discuss the provenance of the liquid layer between rafted layers and outline complementary studies on the consolidation and strength of rafted ice.

3.2 Types of rafted sea ice

Rafting occurs when driving forces such a winds or currents cause ice floes to collide such that one floe is pushed above or below the other, resulting in a layered structure (Tuhkuri and Lensu, 1997). Two types of rafting have been identified: a) simple rafting, where the two ice sheets interact along a straight edge and one sheet ‘simply’ overrides the other and b) finger rafting, where the interacting sheets fracture along lines perpendicular to their interacting edge and form fingers. Alternate fingers are then over-thrust and under-thrust, leaving an interlocked structure (Weeks and Kovacs, 1970). Multiple rafting has also been known to occur in some regions. In this case, ice floes override one another multiple times to produce thick sea ice features. These processes are illustrated in Figures 3.1 and 3.2.

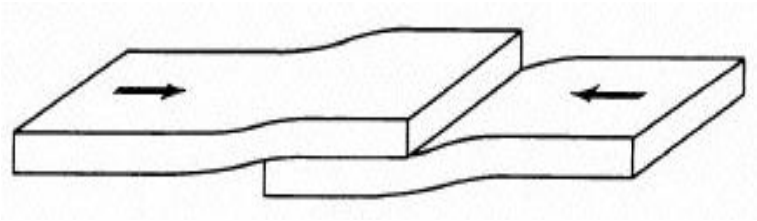

Figure 3.1. Schematic of simple rafting. Image taken from Sanderson (1988).

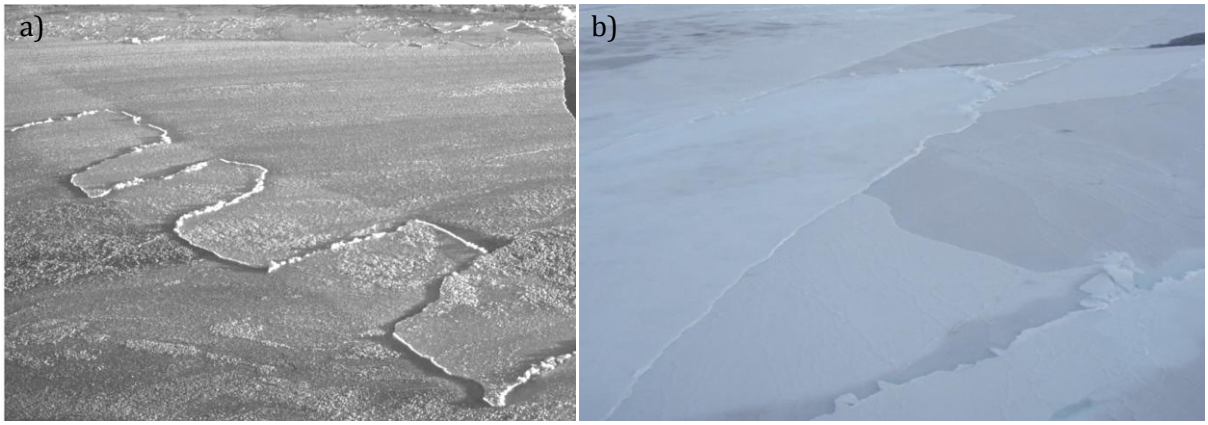

Figure 3.2. Photographs of a) finger rafting of thin sea ice in the Amundsen Sea (courtesy of W. F. Weeks, On Sea Ice, submitted to University of Alaska Fairbanks Press, 2008) and b) multiple rafting of large sea ice floes in Antarctica (courtesy of R. Willatt, CPOM).

3.3 Rafting versus ridging

To date rafting has not received much attention in the literature. This is perhaps because in the Arctic, ridges and multiyear sea ice are the key design features for ice load calculations on offshore structures (Hopkins et al., 1999; Sammonds et al., 1998). There are also practical difficulties in identifying rafted ice thicker than 0.15-0.20 m in aerial imagery or of any other thickness in laser profiles or under-ice sonar records (Babko et al., 2002). Previous studies have focussed on the conditions that are favourable for rafting as opposed to ridging to take place (Hopkins et al., 1999; Parmerter, 1975; Tuhkuri and Lensu, 1998; 2002; Vella and Wettlaufer, 2008; Weeks and Kovacs, 1970) or on modelling the rafting process itself (Li and Sun, 2009; Marchenko and Makshtas, 2005). Weeks and Kovacs (1970) concluded from field observations that the transition from ridging to rafting depends on the thickness of the sheets. They proposed that this transition usually occurs at a thickness between 0.15 and 0.3 m, although on occasion thicker ice may raft without breaking. They also noted that rafting tended to occur between ice sheets of similar thickness. Parmerter (1975) developed a mechanical model of simple rafting where he

assumed that rafting can only occur if the maximum stress produced by the deformation does not exceed fracture levels. If fracture occurs, the ice will break into blocks and form a ridge. Numerical simulations revealed that the thicker the ice sheet the higher the maximum stress. Hence a crossover point between ridging and rafting could be found. Parmerter (1975) found that the maximum thickness that an ice sheet can be in order to raft is

$$t_{max} = 14.2 \frac{(1 - v^2)}{\rho_w g} \frac{\sigma^2}{E}, \tag{3.1}$$

where v is Poisson's ratio, ρ_w is the density of water, σ is the (bending) strength of the ice and E is Young's Modulus. Using typical young ice properties he found that the maximum thickness that an ice sheet can be to raft is ~17 cm. However, he noted that the variability in ice properties might allow for the occasional rafting of much thicker ice.

There are a few observations of rafting of much thicker ice (Babko et al., 2002): Kovacs (1970) observed rafting between 2 m thick ice sheets near Hershel Island; in the central Beaufort Sea, Kovacs and Mellor (1974) observed 3.3 m thick rafted ice.

Numerical simulations carried out by Hopkins et al. (1999) showed that rafting of thicker ice sheets (0.5-0.9 m) was possible. However they noted that the rafting was preceded by a rubble building stage, where the interacting sheets bumped together causing the floe fronts to abrade and break-up forming a pile of rubble. The rubble then served as a ramp lifting one sheet above the other. Vella and Wettlaufer (2008) investigated the effects of rubble building in the rafting process using a simplified version of Parmerter's (1975) model. They found that the presence of rubble between two ice sheets in simple rafting can indeed increase the maximum thickness that ice floes can raft up to 1 m.

Hopkins et al. (1999) suggested thickness inhomogeneity to be an important parameter governing the likelihood between ridging and rafting. They found that simulations run with ice sheets of uniform thickness resulted in rafting, whereas to create ridges it was necessary to use ice sheets of non-uniform thickness. Concurrent ice basin tests run by Tuhkuri and Lensu (1998; 2002), in which two identical sheets were pushed together also showed that sheets of uniform thickness tended to raft. When ice sheets of non-uniform thickness were

used, results showed that ridging was always initiated by a period of rafting. This Tuhkuri and Lensu (2002) suggest implies that ridging and rafting are not two separate processes, but rather different stages of a single process.

If ridging is initiated from rafting one would expect to find rafted layers located between the sail and keel of the ridge. There are some observations of this. For example, Tuhkuri (1999) studied three ridges in the northern Baltic and found that they all contained at least 5 rafted layers. Kankaanpää (1997) studied two ridges in the Baltic and found that in one ridge two ice sheets had rafted and in the other that there were 4 to 5 rafted layers. In the north Caspian Sea, similar features were found containing around 9 fully bonded rafted layers approximately 0.10 to 0.13m thick. Extensive drilling and under-ice surveys revealed that there was no appreciable keel to be found (D. Mayne, personnel communication, 2007). Similarly, Marchenko and Makshtas (2005) surveyed ridges in the Barents sea and found that the ridges formed from rafted ice had no well defined keels. Figure 3.3 shows a schematic of the structure one might expect to find.

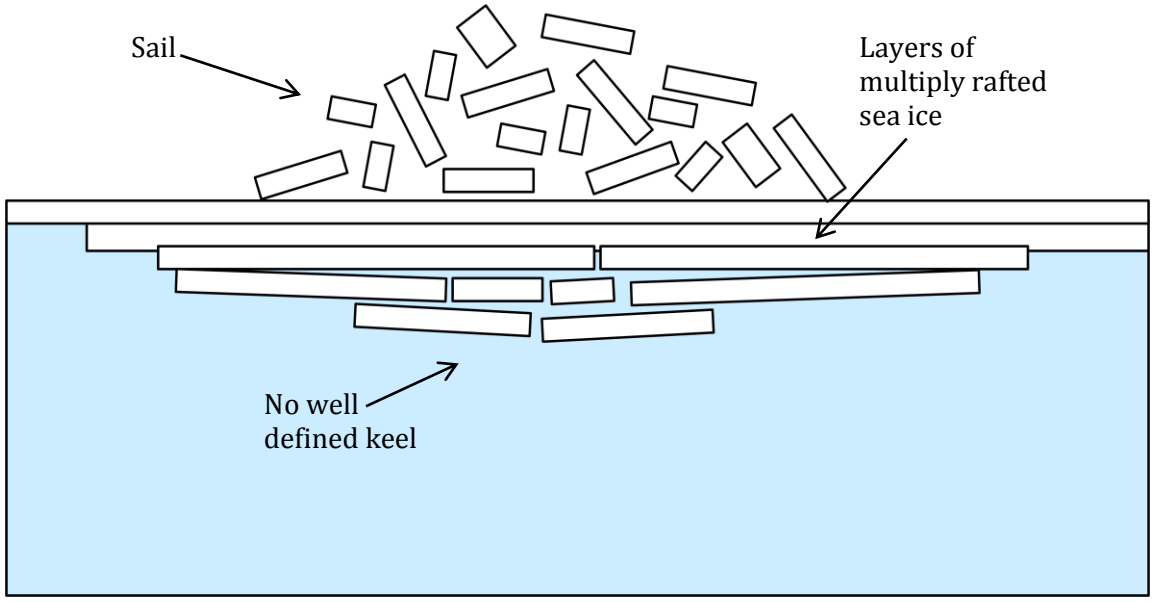

Figure 3.3. Schematic diagram of ridging of rafted sea ice, after Marchenko and Makshtas (2005).

3.4 Mechanics of rafting

Rafting initiates when one ice sheet overrides another and progresses until the frictional force between the sheets arrests motion or the internal stresses in the sheet cause the ice to fracture. The frictional force that resists motion is proportional to the upward acting net buoyancy of the bottom sheet and the coefficient of kinetic friction μ acting between the ice sheets (Hopkins et al., 1999). The rafting force F_r that is required to overcome this is dependent on the area of contact between the two ice sheets and is given by:

$$F_r = \mu \Delta \rho g h L, \tag{3.2}$$

where $\Delta\rho$ is the difference in density between the ice and the water, g is the acceleration due to gravity, h is the thickness of the ice sheet and L is the overlap between the ice sheets. Most of these parameters are quite easy to define except μ which for rafting is dependent on the sliding velocity, the surface roughness, the temperature and the presence of snow or water, all of which are poorly characterized.

Figure 3.4. Photograph of the liquid layer found between two consolidated ice floes, which is ~1-2 mm in thickness (courtesy D. Mayne).

There is a thin layer of liquid between rafting ice floes (Figure 3.4). The presence of a liquid layer acts to reduce frictional forces between the rafting ice sheets and explains why rafted floes have been observed to extend for several hundred metres, even during calm periods where the wind velocity is under 8 ms^{-1} (Weeks and Anderson, 1958). Field studies in the north Caspian Sea have shown that the thickness of this layer can vary from less than 1 mm up to 11 cm suggesting a combination of mechanisms is responsible for the formation of the liquid layer found between rafted ice floes. This topic has surprisingly received little attention in the literature. Here, I discuss possible mechanisms that may contribute to the formation of the liquid layer found between rafted ice sheets.

It has long been known that ice exhibits exceptionally low friction in sliding by comparison to other materials. Its low friction is attributed to a lubricating layer of melt water resulting from frictional heating, whereby heat is generated from the plastic deformation of the asperities on the ice surface (Bowden and Hughes, 1939). Bowden and Hughes measured the electrical conductivity between two electrodes set into the bottom of an ebonite ski sliding on ice. They found that when surface melting was occurring there was a sudden rise in conductivity. Assuming the composition of the melted liquid to be the same as that of the original solution, they estimated the thickness of the liquid film to be ~0.07 mm. The conditions for rafting would be different from those in the experiments of Bowden and Hughes (1939), namely both surfaces are ice, the sliding velocity would be significantly lower (Bowden and Hughes used a velocity of 4 ms^{-1}), and the surface roughness would be greater. I do not consider here how these variables may affect the thickness of the liquid layer, as it is beyond the scope of this thesis, but they are discussed by Oksanen and Keinonen (1982) and Hatton et al. (2009). However, I surmise that the contribution of liquid from frictional heating to the thickness of the water layer would have an upper bound of a few tenths of a millimetre and therefore could not explain the thicker liquid layers observed between rafted layers of sea ice.

Another process which may contribute to the formation of the liquid layer is brine draining from the upper rafted ice sheet into the liquid layer. As the upper sheet is lifted from the sea water it is no longer in hydrostatic equilibrium and this induces a positive hydraulic head in the brine drainage network. This acts gradually to increase the salinity of the liquid layer, and thus reduce its freezing temperature. This is confirmed by observations made on the

physical properties of rafted ice in the Sea of Okhotsk which show that the boundaries between rafted layers are marked by regions of high salinity.

The third mechanism that may be responsible for the formation of the liquid layer is simply fragments of ice caught between the ice sheets acting as spacers which allow seawater to flood in. In the 2 m thick rafted ice which Kovacs (1970) observed, he found a 1.3 m deep cavity between the rafted ice sheets held apart by fragments of ice which had presumably broken off the leading edges during rafting. This could help explain the higher end of the thicknesses observed.

Although the principal mechanism responsible for the liquid layer presence during rafting is not clear, the surfaces of sea ice floes are rarely smooth. Surface asperities, fragments of ice and the natural undulation of the ice sheet will always cause a separation between rafted ice sheets. If this were not the case the water would get squeezed out the sides. For this reason, in this thesis that I have assumed that the liquid layer is initially a thin layer of ocean water trapped between rafted ice sheets.

3.5 Consolidation of rafted ice

Once two layers of rafting ice have ceased moving, the liquid layer between the ice sheets starts to freeze, i.e. the ice sheets start to consolidate. The bonds between the layers are at first weak but strengthen with time to produce a coherent ice sheet. This is of particular interest because the degree of consolidation will control the strength of rafted sea ice.

There has been no published experimental or theoretical work on the consolidation of rafted sea ice. The only systematic experiments on the consolidation of rafted ice were carried out on freshwater ice in the ice tank at the Technical Research Centre of Finland (VTT) (Veitch et al., 1991). In these experiments, an ice sheet was grown to a thickness of 3 cm and sawn into 12 square ice blocks of side 60 cm. The ice blocks were then assembled into stacks of 2, 4 and 6 layers and left to consolidate at a nominal room temperature of -10°C. Thermocouples recorded the temperature in the liquid layer, at the ice surface and at the ice-water interface. Consolidation was determined by finding the time at which the temperature in the liquid layer fell below its freezing point (0°C for freshwater). The

experiment was repeated with ice thicknesses of 6 and 9 cm. Their results showed that it took respectively ~3, 8 and 9 hrs for two layers of rafted ice 3, 6, and 9 cm thick to consolidate. The greater the number of ice layers the faster the consolidation of the respective layers. For example, for 6 layers of ice, the top 3 liquid layers froze faster than the 3 liquid layers in a 4-layer stack of ice.

Marchenko and Chenot (2009) carried out experiments in the cold rooms at University Centre in Svalbard, Norway. Cylindrical samples of fresh water ice (7cm in diameter) were frozen onto a steel rod and a 1 cm gap cut out of the centre sample. The ice was then submerged in a bucket of 34 ppt sea water, held constant at its freezing point, and left to consolidate in a cold room at -21°C. Their results show that it took ~53 minutes for the ice to bond. The ice tended to grow from the centre out, most probably as a consequence of the metal rod, which would conduct heat away at a much greater rate than the water or ice.

Marchenko and Chenot (2009) also carried out consolidation experiments on drifting ice in the Barents Sea in April 2006. They measured the cohesion between two submerged ice disks that were ~15 cm in diameter and 3-4 cm thick and found that after a period of 2 days the disks had not frozen together. They also submerged an ice beam that had dimensions 3 m x 0.5 m x 0.5 m below level ice and found that after a day it was still possible to move the beam using a shovel. During these experiments the mean air temperature was -8°C, fluctuating between -11°C at night to -6°C during the day. While these results are inconclusive they give some indication as to the time scales that are expected for the consolidation between rafted sea ice floes.

3.6 The strength of rafted sea ice

In offshore engineering literature, there is debate as to whether rafted sea ice is weaker than level ice. The argument that rafted ice is weaker is based on the idea that the strength of the bond between rafted layers is lower than the strength of level ice. At present, most ice design load calculations assume that the strength of rafted ice is 10-20% less than that of level ice of the same thickness (Jizu et al., 1991). However, there are no direct experimental data to back this assumption.

Shafrova and Hoyland (2008) compared the strength of freeze bonds between sea ice blocks with the strength of submerged blocks of level ice both in the field and in the laboratory. To set up their field experiment, they cut six ice cubes with dimensions of 24 cm from the ice sheet. Half the cubes were sawn in two at a 45° angle: the remainder were left intact. The cubes were placed in aluminium cages and submerged 0.15 m below sea level. After 48 hrs, the blocks were removed and strength tested under uniaxial compression at a strain rate of 10^{-3} s^{-1}. Their field results show that (i) the freeze bond strength varied from 14-73 kPa, and (ii) the submerged level ice was on average 33 times stronger than the freeze bonded ice. In the laboratory experiments, a similar set up was used, however the major difference was that the cages were modified to include steel springs to provide confining load. Their laboratory results show that after 60 hrs submerged (i) the freeze bond strength varied from 15-197 kPa, and (ii) the level ice was ~7 times stronger than the freeze bonded ice. Shafrova and Hoyland (2008) attributed the higher strengths observed in the laboratory to the confining load. Their results also showed that initially colder, less porous and less saline ice had higher freeze bond strength.

Repetto-Llamazares et al. (2009a) investigated the strength of freeze bonds by conducting direct shear tests in the Hamburgische Schiffbau-Versuchsanstalt (HSVA) ice tank. During an experiment, a saline ice sheet was grown to a thickness of 3-4 cm and cut into 14 cm square blocks. The blocks were conditioned in a freezer to the isothermal test temperature. Two blocks were then pressed together under normal stress and submerged in the large HSVA ice tank. After a specified time, the blocks were removed from the water and tested in direct shear at a loading speed of 42 mm min^{-1} under the same normal stress that was applied during submergence. Experiments were carried out under varying initial ice temperature (-1.2, -7.5, -13°C), normal stress (125, 637, 1205, 2040 Pa) and submerged time (1, 4.5, 10, 20 hrs). Their experiments exhibited both ductile and brittle failure modes, with the latter occurring at higher shear strengths. Shear strengths varied between 1-3 kPa. They found the greater the submerged time the lower the shear strength. However, there were no clear trends in shear strength with variations in temperature and normal stress, which they attributed to uncertainties in experimental procedure. Repetto-Llamazares et al. (2009b) also carried out direct shear tests on samples of rafted ice taken from the keels of model ice ridges, formed in the HSVA ice tank. They found the shear strength of these

rafted ice floes was the same order of magnitude as freeze bond blocks that had been constructed artificially.

The freeze bond strengths observed by Shafrova and Hoyland (2008) and Repetto-Llamazares et al. (2009a, 2009b) cannot be directly related to rafted sea ice found in situ. This is because in their experiments there is no atmospheric flux as the ice blocks are totally submerged in water, whereas in a rafted section the top ice block would be exposed to the atmosphere thus allowing heat to be conducted away from the freeze bond/ liquid layer creating a much stronger bond. These freeze bond strengths may however provide us with a lower bound strength that may be observed between rafted ice blocks that are partially consolidated. They may also be representative of bonds found between the lower ice sheets in multiply rafted sea ice that are submerged below the water line.

Poplin and Wang (1994) compared the mechanical properties of rafted sea ice with first-year landfast sea ice collected in Norton Sound, Alaska. 50 vertically-oriented samples taken perpendicular to the plane of the ice sheet, and 357 horizontally-oriented samples, taken parallel to the ice sheet plane, were tested under uniaxial compression at in situ temperatures. Their results showed that for vertical samples, the mean compressive strength of landfast ice (8.32 MPa) was significantly larger than for rafted ice (3.28 MPa), at a strain rate of 10^{-4} s^{-1}. For horizontal samples the mean compressive strengths of the rafted ice were actually larger (1.55 and 1.06 MPa) than the corresponding landfast ice (1.25 and 0.64 MPa), at strain rates of 10^{-4} and 10^{-5} s^{-1} respectively. Poplin and Wang (1994) attributed these differences to the variation in crystallographic structure. The landfast ice samples contained only columnar ice crystals, whereas, the rafted ice was composed of approximately 50% granular and mixed granular and columnar ice crystals. Since ice loads are usually applied horizontally to offshore structures, this result implies that once consolidated, rafted ice may be a significant ice hazard. Indeed Kovacs (1970) noted that areas of rafted ice were considerably more resistant to penetration by icebreaker than ridges of considerably greater thickness and were the cause of much ramming and, of course, delay.

3.7 Summary

In this chapter, the types of rafted sea ice that have been observed in nature have been described and a review has been made of earlier work that has been carried out on rafted sea ice. It was explained that there are two types of rafting; simple rafting and finger rafting both, of which are able to double up to produce a multiply rafted sections of ice. In the review of earlier work I showed that rafting is most common between thin ice sheets (<0.3 m) of uniform thickness. However, rafting of thicker ice sheets is possible when preceded by a rubble building stage, and non-uniform ice sheets can initiate in rafting although they tend to fail and form a ridge after a short distance of overlap.

The processes that I believe contribute to the formation of the liquid layer found between rafting ice sheets were then discussed. I suggested that frictional heating, brine drainage from the upper ice sheet and seawater may all contribute to the formation of the liquid layer. I also point out that it is unlikely that the liquid layer could maintain itself without surface asperities or fragments of ice holding the ice sheets apart. Therefore given that the liquid layer can be several centimetres in thickness, it is likely that some seawater will flood into the void between the rafted sheets. Hence, for the purpose of the modelling and experimental studies presented in this thesis I have assumed that the liquid layer is initially a thin layer of ocean water trapped between the asperities of the rafted ice sheets.

Corresponding studies on the consolidation and strength of rafted sea ice are then described. I explain that prior to the work presented in this thesis the only systematic experiments on the consolidation of rafted sea ice were carried out by of Veitch et al. (1991) on freshwater ice in the VTT ice tank in Finland. Similarly, Poplin and Wang (1994) are the only researchers that I found in the literature that had carried out a comprehensive study on the mechanical properties of rafted sea ice.

4 Thermodynamic modelling of sea ice

4.1 Introduction

The thermodynamics of sea ice is a complex process involving heat exchanges with the atmosphere and ocean. Typically ice grows from the top down and the latent heat of freezing is conducted away through the ice sheet and released into the atmosphere by radiative and turbulent heat fluxes. To a good approximation ice growth is horizontally homogenous, and therefore is traditionally treated as vertically one-dimensional in sea ice models.

In this chapter I give a brief description of previous sea ice models and how they have developed over the past century. I then present the mushy layer equations that are used to describe heat transport within the sea ice and their application to sea ice modelling. I then present a simple thermodynamic model of sea ice growth, which I later develop into a consolidation model for rafted sea ice (Chapter 6). The model is then forced using parameters that are typical to the environments of the north Caspian Sea and the Arctic and Southern Ocean. Numerical simulations are then compared with ice growth rates observed in the respective areas.

4.2 Previous models of sea ice

Previous research has formulated models to describe the thermodynamic response of the sea ice cover to imposed forcing. Stefan (1891) derived an analytical solution for bare ice growth. In this paper he derived the classic 'Stefan law', where he assumed that the latent heat released by freezing at the bottom surface of the ice sheet is conducted away through the ice driven by a constant temperature gradient, such that

$$\rho_i \mathcal{L} \frac{dH}{dt} = k_i \frac{\left(T_f - T_0\right)}{H}, \tag{4.1}$$

where ρ_i is the ice density, $\mathcal{L}$ the latent heat of fusion, H is the thickness of the ice sheet, t is the time, T_f the freezing temperature of the water, T_0 the temperature at the upper ice

surface and k_i the thermal conductivity of the ice. Solving this for the initial condition, $H = H_0$ at $t = 0$ we find that

$$H^2 = H_0^2 + \frac{2k_i}{\rho_i \mathcal{L}}\theta, \tag{4.2}$$

where

$$\theta = \int_0^t (T_f - T_0)dt \tag{4.3}$$

is commonly referred to as the number of freezing degree-days. This rather basic relationship produced surprisingly good results and as a result is still the basis of many sea ice models today. Stefan did, however, make several assumptions which tended to overestimate the growth rate of an ice cover. Namely, he assumed that there was no thermal inertia, no internal heat sources, no heat flux from the ocean, and a known temperature at the top of the ice cover (Leppäranta, 1993). Later analytical models built on this by for instance adding the influence of a snow layer (Barnes, 1928; Zubov, 1945) or by considering a heat flux from the ocean to the bottom of the growing ice sheet (Allison, 1979; Leppäranta, 1993).

It was not until the 1960s with the introduction of high speed computers that the next real advance in sea ice modelling was made when the first numerical model was introduced (Maykut and Untersteiner, 1971; Untersteiner, 1964). The Maykut and Untersteiner (1971) model is a one-dimensional thermodynamic model that predicts the thickness evolution of multi-year level sea ice subject to a seasonal cycle of atmospheric fluxes, a constant oceanic heat flux and seasonally specified snowfall. Heat transport within the sea ice is governed by the modified heat conduction equation,

$$(\rho c)_{si} \frac{\partial T}{\partial t} = k_{si} \frac{\partial^2 T}{\partial z^2} + A_R, \tag{4.4}$$

where $(\rho c)_{si}$ and k_{si} are respectively, the volumetric specific heat capacity and the thermal conductivity of the sea ice, T is the temperature, z is the vertical coordinate, t refers to time and A_R is a heat source term that describes the internal absorption of solar radiation. Semi empirical equations developed by Untersteiner (1961) were used to describe the thermal properties of the sea ice,

$$(\rho c)_{si} = (\rho c)_i + \gamma \frac{S(z)}{\theta^2} \tag{4.5}$$

and

$$k_{si} = k_i + \beta \frac{S(z)}{\theta}, \tag{4.6}$$

where $(\rho c)_i$ and k_i are respectively, the volumetric specific heat capacity and the thermal conductivity of pure ice, $\theta = T - 273$ is the temperature in °C, $\gamma = 17.15\ \mathrm{MJ\ kg^{-1}K}$ and $\beta = 0.13\ \mathrm{Wm^{-1}}$. The vertically varying salinity profile $S(z)$ was assumed to remain constant (Schwarzacher, 1959), an assumption that is considered to be a limitation in the model. At the upper surface, the incoming and outgoing radiative, sensible and latent heat fluxes were combined with the conduction equation (4.4) to form the surface heat budget. In the absence of surface melting, the surface budget was set to zero and the surface temperature determined by iteration. For a melting surface, the surface temperature was constrained not to exceed 273 K (0°C) and any surplus energy was used to melt the ice, by an amount that was controlled by the latent heat of the sea ice or snow. Similarly, at the ice-ocean interface, ice growth and decay are governed by a balance between the oceanic heat flux and the conductive heat flux in the ice, with any imbalance being compensated for by a change in ice thickness controlled by the latent heat of melting/fusion of the sea ice. Starting from an arbitrary initial condition, the model was integrated numerically until annual equilibrium patterns of temperature and thickness were achieved. Model results generally agreed well with field observations when predicting sea ice conditions in the central Arctic. However, it was later noted that there were uncertainties in values prescribed for the surface albedo, the absorbed solar radiation penetrating into the ice sheet and the oceanic heat flux (Ebert and Curry, 1993). Bitz and Lipscomb (1999) also pointed out that Maykut and Untersteiner (1971) do not make appropriate corrections for the latent heat of melting at the upper surface to account for internal brine-pocket melting. Therefore the model uses more energy than is needed to melt ice at the upper surface.

While the Maykut and Untersteiner (1971) model takes into account most of the important physical processes for modelling sea ice, it is too computationally intensive to be implemented in climate models. Semtner (1976) therefore proposed a simplified version by removing the internal heat source term, prescribing constants for the thermal conductivity and heat capacity, and reducing the vertical resolution of the model to three grid points.

Semtner (1976) also proposed an even more simplified zero version of the model, where a linear temperature profile is assumed for the snow and ice. Due to its simplicity, the zero-layer model has been widely used in climate models to represent the thermodynamic sea-ice component. Semtner (1984) himself has pointed out that the zero-layer model tends to exaggerate the seasonal cycle of sea ice, therefore leading to invalid conclusions about the magnitude of climate change in the polar regions.

The Maykut and Untersteiner (1971) and Semtner (1976) models were the first of their kind in thermodynamics modelling of sea ice and as a result most later formulations are based on these models. For instance, Lemke (1987) coupled the Semtner (1976) model to a mixed layer ocean model; Ebert and Curry (1993) extended the Maykut and Untersteiner (1971) model to include parameterizations of the surface albedo, melt ponds and leads; Bitz & Lipscomb (1999) introduced an energy conserving model that accounts for the effects of internal brine-pocket melting on surface ablation; Taylor and Feltham (2004) developed a thermodynamic-radiative model that explicitly treats melt ponds as an extra phase; and Notz (2005) presented an enthalpy based model.

In the model presented in this thesis I used the same concepts employed in the Maykut and Untersteiner (1971) model, however I have used the mushy layer equations to describe heat transport within the sea ice. Using the mushy layer equations incorporates an extra parameter, the solid fraction, which ensures that energy is conserved at melting interfaces. Therefore to put the model into context I shall now describe the mushy layer theory and its application to sea ice thermodynamics.

4.3 Mushy layers

A mushy layer is a porous medium composed of a nearly pure solid matrix with concentrated liquid trapped within the interstices (pores) of the solid. They form due to a build-up of solute and consequent constitutional supercooling ahead of the freezing interface giving rise to highly convoluted structure that forms the solid matrix of the mushy layer (Worster, 2000). Mushy layers are commonplace in the solidification of alloys (a mixture of two or more components) and as a result arise in a number of geophysical contexts, including freezing of sea ice (as described in Chapter 2.3), solidification of

magma chambers and inner-core solidification. Consequently they have been extensively studied (see Worster, 1992; 1997; 2000 for further details).

Governing equations

The equations governing the internal evolution of a mushy layer are given by the local conservation equations for heat and solute, which expressed in their differential form are

$$c_m \frac{\partial T}{\partial t} + c_l \mathbf{U} \cdot \nabla T = \nabla \cdot (k_m \nabla T) + \mathcal{L}_s \frac{\partial \phi}{\partial t} + A_R \tag{4.7}$$

and

$$(1-\phi)\frac{\partial C}{\partial t} + \mathbf{U} \cdot \nabla C = \nabla \cdot (D_m \nabla C) + r(C - C_s)\frac{\partial \phi}{\partial t}, \tag{4.8}$$

where T and C are the local temperature and the concentration of the interstitial fluid, which are assumed to be uniform over length scales of the inter-dendrite spacing (Worster, 1986). The solid volume fraction, ϕ, describes the proportion of the mush that is solid, where 0 denotes pure liquid and 1 pure solid. The Darcy velocity, **U**, is defined as the volume flux of brine per unit perpendicular cross section area. The effective diffusivity of the solute in the mushy layer, $D_m \simeq (1-\phi)D_l$, where D_l is the diffusivity of the solute. C_s is the concentration of solute that is incorporated into the solid matrix, c_m is the specific heat capacity per unit volume, k_m is the thermal diffusivity, $\mathcal{L}_s$ the latent heat of fusion of the solid per unit volume and $r = \rho_s/\rho_l$ is the density ratio where the subscripts 'm', 'l' and 's' represent properties of the mushy layer, the liquid and solid phases, respectively.

The terms in equation (4.7) from left to right describe, respectively, the rate of change of temperature at a fixed position, the transport of heat caused by the advection of brine, the thermal diffusion, the latent heat released or absorbed in the mush due to internal phase changes and the final term A_R is a source term describing the internal heating due to radiation. Similarly in equation (4.8) the first term describes the rate of change of concentration within a local liquid region, the second term the transport of solute caused by advection, the third term the rate of solutal diffusion and the final term the release or storage of solute into the interstitial fluid due to phase changes. These equations differ from the diffusion equations used in the models of Maykut and Untersteiner (1971) and Ebert and Curry (1993) in that they explicitly account for the evolution of internal solid fraction.

Equations (4.7) and (4.8) are coupled by the assumption that the mushy layer is in local thermodynamic equilibrium. This implies that the temperature and concentration of the solute lie on the liquidus curve in the equilibrium phase diagram. Figure 4.1 shows the equilibrium phase diagram for a typical eutectic binary alloy. The liquidus curve represents the melting/freezing temperature of an alloy as a function of composition marking the separation between a region of pure liquid and one in which the solid and liquid coexist in equilibrium, the latter being the state in the interior of a mushy layer. The solidus curve marks the temperature below which the alloy may form a solid solution of the two components. Below the eutectic point the alloy is a composite solid composed of crystals of both components of the alloy which for sodium chloride solutions is at a temperature of T_E = -21.1°C and a concentration C_E = 233 ppt (Pounder, 1965).

The interface between a mushy layer and a liquid region is a mixture of both dendrites and interstitial fluid. Since the mushy layer quantities are averaged over the scale of the interstitial pores, the interface can be thought of as a region of thickness comparable to the pore scale. Interfacial conditions can then be expressed as a jump across a finite interface (Worster, 2000). The conservation equations of heat and solute across the interface can therefore be calculated by integrating the governing equations (4.7) and (4.8) across the interface, such that

$$\rho_s \mathcal{L} \phi \frac{dh}{dt} = k_m \mathbf{n} \cdot \nabla T|_m - k_l \mathbf{n} \cdot \nabla T|_l \tag{4.9}$$

and

$$(C - C_s)\phi \frac{dh}{dt} = D_m \mathbf{n} \cdot \nabla C|_m - D_l \mathbf{n} \cdot \nabla \mathrm{C}|_l, \tag{4.10}$$

(Worster, 2000) where dh/dt is the velocity of the liquid-mush boundary and **n** is the normal to the interface pointing into the liquid.

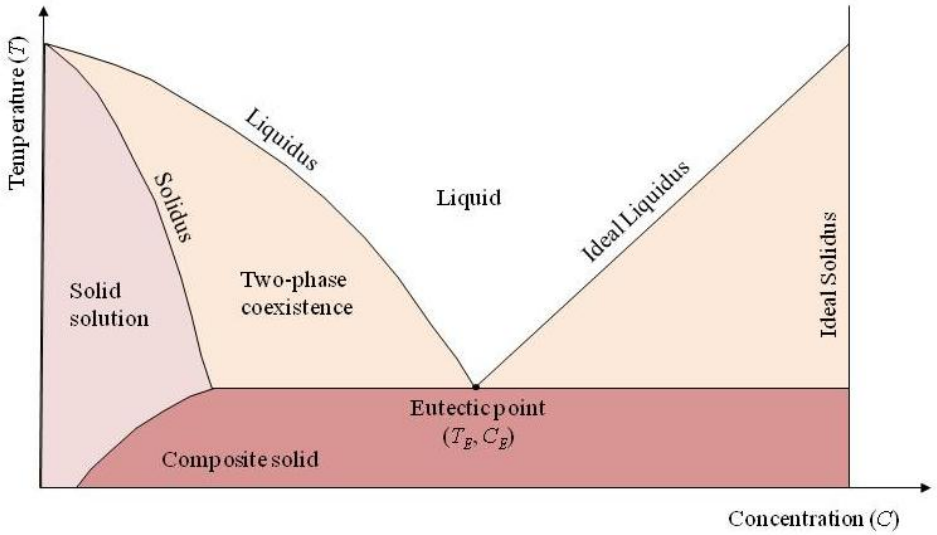

Figure 4.1. Equilibrium phase diagram for a typical eutectic binary alloy showing what phases exist in a sample of bulk concentration C and uniform temperature T. T_E and C_E are the eutectic temperature and concentration respectively. In many mathematical studies the liquidus and solidus are taken to be linear, as shown on the right hand side of this diagram.

Application of mushy layers to sea ice

There have been several experimental and theoretical studies relating mushy layers to sea ice. Wettlaufer et al. (1997a; 1997b) conducted laboratory experiments that simulated the initial growth of sea ice by cooling sodium-chloride solutions from above. They found that the brine initially remains trapped in the sea ice but once the thickness of the ice sheet exceeds a critical value convective overturning (gravity drainage) initiates. This caused high salinity brine to drain out the of sea ice and be replaced with fresher liquid from below, allowing further growth of the ice in the layer and thus an increase in the solid fraction. This critical behaviour has been shown quantitatively to be explained by the mushy layer Rayleigh number (Eq. 2.5), which describes the onset of convection in a mushy layer (Worster and Wettlaufer, 1997). Field experiments also confirmed these results (Wettalufer et al., 2000).

Feltham and Worster (1999) used a mathematical model of a mushy layer to investigate the stability of an interface between a mushy layer and a flowing melt. They found that flow in the melt can trigger instability of a mush-melt interface by inducing a flow in the mushy layer due to the Bernoulli effect. It was suggested by Wettlaufer (1991) that the

corrugations on the underside of perennial sea ice could be formed due to the instability mechanism suggested by Gilpin et al. (1980). Feltham and Worster (1999) therefore compared their instability mechanism to Gilpin et al.'s and found that it required a shear that is ~125 times smaller, which suggests it is likely to be the dominant mechanism.

Taylor and Feltham (2004) used the mushy layer equations to describe heat transport in a thermodynamic-radiative model of melt-pond evolution. Model simulations showed that the presence of melt ponds affects the mass balance significantly through albedo-feedback mechanisms, drainage and the delayed onset of re-freezing at the ice-ocean interface caused by sensible and latent heat storage in the refreezing melt ponds. Model simulations showed good agreement with field data.

Feltham et al. (2006) showed that the general equations describing mushy layers reduce to those used in the model of Maykut and Untersteiner (1971) in the absence of brine advection. This demonstrates that the thermodynamics of sea ice obey the same conservation laws described by the mushy layer theory. Therefore based on the breadth of previous work I assume that sea ice can be well represented by the conservation laws describing the evolution of mushy layers. For the purpose of comparison with our laboratory data I assume that that seawater can be approximated by a solution of sodium chloride (NaCl) and water. This assumption is based on the fact NaCl accounts for ~85% of the mass of dissolved salts in sea water and previous work has shown that there are negligible differences in the structure, strength and radiative properties of sea ice grown from seawater and ice grown from NaCl solutions (Maykut and Light, 1995; Timco, 1980; Weeks and Ackley, 1986; Wettlaufer et al., 1997a).

4.4 One-layer thermodynamic model of sea ice

In this section I present a simple thermodynamic model of sea ice growth that I later develop into a consolidation model for rafted sea ice (Chapter 6). The model does not include any horizontal parameterizations, nor the influence of brine flow (i.e. $\mathbf{U} = 0$ in Eq. 4.7) or a snow cover. I shall first describe the mathematical formulation of the model and the method of solution. I then introduce the parameters that are used to force the model, which are specific to the environments of the north Caspian Sea, the Arctic and the

Antarctic. The results of the numerical simulations are then presented and compared to field data.

Mathematical formulation

Heat transport within the ice is determined from the nonlinear one-dimensional heat diffusion equation,

$$c_{eff}\frac{\partial T}{\partial t} = \frac{\partial}{\partial z}\left(k_{eff}\frac{\partial T}{\partial z}\right) + A_R, \tag{4.11}$$

where c_{eff} and k_{eff} are, respectively, the effective volumetric specific heat capacity and the thermal conductivity of sea ice, T is the temperature within the ice sheet, t is time, and z is the vertical spatial coordinate, which is taken to be positive upwards. The final term, A_R, describes the absorption of solar radiation that penetrates through the sea ice surface and is given by Beer's law,

$$A_R = \kappa_i I_0 (1-\alpha) F_{SW} e^{-\kappa_i z}, \tag{4.12}$$

where κ_i =1.5 m^{-1} is Beer's extinction coefficient, I_0 = 0.4 is the fraction of incident radiation that passes through the surface into the interior of the ice, α = 0.6 is the albedo for bare ice, and F_{SW} is the flux of incoming shortwave solar radiation. Equation (4.11) is identical to the diffusion equation (4.4) used by Maykut and Untersteiner (1971), where the phase change terms are held implicitly within the effective heat capacity and thermal conductivity (see Feltham et al., 2006 for details).

The effective specific heat capacity of the sea ice is given by

$$c_{eff} = c_i - \mathcal{L}_s \frac{T_L(S_{bulk}) - T_L(0)}{\theta^2}, \tag{4.13}$$

where $T_L(S_{bulk})$ is the liquidus (freezing) temperature of sea ice with a bulk salinity S_{bulk}, which is taken to be uniform across the ice sheet, $T_L(0)$ is the liquidus temperature of pure water, $\theta = T\text{-}T_L(0)$, $\mathcal{L}_s = 3.014 \cdot 10^8$ Jm^{-3} is the volumetric heat of fusion of pure ice and c_i = $1.883 \cdot 10^6$ $J(m^3K)^{-1}$ is the volumetric heat capacity of pure ice (Ebert and Curry, 1993). This equation differs from those proposed by Schwerdtfeger (1963) and Feltham et al.

(2006) in that it considers the temperature dependence of the latent heat (see Bitz and Lipscomb, 1999 for details).

The effective thermal conductivity of the sea ice is given by

$$k_{eff} = k_{bi} - (k_{bi} - k_b)\frac{T_L(S_{bulk}) - T_L(0)}{\theta}, \qquad (4.14)$$

where k_{bi} and k_b are the conductivities of bubbly ice and brine respectively. After Schwerdtfeger (1963), k_{bi} and k_b are

$$k_{bi} = \frac{2k_i + k_a - 2V_a(k_i - k_a)}{2k_i + k_a + V_a(k_i - k_a)}k_i \quad \text{W(mK)}^{-1} \qquad (4.15)$$

and

$$k_b = 0.4184(1.25 + 0.030K^{-1}\theta + 0.00014K^{-2}\theta^2) \quad \text{W(mK)}^{-1}, \qquad (4.16)$$

where $k_i = 1.16(1.91 - 8.66.10^{-3}\,K^{-1}\,\theta + 2.97.10^{-5}\,K^{-2}\,\theta^2)$ W(mK)$^{-1}$ is the conductivity of pure ice (Sakazume and Seki, 1978), k_a = 0.03 W(mK)$^{-1}$ is the conductivity of air (Weeks and Ackley, 1986), and V_a = 0.025 is the fractional volume of air in sea ice for sea ice with a salinity of 6ppt (Timco and Frederking, 1996).

Figures 4.2 and 4.3 show the effective specific heat capacity and thermal conductivity of sea ice plotted as functions of temperature and salinity using equations (4.13) and (4.14) respectively. They both exhibit asymptotic behaviour for sea ice, with high specific heat capacities and low thermal conductivities at temperatures above 268 K (-5°C). The thermal properties of the sea ice therefore play an important role in controlling the amount of heat that is transferred through the ice cover and its response to variations in surface or bottom forcing (Eicken, 2003).

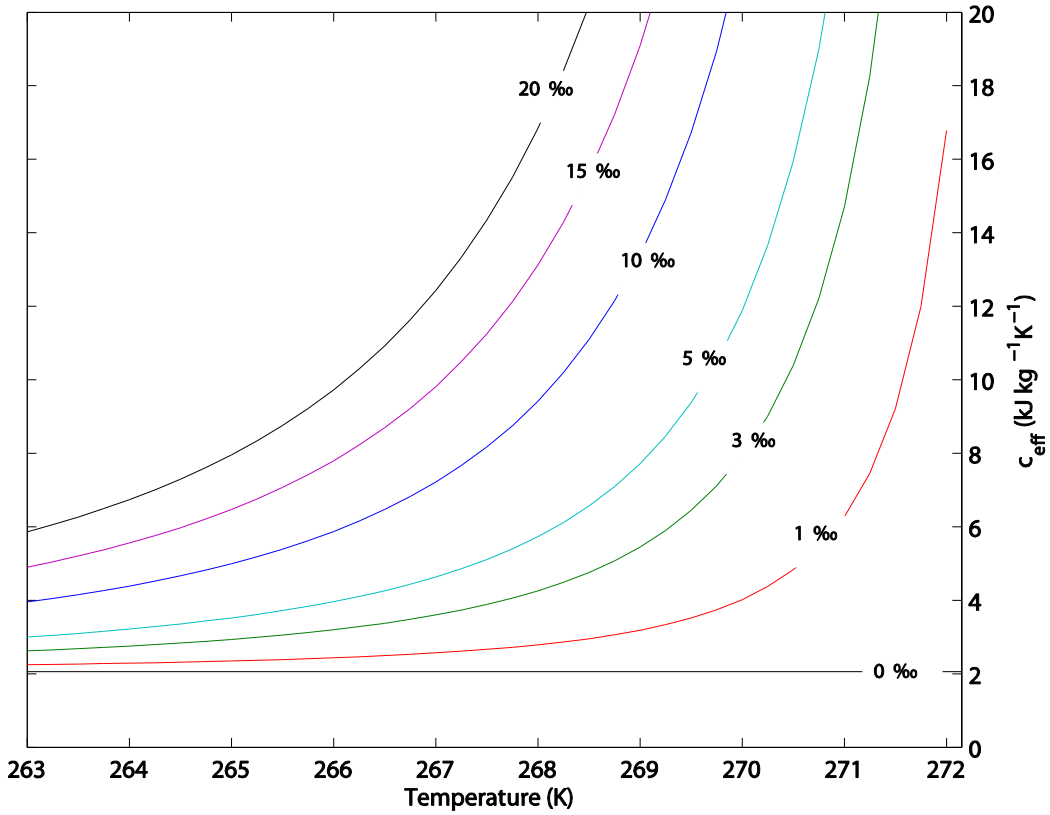

Figure 4.2. The effective specific heat capacity of sea ice plotted as a function of temperature and salinity using equation (4.13).

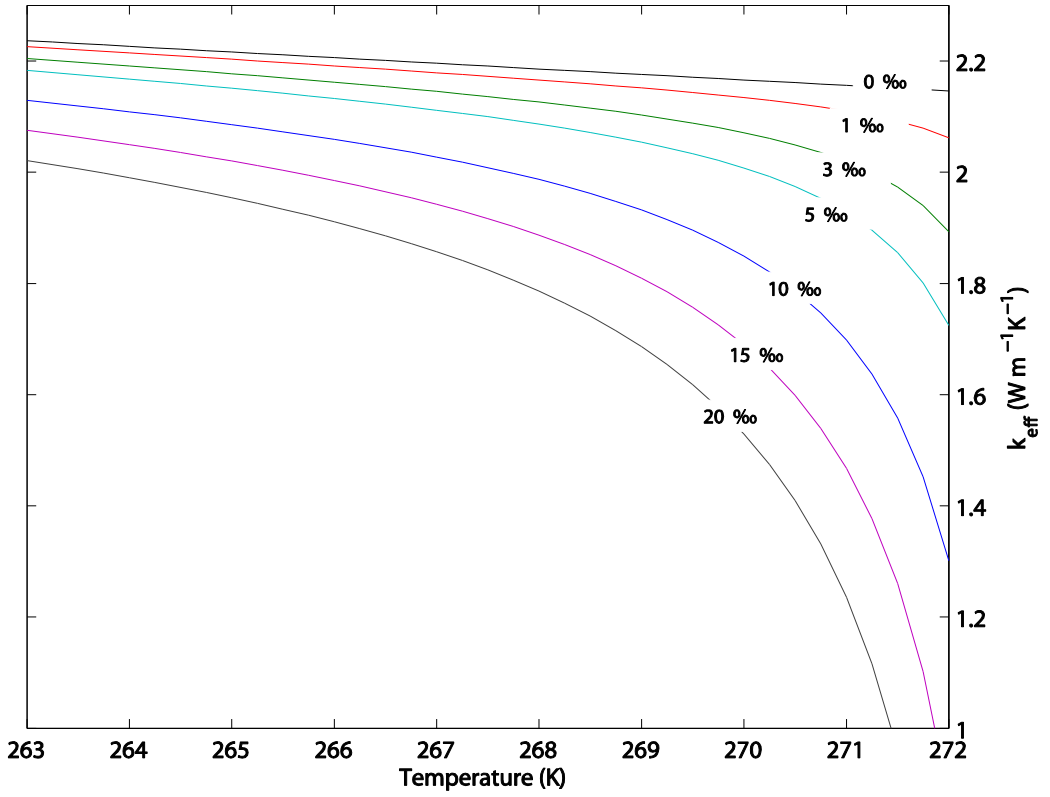

Figure 4.3. The effective thermal conductivity of sea ice plotted as a function of temperature and salinity using equations (4.14) to (4.16).

The sea ice is assumed to be in local thermodynamic equilibrium which implies that the temperature T and brine concentration S_{brine} lie on the liquidus curve in the phase diagram for sea ice. Often the linear fit is assumed for this relationship,

$$T_L(S) = T_L(0) - \Gamma S, \tag{4.17}$$

(Feltham et al., 2006; Taylor and Feltham, 2004) where $T_L(S)$ is the liquidus (freezing) temperature of the brine with salinity S, $T_L(0)$ is the liquidus temperature of pure water and Γ is a positive constant. Notz (2005) has shown this relationship is not adequate for the temperature ranges experienced in sea ice.

Figure 4.4 shows a plot of a linear liquidus curve plotted with experimental data from freezing of NaCl solutions (Weast, 1971) and seawater (Assur, 1958). The figure shows that there is a significant deviation between the linear fit and the experimental data. Therefore for comparisons with laboratory data I shall use a 3rd order polynomial fit suggested by Notz (2005) to approximate the liquidus curve for NaCl solutions

$$T_L(S) = -5.33 \cdot 10^{-7} - 9.37 \cdot 10^{-6} S^2 - 0.0592 S + 273.15 \text{ K}. \tag{4.18}$$

The sea ice is assumed to initially have a linear temperature profile based on the air and sea temperature at the upper and lower boundaries, giving the following initial condition

$$T = \frac{T_0 - T_L(S_{ocean})}{H_0} z + T_L(S_{ocean}) \qquad (t = 0), \tag{4.19}$$

where T_0 is the temperature at the upper surface, $T_L(S_{ocean})$ is the freezing temperature at the salinity of the ocean S_{ocean} and H_0 is the initial thickness of the sea ice.

At the upper surface of the sea ice (z = h_s), it is assumed there is no melting at the ice surface and the net flux, $(F_{net})_0$, is equal to the conductive flux, $-k_{eff}\,\partial T/\partial z$, such that

$$(F_{net})_0 \equiv \varepsilon_i (F_{LW} - \sigma T_0^4) + (1-\alpha)(1-I_0) F_{SW} - F_{sens} - F_{lat} = -k_{eff} \frac{\partial T}{\partial z} \quad (z = h_s), \tag{4.20}$$

where ε_i = 0.99 is the emissivity of bare ice, F_{LW} is the flux of incoming atmospheric longwave radiation, σ = 5.67 x 10^{-8} J(K^4m^2s)$^{-1}$ is the Stefan-Boltzmann constant, and F_{sens} and F_{lat} are the turbulent surface fluxes of sensible and latent heat (Ebert and Curry, 1993; Maykut and Untersteiner, 1971; Taylor and Feltham, 2004).

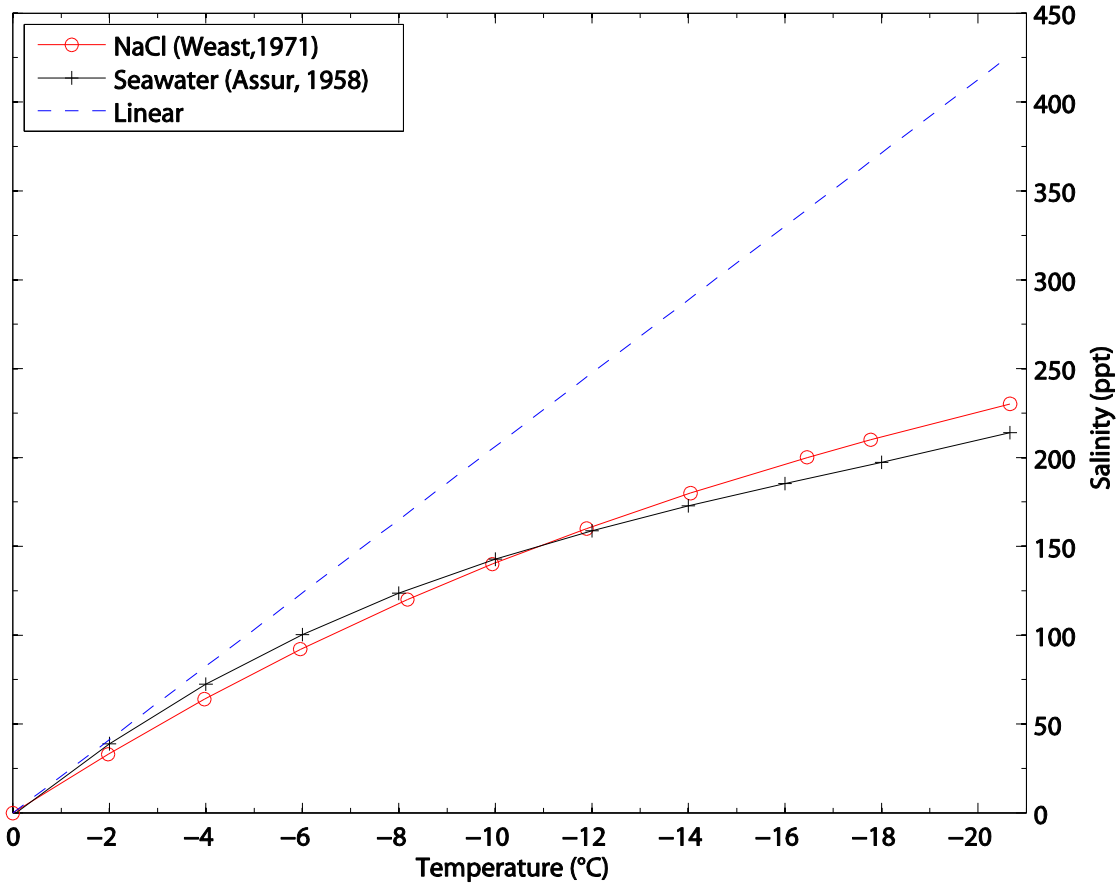

Figure 4.4. Liquidus curves showing the freezing temperature (°C) as a function of salinity (ppt) for sodium-chloride solutions (Weast, 1971), seawater (Assur, 1958) and a linear fit given by equation (4.17) where Γ = 0.0514 (Feltham et al., 2006; Taylor and Feltham, 2004).

At the sea ice-ocean boundary (z = h_{ocean}), the sea ice is held constant at the freezing temperature of the ocean,

$$T = T_L(S_{ocean}) \qquad (z = h_{ocean}), \tag{4.21}$$

and the ice growth rate is given by the Stefan condition,

$$\mathcal{L}_s \phi \left(\frac{\rho_{brine}}{\rho_{ice}}\right) \frac{dh_{ocean}}{dt} = k_{eff} \frac{\partial T}{\partial z} + F_{ocean} \qquad (z = h_{ocean}), \tag{4.22}$$

where the density ratio, $\rho_{brine}/\rho_{ice} = 1.09$, describes the expansion of the liquid upon freezing (Pounder, 1965), F_{ocean} is the heat flux from the ocean directed into the base of the ice sheet and $\phi = 1 - S_{bulk}/S_{ocean}$ is the local solid fraction per unit volume of the sea ice (Wettlaufer et al., 2000). The assumption of uniform salinity across the ice sheet (i.e. S_{bulk} is a constant) implies a non-zero solid fraction at the sea-ice-ocean interface. This implies we are tracking the location of the 'consolidated' ice-ocean interface, which conveys the mathematical advantage that the interface location can be determined explicitly (rather than using an implicit numerical technique) and has been shown to lead to little numerical error (Feltham, 1998).

The system of equations (4.11) – (4.22) comprises a closed partial-differential, initial-boundary value problem. Figure 4.5 is a schematic of the sea ice model showing the governing equations and boundary conditions at the respective interfaces.

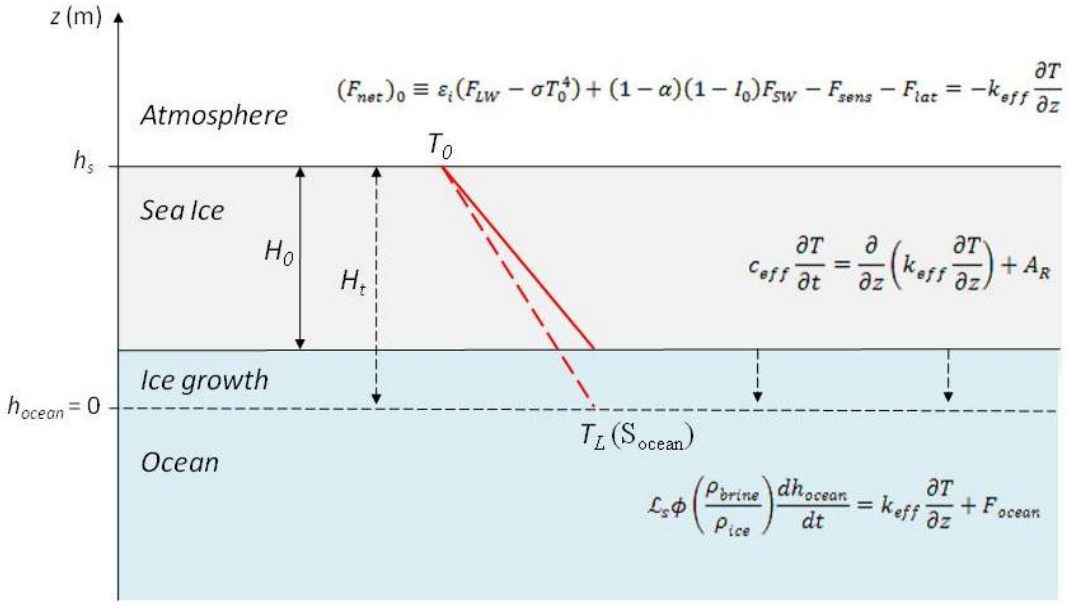

Figure 4.5. Schematic of the thermodynamic model for sea ice growth showing the governing equations and boundary conditions at the respective interfaces. The heat diffusion equation (4.11) is used to determine the vertical heat transport within the sea ice with the initial condition (4.19) approximated by a linear temperature profile (solid red line) based on the temperature at the ice surface (T_0) and liquidus temperature of the ocean [$T_L(S_{ocean})$]. At the upper surface, there is assumed to be no melting so that the net flux is equal to the conductive flux (4.20). At the ice-ocean boundary the temperature is assumed to be at the liquidus temperature of the ocean (4.21) and the rate of ice growth is given by the Stefan condition (4.22). The spatial coordinate z is taken to be positive upwards, so that z = 0 at the ice-ocean interface (h_{ocean}) and $z = H_0, H_1, \ldots H_t$ at the surface of the sea ice (h_s), where H_0 is the initial thickness of the sea ice and H_t is the thickness at a later time t.

Method of solution

The model described in the previous section was coded in MATLAB to determine the rate of ice growth given a set of forcing parameters. The heat diffusion equation (4.11) was solved using the 'pdepe' function, which solves initial-boundary value problems for systems of parabolic and elliptic partial-differential equations (PDEs) in one space variable x and time t. The pdepe solver converts PDEs into ordinary differential equations (ODEs) using a second order spatial discretisation based on a fixed set of nodes. The ODEs are then integrated to obtain approximate solutions at times specified by a time vector. The pdepe function then returns values of the solution on a mesh provided in a distance vector.

In this set-up, a mesh of 11 nodes and a time step of 3 seconds are used. At the end of each time step the ice growth rate was calculated using the Stefan condition (4.22) and the thickness of the ice sheet and initial condition updated. See Appendix A for more details on the MATLAB code for the thermodynamic model of sea ice growth.

Model Parameters

Table 4.1. Forcing data used in the thermodynamic model of sea ice growth

Forcing data	North Caspian Sea	Arctic	Antarctic
F_{LW} (W/m^2)	205 [a]	154.52 [b]	158 [c]
F_{SW} (W/m^2)	76 [a]	0 [b]	0 [c]
F_{sens} (W/m^2)	3 [a]	5.7 [b]	43 [c]
F_{lat} (W/m^2)	-1 [a]	0.5 [b]	-3 [c]
F_{ocean} (W/m^2)	9.7	3*	3*
S_{ocean} (ppt)	6	33	35
S_{bulk} (ppt)	3	17	17
H_0 (mm)	1	1	1

[a] Mean for January 2008 provided by the National Centres for Environmental Prediction (NCEP)
[b] Mean for December 1998 taken from atmospheric SHEBA data
[c] Mean for July 2007 provided by NCEP
* (Perovich and Elder, 2002)

The model was forced using parameters typical to the environments of the north Caspian Sea, the Arctic Ocean and the Antarctic Southern Ocean (see Table 4.1). Constant values were used for the forcing data (F_{LW}, F_{SW}, F_{sens}, F_{lat}, F_{ocean}), the ocean salinity (S_{ocean}) and

the bulk salinity of the sea ice (S_{bulk}). The atmospheric data (F_{LW}, F_{SW}, F_{sens}, F_{lat}) was calculated from averages of the coldest months in the respective locations, using data collected during the Surface Heat Budget of the Arctic (SHEBA) experiment for the Arctic and the National Centres for Environmental Prediction (NCEP) for the north Caspian Sea and the Antarctic. The oceanic heat flux (F_{ocean}) was set to 3 W/m^2 for the Arctic and the Antarctic and 9.7 W/m^2 for the north Caspian. These values were based on data collected over first year sea ice in the Arctic between November to February 1997/98, as part of the SHEBA project (Perovich and Elder, 2002) and data collected in the north Caspian Sea. The bulk salinity (S_{bulk}) of the sea ice was assumed to be uniform across the ice sheet and was set to 17 ppt for the Arctic and the Antarctic and 3 ppt for the north Caspian. These values are towards the higher end of salinities observed in the respective areas and were chosen as several studies have shown that during the early stages of sea ice growth S_{bulk} varies from 16-20 ppt for the Arctic/Antarctic (Cox and Weeks, 1974; Fedotov, 1973; Notz and Worster, 2008). All model runs were initiated with an initial thickness (H_0) set to 1 mm.

Numerical Simulations

In this section, I present the results of numerical simulations that were run to determine growth rates of sea ice in the north Caspian, the Arctic and the Antarctic over the period of a day (1440 minutes) starting from an initial thickness of 1 mm. These results are then compared with field data of young sea ice growth.

Table 4.2. Predicted growth rates of sea ice.

Location	Growth rate in 1 day (cm)
North Caspian Sea	4.01
Arctic	8.10
Antarctic	8.60

Table 4.2 shows the growth rates predicted by our model simulations. The quickest rate was for the Antarctic, then the Arctic and finally the north Caspian. The growth rates for the Arctic and Antarctic are quite similar, which is expected as similar forcing parameters were used. The major difference was in the values used for the sensible heat flux (F_{sens}), which demonstrates the model's sensitivity to this parameter. The growth rate for sea ice in the

north Caspian was approximately half that of polar ice growth. This is expected as temperatures at this latitude are much milder than at the poles.

Figure 4.6 shows the evolution in temperature and ice thickness in our simulations of sea ice growth in the respective areas. In all three plots, the temperature profiles are approximately linear and the growth rates are roughly constant. The major difference between these simulations is the temperatures of the respective areas: In the north Caspian the temperature at the ice surface reached only -2.2°C in a day of ice growth whereas, in the Arctic and the Antarctic the temperature reduces to -8°C and -10°C.

There exists no field data that I am aware of that measures the growth of young sea ice in the north Caspian. However there are many sources for Arctic and Antarctic sea ice growth. For instance, Notz and Worster (2008) investigated the salinity evolution in young sea ice in the Adventfjorden in Svalbard and found that the sea ice had grown 8-9 cm in 24 hrs. Wettlaufer et al. (2000) measured the temperature evolution during the solidification of a lead in the Beaufort Sea and used these temperatures to calculate the rate of ice growth. They found that in 24 hrs the ice had grown ~9.6±1 cm. In the western Weddell Sea, Melnikov (1998) investigated the winter production of sea ice algae and noted that during the first 24 hrs of ice formation from open water the ice had grown to a thickness of 9 cm. All of these observations are in good agreement with those predicted by our simulations. It must be noted that climates can vary significantly from one year to the next, therefore these experimental data are not sufficient to test the model (this will be done in Chapter 5 where the model is tested against experimental data). They do however give confidence that the model can reasonably predict growth rates.

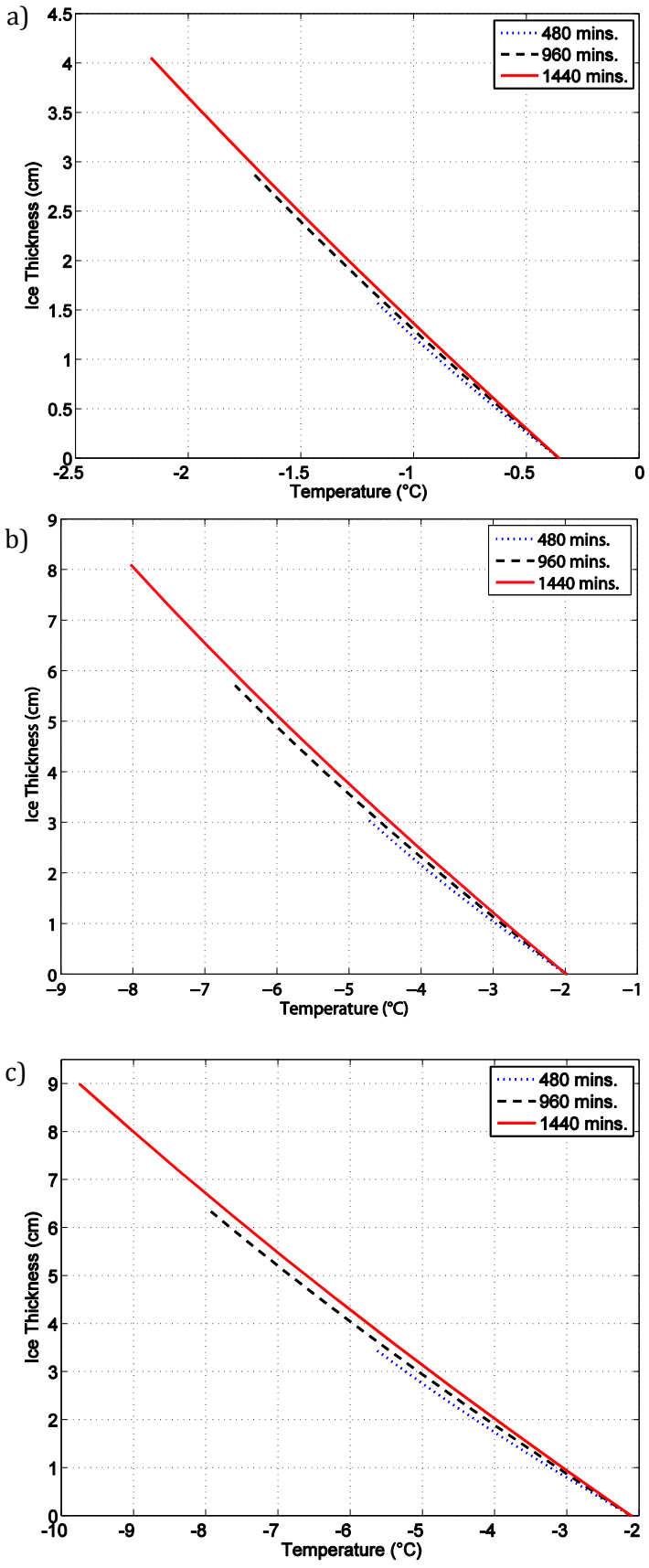

Figure 4.6. The evolution in temperature and ice thickness in our simulations of sea ice growth using parameters representative of a) the north Caspian, b) the Arctic and c) the Antarctic.

4.5 Summary

In this chapter, I presented the mushy layer equations that describe the transport of heat and solute within sea ice. These were then implemented into a simple thermodynamic model of sea ice that predicts growth rates given a set of forcing parameters. The model was then run using parameters representative of the environments of the north Caspian Sea, the Arctic Ocean and the Antarctic Southern Ocean over the period of a day starting from an initial thickness of 1 mm. The results were then compared with field data collected in the Arctic and Antarctic and found to be in good agreement. In Chapter 5, this model will be tested against laboratory data and in Chapter 6 it will be developed into a numerical consolidation model for rafted sea ice.

5 Laboratory grown saline ice

5.1 Introduction

Sea ice is complex material composed of pure ice, brine, air and, depending on the temperature, solid salts. When sea ice grows naturally, it grows from the surface downwards. At the upper surface the temperature is close to the ambient air temperature and at the lower surface the temperature is near to the freezing point of the sea water. As the ice grows, concentrated brine is trapped in the sub-grain boundaries, which with time gradually drain out of the ice and into the underlying ocean. The structure of sea ice is dependent on the growth conditions. Typically, first year sea ice is composed of a thin layer of granular/frazil ice, followed by a transition zone and then a region of columnar/congelation ice. These characteristics make growing sea ice in the laboratory particularly challenging because the ice needs to be perfectly insulated laterally to ensure ice growth from the top down and needs to be in a large enough tank so that any salt surplus from brine drainage does not affect the growth rate. Due to the size constraints encountered in a laboratory, this can only be achieved to a certain extent.

In this chapter, I describe how natural sea ice growth was simulated in the Ice Physics Laboratory at UCL. To carry out the experimental programme, I first had to design and in some cases construct the apparatus. This involved designing containers that were sufficiently insulated to achieve ice growth from the top down, designing heater plates to keep the water at the base of the ice close to its freezing point, designing and constructing thermistor probes with which to measure the temperature in the ice and designing a rig for conducting shear experiments. During ice growth, the temperature was measured at the ice-atmosphere interface and in the air, water and ice using the specially designed thermistor probes. These data were used to estimate the growth rate of the ice, which was used along with the temperatures measured at the ice-atmosphere interface, to test the one-layer model described in the previous chapter. Once the ice had reached the desired thickness, it was then used in the rafted ice consolidation experiments that are described in Chapter 7. To better characterize the laboratory grown saline ice, in this chapter, its physical and mechanical properties shall be described.

5.2 Experimental apparatus

The experiments were set-up in cold room 5 of the Ice Physics Laboratory, which is at the far end of the chamber complex so is undisturbed by other researchers in the laboratory. Cold room 5 has two condensers that work in unison so that when one is on the defrost cycle the other remains running. This enabled the temperature to be controlled to ±1°C. During the entire experimental programme, the cold room temperature was set to -10ºC. To grow the ice, acrylic cylinders (33 cm in diameter and 50 cm in length) were filled with a solution of sodium chloride and water and left to freeze. Solutions of 0.3 (tap water), 6 and 33 ppt were prepared using tap water and table salt to match the concentrations found in fresh water environments, the north Caspian Sea and the Arctic/Southern Oceans respectively. Acrylic was chosen as it is transparent and has a low conductivity (0.2 $Wm^{-1}K^{-1}$) and the cylindrical shape made the containers much easier to insulate uniformly. A diameter of 33 cm was selected to have samples as large as possible while still being possible to manoeuvre. To ensure ice growth from the top down, the acrylic cylinders were insulated with 20 cm thick tubes of polystyrene (made to order from Styrotech Ltd.). Polystyrene was chosen as it has low conductivity (0.03 $Wm^{-1}K^{-1}$) and is easily cut. Within the polystyrene, I fitted 6 m of 60 W trace heating tape (ordered from RS components), which was used to melt the exterior of the ice so that it could be removed from the cylinder when the ice was ready for the rafting experiments. At the base of each cylinder a heater plate was held constant at a temperature of 7°C. This temperature was needed to keep the water at the base of the rafted section near to its freezing point. The heater plates consisted of an aluminium alloy plate with three 100 W heaters evenly spaced within the plate. The temperature of the plate was controlled using a PID500 Tempatron controller fitted with a thermocouple, which controlled the temperature of the plate to an accuracy of ±1°C. Photographs of the experimental set-up for growing laboratory ice are shown in Figure 5.1.

During ice growth, the thickness of the ice was measured with a graduated mm scale rule fixed to the side of the tank. The temperature was measured at the ice-atmosphere interface and in the air, water and ice using the thermistor probes. In total, three sets of thermistor probes 5, 10 and 20 cm in length were constructed to measure the temperature in ice of different thicknesses and 5 single thermistors to measure the temperature of the air and water (see Figure 5.2 for photographs of each type of probe). The probes were supplied

with a direct current of 18.2±0.2 μA and the resistances recorded every 5 minutes using a National Instruments Compact Fieldpoint data logger and LabView control software. In LabView, the resistances were converted into temperatures using the Steinhart-Hart equation,

$$\frac{1}{T} = A + Bln(R) + C[\ln(R)]^3, \qquad (5.1)$$

where T is the temperature in Kelvin, R is the resistance in Ohms and $A = 1.030697 \times 10^{-3}$, $B = 2.38896 \times 10^{-4}$, and $C = 1.57 \times 10^{-7}$ are the Steinhart-Hart coefficients which depend upon the type and model of thermistor and the temperature range of interest. Recorded temperatures were displayed on a graphical interface in real time and the resistances and temperature stored in an .lmv file. Temperature readings are accurate to within ±0.4°C. Further details about the thermistor probes and data logging system are given in Appendix B.

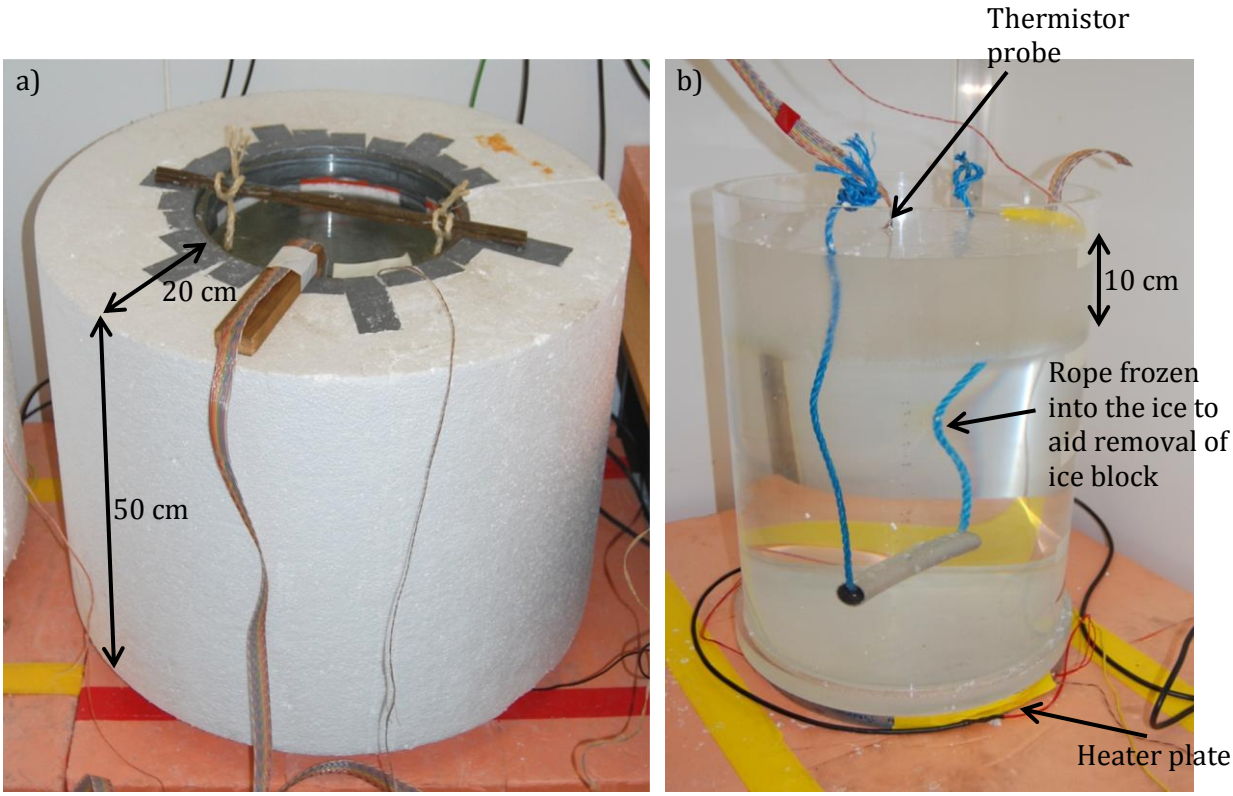

Figure 5.1. Photographs showing the experimental set-up for growing laboratory ice with (a) and without (b) the polystyrene insulation in place.

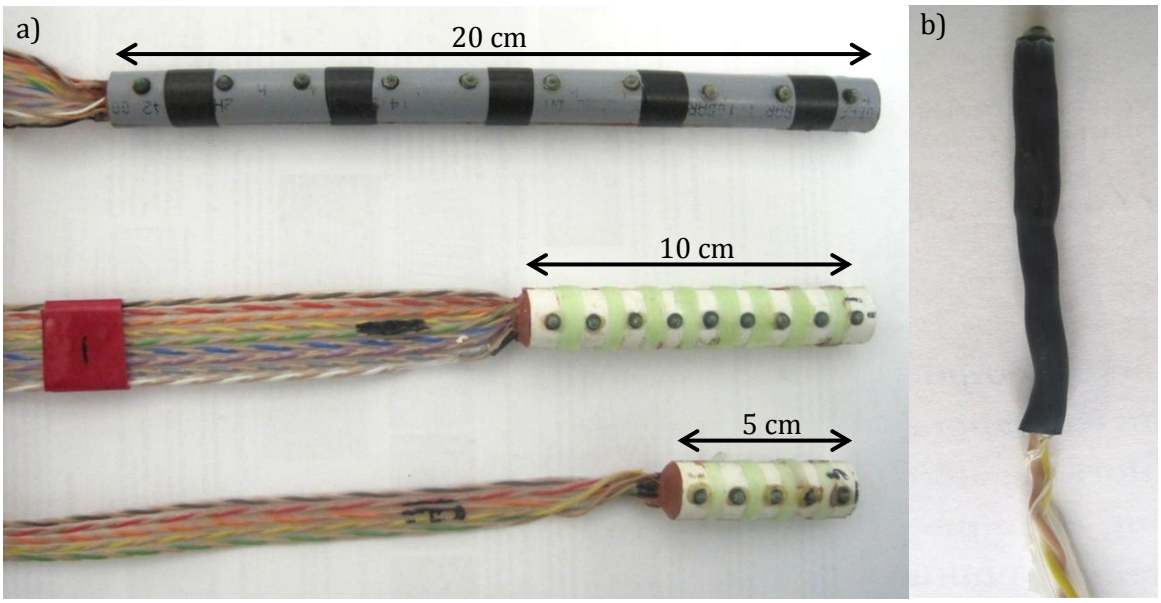

Figure 5.2. Photograph of (a) the 5, 10 and 20 cm thermistor probes and, (b) one of the single thermistors used to measured temperature in the ice and air and water. The 5, 10 and 20 cm probes contain respectively, 5, 9 and 10 thermistors spread evenly over 1 cm intervals for the 5 and 10 cm probes and 2 cm intervals for the 20 cm probes.

5.3 Temperature and thickness measurements

In this section, I describe the temperature and thickness measurements that were recorded during ice growth. This is only done for the ice grown for the standard case rafted ice experiment, as the model shall only be tested against this data. For the standard case, ice was grown from a 6 ppt solution of NaCl and water to a thickness of 7cm.

In Figure 5.3, the temperature time-traces for the ice grown for the standard case rafted ice experiment are shown. The temperature was measured at the ice surface (marked 0 cm on the plot) and at depths of 1, 2, 3, 4 and 5 cm below the ice surface. The figure shows that the temperature of the solution at first cools from 6°C to 2°C. The surface waters then stratify and ice starts to form as soon as the liquid has reached its freezing temperature (-0.36°C for a solution of 6 ppt). This can clearly be seen in the temperature traces because as soon as a thermistor becomes engulfed in the ice the temperature drops rapidly, whilst those that remain in the liquid region stay at roughly the same temperature. Therefore the growth rate of the ice can be estimated by determining the time at which the temperature measured by a given thermistor drops below the freezing temperature (c.f. Wettlaufer et al., 2000). The time that this takes place for each thermistor is indicated by the arrows shown in Figure

5.3. To test this method, the growth rate was also measured independently using a graduated ruler. In Figure 5.4, the growth rate inferred from temperature data is compared to those measured by the ruler. The figure shows that ice growth started after 400 minutes and was linear in the first 2000 minutes, after which it gradually departs from linearity as the thickness of the ice increases. The ice thicknesses inferred from temperature traces are in fairly good agreement with those measured manually. Therefore I am confident that this method can be used to estimate the growth rate for the experiments presented in this thesis.

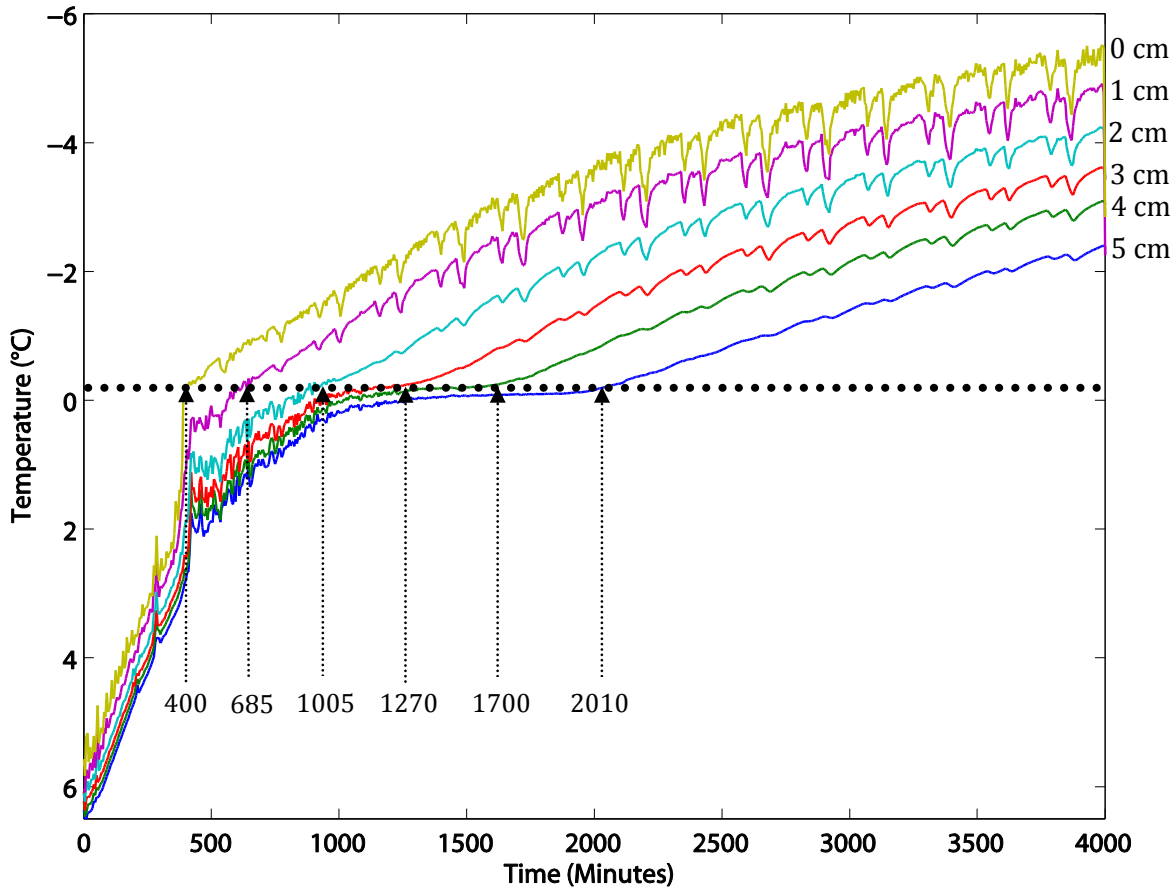

Figure 5.3. Temperatures recorded in the ice plotted as a function of time. The location/depth of the individual thermistor is shown on the right-hand side of the graph, where 0 cm corresponds to the ice surface. Note that the thermistors remain at roughly the same temperature while they are in the liquid region (accentuated by the dotted line .....) but once the ice has engulfed the thermistor its temperature decreases. The times that this takes place for each thermistor is indicated by the arrows.

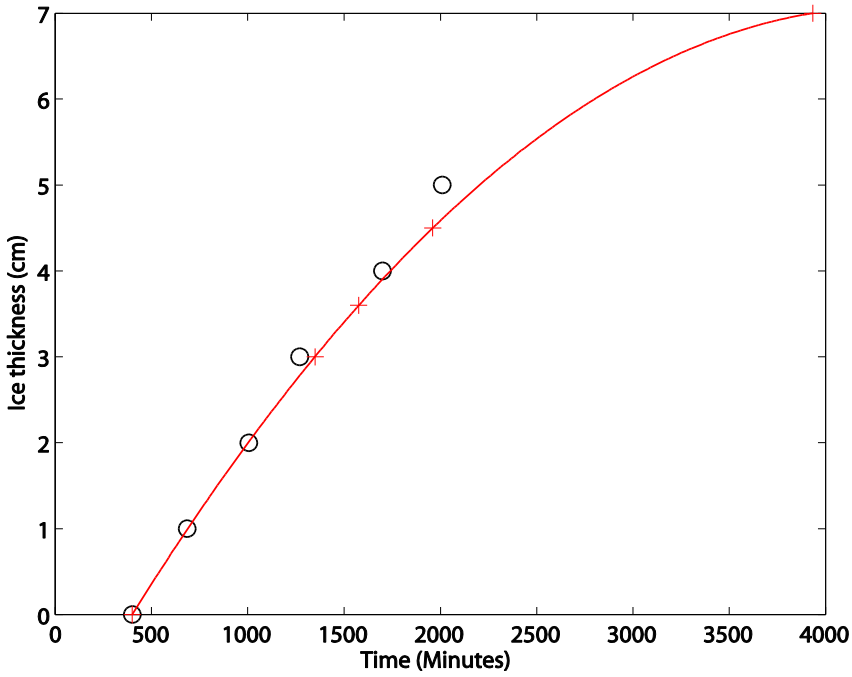

Figure 5.4. Plot of the ice thickness as a function of time measured during laboratory experiments on saline ice. The values that were measured using a ruler are shown by the red crosses with a quadratic fit to the data and those that were inferred from the temperature traces are shown by the black circles.

5.4 Testing the one-layer model

To test the one-layer model described in the previous chapter the model was forced using the temperatures recorded directly at the ice surface and the growth rate inferred from the laboratory experiments. This means that the boundary condition at the ice-atmosphere interface (Eq. 4.20) reduces to $T = T_0$. The Stefan condition at the base of the growing ice sheet (Eq. 4.22) no longer needs to be solved and the thickness of the ice sheet can simply be updated every time step. I assume that in the laboratory no shortwave radiation penetrates into the ice so that the last term in Eq. 4.11 is neglected. The temperature at the ice surface was measured using a single thermistor probe (shown in Figure 5.3 at a depth of 0 cm). Because temperature was only measured every 5 minutes, I fit a quadratic to the data and evaluate it over intervals of 3 seconds as this was the time step used in the model. Likewise, the growth rate was approximated by fitting a quadratic to the ice thickness data shown in Figure 5.4 and scaled back to zero so that the first time step in the model is when the ice had just started growing in the experiments (i.e. at 400 minutes). The simulation was

run for 3600 minutes (i.e. 4000 – 400 = 3600 minutes) so that the results could be directly compared with the temperature traces recorded during growth of the laboratory ice.

In Figure 5.5, the output from the numerical simulation of laboratory ice growth is given, which shows the temperature distribution in the ice at various time steps. For comparison, the temperatures recorded by the thermistors at 3600 minutes in the laboratory experiments are also plotted (circles in Figure 5.5). Results show that the ice grew 7 cm in 3600 minutes and the ice temperature gradually decreased as the ice grew. The temperature distribution simulated by the model is in good agreement with that measured by the thermistors. Therefore I am confident that the one layer model correctly solves the heat diffusion equations and can now be developed into a two layer model that can be compared with laboratory experiments on rafted ice.

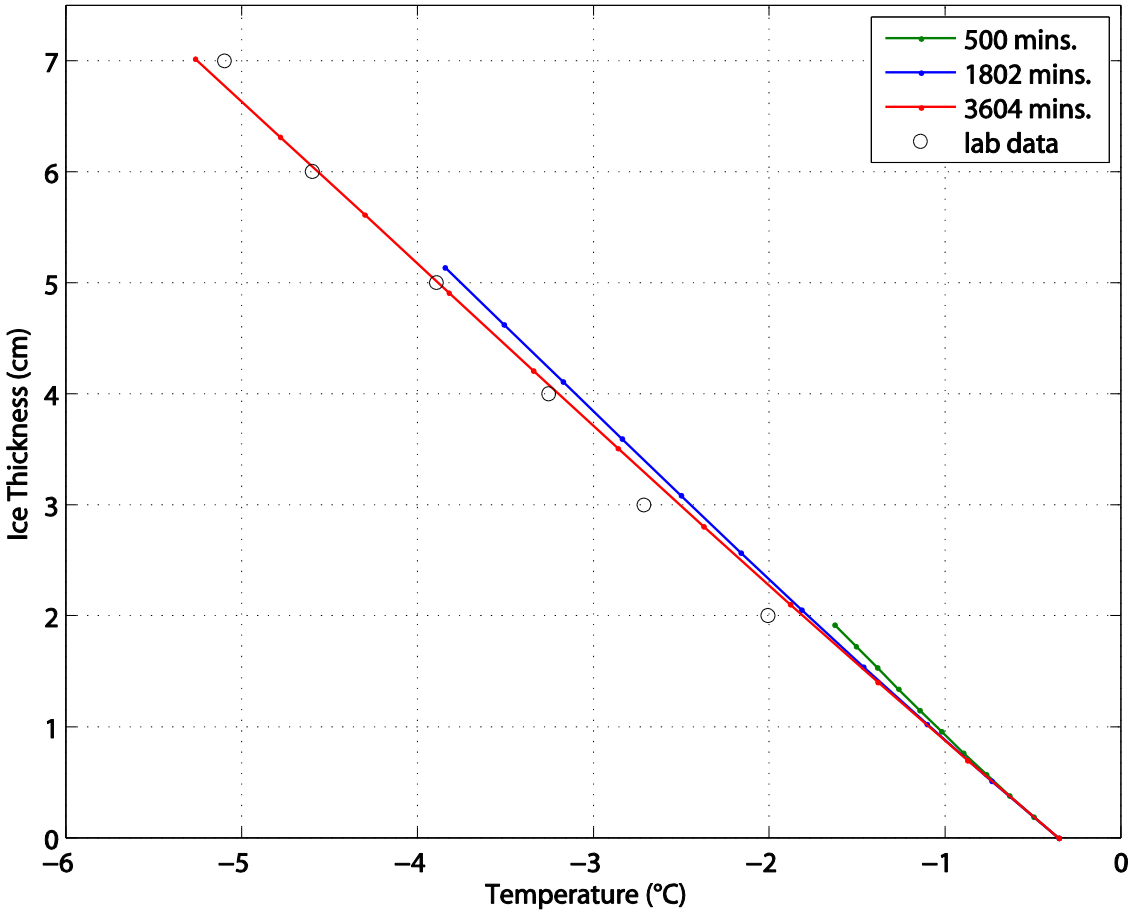

Figure 5.5. Output from the numerical simulation of laboratory ice growth, that was forced using the temperature recorded at the ice surface and growth rate measured during the experiments. In this simulation, I used a mesh of 11 nodes which means that a temperature was found for 11 points spread evenly across the ice sheet. These points are shown by dots at the respective time steps.

5.5 The physical and mechanical properties of the laboratory grown sea ice

To gain a better understanding of the physical and mechanical properties of the ice grown in the laboratory the salinity, density, porosity (brine and air volume), crystal texture, compressive strength and shear strength were investigated. This was done so that the 'level ice' properties could be later compared with 'rafted ice' properties, which shall be presented in subsequent chapters. These properties were determined for ice grown from tap water and 6 and 33 ppt solutions of NaCl (unless stated otherwise) as these are the salinities used in the rafted ice experiments. I was not able to measure many of these properties for the freshwater ice, as I was unable to extract intact cores. This was because the ice was extremely brittle and a slight misalignment of the corer would result in the ice fracturing.

Figure 5.6. Photograph of the 9 cm corer being used in the laboratory. The corer takes cores that are 9 cm in diameter and can be up to a meter in length. This was not ideal for the thinner ice; however this length was necessary for the thicker rafted ice experiments. The corer was designed by Kovacs Enterprises, on loan from the British Antarctic Survey.

Density, Salinity, Porosity

Density, salinity and porosity were determined for laboratory ice grown to thicknesses of 7 and 27 cm. The former represents the ice thickness used in the standard case rafted ice experiments and the latter the thickness of the samples used in the 'level ice' shear tests. A core of the ice was taken using a 9 cm diameter corer (see Figure 5.6). The core was either cut into ~1 cm sections to see the variation of these properties with depth or kept intact to give the 'bulk' properties of the ice. To calculate density, the mass and volume of the sample were measured. Mass was measured using Gateweigh scales (model NWT-6K) accurate to 2 g. Volume was estimated either by measuring linear dimensions of the sample (to 0.5 mm) or submerging the sample in methylated spirits (ρ = 0.828 Mg m^{-3}) and measuring the volume of displaced fluid accurate to 2 ml. The first method was preferred for the larger samples whose dimensions could be easily measured, whereas the second was more practical for the smaller 1 cm sections. The temperature of the larger samples was measured by drilling a hole into the centre of the sample and measuring the temperature using a handheld HANNA thermometer, which is accurate to ±0.4°C. This method was not practical for the 1 cm sections, and so the temperature of these sections was estimated using the thermistor probes which were frozen into the ice during the growth and averaged over the thickness of the sample. Salinity was measured by melting the sample and measuring the salinity using a temperature compensated MISCO digital refractometer (model # PA203X), which takes readings accurate to ±0.5 ppt. Porosity was calculated using Cox and Weeks (1983) equations (Eqs. 2.2 and 2.3 in Chapter 2), which calculate brine and air volumes from the measured density, temperature and salinity.

Table 5.1 shows the temperature, salinity, density, and porosity for the ice samples that were melted down whole. The salinity measurements show that that for solutions of 6 and 33 ppt the salinity of the ice varied from 1.7 – 2.7 ppt and 10.1 - 10.8 ppt respectively. This is approximately a third of the initial concentration of the ice, which indicates that brine is draining out of the ice sheet and into the water below. Indeed in some of the longer samples brine drainage channels up to 1 cm in diameter were occasionally observed. Measurements of the salinity of the water below the ice show that after 7 cm of ice growth, the salinity increased from 6±0.5 ppt to 7±0.5ppt and from 33±0.5 ppt to 37±0.5 ppt. This will mean that in the rafted ice experiments, the salinity of the liquid layer between two rafted ice

blocks will initially be ~10-15% higher than expected. This will act to increase the consolidation time of the rafted ice as the liquid layer will have to be cooled to a lower temperature before it freezes. In the open ocean, brine draining from sea ice would (in most cases) be swept away by currents, so that the sea water remains at a constant salinity. Ideally, the experimental apparatus would have a water recirculation system to keep the salinity constant or a large enough tank so that salt surplus need not be considered. However, within my experimental constraints this was not possible. The effects of this on the rafted ice experiments will be discussed in more depth in Chapter 7.

Table 5.1. Temperature, salinity, density and porosity of laboratory grown ice.

Initial salinity of water (ppt)	Ice thickness (cm)	Average Temperature (°C)	Ice Salinity (ppt)	Density (Mg m^{-3})	Porosity (%)
0.3	7	-2.13	0	0.914	0.36
6	7	-3.16	1.7	0.907	4.70
6	13	-	2	-	-
6	19	-	1.8	-	-
6	24	-	2	-	-
6	27	-4.2	2.7	0.918	4.00
33	7	-4.17	10.8	0.930	14.9
33	27	-6.0	10.1	0.926	10.1

Note: where there are dashes '-' in the table no value was measured as it was not realised until later in the experimental programme that these were important parameters to measure.

It was found that the highest density was for the ice grown from 33 ppt solution, followed by the 6 ppt solution and then the 0 ppt solution. An increase in the ice density is expected with higher concentrations of solutions as the addition of salt to water increases its density and thus the density of the brine cells within the ice lattice. The value obtained for the 7cm, 6 ppt solution is lower than expected which is probably due to brine draining out of the ice during handling. The porosity of the laboratory ice also increased with increasing concentration of the initial solution. This is because more salt is retained in the ice and the internal brine volume is larger.

Figures 5.7 to 5.9 show the variation in temperature, salinity, density and porosity with depth for each concentration of solution. In the case of the ice grown from 6 ppt solution, the salinity at the top of the ice was very low or effectively zero. Below this top layer,

salinity gradually increased with depth to a salinity of 1-1.5 ppt. Similarly, the porosity at the top of the ice was very low indicating very few air or brine bubbles at the ice surface. This was confirmed by observations of the ice in thick section where the surface of the ice was visibly clear in comparison to opaque (bubbly) ice below. By contrast, for the ice grown from 33 ppt solution, higher salinities were observed at the top and bottom of the ice sheet yielding c-shaped profiles, which are characteristic of young sea ice growth in the Arctic and Southern Oceans. In addition, for the case of ice grown from 33 ppt solution, there was always a thin layer of high salinity water at the ice surface. This is most likely a result of brine expulsion, whereby brine is squeezed up onto the ice surface during the initial stages of ice formation (Martin, 1979).

Notz and Worster (2008) found in their experiments carried out in Adventfjorden, Svalbard, to measure the evolution of bulk salinity in young sea ice, that there was no increase in salinity towards the top of the ice. They attributed this to calm growth conditions found in the hole that was cut into the surrounding sea ice. Natural sea ice often grows in turbulent conditions meaning that a dense suspension of frazil ice forms, which upon consolidation trap a large percentage of interstitial brine. In the laboratory, there is very little frazil ice formation, which might explain the low salinities observed in the case of the ice grown from a solution of 6 ppt. However, this still would not explain the higher salinities observed towards the top of the ice grown from a 33 ppt solution.

The density and porosity of the ice also has a tendency to increase with depth. This is most probably due to the growth structure of the ice: a thin granular layer, followed by a transition zone and finally columnar ice. In columnar ice brine is predominantly concentrated along the grain boundaries. As temperature increases so does the liquid fraction (i.e. quantity of brine or water) so that towards the base of the ice sheet the solid fraction approaches zero.

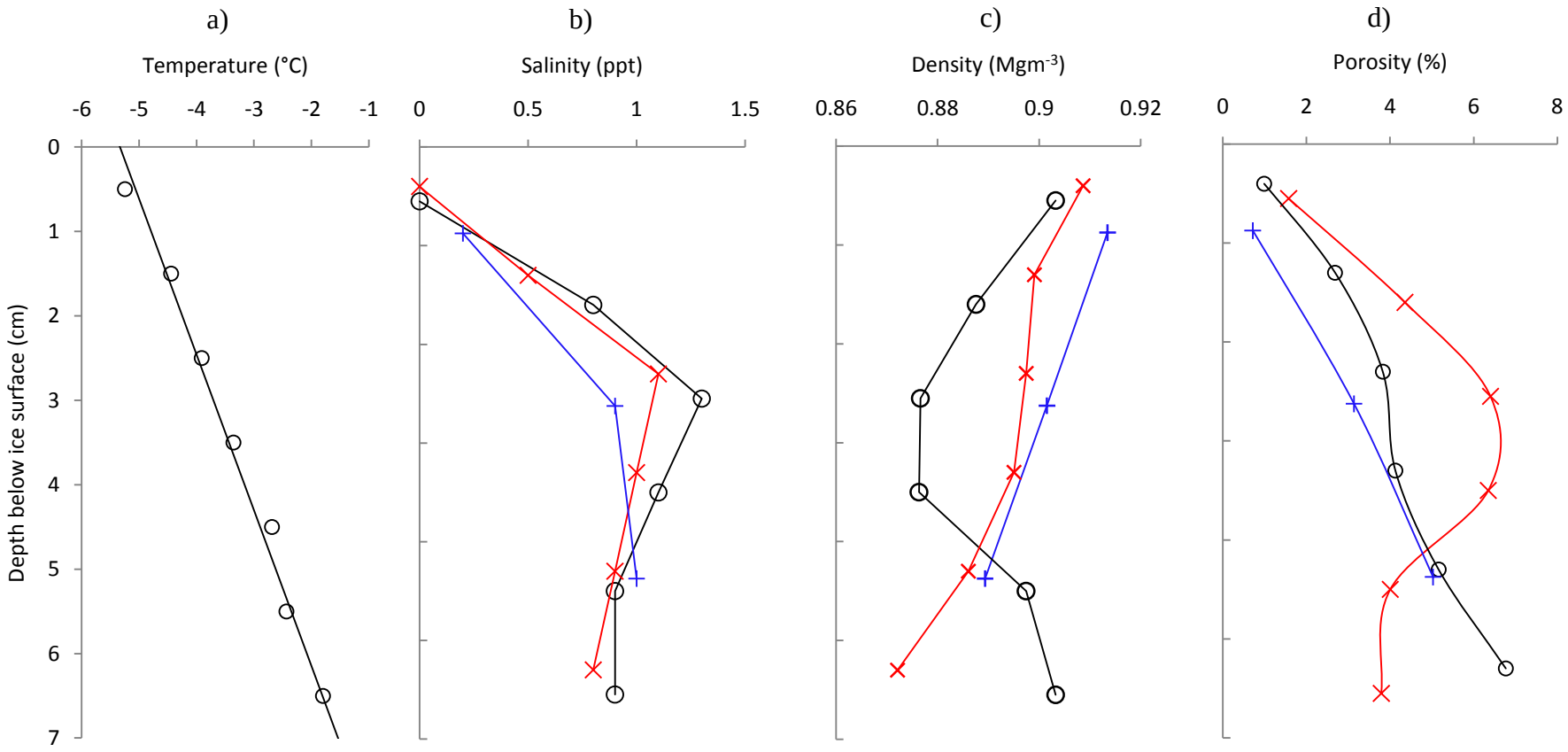

Figure 5.7. The temperature (a), salinity (b), density (c), and porosity (d) variation with depth of 3 cores taken from the laboratory ice that was grown from a 6ppt solution of NaCl to a thickness of 7 cm.

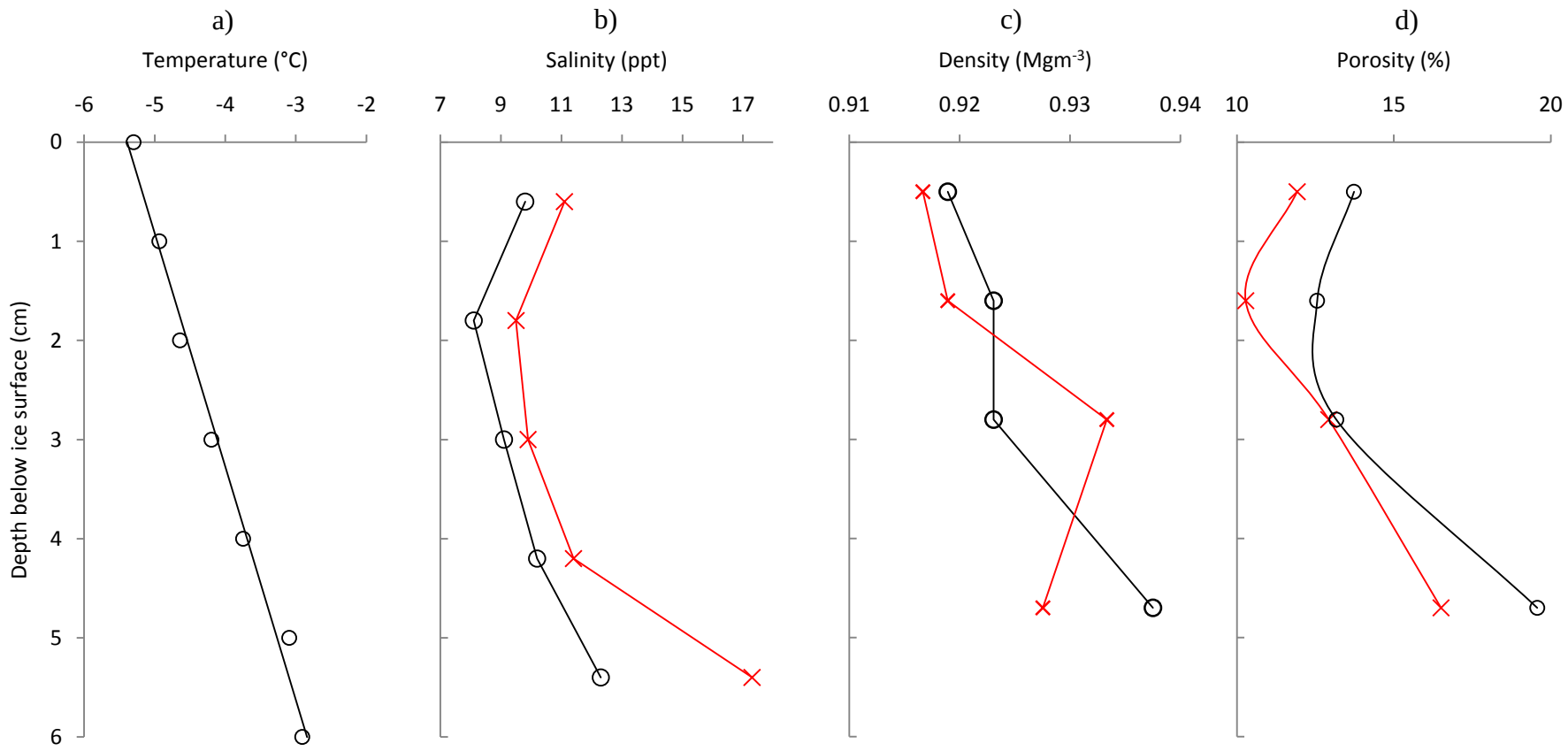

Figure 5.8. The temperature (a), salinity (b), density (c), and porosity (d) variation with depth of 2 cores taken from the laboratory ice that was grown from a 33ppt solution of NaCl to a thickness of 7 cm.

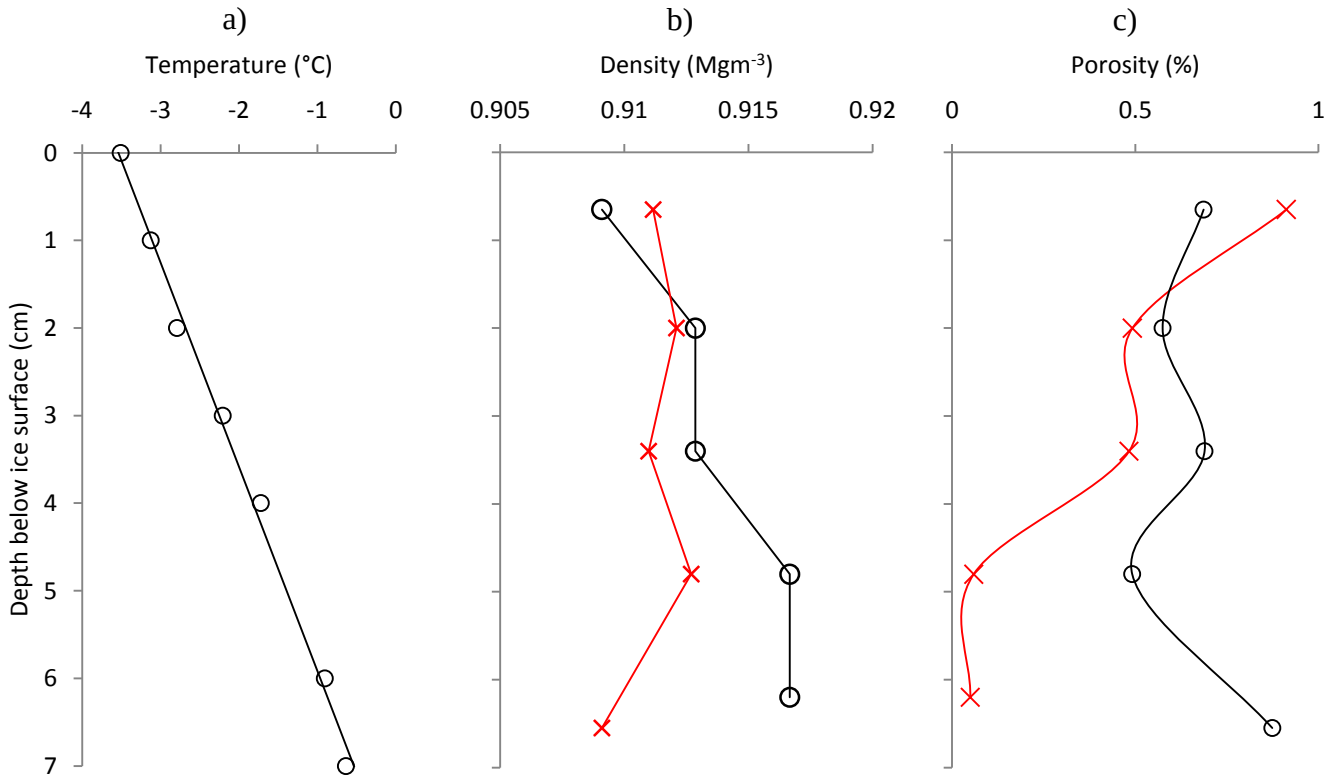

Figure 5.9. The temperature (a), density (b), and porosity (c) variation with depth of 2 cores taken from the laboratory ice that was grown from tap water (0.3 ppt) to a thickness of 7 cm.

Crystal structure

The crystal texture of the laboratory ice that was grown from a 6 ppt solution of NaCl was observed by making thick (~5mm thick) and thin (~1mm thick) sections and viewing them under crossed polarising lenses. A typical thick section, given in Figure 5.10, shows the overall structure of the laboratory-grown ice. From top to bottom, there is ~1 cm of granular ice, followed by a 2-3 cm transition zone, where crystals compete for survival, before columnar ice becomes established. Figure 5.11 shows two thin sections of the laboratory ice that were cut (a) perpendicular (horizontal) and (b) parallel (vertical) to the growth direction. The figure shows that the crystals c-axes are randomly oriented in the horizontal plane and vary in size from ~0.5-2.5 cm. In the vertical, the crystals are columnar and are longer than the length of the slide, which is 9 cm.

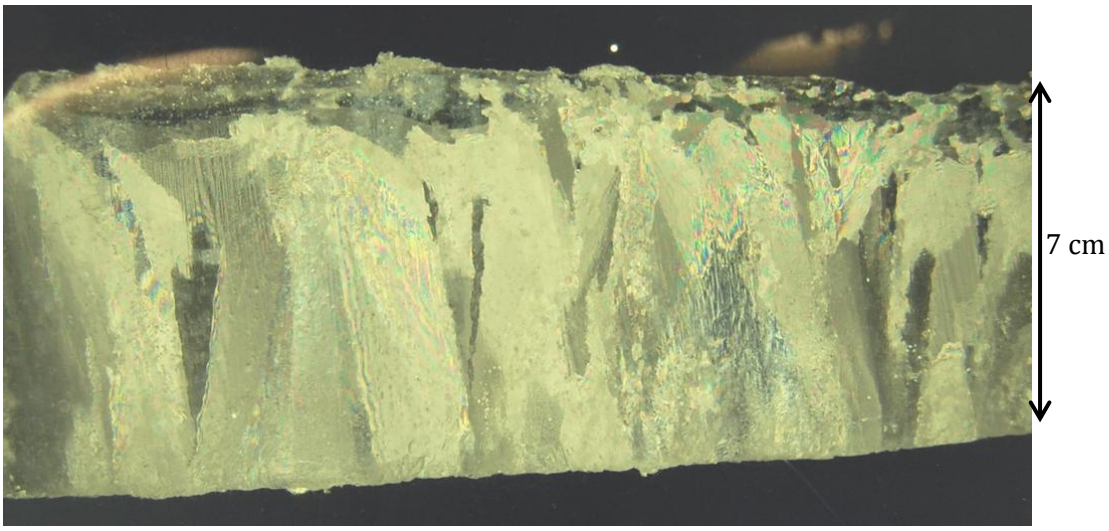

Figure 5.10. Thick section of the laboratory ice cut parallel to the growth direction and viewed under crossed polarising lenses.

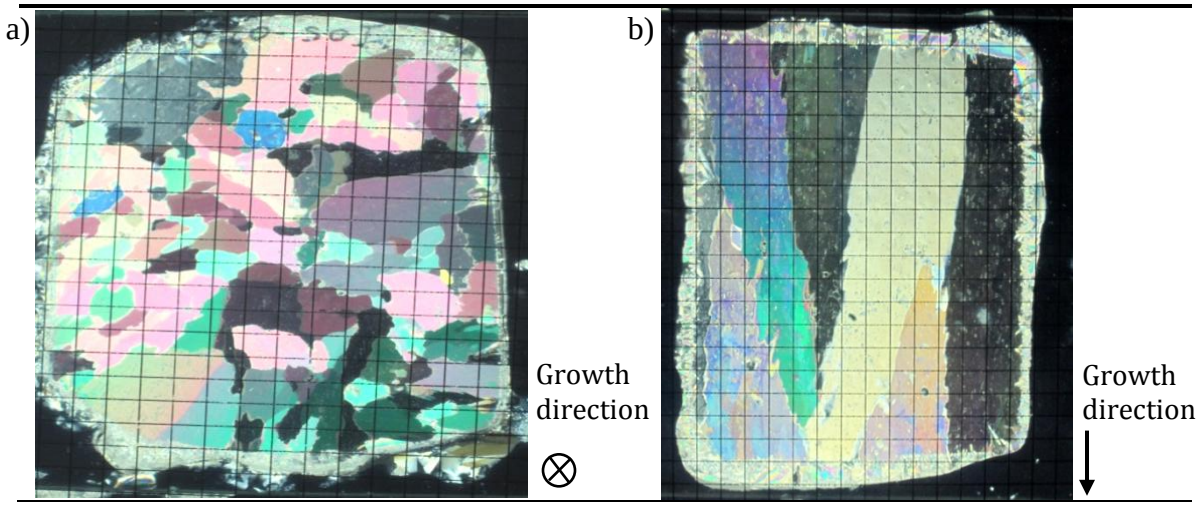

Figure 5.11. Thin sections of laboratory grown ice that were cut (a) horizontal and (b) vertical to the growth direction. The photographs of the thin sections were taken through crossed polarising lenses, with a 0.5 cm^2 grid placed on top.

Compressive strength

The compressive strength of laboratory-grown ice was determined by conducting uniaxial compression tests in a 200kN closed-loop servo-hydraulic universal testing machine, fitted with a temperature-controlled environmental chamber in the Rock and Ice Physics Laboratory. One salinity, 6 ppt, was tested. Ice was grown to a thickness of 25 cm and cores taken using a 9 cm diameter corer. The ends of the core were then cut using a band saw and milled flat to 10μm precision, to ensure that the surfaces in contact with the loading platens were flat and parallel. The resulting sample length to diameter ratio of 2.6:1 is sufficient to achieve uniform stress in the mid-section of the sample (Schwartz et al., 1981). Samples were tested directly after preparation to be able to determine the strength in a state as close to in situ as possible. The sample was centred on the pedestal of the test machine. The environmental chamber was cooled to a nominal temperature of -10°C and held constant to ±1°C. A loading piston, fitted with a steel plate and hemispherical alignment seats, was then slowly brought into contact with the ice sample. Two linear voltage differential transducers (LVDT) were positioned, one in the vertical to measure uniaxial deformation, and the other between a pair of extendable arms located at the centre of the sample to measure radial deformation. Load was applied via the actuator of the testing machine and measured using a load cell.

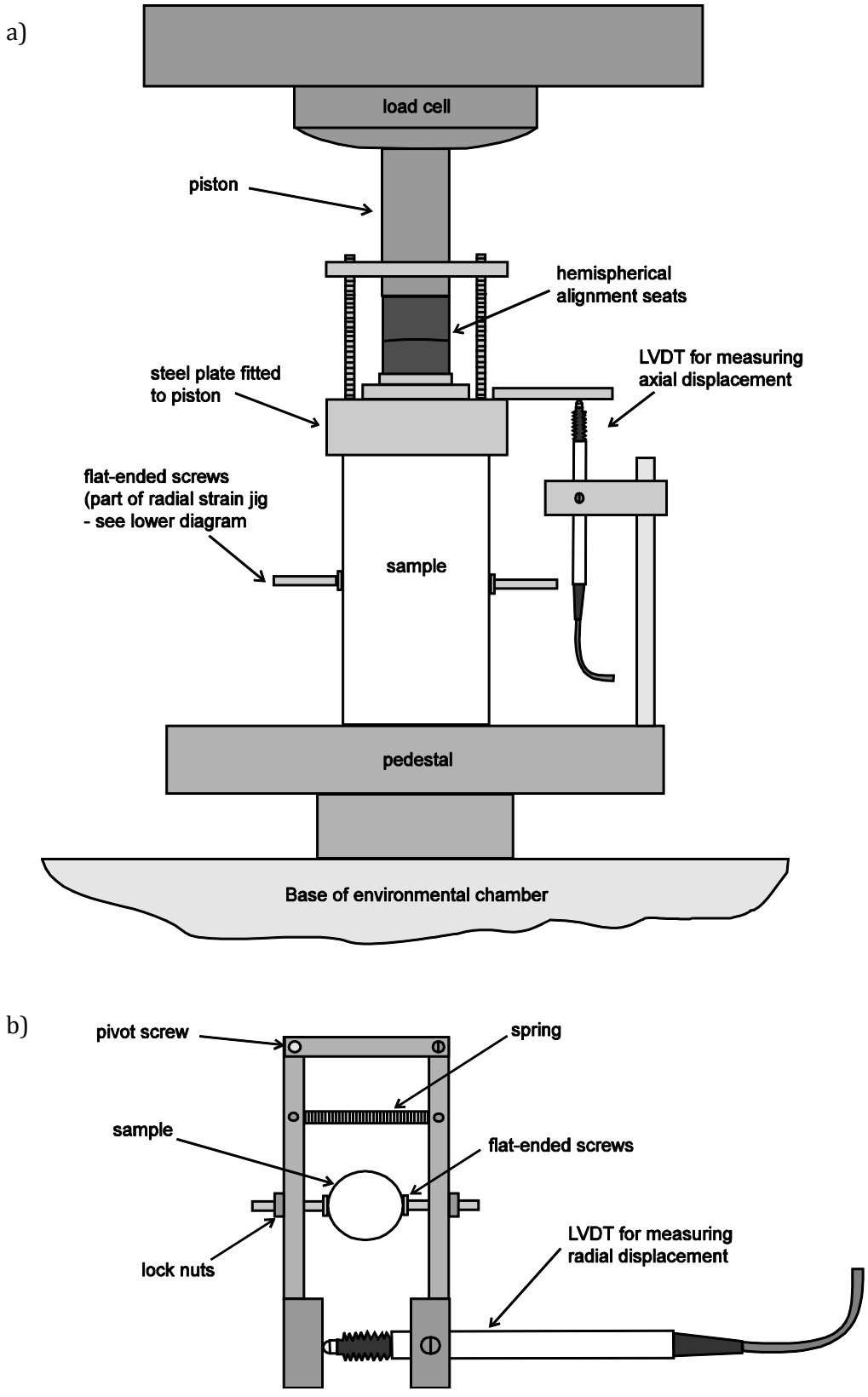

Figure 5.12. Schematic diagram of the uniaxial compressive strength experiment showing: a) the loading components and positions of the axial displacement transducer and the radial strain jig and, b) a plan view of the radial displacement jig.

Displacement, time and load were logged and monitored in real time using a National Instruments data acquisition card and LabView software. LVDTs and the load cells were calibrated using a micrometer screw gauge and a dead load tester respectively to within 1% accuracy. All tests were done at an actuator displacement rate of 30 mm min^{-1} (which corresponds to nominal strain rate of $2 \cdot 10^{-3}$ s^{-1} for this length sample). Figure 5.12 shows a schematic of a fully instrumented sample in the test machine.

Prior to each test, the sample was weighed and its linear dimensions recorded for determining density. Immediately after loading, a hole was drilled into the centre of the sample and its temperature measured using a handheld HANNA thermometer, which is accurate to ±0.4°C. The remaining ice sample was then removed and melted to determine salinity. Porosity was calculated as described above.

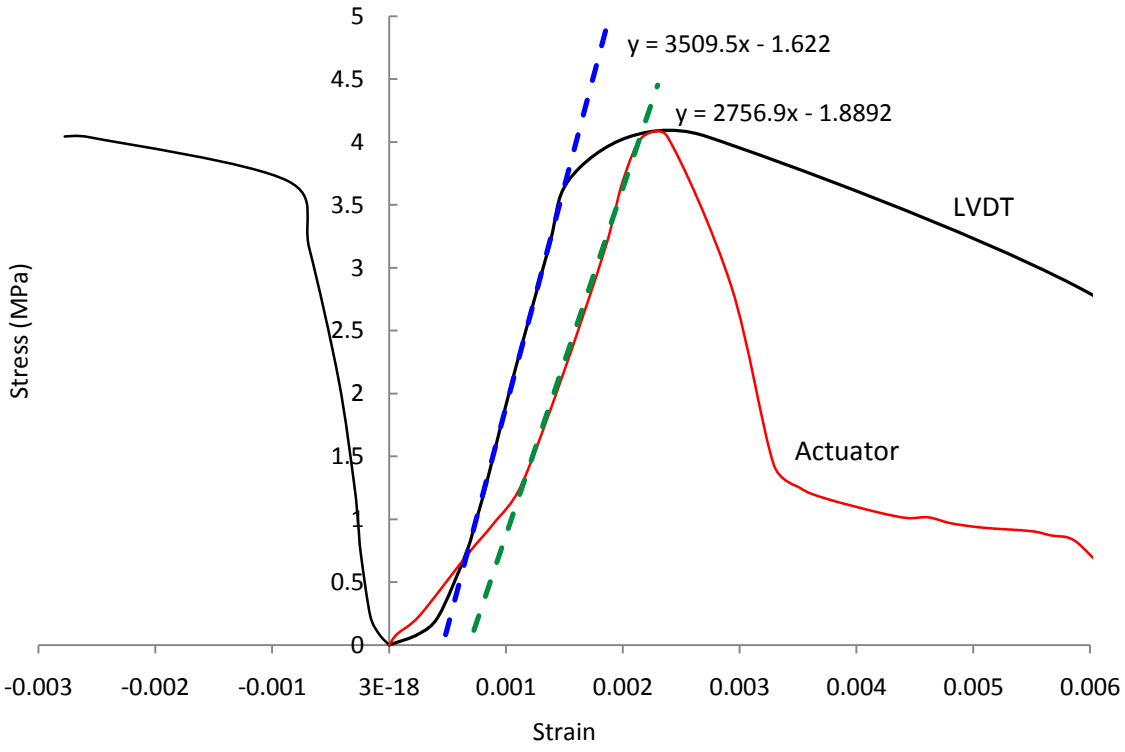

Figure 5.13. Stress-strain curve for the uniaxial compression of a 6 ppt sample of laboratory ice. The curve on the negative strain axis shows the radial strain and those on the positive axis show axial strain as measured by the sample LVDT (black line) and the actuator LVDT (red line). The dashed blue and green lines show the effective elastic modulus for the respective curves.

Figure 5.13 shows a typical stress-strain curve for the uniaxial compression of a 6 ppt sample of laboratory ice. Both axial strain (as measured by the actuator and the LVDT) and radial strain (on the negative strain axis) are plotted. The difference between the axial strain as measured by the sample and actuator LVDTs yields the stiffness of the test machine, as the sample LVDT is measuring both the elastic and in-elastic deformation of the ice. The sample LVDT shows that deformation is at first strongly elastic, followed by a small amount of strain hardening up to peak stress and subsequent elastic-ductile failure.

Compressive strength was taken as the maximum load divided by the initial cross-sectional area of the sample. Effective modulus was calculated from the slope of the sample stress-strain curve during elastic deformation (blue dashed line in Figure 5.13). The effective Poisson's ratio is the ratio between radial strain and axial strain. They are termed 'effective' as ice deformation is not truly elastic due to the delayed elastic response of ice from sliding at the grain boundaries (Timco and Weeks, 2010).

Table 5.2. The compressive strength, effective modulus, effective Poisson's ratio, ice temperature, salinity, density and porosity for laboratory ice grown from a 6 ppt solution.

Compressive strength (MPa)	Effective modulus (GPa)	Effective Poisson's ratio	Ice temperature (°C)	Ice salinity (ppt)	Density (Mg m^{-3})	Porosity (%)
2.99±0.04	3.17	0.07	-3.3	1.6	0.919	2.79
4.04±0.05	3.51	0.36	-4.3	1.6	0.916	2.51
6.12±0.08	4.37	-	-5.1	1.5	0.902	3.69

Note: I was not able to get a Poisson's ratio for the last core as the radial jig slipped during the test.

In Table 5.2, compressive strength, effective modulus and effective Poisson's ratio for 6 ppt laboratory grown ice are given for ice cores taken from a single sheet. The results show that the compressive strength of the ice increased from 3 MPa at -3.3°C to 6 MPa at -5.1°C over the course of the tests. The reason for the decrease in temperature during the course of testing is that once one core has been taken from the ice sheet, a void is left in the remaining ice, and is exposed to the cool air of the cold room. Since experiments were done over the course of an afternoon, this meant that the temperature of the remaining ice gradually cooled with time. The increase in the compressive strength is almost exponential,

conforming to the increase in plastic flow stress with decreasing temperature (c.f. Glen's law). The effective modulus of the ice also increased from 3.2 GPa to 4.4 GPa over this temperature range. (Typical values for the effective modulus of sea ice range from 1 to 5 GPa.) The effective Poisson's ratio ranged from 0.07 to 0.36. These values compare to a range of 0 to 0.2 measured by Wang (1981) on columnar ice in the vertical direction . More experiments need to be done before any concrete conclusions about Poisson's ratio can be drawn.

Shear strength

The shear strength of 'level ice' was measured using the asymmetric four-point bending rig (AFPB). This was done for the laboratory ice grown from 6 and 33 ppt solutions of NaCl. (Freshwater cores could not be obtained as discussed above). I designed a test apparatus based on that of Frederking and Timco (1984a). The AFPB rig consisted of two rectangular stainless steel plates (dimensions 9 x 30 x 2.5 cm) with two bars, 12 mm in diameter, mounted on each plate. The bottom plate was fixed to the pedestal of the 200 kN closed-loop, servo-hydraulic test machine, whilst the upper plate was free to rotate about the load-application point. Samples were taken using the 9 cm diameter corer and tested within ~10 minutes of coring so that the shear strength could be measured in a state as close to in situ as possible. Samples were loaded with the long axis of columnar grains normal to the loading axis. Plates were aligned so that bars were positioned asymmetrically about the loading axis and the centre of the specimen. Pieces of foam tubing, commonly used to insulate pipes in plumbing, were placed between the loading bars and the ice to provide stress relief. Load was applied to the upper plate via a pair of hemispherical alignment seats, which ensured that the load was evenly applied across the plate. Displacement, time and load were monitored in real time and logged using a National Instruments data acquisition card and LabView software. During all tests, the environmental chamber was held at a nominal temperature of -10°C and the nominal actuator displacement rate was 30 mm min^{-1} (which corresponds to a nominal strain rate of $5.7 \cdot 10^{-3}$ s^{-1} for this loading configuration). Figure 5.14 shows a photograph of an ice core loaded in the AFPB rig. Notice in this picture that the outer pins generate a clockwise rotation whilst the inner pins create a counteracting force in the counter-clockwise direction, producing a near pure stress state in the centre of the specimen.

The set-up differs from that described by Frederking and Timco (1984a) in that they used rectangular beams of ice, whereas in these tests I used cylindrical cores. Cores were used as they could easily be taken using a core auger and enabled samples to be tested directly after coring. Therefore before I can begin to interpret data the shear stresses for a beam of circular cross section must first be calculated using simple beam theory.

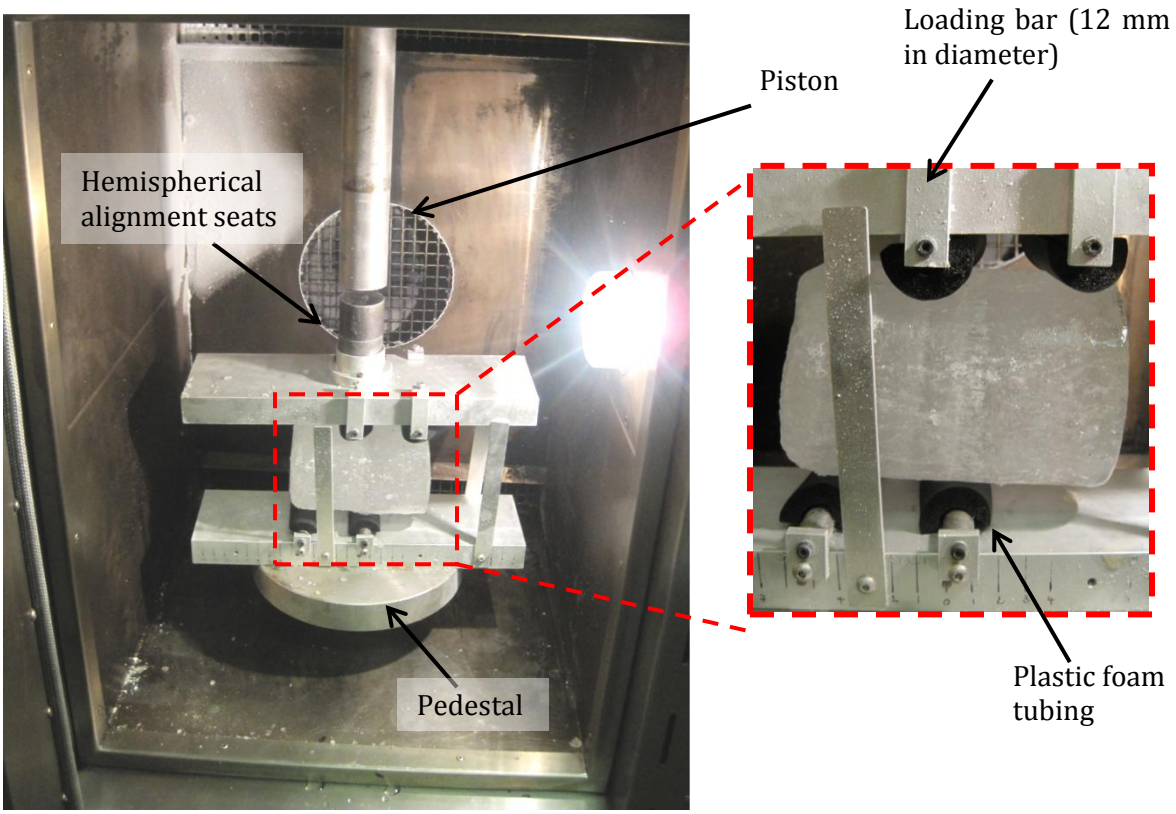

Figure 5.14. Photograph of a sample in the asymmetric four-point bending rig, which is fixed to the pedestal of a 200 kN closed-loop, servo-hydraulic test machine, fitted with an environmental chamber.

When considering the distribution of shear stresses over a circular cross section (Figure 5.15a) it can no longer be assumed that the shear stresses act parallel to the shearing force V (as they do for a rectangular beam). In fact, it can be easily proved that at point p (on the boundary of the cross section) the shearing stress must be tangential to the boundary. This observation follows from the fact that the outer surface of the beam is stress free, and so the shear stress acting on the cross section can have no component in the radial direction (Timoshenko, 1941). Although there is no simple way to find the shear stresses acting

throughout the entire cross section, the shear stresses at the neutral axis (where the stresses are the largest) can be determined by making the assumptions that the shear stresses act parallel to the y axis and have constant intensity across the width of the beam. Since these assumptions are the same as those used in deriving the shear formula,

$$\tau = \frac{V \int y dA}{b I_z} \tag{5.2}$$

(Timoshenko, 1941), this can be used to calculate the stresses at the neutral axis. In this expression, V is the shearing force, I_z is the moment of inertia, $\int y dA$ is the area moment of the segment of the circle above the line *pp* and b denotes the length of the cord *pp* (see Figure 5.15b). From Pythagoras's theorem, the area of the element *mn* is $dA = 2\sqrt{r^2 - y^2}\, dy$. Substituting this into equation (5.2) and integrating between r (the radius of the circle) and y_1 (the lower limit of the segment), we obtain,

$$\tau = \frac{V(r^2 - {y_1}^2)}{3 I_z}. \tag{5.3}$$

This is a parabolic distribution such that the maximum shear stress τ_{max} is obtained for $y_1 = 0$, i.e. for the neutral axis of the cross section. Therefore substituting in for $I_z = \pi r^2/4$, the maximum shear stress at centre of a beam of circular cross section is given by

$$\tau_{max} = \frac{4}{3} \frac{V}{\pi r^2}. \tag{5.4}$$

In the case of the AFPB, the shear force V is dependent on the geometry of the load application. Following Frederking and Timco (1984a), the shear stress within the inner loading pins can be calculated from free body diagrams and static equilibrium (see Figure 5.16). Therefore assuming simple beam theory applies, the maximum shear stress for a circular beam in asymmetric four-point bending is given by

$$\tau_{max} = \frac{4}{3} \frac{(1 - \alpha)}{(1 + \alpha)} \frac{P_{max}}{\pi r^2} \tag{5.5}$$

where P_{max} is the maximum the shear load applied, r is the radius of the core, α relates to the loading geometry. This assumption implies that local stresses generated by the concentrated forces acting on the beam (i.e. normal forces) are not considered.

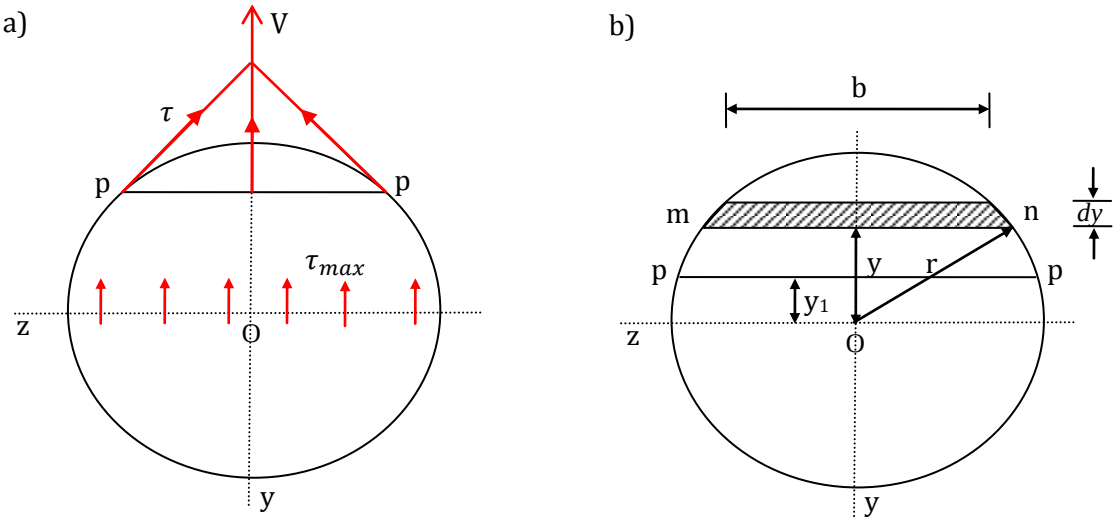

Figure 5.15. Circular cross section showing a) the shear stresses acting a circular beam and b) the differential area and the limits of the line integration.

To compare this set up to that used by Frederking and Timco (1984a; 1986), initial tests were done on columnar grained saline-ice using similar test conditions. This meant growing ice from a 33 ppt solution of NaCl and water to a thickness of 35 cm, positioning the loading bars 13 cm and 1.3 cm from the centre line ($\alpha = 0.1$) and setting the actuator displacement rate to 30 mm min^{-1}. The results of these tests showed that the average shear strength was 580 kPa (see Table 5.3). This is in good agreement with the results of Frederking and Timco (1984a) who found that for granular/discontinuous-columnar grained sea ice the average shear strength was 550 ±120 kPa and is in the same range as those measured by Frederking and Timco (1986) who found that the horizontal shear strength of columnar grained ice at -12°C was 760 kPa and 560 kPa at -2°C. The results also showed that the shear strength had very little dependence on the actuator displacement rate.

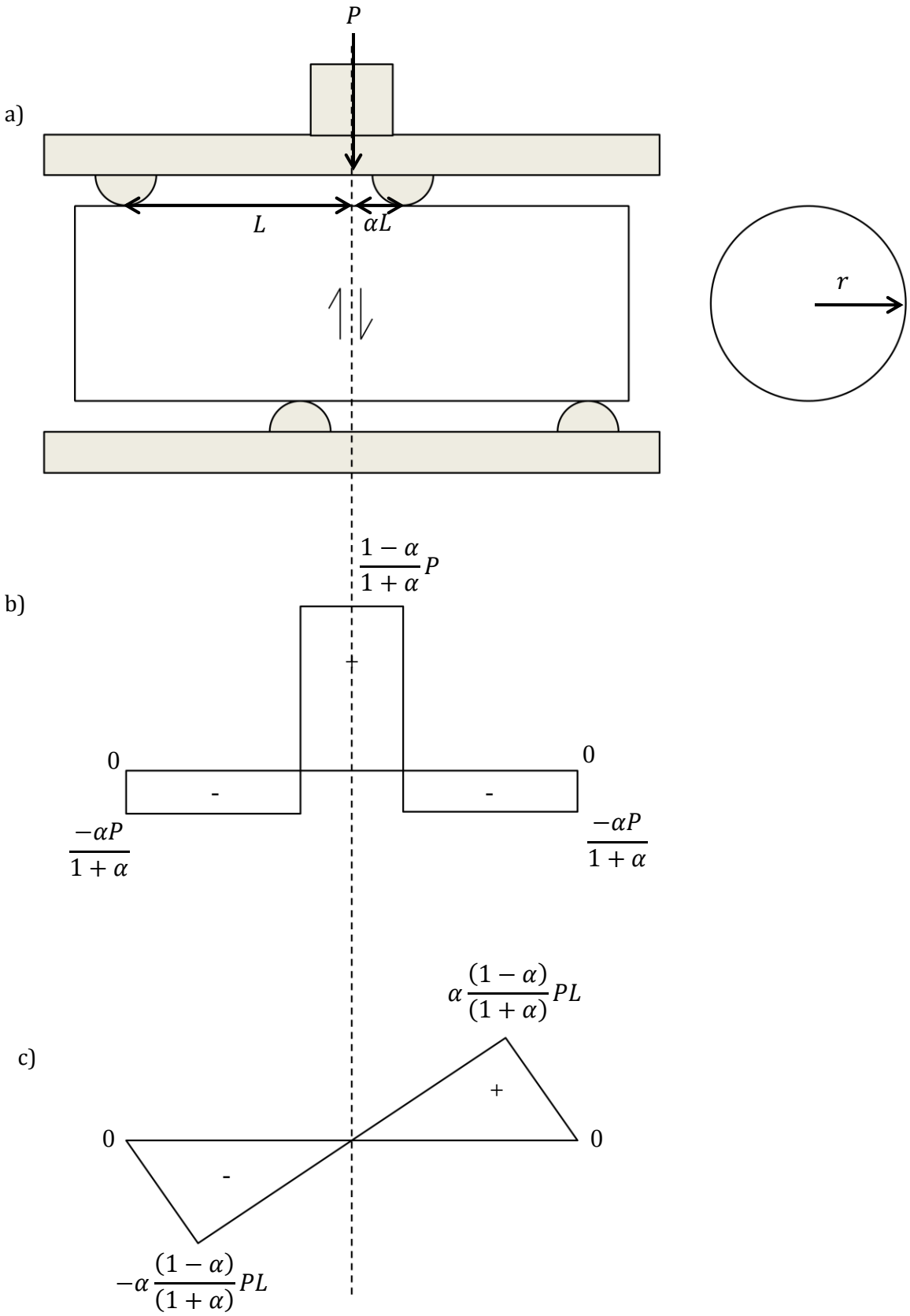

Figure 5.16. Asymmetric four-point bending rig showing diagrams of a) the experimental set-up b) the shear forces and c) the bending moments (after Frederking and Timco, 1984a).

Having shown that the AFPB rig can be used with cylindrical cores and produce results consistent with previous investigators, I then performed a series of tests under similar conditions to those of the rafted ice experiments (c.f. Chapter 7). Initially core lengths were 15 cm and the position of the outer and inner loading bars were 5 cm and 0.5 cm from the centre line. Results of all the shear tests and the test conditions are presented in Table 5.3.

In the case of the samples grown from 6 ppt solution, when the ice thickness was 15 cm the core would not fail in shear and the inner loading bars indented into the ice causing the sample to split along the grain boundaries of the columnar grains. At thicknesses greater than 19 cm it was possible to achieve shear failure. This indicates that there is a critical core length, between 15 and 19 cm, below which the ice will no longer fail in shear. Beyond this critical length the results were independent of core length with shear strengths ranging from 550 to 650 kPa. In the case of the 33 ppt tests, none of the samples failed in shear with loading pin positions of 0.5 and 5 cm. When widened to positions of 1 and 10 cm, it was a possible to make a sample of 27 cm fail in shear.

In all shear tests, the actual failure plane always extended between the inner two loading points. Figure 5.17 shows a typical stress-time curve for the level ice shear experiments. The figure shows that deformation is strongly elastic and failure occurs abruptly with an instantaneous drop in load.

From the above description it is clear that samples must exceed a critical length before shearing occurs. Below this length, local crushing causes the beam to split along grain boundaries. Ice structure also plays a role. Ice grown from 33 ppt salinity has greater brine volume than the less saline ice making it locally weaker. Hence it would collapse more readily and so longer sample lengths are necessary. The diameter of the sample would also have an effect on the stresses generated, and although it was not varied, we see that the ratio of sample length to sample diameter needs to exceed 2 (19/9 in the 6 ppt case) for shear failure to occur. This is in agreement with data from numerous compression tests. It was also noted that in the 33 ppt case, widening of the loading pin positions initiated shearing in the 30cm samples. This is as expected since wider pin positions create a greater bending moment which would favour of shear failure.

Table 5.3. Results of the shear tests carried out on laboratory ice grown from solutions of 6 ppt and 33 ppt concentration.

Initial salinity of water (ppt)	Shear strength (kPa)	Bar positions (cm)		Actuator rate	Ice thickness (cm)	Ice Temperature (°C)	Ice Salinity (ppt)	Density (Mg m^{-3})	Porosity (%)
		Inner	Outer	(mm min^{-1})					
6	did not fail in shear	0.5	5	30	15	-	2	-	-
6	641±36	0.5	5	30	19	-	1.9	-	-
6	539±30	0.5	5	30	19	-	1.9	-	-
6	649±36	0.5	5	30	19	-20	2	-	-
6	599±33	0.5	5	30	22	-	2	-	-
6	651±36	0.5	5	30	22	-	2	-	-
6	597±33	0.5	5	30	27	-3.9	2.5	0.917	3.99
33	did not fail in shear	0.5	5	30	15	-4.1	9.8	0.924	14.2
33	did not fail in shear	0.5	5	30	19	-5.3	9.5	0.921	11.1
33	did not fail in shear	0.5	5	30	27	-5.7	8.8	0.919	9.84
33	465±26	1	10	30	27	-6.6	8.9	0.916	9.07
33	446±25	1	10	30	27	-5.6	8.8	0.907	11.2
33	587±33	1.3	13	30	35	-	-	-	-
33	572±32	1.3	13	0.5	35	-	-	-	-

Note: where there are dashes '-' in the table no value was measured as it was not realised till later in the experimental programme that these were important parameters to measure.

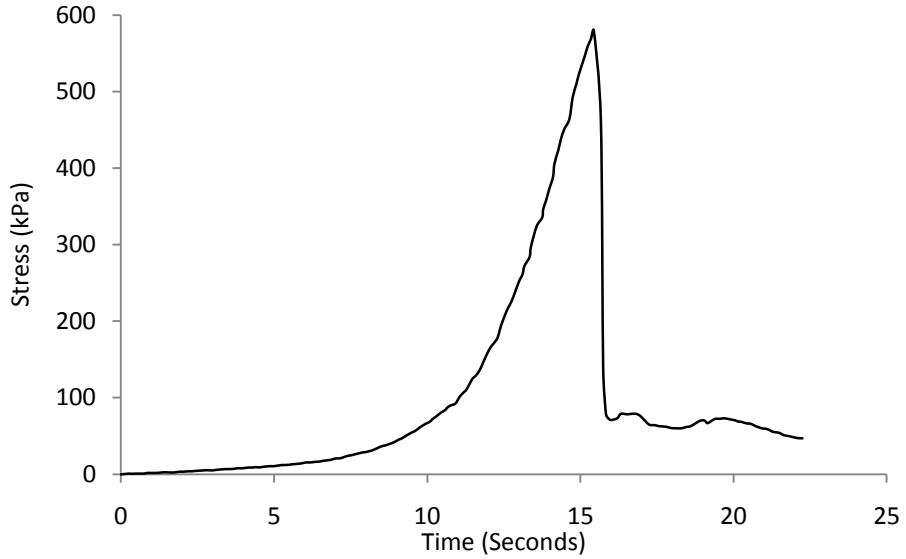

Figure 5.17. Typical stress-time curve for the shear strength of the laboratory ice grown from a 6 ppt solution of NaCl and water.

5.6 Summary

The one-layer model described in the previous chapter was tested against laboratory data using the temperatures recorded directly at the upper ice surface and the growth rate inferred from the laboratory experiments. Results showed that the temperature distribution simulated by the model is in good agreement with experimental measurements. The physical and mechanical properties of the laboratory grown ice were examined. Results showed that in general the ice salinity, density, and porosity increased with the initial concentration of the solution from which the ice was grown. The crystal texture of the laboratory ice was made up of ~1 cm of granular ice, followed by a 2-3 cm transition zone, and then a zone of columnar ice growth. The compressive strength of the 6 ppt ice increased from 3 MPa at -3.3°C to 6 MPa at -5.1°C over the course of the tests. The shear tests showed that for ice grown from 6 ppt solution a critical length between 15 and 19 cm is required for failure of a 9 cm diameter cylindrical sample, corresponding to a minimum length to diameter ratio of at least 2. Once this critical length had been exceeded, all core samples failed under shear with shear strengths between 550 and 650 kPa.

6 A numerical model for the consolidation of rafted sea ice

6.1 Introduction

In this chapter, I present a one-dimensional thermal-consolidation model for rafted sea ice that I developed to investigate physical processes that are important in the consolidation of rafted sea ice. This has recently been published in the Journal of Geophysical Research – Oceans (see Appendix C). The model calculates how long it will take for the layers of ice in a rafted section to effectively bond into a coherent ice sheet, once the ice sheets have ceased moving. I first consider the consolidation between two layers of rafted sea ice (i.e. simple rafting) and then extend the model to include a third layer (i.e. multiple rafting). I only consider regions of rafted ice that extend over large enough distances so that horizontal effects need not be taken into account. The rafted ice is assumed to be composed of layers of sea ice of equal thickness, separated by thin layers of ocean water. The thin layers of ocean water between the ice sheets are assumed to initially form because large surface asperities or fragments of snow and ice get caught between the ice sheets during rafting and act as spacers allowing seawater to flood in (c.f. Chapter 3). I assume that multiple rafting takes place simultaneously. This assumption is justified by the fact that most samples of multiply rafted sea ice show layers in a rafted section are of roughly equal thickness, suggesting that the ice sheets rafted in quick enough succession such that thermodynamic growth of the adjacent level ice was minimal.

I shall present the paper as it was published with the exception that the discussion section has been adapted to make it more relevant to this thesis. The mathematical formulation of the consolidation model and the method of solution are described in sections 6.2 and 6.3. In section 6.4, I present the parameters that are used to force the model that are typical of the environments of the north Caspian and the Arctic and Southern Oceans. In section 6.5, the results of the numerical simulations are presented and the sensitivity of the model to certain key parameters is examined. A discussion of the results and concluding remarks are presented in section 6.6.

6.2 Mathematical Formulation

Consider the situation where 2 identical ice sheets of initial thickness H_0 have rafted, such that there is a liquid layer of initial thickness h_0 located between adjacent sheets (Figure 6.1). The sea ice is described as a mushy layer, a rigid matrix of pure ice immersed in its brine (Feltham et al., 2006), and the liquid layer is a thin layer of ocean water, trapped between the asperities of the ice sheets. The internal temperature of each ice sheet is determined from the nonlinear one-dimensional heat diffusion equation,

$$c_{eff}\frac{\partial T}{\partial t} = \frac{\partial}{\partial z}\left(k_{eff}\frac{\partial T}{\partial z}\right) + A_R, \tag{6.1}$$

where c_{eff} and k_{eff} are, respectively, the effective volumetric specific heat capacity and the thermal conductivity of sea ice, T is the temperature within the ice sheet, t is time, and z is the vertical spatial coordinate, which is taken to be positive upwards. The final term, A_R, describes the absorption of solar radiation that penetrates through the upper sea ice surface, which is taken to be

$$A_R = \kappa_i I_0 (1-\alpha) F_{SW} e^{-\kappa_i z}, \tag{6.2}$$

where κ_i=1.5 m^{-1} is Beer's extinction coefficient, $I_0 = 0.4$ is the fraction of incident radiation that passes through the surface into the interior of the ice, $\alpha = 0.6$ is the albedo for bare ice, and F_{SW} is the flux of incoming shortwave radiation (Ebert and Curry, 1993; Maykut and Untersteiner, 1971).

The effective volumetric heat capacity and thermal conductivity of sea ice are given by,

$$c_{eff} = c_i - \mathcal{L}_s \frac{T_L(S_{bulk}) - T_L(0)}{\theta^2} \tag{6.3}$$

and

$$k_{eff} = k_{bi} - (k_{bi} - k_b)\frac{T_L(S_{bulk}) - T_L(0)}{\theta}, \tag{6.4}$$

(Bitz and Lipscomb, 1999; Feltham et al., 2006), where $T_L(S_{bulk})$ is the liquidus (freezing) temperature of sea ice with a bulk salinity S_{bulk}, which is taken to be uniform across the ice

sheet, $T_L(0)$ is the liquidus temperature of pure water, $\theta = T - T_L(0)$, $\mathcal{L}_s = 3.014 \cdot 10^8$J m^{-3} is the volumetric heat of fusion of pure ice and $c_i = 1.883 \cdot 10^6$ J(m^{3}K)$^{-1}$ is the volumetric heat capacity of pure ice (Ebert and Curry, 1993) and k_{bi} and k_b are the conductivities of bubbly ice and brine respectively.

After Schwerdtfeger (1963), k_{bi} and k_b are

$$k_{bi} = \frac{2k_i + k_a - 2V_a(k_i - k_a)}{2k_i + k_a + V_a(k_i - k_a)} k_i \quad \text{W(mK)}^{-1} \tag{6.5}$$

and

$$k_b = 0.4184(1.25 + 0.030K^{-1}\theta + 0.00014K^{-2}\theta^2 \quad \text{W(mK)}^{-1}, \tag{6.6}$$

where $k_i = 1.16(1.91 - 8.66 \cdot 10^{-3}\text{K}^{-1}\theta + 2.97 \cdot 10^{-5}\text{K}^{-2}\theta^2)$ W(mK)$^{-1}$ is the conductivity of pure ice (Sakazume and Seki, 1978), $k_a = 0.03$ W(mK)$^{-1}$ is the conductivity of air (Weeks and Ackley, 1986), and $V_a = 0.025$ is the fractional volume of air in sea ice for sea ice with a salinity of 6ppt (Timco and Frederking, 1996).

The sea ice is assumed to be in local thermodynamic equilibrium which implies that the temperature T and brine concentration S_{brine} lie on the liquidus curve in the phase diagram for sea ice, i.e. $T = T_L(S_{brine})$. The liquidus curve can be approximated by the liquidus curve for sodium chloride solution (Notz, 2005; Weast, 1971),

$$T_L(S) = -5.33 \cdot 10^{-7} - 9.37 \cdot 10^{-6}S^2 - 0.0592S + 273.15 \text{ K}. \tag{6.7}$$

The sea ice is assumed to initially have a linear temperature profile based on the air and sea temperature at the upper and lower boundaries, giving the following initial condition,

$$T = \frac{T_0 - T_L(S_{ocean})}{H_0} z + T_L(S_{ocean}) \qquad (\text{t} = 0), \tag{6.8}$$

where T_0 is the temperature at the upper surface, $T_L(S_{ocean})$ is the freezing temperature at the salinity of the ocean S_{ocean} and H_0 is the initial thickness of the sea ice.

At the upper surface of the sea ice ($z = h_s$), it is assumed there is no melting so that the net flux, $(F_{net})_0$, is equal to the conductive flux, $-k_{eff}\,\partial T/\partial z$, such that

$$(F_{net})_0 \equiv \varepsilon_i(F_{LW} - \sigma T_0^4) + (1-\alpha)(1-I_0)F_{SW} - F_{sens} - F_{lat} = -k_{eff}\frac{\partial T}{\partial z} \quad (z = h_s), \tag{6.9}$$

where ε_i = 0.99 is the emissivity of bare ice, F_{LW} is the flux of downward longwave radiation, $\sigma = 5.67 \cdot 10^{-8}$ J(K^{4}m^{2}s)$^{-1}$ is the Stefan-Boltzmann constant, and F_{sens} and F_{lat} are the sensible and latent heat fluxes (Ebert and Curry, 1993; Maykut and Untersteiner, 1971; Taylor and Feltham, 2004).

At the interior interfaces ($z = h_a, h_b$), i.e. the interfaces above and below the liquid layer, the boundary conditions are

$$T = T_L(S_{liquid}) \qquad (z = h_a, h_b) \tag{6.10}$$

and

$$\mathcal{L}_s\phi\left(\frac{\rho_{brine}}{\rho_{ice}}\right)\frac{dh_{a,b}}{dt} = k_{eff}\frac{\partial T}{\partial z} \qquad (z = h_a, h_b), \tag{6.11}$$

where S_{liquid} is the salinity of the liquid layer, $\phi = 1 - S_{bulk}/S_{liquid}$ is the local solid fraction per unit volume of the sea ice, $\rho_{brine}/\rho_{ice} = 1.09$, describes the expansion of the liquid upon freezing (Pounder, 1965), dh/dt is the velocity of the respective boundary and $\partial T/\partial z$ is the temperature gradient in the ice at the boundary.

At the sea ice-ocean boundary ($z = h_{ocean}$), the sea ice is held constant at the freezing temperature of the ocean,

$$\mathrm{T} = \mathrm{T_L}(\mathrm{S_{ocean}}) \qquad (z = h_{ocean}). \tag{6.12}$$

The ice growth rate at the ice-ocean boundary is given by the Stefan condition,

$$\mathcal{L}_s\phi\left(\frac{\rho_{brine}}{\rho_{ice}}\right)\frac{dh_{ocean}}{dt} = k_{eff}\frac{\partial T}{\partial z} + F_{ocean} \qquad (z = h_{ocean}), \tag{6.13}$$

where F_{ocean} is the heat flux from the ocean directed into the base of the ice sheet. The adoption of a non-zero solid fraction at the sea-ice-ocean interface, $\phi(z = h_{ocean}) = 1 -$

S_{bulk}/S_{ocean}, where S_{bulk} is a constant, is an approximation in that S_{bulk} will vary throughout the interface region (Notz and Worster, 2008). This implies we are tracking the location of the 'consolidated' ice-ocean interface, which conveys the mathematical advantage that the interface location can be determined explicitly (rather than using an implicit numerical technique) and has been shown to lead to little numerical error (Feltham, 1998).

Since the liquid layer is narrow, salt diffusion maintains a uniform salinity inside the liquid layer on the timescale of changes in diffusive heat flux in the surrounding ice sheets provided that $(h/H)^2 \ll Le$ where h is the liquid layer thickness, H is the ice layer thickness, and Le is the Lewis number, defined to be the diffusion rate of salt divided by the effective thermal diffusivity of sea ice and equal to approximately 10^{-2} (Feltham, 1998). For the calculations presented here, this condition is satisfied and therefore the temperature of the liquid layer T_{liquid} is uniform and equal to the local liquidus temperature,

$$T_{liquid} = T_L(S_{liquid}). \tag{6.14}$$

The liquid layer is initially assumed to consist of ocean water and, as it freezes, a fraction of salt f' is released into the liquid layer. This assumption is based upon the observation that the liquid layer becomes increasingly salty as freezing progresses (see section 6.4). It is not entirely clear by what mechanism salt is being released into the liquid layer. I speculate that brine is being released from the newly forming ice at the base of the upper ice sheet. Therefore conservation of salt implies

$$S_{liquid} = S_{ocean} + f' \frac{\Delta h_a}{h_t} S_{ocean}, \tag{6.15}$$

where Δh_a is the amount of freezing at the base of the upper ice sheet and h_t is the thickness of the liquid layer at time *t*. In the experiments described in section 6.4 it was impractical to measure Δh_a but the liquid layer thickness could be measured. Therefore for the purposes of comparison with observations, and because the error it introduces is small compared with uncertainty in the measurement of the liquid layer salinity, I assume that

$\Delta h_a = f'' \Delta h_b$, where f'' is a constant and Δh_b is the amount of freezing at the lower layer. Then, since $\Delta h_a = h_0 - h_t - \Delta h_b$, equation (6.15) can be re-written as

$$S_{liquid} = S_{ocean} + f S_{ocean} \left(\frac{h_0}{h_t} - 1 \right), \tag{6.16}$$

where $f'' = f'/(1 + f'')$. The rate of change of h_t can be deduced from the difference in the Stefan conditions at the boundaries above and below the liquid layer, so that

$$\frac{dh_t}{dt} = \frac{k_{eff}}{\phi L} \frac{\rho_{ice}}{\rho_{brine}} \left(\frac{\partial T_a}{\partial z} - \frac{\partial T_b}{\partial z} \right), \tag{6.17}$$

where $\partial T_a/\partial z$, $\partial T_b/\partial z$ are the temperature gradients at the boundaries above ($z = h_a$) and below ($z = h_b$) the liquid layer respectively. The system of equations (Eqs. 6.1 to 6.17) comprises a closed partial-differential, initial-boundary value problem.

When considering the consolidation between three layers of rafted ice, I assume that the layers of ice are of equal thickness and are separated by 2 thin layers of ocean water also initially of equal thickness. The mushy layer equations described above are used to determine the vertical heat transport within the ice sheets (Eqs. 6.1 to 6.7) and are subject to the same initial condition (Eq. 6.8) and boundary conditions that describe the heat fluxes at the ice-atmosphere interface (Eq. 6.9), the ice-liquid layer interfaces (Eqs. 6.10 & 6.11), and the ice-ocean interface (Eqs. 6.12 & 6.13). The rate at which the liquid layers reduce with time is then determined from the difference in the Stefan conditions at the respective interfaces (Eq. 6.17).

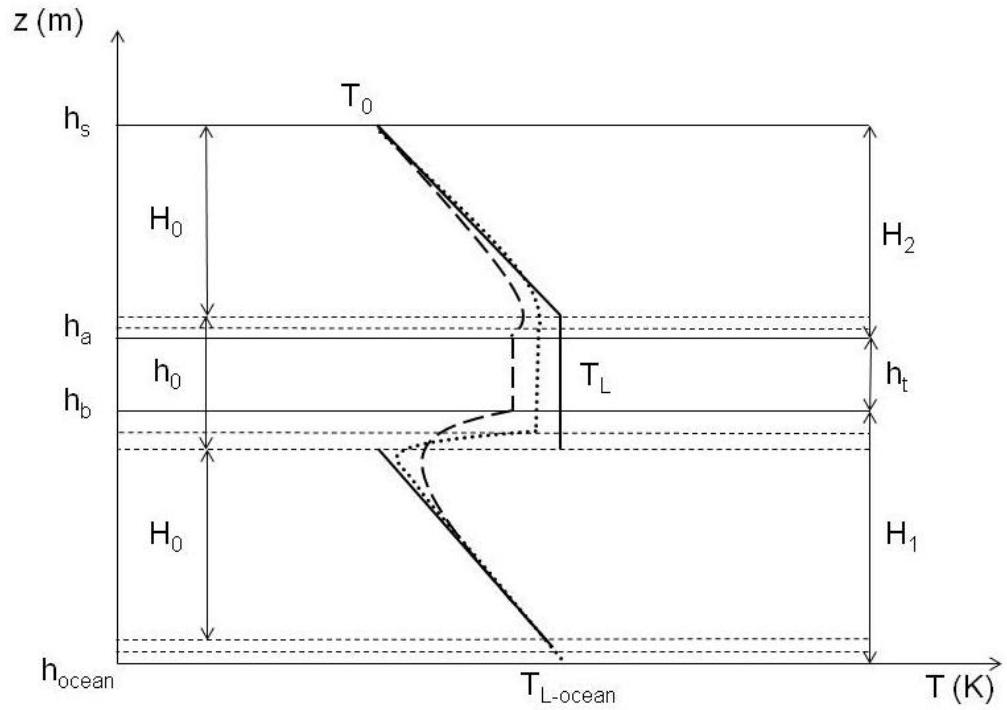

Figure 6.1. Schematic of the consolidation model illustrating how the temperature profiles, thickness of the ice sheets and the liquid layer evolve with time. H_0 and h_0 are the initial thicknesses of the ice sheets and the liquid layer, respectively, and $H_{1,2}$ and h_t are the thicknesses at a later time t. T_0 is the temperature at the ice-atmosphere interface, T_L is the liquidus temperatures in the liquid layer and $T_{L\text{-}ocean}$ is the liquidus temperature of the ocean. The dashed lines at the interfaces between the ice sheets and the liquid layer and the lower ice sheet and the ocean indicate the movement of these interfaces due to freezing, where h_a is the location of the freezing front above the liquid layer, h_b is the location of the freezing front below the liquid layer, and h_{ocean} is the location of the freezing front at the ice-ocean interface. The bolder lines denote the temperature profiles in the ice sheets and the liquid layer, where the solid line depicts the initial temperature in the ice sheets and the liquid layer and the dotted and dashed lines the temperature at later times.

6.3 Method of Solution

The model described in the previous section was coded in MATLAB. The heat diffusion equation (Eq. 6.1) was solved for each ice sheet using the 'pdepe' function using a mesh of 101 nodes and a timestep of 3 seconds. The calculated temperature distribution was then used to determine the temperature gradient and the thermal conductivity (Eq. 6.4) at the growing ice interfaces. These were used, along with the volumetric latent heat, the solid fraction and the density ratio in the Stefan condition (Eq. 6.11 & 6.13) to calculate the rate of ice growth at the respective interfaces. The amount of growth was then used to determine the concentration of the liquid layer (Eq. 6.16) and the thickness of the liquid layer (Eq.

6.17). The temperature of the liquid layer (Eq. 6.14), the thickness of the ice slabs and the initial condition were then updated for the next time step. See Appendix D for more details on the MATLAB code for the consolidation model.

Initial runs revealed that when the fraction of salt released into the liquid layer (f) is greater than zero the thickness of the liquid layers reduced asymptotically with time, such that there always remained a thin saline liquid layer. Complete solidification of the liquid layer will only occur if the temperature reaches the Eutectic temperature is reached (-22.9ºC for $NaCl{\cdot}2H_2O$). It is known from field observations that the layers of ice do in fact consolidate. The model assumes that the surfaces of the ice slabs are smooth, whereas, in reality, they are rough. At some stage the surface asperities will grow sufficiently in size to effectively bond the slabs together. I therefore imposed a 'cut-off' in the program such that when the liquid layer reaches the size of the surface asperities (h_{sa}) (i.e. the surface roughness) the adjacent ice sheets can be considered consolidated.

6.4 Model Parameters

The model was forced using parameters typical to the environments of the north Caspian Sea, the Arctic Ocean and the Antarctic Southern Ocean (see Table 6.1). Constant values were used for the forcing data (F_{LW}, F_{SW}, F_{sens}, F_{lat}, F_{ocean}), the ocean salinity (S_{ocean}) and the bulk salinity of the sea ice (S_{bulk}). The atmospheric data (F_{LW}, F_{SW}, F_{sens}, F_{lat}) was calculated from averages of the coldest months in the respective locations, using data collected during the Surface Heat Budget of the Arctic (SHEBA) experiment for the Arctic and the National Centres for Environmental Prediction (NCEP) for the north Caspian Sea and the Antarctic. The oceanic heat flux (F_{ocean}) was set to 3 Wm^{-2} for the Arctic and the Antarctic and 9.7 Wm^{-2} for the north Caspian. These values were based on data collected over first year sea ice in the Arctic between November to February 1997/98, as part of the SHEBA project (Perovich and Elder, 2002) and data collected in the north Caspian Sea.

Table 6.1. Parameters used for our model calculation

Forcing data	North Caspian Sea	Arctic	Antarctic
F_{LW} (Wm^{-2})	205 [a]	154.52 [b]	158 [c]
F_{SW} (Wm^{-2})	76 [a]	0 [b]	0 [c]
F_{sens} (Wm^{-2})	3 [a]	5.7 [b]	43 [c]
F_{lat} (Wm^{-2})	-1 [a]	0.5 [b]	-3 [c]
F_{ocean} (Wm^{-2})	9.7	3 [*]	3 [*]
S_{ocean} (ppt)	6	33	35
S_{bulk} (ppt)	1	5	5
f (%)	27	27	27
h_{sa} (mm)	0.5	0.5	0.5
h_0 (mm)	5	5	5
H_0 (m)	0.2	0.2	0.2

[a] Mean for January 2008 provided by the National Centres for Environmental Prediction.
[b] Mean for December 1998 taken from atmospheric SHEBA data.
[c] Mean for July 2007 provided by NCEP.
[*] (Perovich and Elder, 2002).

The fraction of salt (f) released into the liquid layer was estimated from consolidation experiments that were carried out on rafted sea ice in the HSVA ice tank (see Appendix F). Salinity measurements were made of the upper liquid layer of a 3-layer section of multiply rafted of sea ice by drilling a hole down to the layer and sampling the liquid with a pipette. The salinity and temperature of the sample were then recorded using the WTW conductometer (LF191). The results of this experiment showed that as the thickness of the liquid layer decreased the salinity of the layer gradually increased. From conservation of salt, f can be estimated from

$$f = \frac{S_t - S_{ocean}}{S_{ocean}} \frac{1}{h_0/h_{sa} - 1}, \tag{6.18}$$

where $S_t = 77.3$ ppt is the concentration of the liquid layer immediately prior to the upper two layers of ice becoming consolidated, $S_{ocean} = 32.8$ ppt is the concentration of the tank water prior to commencing the experiment, h_0 is the initial thickness of the liquid layer and h_{sa} is the surface asperity height. The mechanism by which a fraction of the salt is released from the sea ice formed as the liquid layer freezes is not entirely clear. I speculate that the mechanism involved is brine convection highly localized to the vicinity of the interface

between the ice and liquid layer, probably at a lengthscale of the order of the crystal spacing itself. Brine convection is discussed in more detail in Notz and Worster (2008).

A plot of h_{sa} versus f is shown in Figure 6.2. The plot shows that based on equation (6.18) the surface asperity height lies in the range of 0 to 1.27 mm. For our simulations h_{sa} was arbitrarily set to 0.5 mm making the fraction of salt released $f = 27$ % (f' is approximately twice this value if one considers salt release only from freezing at the upper surface of the liquid layer and roughly equal freezing rates at the upper and lower interfaces).

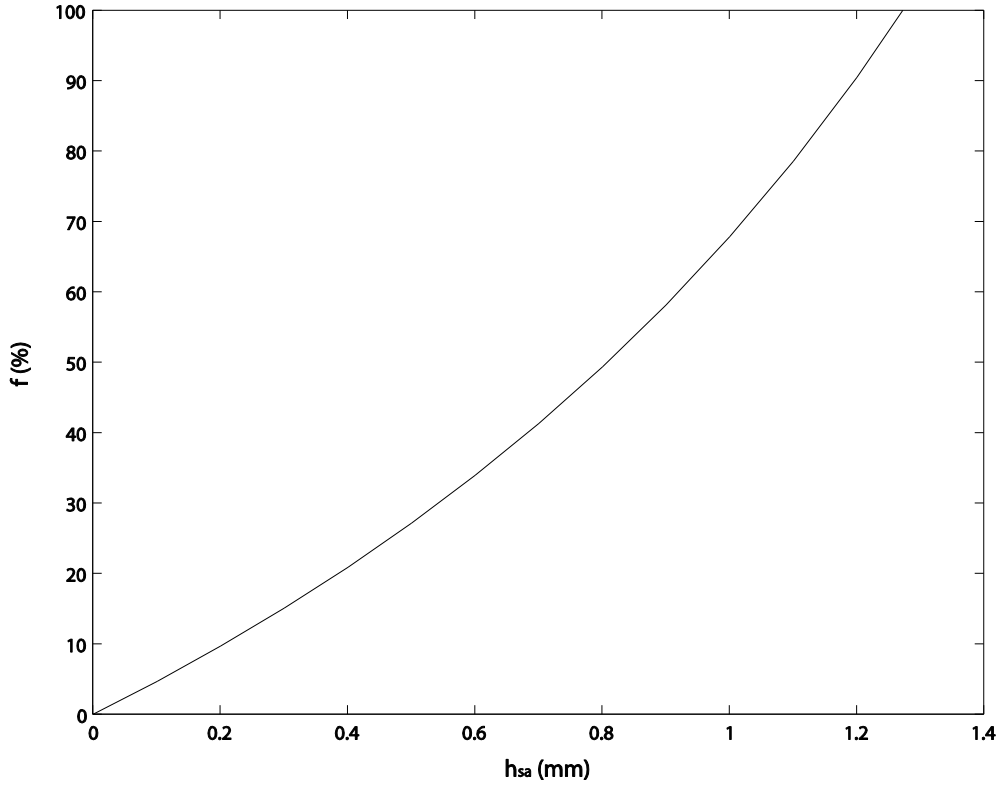

Figure 6.2. Dependence of the fraction of salt released (f) into the liquid layer on the surface asperity height (h_{sa}), based on data collected during the HSVA ice tank experiments.

6.5 Numerical simulations

In this section I present the results of our simulations. First, I describe the results for simple rafting and then multiple rafting. After this I present a series of tests that were performed in order to test the model's sensitivity to certain parameters.

Simple rafting

The model was run for two layers of simply-rafted sea ice using parameters typical of the environments of the north Caspian and the Arctic and Southern Oceans (see Table 6.2). The results show that the ice sheets all consolidated in under 15 hours (900 minutes). The quickest rate was by far the north Caspian, followed by the Antarctic, and then, finally, the Arctic.

Table 6.2. Consolidation rates predicted by the model for two layers of rafted sea ice using the parameters given in Table 6.1.

Location	Time to Consolidation (Minutes)
North Caspian	80
Arctic	891
Antarctic	542

Figure 6.3 shows the variation in the thickness of the liquid layer and its temperature with time. The figure shows that as the thickness of the liquid layers reduces so does the temperature of the liquid layer. This is because as the liquid layer freezes, increasing amounts of salt are released into the remaining liquid layer, thereby reducing its freezing temperature. Figure 6.3b shows that prior to consolidation the temperature of the liquid layer reduced to 265.5 K (-7.65ºC), which corresponds to salinity of 113 ppt (calculated by inverting Eq. 6.7).

Figure 6.4 shows the evolution of the temperature profiles in each ice sheet for the Arctic. This is of interest because the rate of consolidation is dependent on the temperature gradient either side of the liquid layer (Eq. 6.17). The top plot represents the ice sheet that is in contact with the atmosphere and the bottom plot the ice sheet that is in contact with the ocean. The dotted line shows the initial condition and the solid line the temperature profile when the upper layer has consolidated. The figure shows that the temperature in the ice sheets is initially linear and then gradually evolves to re-establish an almost linear temperature profile throughout the two ice sheets.

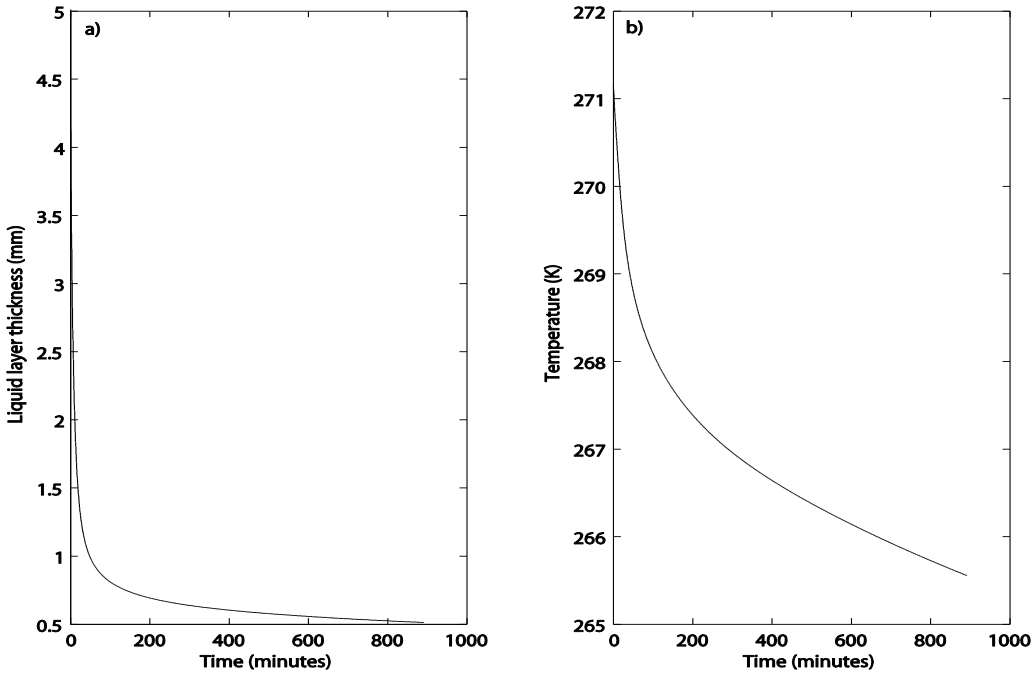

Figure 6.3. Shows the evolution of the thickness of the liquid layer (a) and temperature in the liquid layer (b) with time, using parameters representative of the Arctic.

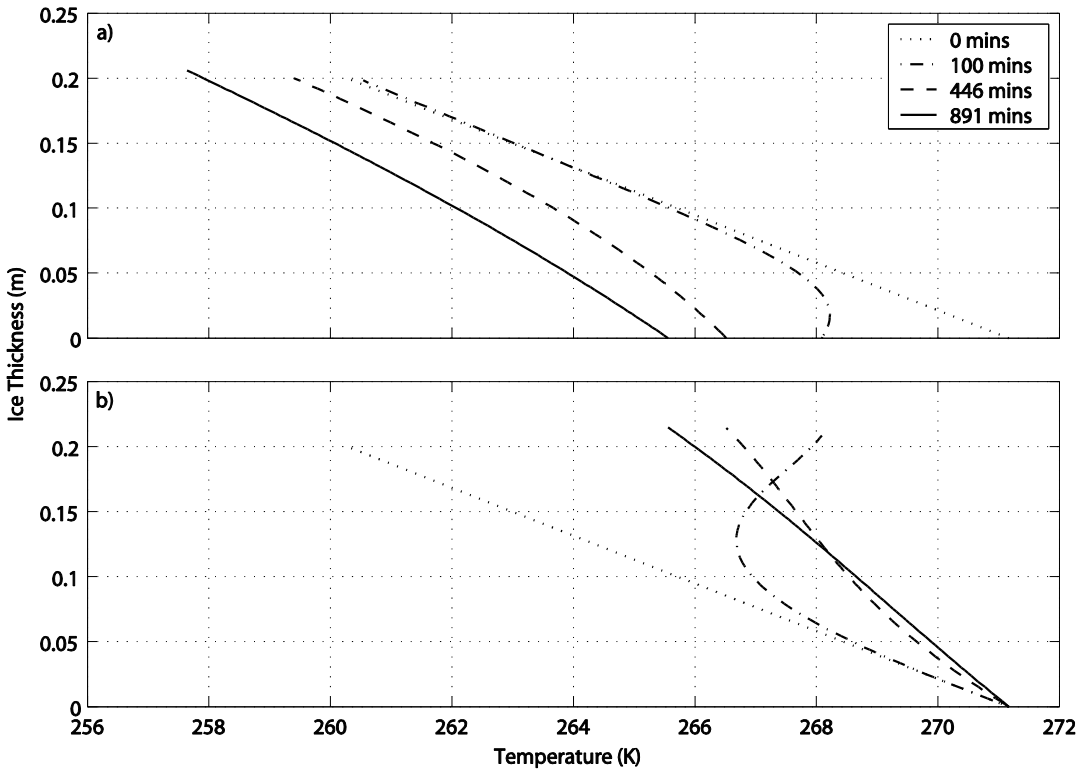

Figure 6.4. Shows the evolution of the temperature profiles in a two-layer rafted section of sea ice using parameters representative of the Arctic, where a) represents the ice sheet that is in contact with the atmosphere and b) the ice sheet that is in contact with the ocean. The dotted line shows the initial condition, the dash-dot line the temperature at 100 minutes, the dashed line the temperature at 446 minutes and the solid line the temperature profile when the liquid layer has consolidated (at 891 minutes).

Multiple rafting

In this section, I present the results for a 3-layer, multiply-rafted section of sea ice (see Table 6.3). The results show that using parameters representative of the north Caspian Sea, it took 80 minutes for the ice sheets to consolidate, whereas when using Arctic and Antarctic parameters it took significantly longer to freeze. This is principally due to the differences in the salinity of the ocean and the sea ice. In each case the upper liquid layer froze faster than the lower layer, which is as I would expect as the upper layer is close to the colder temperatures of the atmosphere. The time difference in the case of the north Caspian is however very small indicating that the liquid layers are sufficiently thin that the heat released on freezing can be readily absorbed by the surrounding ice, such that both liquid layers freeze almost simultaneously. This might explain why multiple rafting is a predominant ice hazard in the region. It is also interesting to note that in the cases of the Arctic and the Antarctic that the consolidation time for the upper liquid layer was ~0.7 times shorter than the consolidation time for 2-layers of rafted ice (comparing Table 6.2 & 6.3), indicating the effect that the oceanic heat flux and ocean temperature have on the consolidation process

Table 6.3. Consolidation rates predicted by the model for 3-layers of multiply rafted sea ice using the parameters given in Table 6.1.

Location	Time to Consolidation (Minutes)	
	Upper Liquid layer	Lower liquid layer
North Caspian	78	80
Arctic	640	2198
Antarctic	423	1783

Figure 6.5 shows the evolution of the temperature profiles in 3-layers of multiply-rafted sea ice using parameters representative of the Arctic. Plot a) represents the ice sheet that is in contact with the atmosphere, b) the ice sheet that is in the centre of the rafted section and c) the ice sheet that is in contact with the ocean. The dotted line shows the initial condition and the solid line the temperature profile when the upper layer consolidated. The figure shows that the temperature at the upper liquid layer decreases with time until it consolidates at 640 minutes. The adjacent ice sheets were then merged and the program continued until

the lower liquid layer consolidated (see Figure 6.6). Figure 6.6 shows that the temperature of the lower liquid layer is now decreasing with time until it freezes after 2198 minutes.

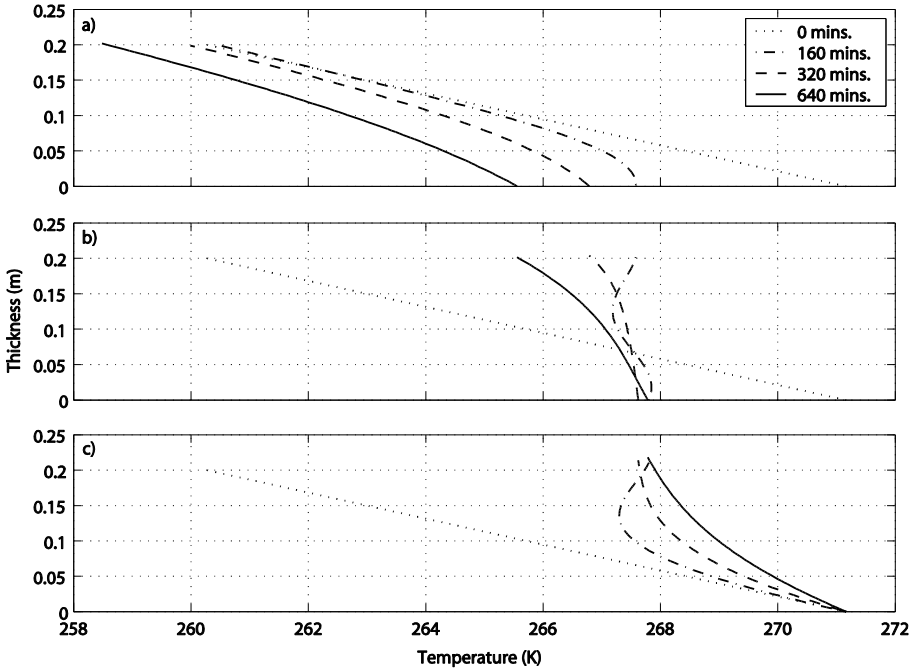

Figure 6.5. The evolution of the temperature profiles in a 3-layer section of rafted sea ice using parameters specific to the Arctic, where a) represents the ice sheet that is in contact with the atmosphere, b) the ice sheet that is in the centre of the rafted section c) the ice sheet that is in contact with the ocean. The dotted line shows the initial condition, the dash-dot line the temperature at 160 minutes, the dashed line the temperature at 320 minutes and the solid line the temperature profile when the upper layer has consolidated (at 640 minutes).

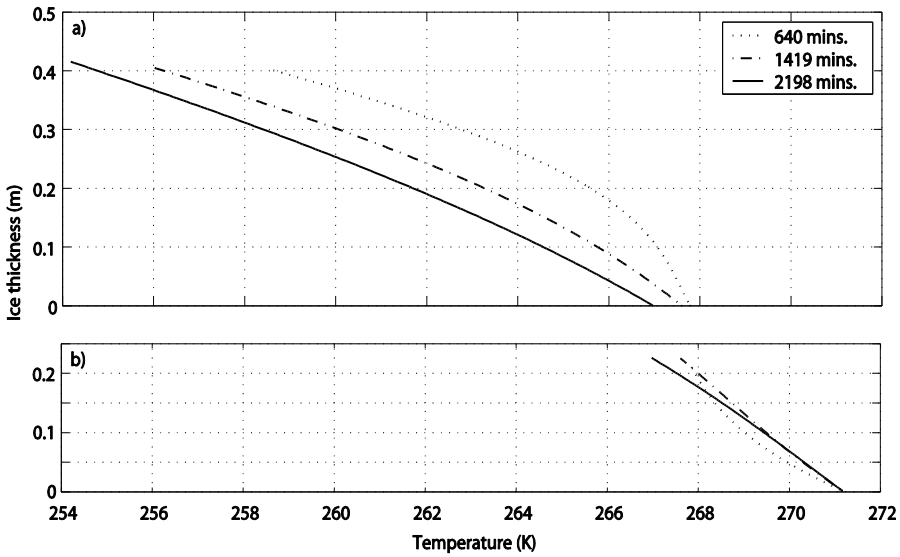

Figure 6.6. Shows the evolution of the temperature profiles after the top two ice sheets shown in figure 6.5 have frozen together, where a) represents the consolidated top two ice sheets and b) the remaining ice sheet that is in contact with the ocean. The dotted line shows the temperature profile when the upper liquid layer consolidated (640 minutes), the solid line the

temperature when the bottom liquid layer consolidated (2198 minutes), and the dashed line mid-way between these two points (1419 minutes).

Sensitivity Studies

Since it is the first time that the consolidation of rafted sea ice has been investigated numerically it is important to investigate the model's sensitivity to certain parameters that are not well known. Sensitivity of the model to candidate parameters will highlight physical processes that are important in the consolidation of rafted sea ice. To do this analysis a standard case was first be chosen, which is taken to be the parameters for the Arctic listed in Table 6.1. In each sensitivity study multiple runs were made varying one parameter at a time, within a conceivable range, whilst holding the others constant at the standard case values. Performing a sensitivity test in this way assumes that the parameters are independent of each other, which is not necessarily the case. However, it does give some indication as to the effects they will have on the model. The parameters I examine are the initial liquid layer thickness h_0, the initial ice thickness H_0, the bulk salinity of the sea ice S_{bulk}, the salinity of the ocean S_{ocean}, the fraction of salt released into the liquid layer f, the surface asperity height h_{sa} and the forcing data (F_{LW}, F_{SW}, F_{sens}, F_{lat}, F_{ocean}).

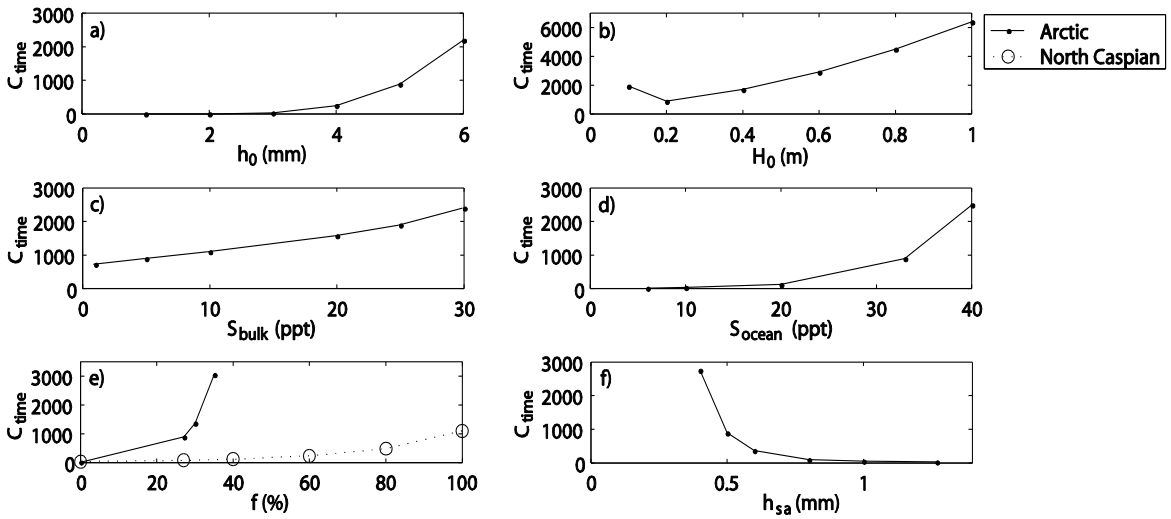

Figure 6.7. Dependence of the consolidation time (C_{time}) in minutes on a) the initial liquid layer thickness h_0, b) the initial ice thickness H_0, c) the bulk salinity of the sea ice S_{bulk}, d) the salinity of the ocean S_{ocean}, e) the fraction of salt released into the liquid layer f, where the solid line and the dashed line show the simulations run with parameters specific to the Arctic and the north Caspian respectively, and f) the surface asperity height h_{sa}.

The dependence of the consolidation time (C_{time}) on h_0, H_0, S_{bulk}, S_{ocean}, f, and h_{sa} is shown in Figure 6.7. Figure 6.7a shows the dependence of the C_{time} on h_0. The figure shows that the larger h_0 the longer the C_{time}. When h_0 is below 3 mm the C_{time} is very rapid and for thicknesses greater than 4 mm C_{time} increases by almost a factor of three for every millimetre increase in h_0. For values greater than 6 mm model runs showed the liquid layer did not consolidate and started to rise after about 6000 minutes (see Figure 6.8). Figure 6.9 shows the temperature profiles when h_0 was set to 7 mm. The solid lines show the temperature profiles in the ice sheets when the liquid layer thickness started to increase (at 5847 minutes). At this point, the temperature profiles are linear and of negative gradient, which promotes "melting" at the top of the lower ice sheet and freezing at the base of the upper ice sheet. The term "melting" is in quotation marks because what is driving the phase change is the difference in salinity of the liquid layer and ice sheet; technically the lower ice layer is said to dissolve, rather than melt (Woods, 1992). What drives the heat transport into the liquid layer is the fact that the temperature of the liquid layer, being at the liquidus temperature appropriate to its high salinity, is lower than the temperature in the lower ice sheet. Sensible heat is extracted from the lower ice layer and converted into the latent heat of the liquid phase. Since the base of the ice sheet above the liquid layer is freezing and the top of the ice sheet below the liquid layer is "melting", the liquid layer is migrating downwards. To investigate this, the location of the freezing fronts was plotted against time (see Figure 6.10). Figure 6.10 shows that after an initial rise that both liquid layers have migrated downwards by ~0.1 m in about 6000 minutes.

Figure 6.7b shows the dependence of the C_{time} on H_0. The figure shows that at both large and small ice layer thicknesses, the consolidation time increases. At large H_0 this is due to the reduced extraction of heat from the liquid layer to the atmosphere through the upper ice layer. At low H_0, the rate of diffusion of heat from the ocean into the liquid layer through the lower ice sheet is enhanced slowing down consolidation.

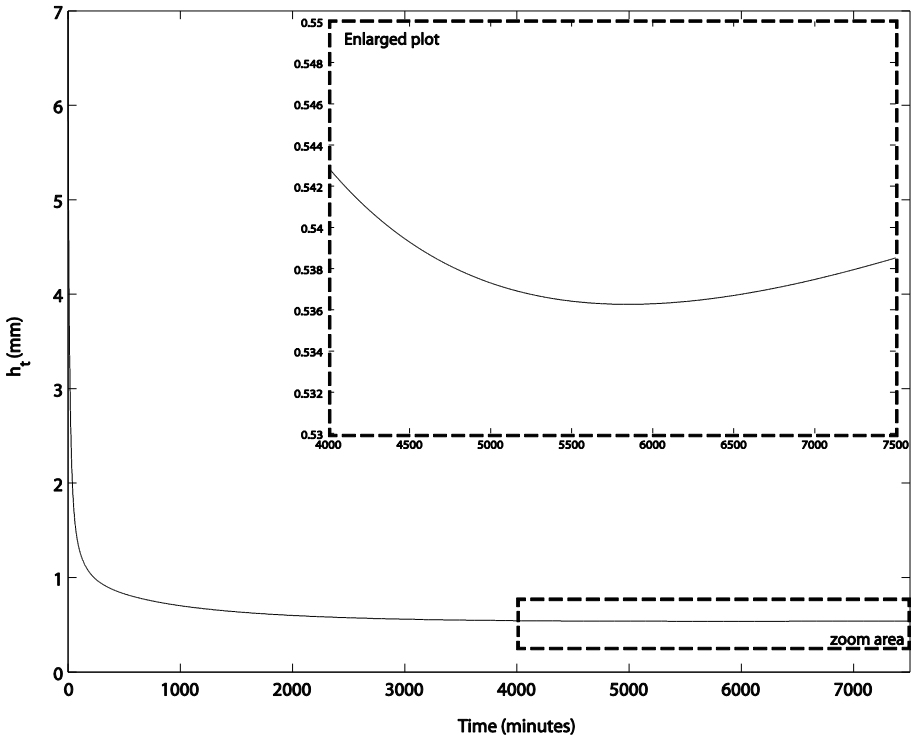

Figure 6.8. The rate at which the thickness of the liquid layer (h_t) is reducing with time in minutes when h_0 = 7 mm, where the enlarged plot shows a zoom of the area in the dashed box.

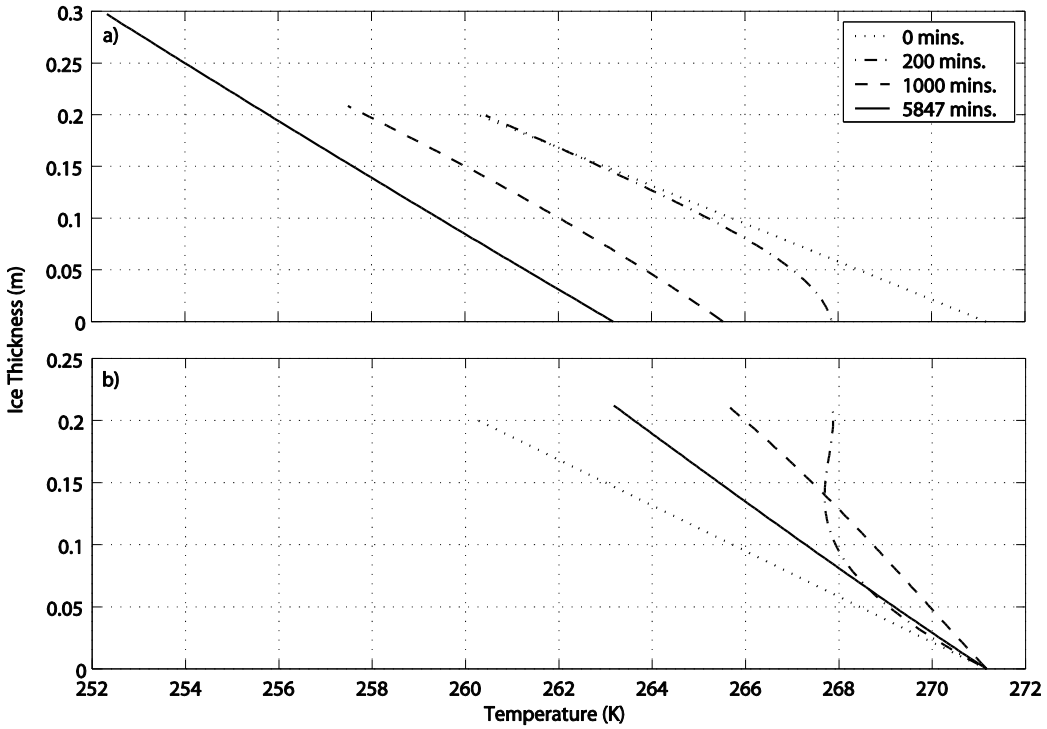

Figure 6.9. The temperature profiles in the ice sheets when h_0 = 7 mm. The dotted line shows the initial condition and the solid line the temperature distribution when the liquid layer started to rise.

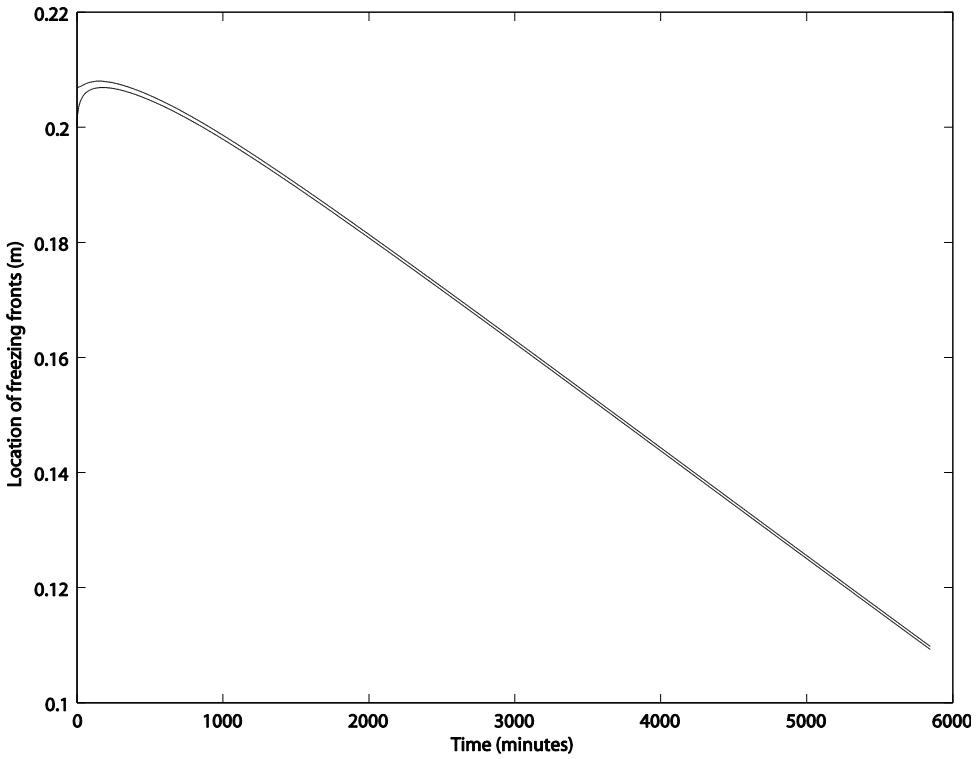

Figure 6.10. Location of the freezing fronts with time when h_0 = 7 mm.

Figure 6.7c shows the model's sensitivity to S_{bulk}. The plot shows that C_{time} increases with increasing S_{bulk}. This is because an increase in S_{bulk} lowers the thermal conductivity of the sea ice and increases its specific heat capacity, which reduces the ability of the sea ice to conduct heat away to the atmosphere, thus retarding the consolidation time.

Figure 6.7d shows that the greater S_{ocean} is the greater the C_{time}. This is because an increase in S_{ocean} lowers the freezing temperature of the ocean, thereby decreasing the initial temperature gradients in the ice sheets and thus the diffussional heat fluxes through them so that the C_{time} is increased. In addition, an increase in S_{ocean} also increases the initial salinity of the liquid layer, such that as consolidation proceeds the liquid layer gets increasingly salty. At the high salinities reached just prior to the consolidation (~110 ppt using standard case parameters) the non-linearity of the liquidus curve causes a greater than linear decrease in the freezing temperature of the liquid layer, which acts to further retard the consolidation time. This is why on the plot we see a greater than linear increase in C_{time} for salinities higher than ~20ppt, despite the fact that it has little effect on the freezing temperature of the ocean.

To explore the uncertainty in the brine release process the dependence of C_{time} on f for both the Arctic and north Caspian parameters was investigated while h_{sa} was held constant at 0.5 mm (see Fig. 7e). As the fraction of salt released into the liquid layer during freezing f increases, the consolidation time increases because the freezing temperature of the liquid layer decreases. For f greater than 35 % there are no points for the Arctic because under these conditions the liquid layer did not consolidate. Conversely, for the north Caspian the effect of varying f from 0 to 100 % varied the consolidation time between 30 to 1000 minutes. This is due to the differences in the salinity of the sea water.

Figure 7f shows the sensitivity of the model to the surface asperity height h_{sa}. The figure shows C_{time} increases with decreasing h_{sa}. This makes sense since the smaller the surface roughness the greater the quantity of liquid that has to freeze before the asperities can effectively bond.

The sensitivity of the model to the forcing data is shown in Figure 6.11. This shows that the C_{time} is sensitive to the incoming longwave F_{LW} and shortwave F_{SW} radiation, and the sensible F_{sens} and the latent heat F_{lat} fluxes; and rather insensitive to changes in the oceanic heat flux F_{ocean}. Since the variation in the radiative fluxes tends to be larger than the variation in the sensible and latent heat fluxes, changes in the radiative fluxes will tend to have a greater influence on the consolidation time. Note that in Figure 6.11b F_{SW} is only varied from 0 to 125 Wm^{-2}. This is because for values higher than 125 Wm^{-2} the ice sheets did not freeze.

From the above sensitivity analysis it is apparent that the time taken for two ice sheets to consolidate is a function of a) how effectively heat can be transported through the ice and b) how much liquid has to be frozen. The ice thickness (H_0), the bulk salinity of the ice (S_{bulk}), the salinity of the ocean (S_{ocean}) and the atmospheric variables (F_{LW}, F_{SW}, F_{sens}, F_{lat}) all affect the transport of heat via the temperature gradients and the conductivity and the heat capacity. The thickness of the gap (h_0), the surface asperity height (h_{sa}) and the fraction of salt release (f) all have to do with the amount of energy that is needed to freeze the liquid.

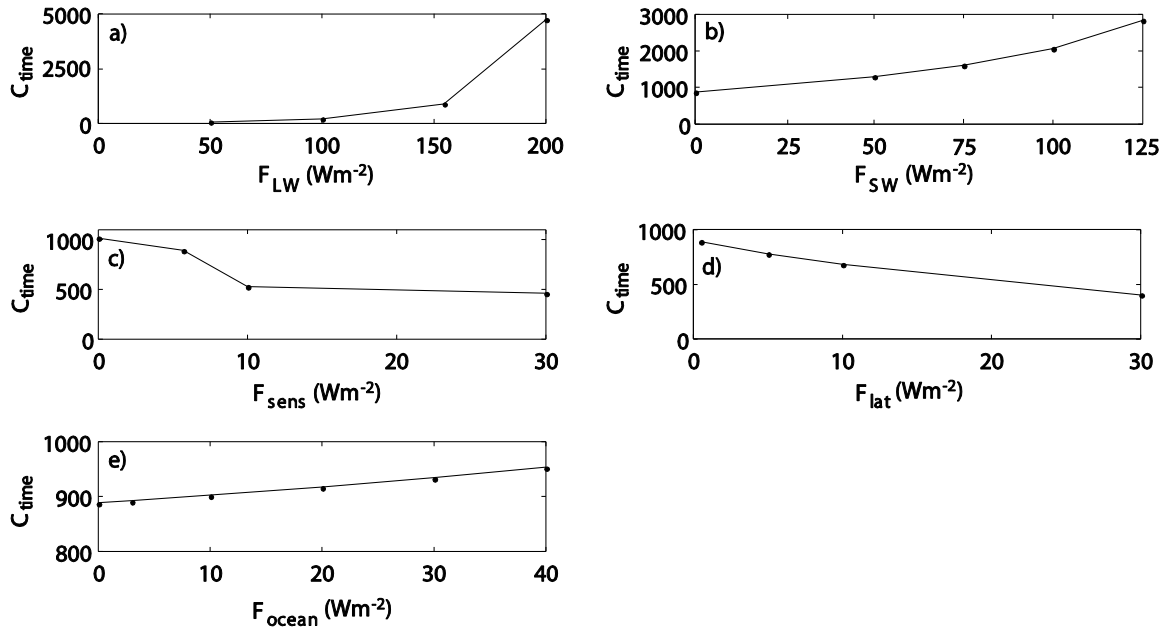

Figure 6.11. Dependence of the consolidation time (C_{time}) in minutes on a) the downward longwave radiation flux F_{LW}, b) the downward shortwave radiation flux F_{SW}, c) the sensible heat flux F_{sens}, d) the latent heat flux F_{lat}, and e) the oceanic heat flux F_{ocean}.

6.6 Discussion and Conclusions

In this chapter, I have presented a one-dimensional, thermal-consolidation model for rafted sea ice. I considered the consolidation between both 2-layers and 3-layers of rafted sea ice. The results showed, using the parameters representative of the north Caspian, Antarctic and Arctic, that it took respectively about 1, 9 and 15 hours for two-layers of rafted sea ice to consolidate. The consolidation time for 3-layers of ice in the north Caspian was the same as for 2-layers of ice, indicating that the liquid layers are sufficiently thin that the heat released on freezing can be readily absorbed by the surrounding ice sheets. Conversely, it took significantly longer for 3-layers of rafted ice to freeze in the Antarctic (30 hours) and the Arctic (37 hours). The rapid consolidation of rafted ice in the Caspian Sea is due to the low salinity (6ppt) of the water. Rapid consolidation might also permit subsequent rafting of the consolidated layers and may help to explain the prevalence of multiply rafted ice in the region.

A number of sensitivity studies were conducted to determine the effect that variations in model parameters and forcing fluxes had on the consolidation time for simply rafted Arctic sea ice. The results showed that typical variations in the oceanic heat flux and the sensible

and latent heat fluxes had little effect on the consolidation time. However, the model was highly sensitive to changes in the initial thickness of the liquid layer h_0, the ice thickness, the salinity of the ocean, the fraction of salt release during freezing f, the surface asperity height h_{sa} and the downward radiative fluxes. Most of these parameters can be quite well constrained because they have been widely researched, however h_0, f and h_{sa} are not well known. Therefore further investigation of these parameters is needed before any concrete conclusions can be drawn about the rate of consolidation of rafted sea ice features.

Investigating h_0 could be done rather easily by sampling cores of rafted sea ice and physically measuring the size of the consolidated liquid layer. In addition, h_0 can also easily be constrained in experiments. It is, however, considerably more difficult to investigate the fraction of salt release during freezing and the average surface asperity height (surface roughness) between rafted floes. This is because, firstly, it is not entirely clear by what mechanism salt is being released into the liquid layer and, secondly, the surface roughness will depend on many parameters including the amount of overlap between rafting floes, the amount of fluid present during rafting, the speed that the ice sheets are sliding past one another, the buoyancy/weight of the ice sheet and so on.

On the basis of the consolidation experiments that were carried out at the HSVA ice basin the surface asperity height was calculated to be between 0 and 1.27 mm. The experiments showed that the salinity of the liquid layer gradually increased with time, therefore indicating that there was a fraction of salt being released into the liquid layer. The fraction of salt that is being released, however, is somewhat uncertain due to the logistics of sampling such a tiny quantity of liquid. Results showed that prior to the top 2 layers of a 3 layer stack becoming consolidated the salinity had reached 77.3 ppt. This shows that brine is being released from the newly forming sea ice (as assumed in the model) and/or that brine is draining out from the ice sheet above into the liquid layer.

For brine drainage to occur there needs to be sufficient forcing (e.g. buoyancy forcing) and the ice needs to be sufficiently permeable. Cox and Weeks (1975) found that for brine volumes below a critical value of ~5%, the ice is effectively impermeable to fluid transport and brine drainage stops altogether (c.f. Chapter 2). Using the Frankenstein and Garner (1967) equation (Eq. 2.1) the brine volume can be calculated for a variety of salinity and

temperatures (see Figure 6.12). According to the 5% brine volume criteria Figure 6.12 shows that for bulk salinities of 1 and 5 ppt the ice needs to be warmer than -1ºC (272 K) and -5ºC (268 K), respectively, for brine drainage to occur. Therefore, based on this theory, for the Arctic and Antarctic parameters used in our numerical simulations, initially only the bottom 6 cm of the ice sheets (see Figure 6.4) above the liquid layer and at the ice-ocean interface would be sufficiently permeable for brine drainage to take place. (In the case of the north Caspian Sea, only the bottom 2 cm of the ice sheets above the liquid layer and at the ice-ocean interface would initially be sufficiently permeable). In particular, this means that even if a positive hydraulic head is produced during the rafting process, flushing will not occur.

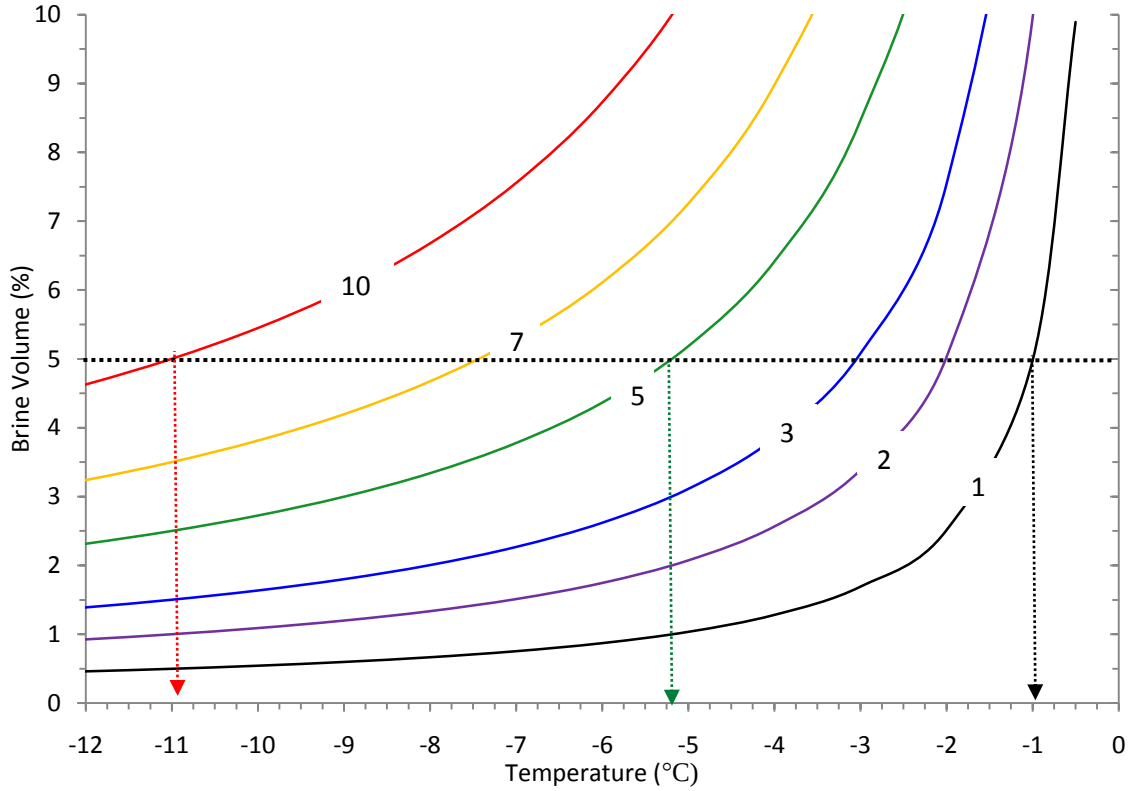

Figure 6.12. Brine volume (%) as a function of temperature (°C) and salinity (ppt) calculated using the Frankenstein and Garner (1967) equation (2.1).

Theoretical and experimental studies on the convection of mushy layers have shown that for convective overturning (gravity drainage) to occur in sea ice the local Rayleigh number (*Ra*) must exceed a critical value $Ra_c \sim 10$ (Notz and Worster, 2008; Wettlaufer et al., 1997b; Worster, 1992; 2000). I therefore calculated the Rayleigh number (Eq. 2.5) as a

function of depth for various stages during the consolidation process for the Arctic, Antarctic and north Caspian parameters used in our numerical simulations.

Figure 6.13 shows the Rayleigh number profiles calculated for the two-layer Arctic simulation. The figure shows that at no stage during the consolidation process did the Rayleigh number approach Ra_c. The same was true for the Antarctic and north Caspian simulations. Therefore based on the brine volume and Rayleigh number calculations for the parameters presented here there would be no brine drainage during the consolidation process. This implies that brine is only released from the newly forming ice. The issue of brine drainage will be re-visited in chapters 7 and 8, where the laboratory data is presented and used to test the model.

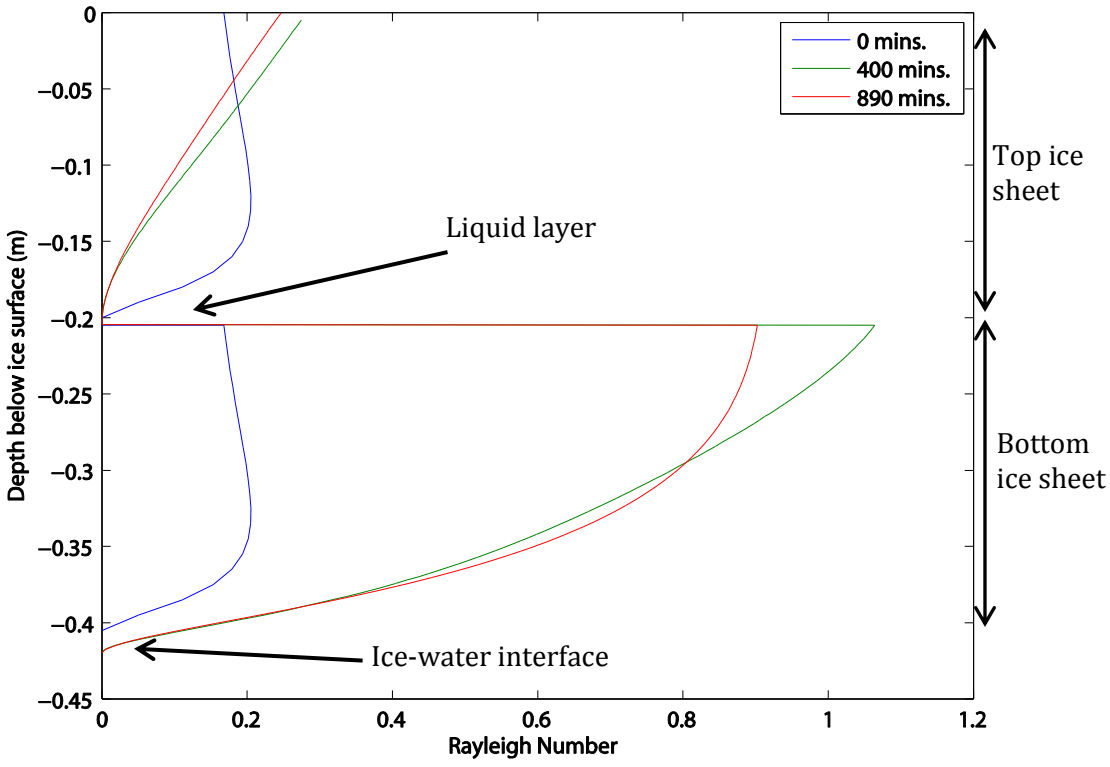

Figure 6.13. Rayleigh number profiles calculated at various stages during the consolidation process for the two-layer Arctic case.

To my knowledge there is no published experimental work on the consolidation of rafted sea ice. Marchenko and Chenot (2009) carried out some consolidation experiments on drifting ice in the Barents Sea in April 2006. They measured the cohesion between two

submerged ice disks that were ~15 cm in diameter and 3-4 cm thick and found that after a period of 2 days that the disks had not frozen together. They also submerged an ice beam that had dimensions 3x0.5x0.5 m below level ice and found that after a day it was still possible to move the beam using a shovel. While these results are inconclusive they give a lower bound to the consolidation time. In the next chapter, I shall present consolidation experiments that were carried out in the UCL Ice Physics Laboratory to investigate the consolidation of rafted sea ice. These shall then be used in Chapter 8 to test the consolidation model.

7 Laboratory experiments on the consolidation of rafted sea ice

7.1 Introduction

To investigate the consolidation of rafted sea ice, I performed a series of experiments in the Ice Physics Laboratory, at the UCL. The purpose of these experiments was to test the rafted ice consolidation model described in Chapter 6. My model simulations showed that the consolidation process is sensitive to the fraction of salt released into the liquid layer, the initial thickness of the liquid layer between adjacent sheets, the salinity of the ocean (which in turn influences the bulk salinity of the ice), the thickness of the ice sheets and the downward longwave and shortwave radiation. Most of these parameters can be quite well constrained as they have been widely researched. For instance, it is well known that the ocean has a salinity of 30-35 ppt (6 ppt for the north Caspian Sea) and previous studies have shown that rafting is most common between thin ice sheets <17 cm thick (Parmerter, 1975). However, there is no published data on the initial thickness of the liquid layer between adjacent sheets and the fraction of salt released into the liquid layer.

In this experimental programme, I shall investigate the effect salinity, ice thickness and the thickness of the gap between ice sheets has on the consolidation process. I shall not, however, consider the effects of variations in longwave and shortwave radiation. In nature, these fluxes are important for calculating the temperature at the ice-atmosphere surface in the boundary condition (Eq. 6.9). In addition, shortwave radiation also contributes to the internal phase changes (Eq. 6.2) as it can penetrate deep into the ice. In the laboratory, shortwave radiation would come from the lights and longwave radiation from the objects and walls in the cold room. It would be rather hard to calculate let alone control these parameters. In any case, the temperature at the ice-atmosphere surface is measured and is used to force the boundary condition. It would be possible to vary the temperature of the cold room between 0 and -30°C, however due to time constraints this parameter was not varied.

To simulate a section of rafted sea ice, layers of laboratory grown sea ice were stacked on top of one another with spacers between adjacent ice sheets allowing water from the tank below to flood in. The rate of consolidation was then monitored using a combination of temperature readings recorded in the ice and liquid layer and salinity measurements of the liquid layer. Once the ice blocks had consolidated, cores were taken and the physical and mechanical properties measured. In this Chapter, the experimental set up is described in section 7.2. The results of the consolidation experiments and the physical properties of the rafted ice are described in sections 7.3 and 7.4. A discussion of the results is presented in section 7.5 and final conclusions are drawn in section 7.6.

7.2 Experimental set-up

A series of consolidation experiments were set up in the Ice Physics Laboratory to investigate the consolidation of rafted sea ice. A total of 7 tests were done whilst varying the initial salinity of the solution from which the ice was grown, the ice thickness and the thickness of the gap between adjacent ice sheets. The parameters used in each test are outlined in Table 7.1. Solutions of 0, 6 and 33 ppt were chosen to replicate salt concentrations found in freshwater environments, the north Caspian Sea and the Arctic/Southern Oceans. Ice thicknesses of 7, 10 and 14 cm were selected, as previous work indicates that rafting is most common between thin ice sheets <17 cm thick (Parmerter, 1975). Furthermore, ice thicker than this took a considerable time to grow and became too heavy for me to lift. Gap thicknesses of 0.5, 1 and 2 cm were used as it was not possible to make the gap thickness any less than 0.5 cm due to the presence of a thermistor probe between adjacent ice sheets. In addition, larger gap sizes helped in the sampling of the liquid layer for salinity measurements. The "standard case" was chosen to have an initial solution salinity of 6 ppt, an ice thickness of 7 cm and a gap thickness of 1 cm. I chose these initial test conditions to optimize the number of experiments that could be done by using low salinity and thin ice blocks.

To set up an experiment, ice was grown simultaneously in two large acrylic cylinders to the required ice thickness to within an accuracy ±1 cm (c.f. Chapter 5). To remove the ice, trace heating, embedded within the polystyrene insulation (see Figure 7.2), was turned on and left until the ice became free. The ice was then lifted out from one cylinder, sawed flat

and stacked on top of the other ice block. Prior to assembly, 3 spacers were frozen on to the surface of the lower ice block, a single thermistor was fixed into place and a hole was drilled to allow water to flood from the water below into the gap. At the base of the cylinder a heater plate was held constant at a temperature of 7±1°C. This temperature was needed to keep the water below the rafted section near to its freezing point. Once assembled, the ice blocks were then left to consolidate in a room held at a nominal temperature of -10±1°C. Figure 7.1 shows a schematic of the experimental set-up.

Table 7.1. Consolidation test parameters

Test no.	Initial salinity of solution (ppt)	Ice thickness (cm)	Gap thickness (cm)
1*	6	7	1
2	0	7	1
3	33	7	1
4	6	10	1
5	6	14	1
6	6	7	0.5
7	6	7	2

* Standard case

During each test, temperature was recorded every 5 minutes in the ice blocks and the liquid layer. Depending on the ice thickness temperature was recorded in the ice blocks using the 5, 10 or 20 cm probes (c.f. Chapter 5). The probe was positioned so that the first thermistor in the probe was approximately 1 cm below the ice surface. In the liquid layer temperature was recorded using a single thermistor positioned approximately midway between the two sheets. Corrosive conditions of the saline water meant that some of the thermistors deteriorated over the course of the experimental programme. This could clearly be seen in the temperature traces as the readings would change erratically or would not register at all. I omitted these readings from the graphs. There were, however, enough thermistors working correctly to see temperature trends needed for the consolidation experiments. The salinity of the liquid layer was measured daily by taking samples through a hole that was drilled into the side of the acrylic cylinder and sealed with a suba seal (re-sealable bung). Samples were extracted from the liquid layer using a hypodermic needle and syringe (see Figure 7.2) and the salinity measured using a MISCO digital refractometer (model # PA203X), which takes readings accurate to ±0.5 ppt. The temperature and salinity measurements were then

used, along with cores taken at specific times of interest, to determine the rate of consolidation of the ice blocks.

In addition to measuring the temperature in the ice blocks and the liquid layer, during the standard case experiment the temperature was also measured at the ice-atmosphere surface and in the water below the rafted section. The temperature at the ice surface was measured using a single thermistor probe placed on the top of the rafted section. Temperature in the water below the rafted section was measured using a 20cm probe positioned so that the top thermistor in the probe was at ice-water interface. The temperatures recorded in the water were then used to estimate the rate of ice growth by finding the time that a thermistor became engulfed in ice (as was done in Chapter 5). These data are later used in Chapter 8 to test the rafted ice consolidation model.

Once the salinity of the liquid layer had remained constant for at least 3 days, the experiment was terminated and cores were taken using a 9 cm diameter corer. A total of three cores could be taken from each experiment: two of the cores were sheared to determine the strength of the liquid layer and the remaining core used for a combination of crystallographic analysis and salinity, density and porosity measurements. The results of the shear tests are described in Chapter 9, along with a series of shear experiments that were performed under increasing states of consolidation.

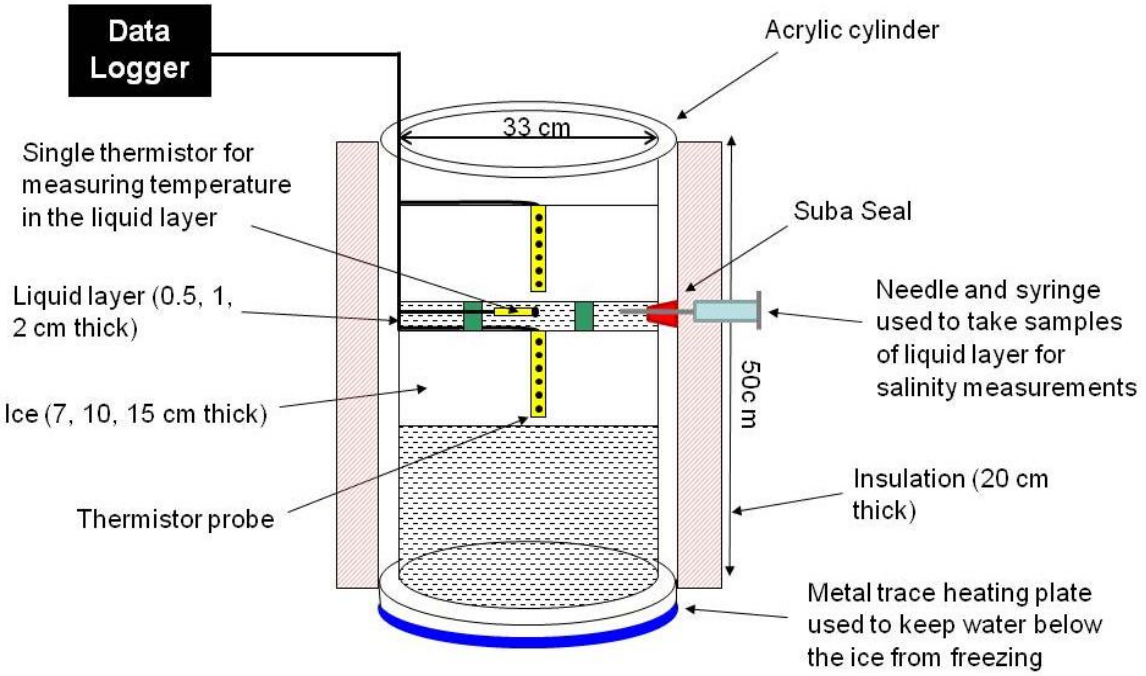

Figure 7.1. Schematic diagram showing the experimental set-up for the rafted ice consolidation experiments.

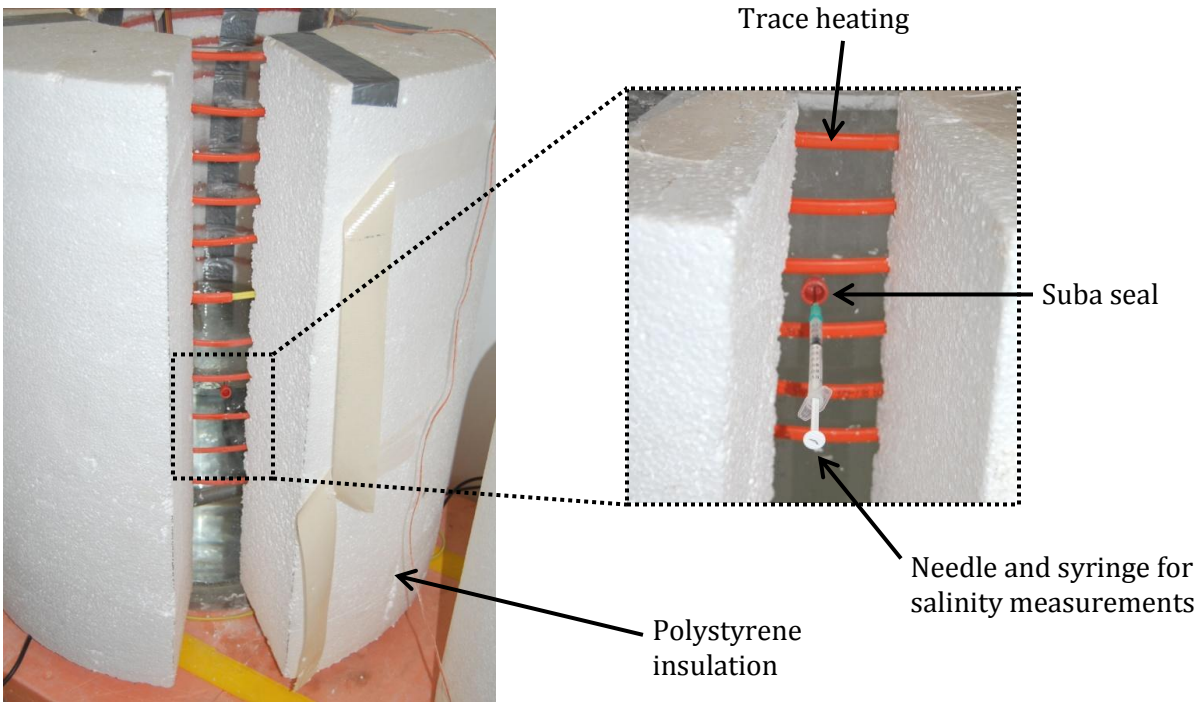

Figure 7.2. Photograph showing the trace heating embedded in the polystyrene and the suba seal, needle and syringe.

7.3 Results

In this section, the results of the consolidation experiments carried out in the Ice Physics Laboratory at UCL are described. First, I describe the results for the standard case (Test 1) and discuss how the temperature and salinity measurements are used to determine the rate of consolidation. I then describe the effect salinity, ice thickness and the thickness of the gap between ice sheets has on the consolidation process. In Appendix E, all the plots from each consolidation experiments are presented.

Standard case

In Figure 7.3, the temperature time-traces for the standard case rafted ice experiment are shown. The top and bottom plots represent the temperature traces recorded by the 5 cm thermistor probes located in the upper and lower ice blocks, respectively. In this figure I have shown the 'initial growth stage' of the ice blocks as well as the 'consolidation stage' so that the changes in temperature during the assembly process can be observed. The small scale variations in temperature (i.e., the wiggles in the temperature traces) are caused by the cold room defrost cycle, which took place every 4 hrs. This had the effect of warming the cold room by ~1°C, which in turn caused the ice to warm by less than 0.25°C. The wiggles could be seen more clearly in the lower ice block during the 'initial ice growth' stage as this container was situated closer to the condenser in the cold room. However, during the 'consolidation stage' the wiggles were more prominent in the upper ice block, as this block was now closer to the condenser and the lower ice block was now insulated from the cold room fluctuations. During the initial growth stage, the temperature of the solution cooled from 6-7°C to -0.4°C. The thermistors then gradually, one by one, started to cool as they became engulfed in ice as the ice-water interface advanced (c.f. Chapter 5). Once the ice thickness had reached 7 cm, the trace heating was turned on and left till the ice became free from the cylinder walls. This took on average 40-50 minutes for the standard case experiment. This had the effect of warming the ice block by ~1-2°C, which can be seen in temperatures recorded in the upper block (Figure 7.3a). Once the ice blocks were assembled (i.e., the consolidation stage), the temperature in the upper ice block decreased at first slowly in the first ~250 minutes, there was then a period of rapid temperature decrease, which gradually levelled out and became roughly constant after 18000 minutes. In the lower block (Figure 7.3b); initially a rise in temperature was recorded in the first ~250

minutes, as heat was conducted from the liquid layer and/or the surrounding water into the lower ice block. The temperature then decreased at first rapidly with time and then changed to a more gradual decrease.

Figure 7.4 shows the temperature evolution of the liquid layer between the two rafted ice blocks as recorded by the single thermistor probe during the standard case experiment. The figure shows that, similar to the temperature in the upper ice block, there is a sort of plateau in the first ~250 minutes where there is very little change in temperature. After this, the temperature in the liquid layer decreased rapidly from -0.8°C to -3°C. The temperature then gradually flattened with time up until the end of the experiment reaching a final temperature of -7.4°C. It is interesting to note that after the rapid decrease in temperature the 'wiggles' in the temperature traces become more prominent perhaps indicating that liquid layer has frozen. It is difficult to pinpoint an exact time for this change in behaviour, as it is a gradual process occurring over several hundred minutes. By enlarging the plot over the time period for which this decrease takes place and fitting a best fit line to the data recorded during rapid decrease I estimate that rapid cooling ceased after around 700 minutes.

In addition to measuring the temperature in the liquid layer its salinity was also measured by taking samples with the needle and syringe. These values are plotted against time in Figure 7.5. In this plot I have also included salinity measurements that were estimated by inverting the temperature recorded in the liquid layer T_{liquid} using the linear,

$$S_{liquid} = \frac{-T_{liquid}}{\Gamma}, \tag{7.1}$$

and non-linear,

$$S_{liquid} = -17.6T_{liquid} - 0.389{T_{liquid}}^2 - 0.00362{T_{liquid}}^3, \tag{7.2}$$

liquidus curves (obtained by inverting Eqs. 4.17 and 4.18), where the parameter $\Gamma = 0.0514$ is calculated assuming a solution of 35 ppt solution freezes at a temperature of -1.8°C. It is evident that non-linear inversion is a much better fit to the data than the linear inversion, especially at salinities greater than 50 ppt. The fact that non-linear inverted temperature readings are in good agreement with the measured samples also demonstrates

that the assumption made in the model that the liquid layer is held at its freezing temperature is reasonable. The figure shows that similar to the temperature in the liquid layer, in the first ~250 minutes the salinity of the liquid layer increased only fractionally. The salinity then increased rapidly from ~14 ppt to 50 ppt and then gradually levelled out reaching a final salinity of 110 ppt by the end of the experiment. Salinity samples of the liquid layer could no longer be taken after 23040 minutes (16 days) either because the liquid layer had frozen to such an extent that no more brine could be extracted or because no further liquid remained in the vicinity of the sampling area. In either case, the last 3 samples that were taken showed that salinity remained constant at 100 ppt over the period of 3 days. Constant salinity was one indicator that the experiment could be terminated, which was done after a further two days.

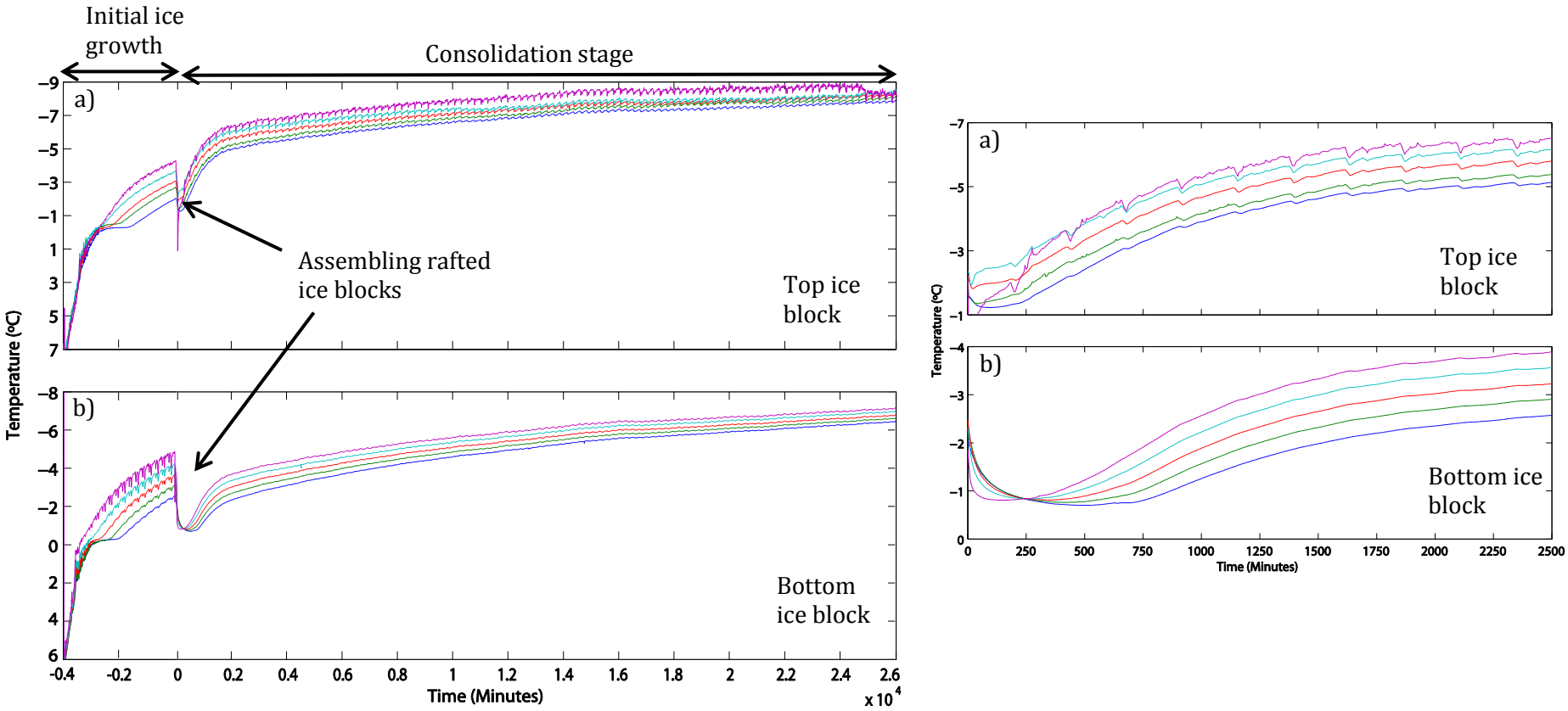

Figure 7.3. Temperature-time traces for the standard case rafted ice experiment where plot a) shows the temperatures recorded by the thermistor probe in the top ice block and plot b) shows the temperatures recorded in the bottom ice block. The different coloured curves represent the individual thermistors in the probes where the top thermistor is positioned ~1 cm below the ice surface of the respective ice block. Negative time refers to the 'initial ice growth' stage and positive time refers to the 'consolidation stage'. The enlarged plot shows a zoom of the first 2500 minutes of consolidation process.

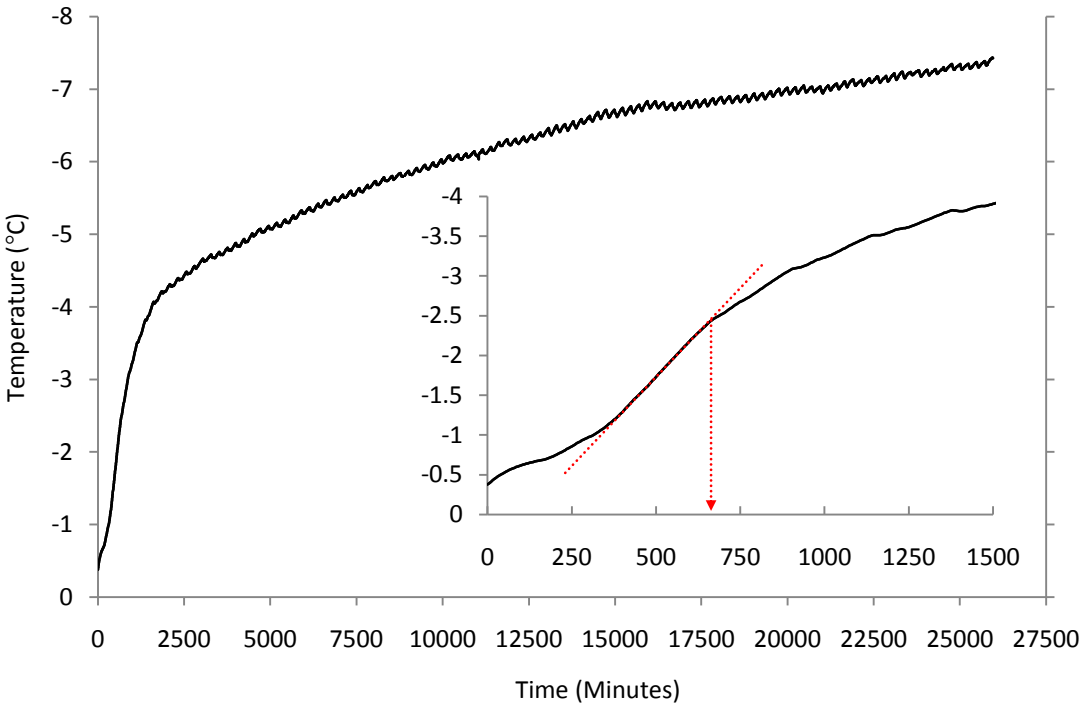

Figure 7.4. Temperature evolution of the liquid layer during consolidation of the standard case experiment recorded by the single thermistor probe located in the gap between the two ice blocks. The enlarged plot shows a zoom of the first 1500 minutes of consolidation.

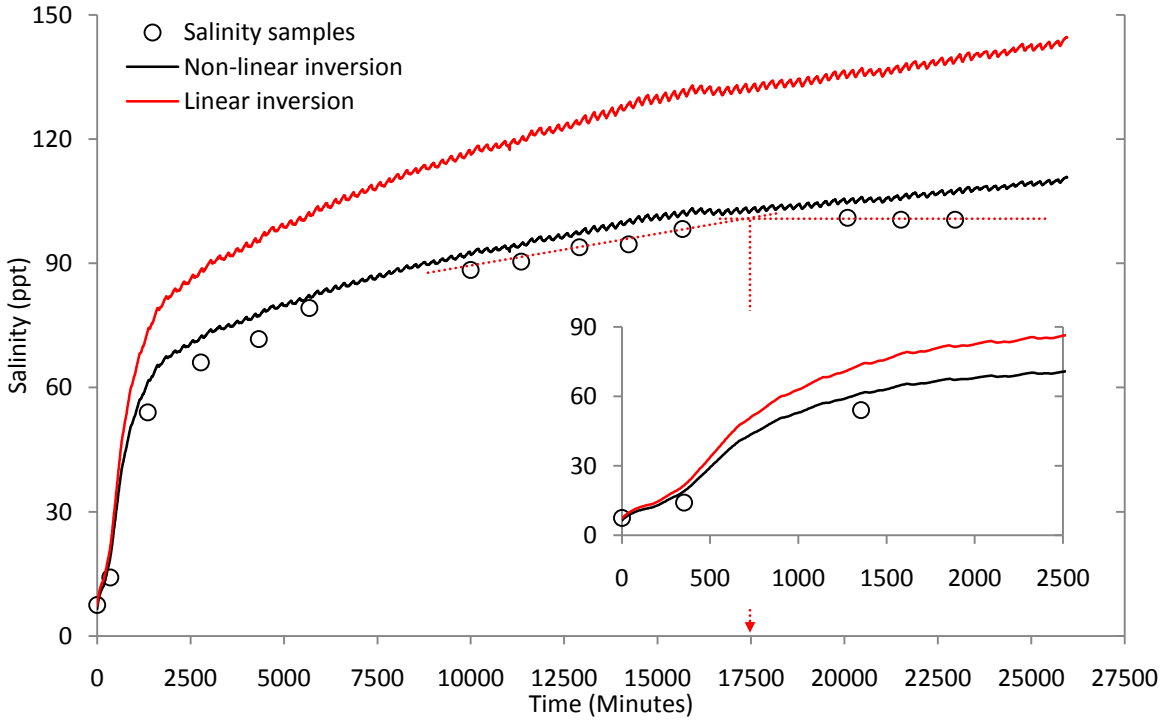

Figure 7.5. Salinity evolution in the liquid layer during the standard case experiment. The circles represent the samples that were taken with a needle and syringe; red line the temperature readings that were inverted using the linear liquidus curve (Eq. 7.1) and the black line the temperature readings that were inverted using the non-linear liquidus curve (Eq. 7.2). The enlarged plot shows a zoom of the first 2500 minutes of consolidation.

Figure 7.6 shows the temperature recorded in the ice blocks and the liquid layer as a function of depth and time for the standard case. The dotted line shows the temperature in the ice blocks prior to when the trace heating had been turned on and the solid lines the temperature profiles at different times of interest during the 'consolidation stage'. The temperature profile in the ice blocks is initially linear with depth, with low temperatures toward the top of the ice blocks (-4°C to -5°C) and warmer temperatures towards their base (-1°C to -2°C). The temperature in the upper block was initially 0.5°C warmer than the bottom ice block. This is because the temperature of the solution from which the block was grown was 1°C warmer than the lower block (see Figure 7.3a): experimental limitations meant that the temperatures of these solutions could be controlled to within ±1°C. In the first 5 minutes of consolidation, the temperature in the upper block rose by ~1°C, which is a consequence of the trace heating. This increase was much greater (~4°C) in the top thermistor, which is more than likely due to the thermistor malfunctioning as at later times the recorded temperature tended to sporadically change for no apparent reason. After ~250 minutes, the temperature in the upper block had re-established a linear temperature profile and in the lower ice block, the temperature had increased to a constant temperature of -0.8°C. During this time period, there was also very little change in temperature and salinity in the liquid layer suggesting that either there was no freezing of the liquid layer and the salinity simply increased due to brine draining from the upper ice block and/or freezing took place predominately at the top of the lower ice block so that the brine released on freezing, being more dense than the liquid layer above, would not significantly increase the salinity in the liquid layer. After this, the temperature in both ice blocks continued to cool until the experiment was stopped after 25900 minutes (17days, 23hrs, 40mins). An almost linear temperature profile was achieved throughout both ice blocks and the liquid layer after ~1300 minutes. This has been accentuated by the dashed orange line that has been extended to the bottom of the lower ice block.

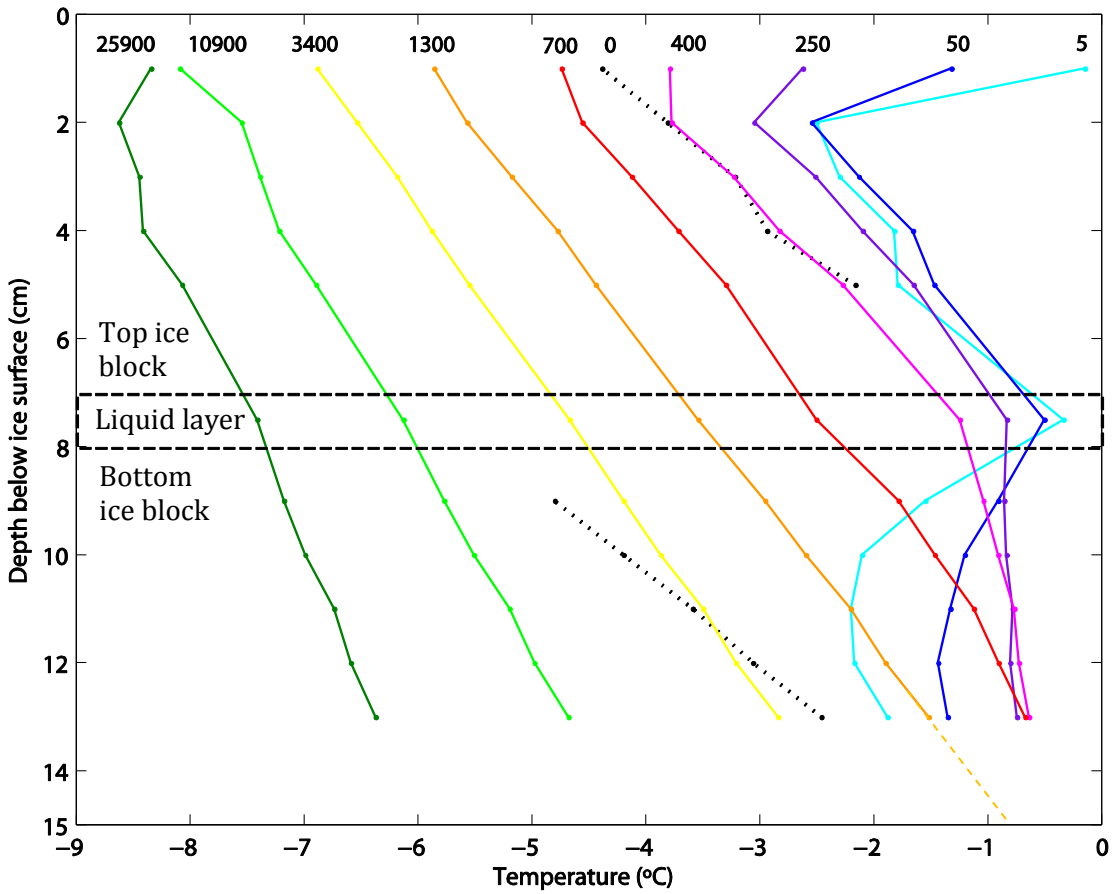

Figure 7.6. The temperature evolution in the ice sheets and the liquid layer as a function of depth and time for the standard case experiment. The dotted lines show the temperature in the ice blocks prior to when the trace heating had been turned on and the solid lines the temperature profiles at different times of interest.

In addition to measuring the temperature in the ice blocks and the liquid layer, during the standard case experiment, a 20cm probe was positioned at the base of the rafted section to measure the amount of growth at the bottom of the lower ice block. Figure 7.7 shows the temperatures recorded in the bottom ice block during the consolidation experiment using the 5 cm probe that was frozen into the ice during its formation (solid lines) and the 20 cm probe that was positioned in the water below the rafted section (dotted lines). It is evident that the top thermistor in the 20 cm probe (positioned at a depth of 7 cm) had actually just frozen into the ice during the initial growth stage therefore growth could only be estimated from the thermistors below this point. There are also no readings at depths of 21 and 23 cm because these two thermistors were not functioning correctly. In the first 250 minutes, a rise in temperature was recorded by all the thermistors as the probe was submerged into the warmer water below. The thermistors in the water then remained at roughly the same

temperature until, one by one, they started to cool as they became engulfed in ice as the ice-water interface advanced. Therefore by finding the time at which the temperature measured by a given thermistor drops below the freezing temperature the growth rate can be estimated (as was done in Chapter 5). The time that this takes place for each thermistor is indicated by the arrows on the plot where the dotted line shows the freezing temperature (-0.445°C) for a 7.5 ppt solution of NaCl. Figure 7.8 shows the position of the ice-water interface as a function of time as inferred from the temperature measurements. By fitting a quadratic to the data the time that ice growth started at the base of the rafted section can be estimated (i.e. 7 cm on the plot). It was found that ice growth started ~1400 minutes after the start of the consolidation experiment. This is around the time that a linear temperature profile was achieved throughout both ice blocks and the liquid layer.

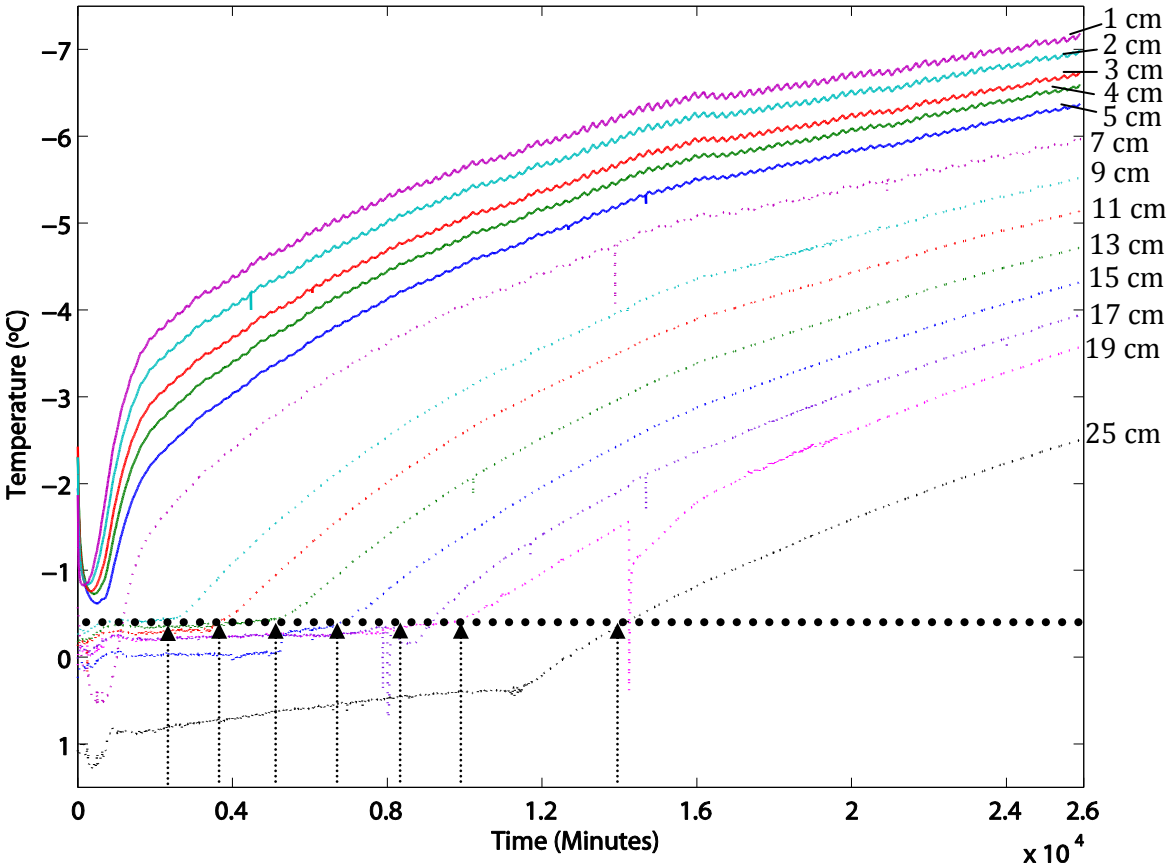

Figure 7.7. Temperatures recorded in the bottom ice block during the standard case experiment. The solid lines show the temperatures recorded by the 5 cm probe that was frozen into the ice block during its formation. The dotted lines show the temperatures recorded by the 20 cm probe that was positioned at the base of the rafted section. The location/depth of the individual thermistor is shown on the right-hand side of the graph, where 0 cm corresponds to top of the bottom ice block (i.e. below the liquid layer). The bold dotted line shows the freezing temperature for a 7.5 ppt solution (-0.45°C) and the arrows the times at which a given thermistor reduces below the freezing temperature.

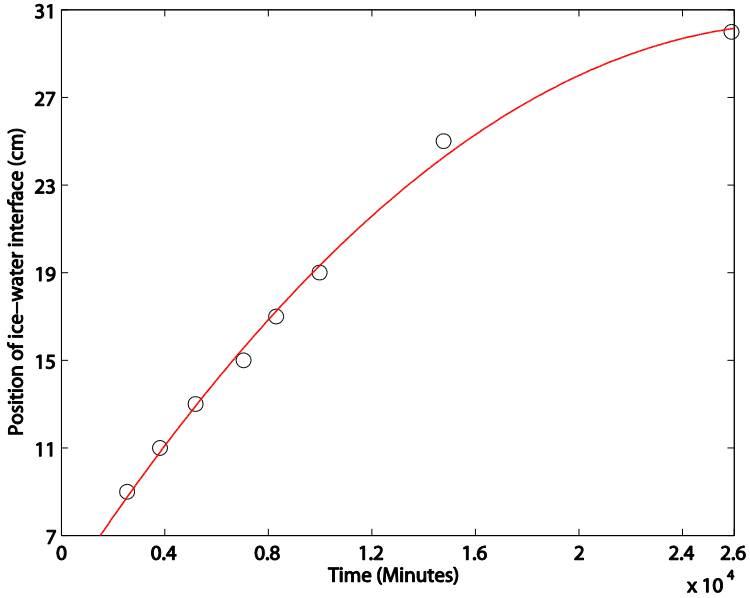

Figure 7.8. Position of the ice-water interface as a function of time as inferred from the temperature traces with a quadratic fit to the data. The final point on the graph was measured at the end of the experiment when a core was taken.

Now that I have presented the temperature and salinity plots for the standard experiment a key question is at what point did the ice blocks consolidate? Is it when:

- the temperature in the lower ice block starts to cool (~250 minutes)?
- the temperature in the liquid layer stops decreasing rapidly (~700 minutes)?
- a linear temperature profile is achieved throughout the ice blocks and the liquid layer (~1300 minutes)?
- the salinity in the liquid layer becomes constant (~20000 minutes)?

To investigate this, I repeated the same experiment (within the limits of experimental error) six times taking cores at different times of interest. In Table 7.2, the times at which cores were taken and stages of consolidation are presented. The results show that at 460 minutes, the ice was not sufficiently bonded to allow to core through both ice blocks and the lower ice block was pushed away by the corer. At 770 minutes, it was possible to take a core of both ice blocks; however the bond was so weak that the core fell apart. When viewing the remaining ice in the acrylic cylinder it was clear that the ice blocks had physically bonded and there was no liquid layer present. This coincides with the time that the temperature in the liquid layer stopped decreasing rapidly (see Figure 7.4). By 1610 minutes, the ice had sufficiently bonded to take an intact core; however a weak layer could still be felt on

coring. By 11300 minutes, resistance to coring was consistent, indicating that there is no weak layer present. From these data it is still not obvious what to define as consolidated. Is it when the ice has physically bonded? Or when it has reached its maximum strength? Certainly the latter is of more interest to engineers when calculating loads for offshore structures. For the remainder of this chapter, I shall refer to two states of consolidation: 'thermodynamic' and 'mechanical'. Thermodynamic consolidation refers to the time that sheets had physically bonded, which I take to be the time that the temperature in the liquid layer stops decreasing rapidly and changed to a more gradual decrease. This was estimated by fitting a best fit line to the temperature data recorded during rapid decrease and finding the time that the readings started to deviate from this trend (see enlarged plot in Figure 7.4). Mechanical consolidation refers to the time that the ice blocks had reached a stable strength. In Chapter 9, I investigate the strength of the bond between two rafted ice blocks by shearing cores under increasing states of consolidation. These results showed that the rafted ice had reached its full strength around the time that the salinity of the liquid layer became constant (as measured by the salinity samples extracted with a needle and syringe). This I estimate by fitting a best fit line to the data recorded just prior to the salinity becoming constant and finding the crossover point with the constant salinity values (as shown in Figure 7.5). Based on these assumptions, I estimate that the standard case rafted ice blocks had thermodynamically consolidated after ~700 minutes (11hrs, 40mins) and mechanically consolidated after ~17500 minutes (12days, 3hrs, 40mins).

Table 7.2. Times that cores were taken of the standard case rafted ice experiment

Time core taken (Minutes)	Consolidated (Yes/No)	Experimental Notes
460 (7hrs, 40mins)	No	Could only core through upper ice block - lower ice block pushed away with pressure of coring
770 (12 hrs, 50mins)	Yes	No liquid layer present – very weak bond core broke in two
1110 (18hrs, 30mins)	Yes	No liquid layer present – very weak bond core broke in two
1610 (1day, 2hrs, 50mins)	Yes	Felt a weak layer when coring
7250 (5days, 50mins)	Yes	Felt strong when coring
11,300 (7days, 20hrs)	Yes	Felt very strong when coring – no obvious weak layer

Salinity

To investigate the effect salinity had on the consolidation process, the initial salinity of the solution used in the experiment was varied between 0, 6, and 33 ppt whilst the ice thickness and gap thickness were held constant at the standard case values. Figure 7.9 shows the temperatures recorded in the liquid layer for each of the salinity variations. From the figure it is clear that changes in the initial salinity of the solution significantly influence the consolidation behaviour. For instance, it is clear that the more concentrated the initial salinity of the solution the lower the initial temperature of the liquid layer. This is because, as we saw before, the salinity of the liquid layer is closely linked to its freezing temperature and can be well represented by the inverted non-linear liquidus curve (see Figure 7.5). It is also apparent that for each of the curves there is initially a period where there is little or no change in temperature, followed by a phase of rapid temperature decrease. These changes in behaviour take place at approximately 800, 250 and 400 minutes for the 0, 6 and 33 ppt solutions, respectively. The times that these changes take place also (as mentioned in the standard case experiment) coincide with the times that the temperatures in the upper and lower ice blocks start to decrease for the respective solutions (see Figure 7.10). In the saline experiments, the fact that the salinity of the liquid layer also increased during this initial period suggests that either brine was draining into the liquid layer from the upper ice block and/or freezing took place predominately at the top of the lower ice block and the brine released on freezing slightly increased the salinity of the liquid layer. In the freshwater experiments, it is a very different scenario as the liquid layer must first freeze before the temperature can reduce below 0°C (which takes place at ~430 minutes). Once below zero, the temperature in the liquid layer decreases at first rather slowly and then rapidly jumps from just below 0°C to -2.5°C. This delayed jump in temperature was also observed by Veitch et al. (1991) who found that it took ~480 minutes for two layers of 6 cm freshwater ice to consolidate. I speculate that this delayed cooling in the freshwater experiments is caused by the latent heat released upon freezing which first needs to escape to the atmosphere before subsequent cooling can take place. It is likely that this takes place earlier in the saline water experiments because the increasing salinity of the liquid layer causes a reduction in the freezing temperature, allowing the ice blocks to start cooling before they have consolidated.

From the above it is evident that the freshwater and salt water cases are different and it is clear that my previous definitions of thermodynamic and mechanical consolidation cannot apply in the fresh water case. Therefore for the freshwater case I take thermodynamic consolidation to be the time that the temperature in the liquid layer reduced below 0°C and mechanical consolidation to be the time that the temperature in the ice block and liquid layer became roughly constant.

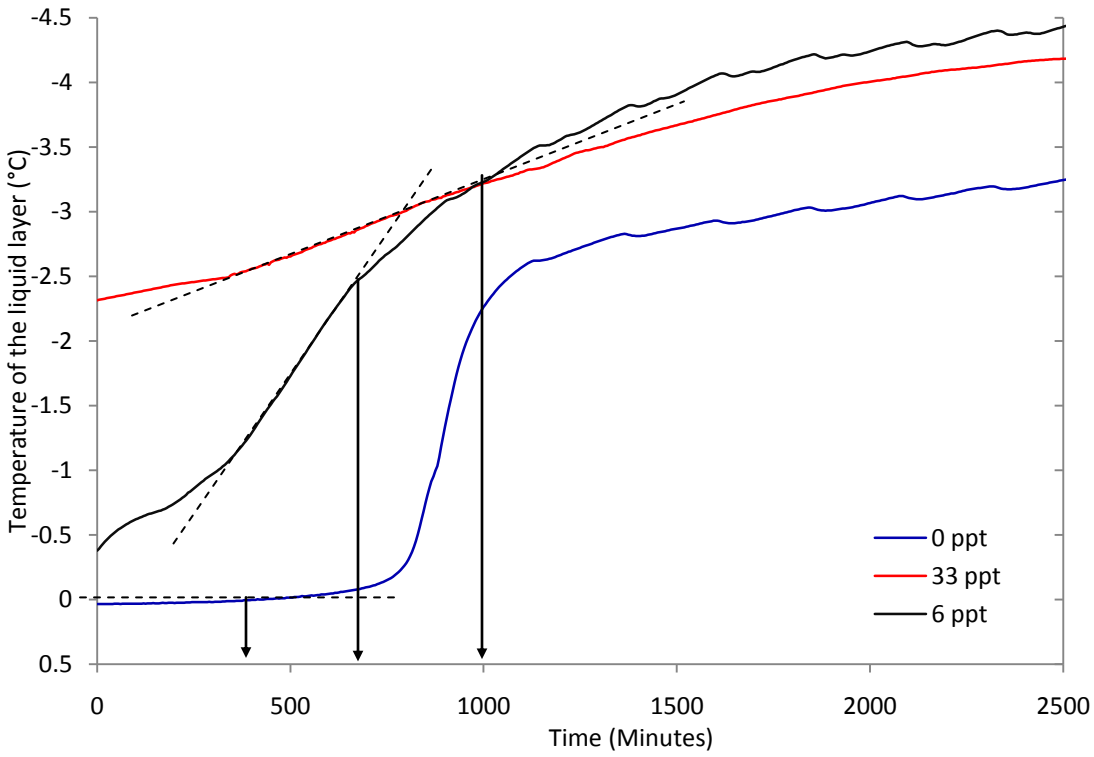

Figure 7.9. Temperature measured in the liquid layer for the 0 ppt (blue line), 6 ppt (black line) and 33 ppt (red line) consolidation experiments. The times that I estimate the ice blocks have thermodynamically consolidated are shown by the arrows superimposed on the plot.

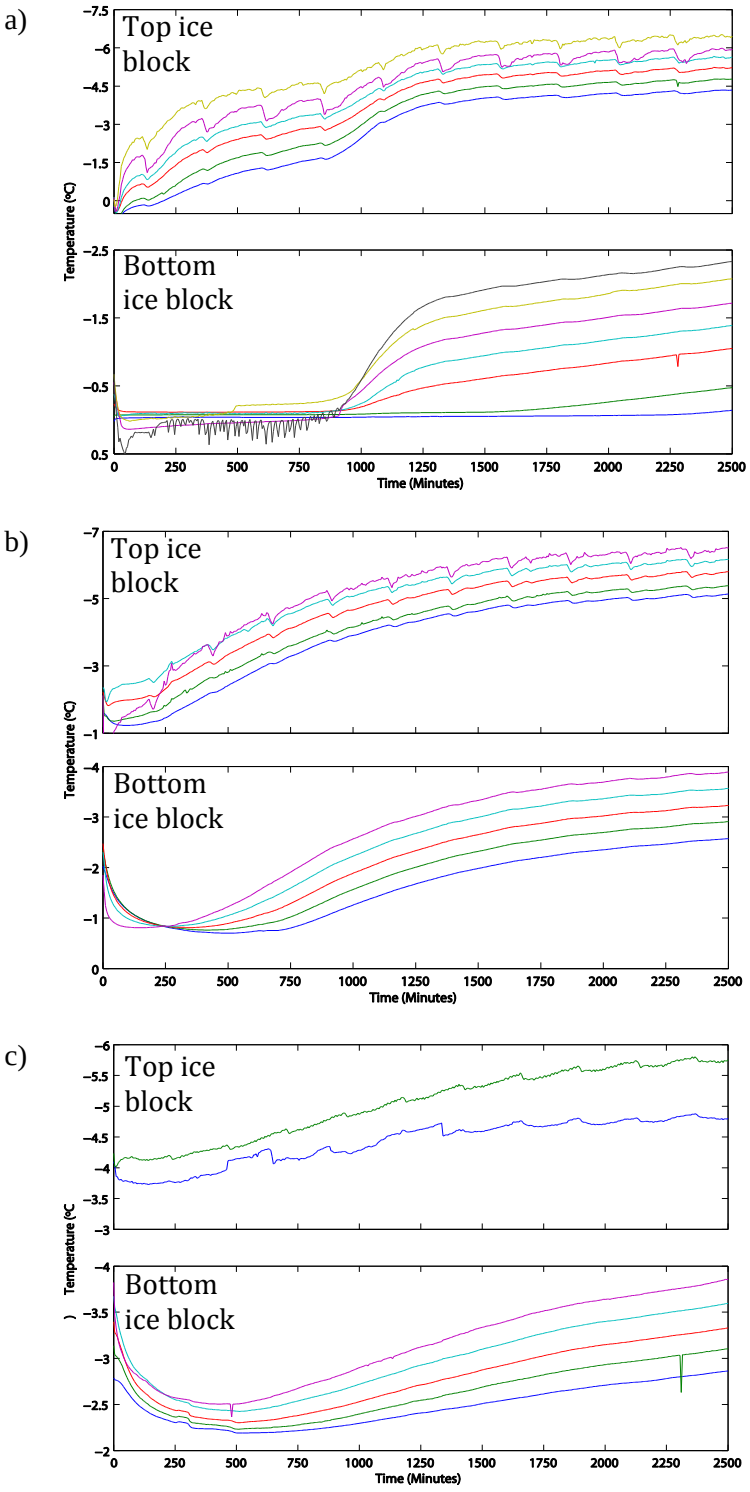

Figure 7.10. Temperature-time traces recorded in the top and bottom ice blocks for the 0 ppt (a), 6 ppt (b) and 33 ppt (c) experiments. The different coloured curves represent each thermistor in the probe where the top thermistor is positioned ~1 cm below the ice surface of the respective block. There are only two curves in the top ice block in the 33ppt experiment as the rest of the thermistors in this probe had corroded.

Table 7.3. The consolidation times for each of the different solution concentrations, where the ice and gap thicknesses were held constant at respectively 7 and 1 cm (see Table 7.1).

Initial salinity of solution (ppt)	Time that the ice had consolidated (minutes) Thermodynamic	Mechanical
0	~430 (7 hrs)	~5000 (3day, 11hrs, 20mins)
6*	~700 (11hrs, 40mins)	~17500 (12days, 3 hrs, 40mins)
33	~1000 (16hrs, 40mins)	~50000 (34days, 17hrs, 20mins)

* Standard case

In Table 7.3, the times estimated for thermodynamic and mechanical consolidation for each of the different concentrations are presented. The results show that increasing the initial salinity of the solution increases both the thermodynamic and mechanical rates of consolidation substantially. This is because increasing the salinity of the solution increases the initial salinity of the liquid layer (as can be seen in Figure 7.9), increases the bulk salinity of the ice blocks and reduces the initial temperature gradients in the ice blocks (as can be seen in Figure 7.10), all which act to slow down the rate of consolidation. This is because an increase in the initial salinity of the liquid layer increases its specific heat capacity, which means that more energy is needed to cool the liquid layer down to its freezing temperature. The more saline the ice blocks, the lower their thermal conductivity and the higher their specific heat capacity, both of which act to reduce the rate that heat can be transferred through the ice to the atmosphere. In addition, if brine drainage or flushing plays a role in the consolidation process it is likely that the more saline ice blocks have a higher brine volume and concentration thus increasing the permeability of the ice and the density difference between the brine in the upper ice block and the liquid layer which is the driving force for convection overturning (i.e. gravity drainage). This would therefore cause high salinity brine to drain into the liquid layer thus increasing its salinity and hence the consolidation time (this shall be discussed in more detail later). Also the more concentrated the solution, the lower the freezing temperature at the ice-water interface, therefore assuming that the temperature at the ice-atmosphere surface is similar for the different concentrations, this would decrease the initial temperature gradients in the ice blocks and thus the diffusional heat fluxes through them, so that the rate of consolidation is decreased.

Ice thickness

The initial thickness of the ice blocks was varied between 7, 10 and 14 cm to investigate the effect that ice thickness had on the rate of consolidation of the ice grown from a 6 ppt solution of NaCl. In Figure 7.11, the temperatures recorded in the liquid layer for each of the different ice thicknesses are plotted against time. The figure shows that all of the curves start and end at roughly the same temperature. The difference between them is the length of the period where there is little change in temperature and the steepness of the gradient during rapid temperature decrease. The start time and rate of temperature decrease is shorter and steeper the thinner the ice blocks used in the experiment. This is because the thicker the ice blocks, the longer it takes for heat to be extracted out through the top ice block. This therefore reduces the rate of freezing causing the salinity and in turn the temperature in the liquid layer to change at a slower rate.

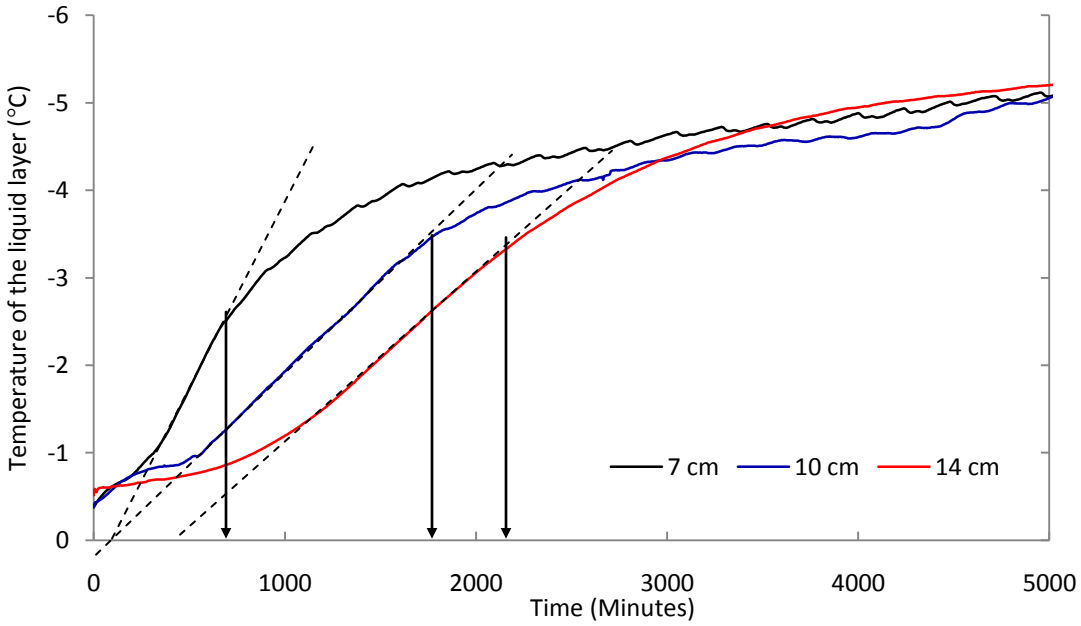

Figure 7.11. Temperature measured in the liquid layer for the consolidation experiments grown from a 6 ppt solution of NaCl to ice thicknesses of 7 cm (black line), 10 cm (blue line) and 14 cm (red line). The times that I estimate the ice blocks have thermodynamically consolidated are shown by the arrows superimposed on the plot.

In Table 7.4, the consolidation times for each thickness are presented. The results show that doubling the thickness of the ice sheet increased the thermodynamic consolidation time by just over a factor of three. This is considerably more change than was seen for variations in

the salinity of the solution used in the experiment. This suggests that changes in the thermal properties of the ice have less of an influence on the rate of heat transfer through the ice than the thickness of the ice block itself. In contrast, the influence of salinity on the mechanical consolidation time is much greater than the influence of the ice thickness. This is probably because once thermodynamically consolidated the brine for the different ice thicknesses is of similar concentration (as can be seen in Figure 7.11) and will therefore continue to cool at a fixed rate dependent on the ice thickness. However, in the 33 ppt case it is likely that the brine in the liquid layer is of higher concentration and therefore will take longer to reach equilibrium salinity appropriate to the cold room temperature.

Table 7.4. The consolidation times for the different ice thicknesses, where the initial salinity solution and the gap thickness were held constant at respectively 6 ppt and 1 cm (see Table 7.1).

Initial thickness of the ice blocks (cm)	Time that the ice had consolidated (minutes) Thermodynamic	Mechanical
7*	~700 (11hrs, 40mins)	~17500 (12days, 3 hrs, 40mins)
10	~1620 (1day, 3hrs)	~21400 (14days, 21hrs)
14	~2200 (1day, 12hrs, 40mins)	~26800 (19days, 20hrs, 40mins)

* Standard case

Gap thickness

To investigate the effect the size of the gap between rafted ice blocks had on the consolidation process, the gap thickness was varied between 0.5, 1 and 2 cm. Figure 7.12 shows the temperature-time traces recorded in the liquid layer for each of the different gap thicknesses. The figure shows that similar to the other tests there are two stages of behaviour; a period where there is little or no change in temperature of the liquid layer followed by a stage of rapid temperature decrease. The length of this initial period and the steepness of the gradient during rapid temperature decrease are longer and less steep the thicker the gap thickness used in the experiment. This is because the thicker the gap the more heat needs to be extracted to freeze it and hence the longer the consolidation time. It is also interesting to note that prior to the rapid temperature decrease in the 2 cm gap experiment there is practically no change in temperature whereas in the 0.5 cm experiment

the temperature of the liquid layer has cooled by a considerable amount. This suggests that the lower ice block is not cold enough to absorb enough heat to allow the liquid layer to freeze, at least up to the point where the thermistor is located (~midway between the two blocks). Conversely, in the 0.5 cm gap experiment the temperature of the liquid layer has cooled by a considerable amount signifying that there has been significant freezing during this initial period.

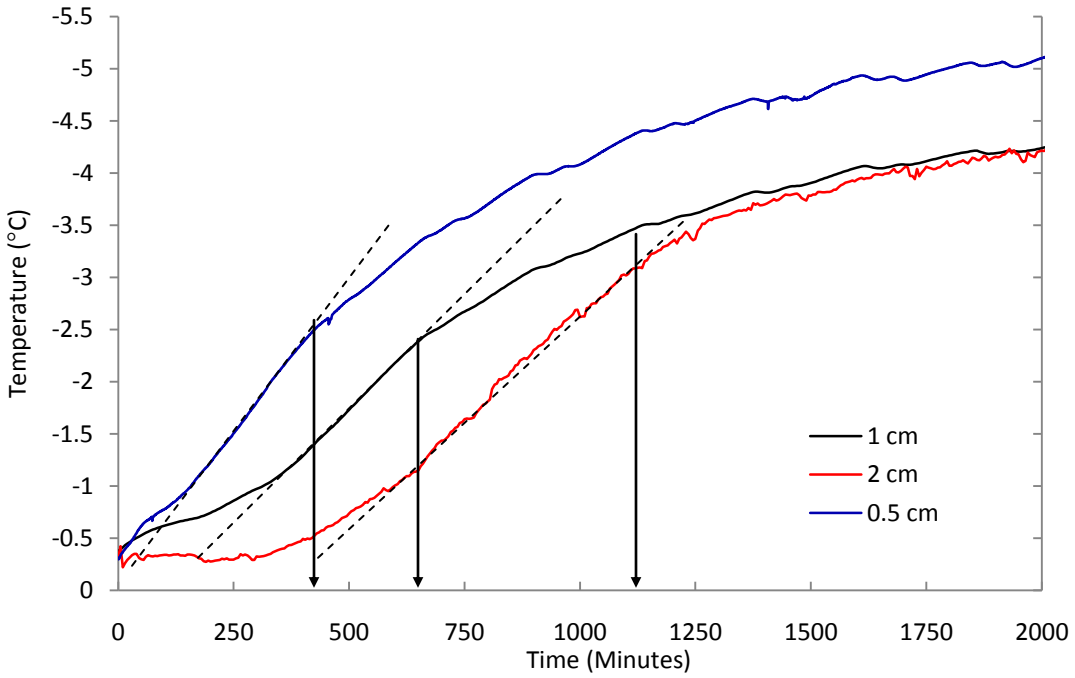

Figure 7.12. Temperature measured in the liquid layer for the consolidation experiments with gaps of 1 cm (black line), 0.5 cm (blue line) and 2 cm (red line) thickness. The times that I estimate the ice blocks have thermodynamically consolidated are shown by the arrows superimposed on the plot.

In Table 7.5, the results for the various gap thicknesses are presented. The results show that increasing the thickness of the liquid layer (or gap) between the ice blocks increases both the thermodynamic and mechanical consolidation times almost linearly. This indicates that the rate of heat transfer remains roughly constant and that freezing takes place at a constant rate.

Table 7.5. The consolidation times for the different gap thicknesses, where the initial solution salinity and the ice thickness were held constant at respectively 6 ppt and 7 cm (see Table 7.1.).

Initial thickness of the gap (cm)	Time that the ice had consolidated (minutes) Thermodynamically	Mechanically
0.5	~420 (7hrs)	~10000 (6days, 22hrs, 40mins)
1*	~700 (11hrs, 40mins)	~17500 (12days, 3 hrs, 40mins)
2	1120 (18hrs, 40mins)	~32900 (22 days, 20hrs)

* Standard case

7.4 Physical properties of the rafted ice

To gain a better understanding of the physical properties of the rafted ice, the salinity, density, porosity and crystal structure of the ice was examined. This was only done for the rafted ice used in the standard case experiment and the 33 ppt experiment. I would have also done this for the freshwater rafted ice, but the ice was too brittle and it was not possible to extract intact ice cores without the core fracturing in several places.

Salinity, Density and Porosity

To determine the salinity, density and porosity of the rafted ice a core was taken using a 9 cm diameter corer. The core was then cut in half along its length. One side of the core was separated into 1) the upper ice block, 2) the lower ice blocks and 3) the consolidated liquid layer, and the 'bulk' salinity, density, and porosity of the separate layers were determined using the same methods previously described in Chapter 5.5. The other half of the core was cut into 1-2 cm sections in order to measure the salinity change with depth. Ideally, I would have also calculated the density and porosity for the smaller sections to see their variation with depth (as I did for the level ice properties). However, due to the limited number of cores I could take from one experiment and because I believe that getting an accurate salinity profile is of greater importance for estimations of brine drainage processes this was not done. I calculated the maximum density variation with depth by solving equation (2.3) for ρ_{si}, setting the air volume equal to zero and using the measured salinity profile and temperature data recorded by the thermistor probes. This therefore gave an 'upper bound'

for the rafted ice density. Using the calculated density, I also estimated the maximum brine volume.

In Table 7.6 the temperature, salinity, density and porosity determined for the upper and lower ice blocks and the liquid layer are given. The salinity measurements show that in the 6 ppt case, there was little change in the upper ice block when compared to the bulk salinity measured for level ice (1.7-2 ppt, see Table 5.1). However, in the 33 ppt case there was a 20% reduction in the salinity of the upper ice block. This indicates that brine either drained out of the block during the coring or the handling of the core, or during the rafting experiment itself. The bulk salinities of the liquid layer are in both cases more than 50% lower than the initial salt concentration of the liquid layer. There is uncertainty in the measurements due to the difficulty of identifying the exact boundaries of the liquid layer. The bulk salinities of the liquid layer are, in both cases, within the uncertainties the same as that of the lower ice block. However this is not the case when viewed as a function of depth (see Figures 7.13 and 7.14) where the salinity of the liquid layer is always fractionally higher than the surrounding ice. The high bulk salinities of the lower ice blocks are caused by the high salinity of the newly forming ice at the base of the rafted section. The salinity of the newly forming ice is also probably higher than may be expected because any brine that drains out of the ice and into the water below remains trapped and therefore accumulates gradually. So as the growing ice-water interface advances, higher salinity brine is trapped between the dendrites. Measurements made of the water below the rafted section show that the salinity increased from 7±0.5 ppt to 22±0.5ppt and from 37±0.5 ppt to 64±0.5 ppt over the course of the experiment. In the open ocean, brine draining from the ice would (in most cases) be swept away by currents, so that the sea water at the base of the rafted section remains at a constant salinity. Ideally, the experimental apparatus would have a water recirculation system to keep the salinity constant or a large enough tank so that salt surplus need not be considered. Within experimental laboratory constraints this was not possible. This would only have a small effect on the thermodynamic consolidation time as there was no ice growth at the base of the rafted section during this stage and unless there was significant brine drainage the salinity and hence temperature at the base of the rafted section would remain roughly constant. Once ice growth starts it is likely that brine drains out of the newly forming ice thus reducing the temperature at the base of the rafted section. This would also reduce the temperature gradient in the ice blocks and the diffusional heat

fluxes through them, so that the rate of cooling is reduced. This would prolong the time taken for the rafted ice to reach mechanical consolidation.

Table 7.6. Temperature, salinity, density and porosity of the bulk sections of the rafted ice.

Initial salinity of water (ppt)	Rafted ice section	Ice thickness (cm)	Average Temperature (°C)	Ice Salinity (ppt)	Density (Mg m^{-3})	Porosity (%)
6	Upper block	7	-8.2	1.6	0.910	2.15
6	Liquid layer	1	-7.5	3	0.908	3.67
6	Lower block	30	-5.2	2.9	0.912	4.15
33	Upper block	7	-7.9	8.5	0.915	7.66
33	Liquid layer	1	-7.7	7	0.901	7.85
33	Lower block	19	-7.0	7	0.923	6.14

Figures 7.13 and 7.14 show the variation in temperature, salinity, density and brine volume with depth for the 6 ppt and 33 ppt rafted ice experiments (where density and brine volume where calculated using the upper bound method). The salinity profiles show that the ice blocks have retained similar profiles to those observed in the level ice (comparing Figures 5.7 and 5.8 with Figures 7.13 and 7.14). (For the 6 ppt case, low salinities toward the top of the ice blocks gradually increase to a constant salinity of 1-2 ppt, while for the 33 ppt case, the profiles are C-shaped). The values obtained in the 33 ppt case are however ~2 ppt less than the bulk salinity measured for the whole upper ice block. This demonstrates how much brine drainage can take place during the handling and sectioning of the core. The fact that in the 6 ppt case, the ice blocks in the rafted section have similar profiles and bulk salinities to the level ice suggests that no brine was draining out of the original ice blocks and the salinity of the water increased due to brine draining out of the newly forming ice at the base of the rafted section. In the 33 ppt case it is not as clear as there was a 20-30% reduction in the salinity of the ice blocks which could have taken place during the handling of the ice or during the rafting experiment itself. This will be examined in more detail in the discussion section.

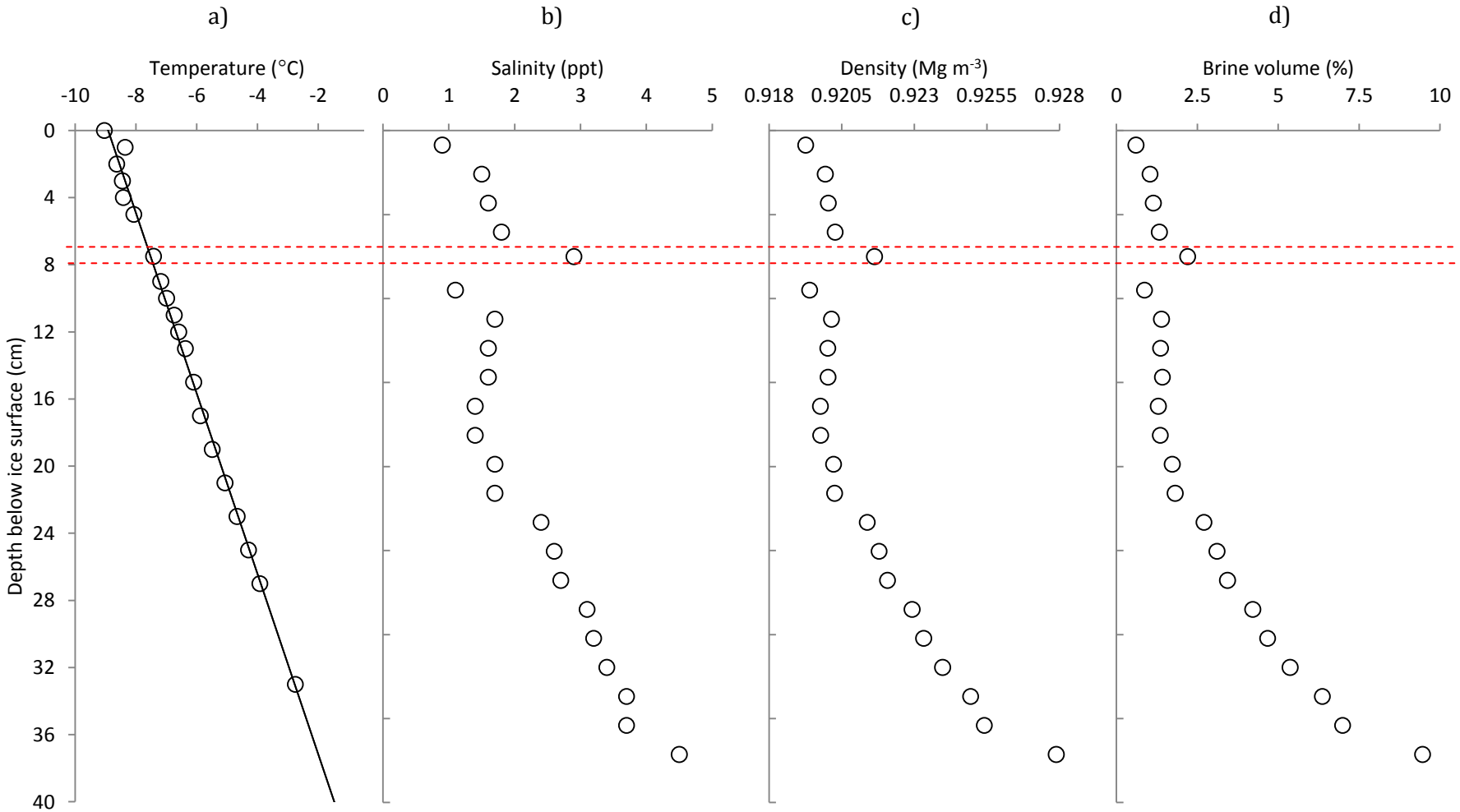

Figure 7.13. The temperature (a), salinity (b), density (c) and brine volume (d) variation with depth for the standard case rafted ice experiment. The position of the liquid layer is shown by the red dashed line superimposed on the plots.

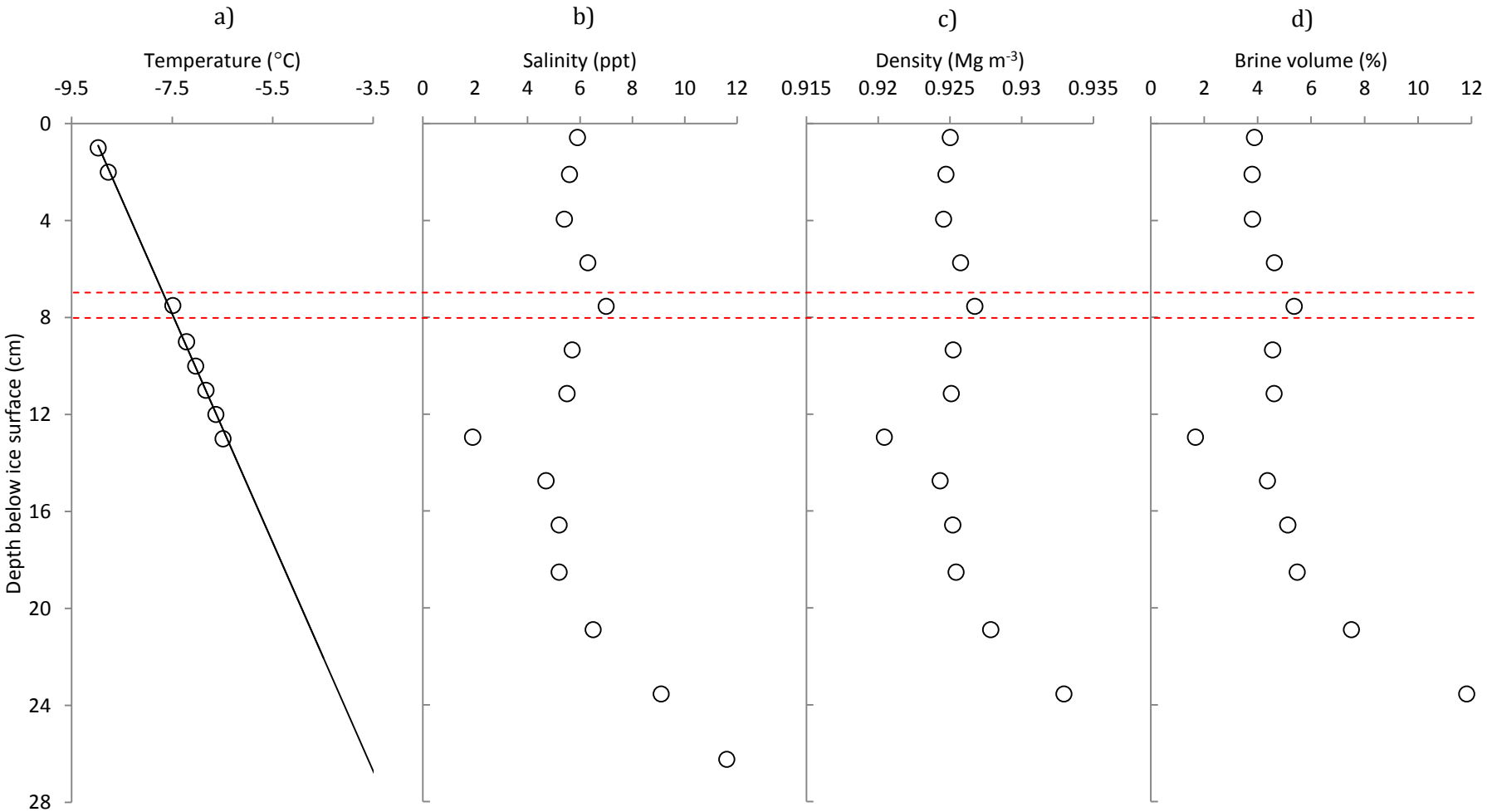

Figure 7.14 The temperature (a), salinity (b), density (c) and brine volume (d) variation with depth for the 33ppt rafted ice experiment. The position of the liquid layer is shown by the red dashed line superimposed on the plots.

Crystallographic analysis

The crystal texture of the rafted ice was observed by making thick (~5mm thick) and thin (~1mm thick) sections and viewing them under crossed polarising lenses. In Figure 7.15, a thick section taken from the standard case rafted ice experiment is shown. From top to bottom, there is 1-2 cm of granular ice, followed by 4-5 cm of columnar ice growth and then the consolidated liquid layer which is ~1cm thick. Below this, there is 1-2 cm of granular and columnar crystals which extend beyond the length of the section. The boundary between the liquid layer and the granular ice below is clearly identifiable, whereas the upper boundary with the ice block above is not so clear. This is because the liquid layer was pushed up into the interstices of the columnar ice forming an interlocking bond. This can be seen more clearly in Figure 7.16, which shows a thin section of the liquid layer made from the same core of ice. The thin section shows that the liquid layer is composed of granular ice with randomly orientated crystals about 2-4 mm in diameter.

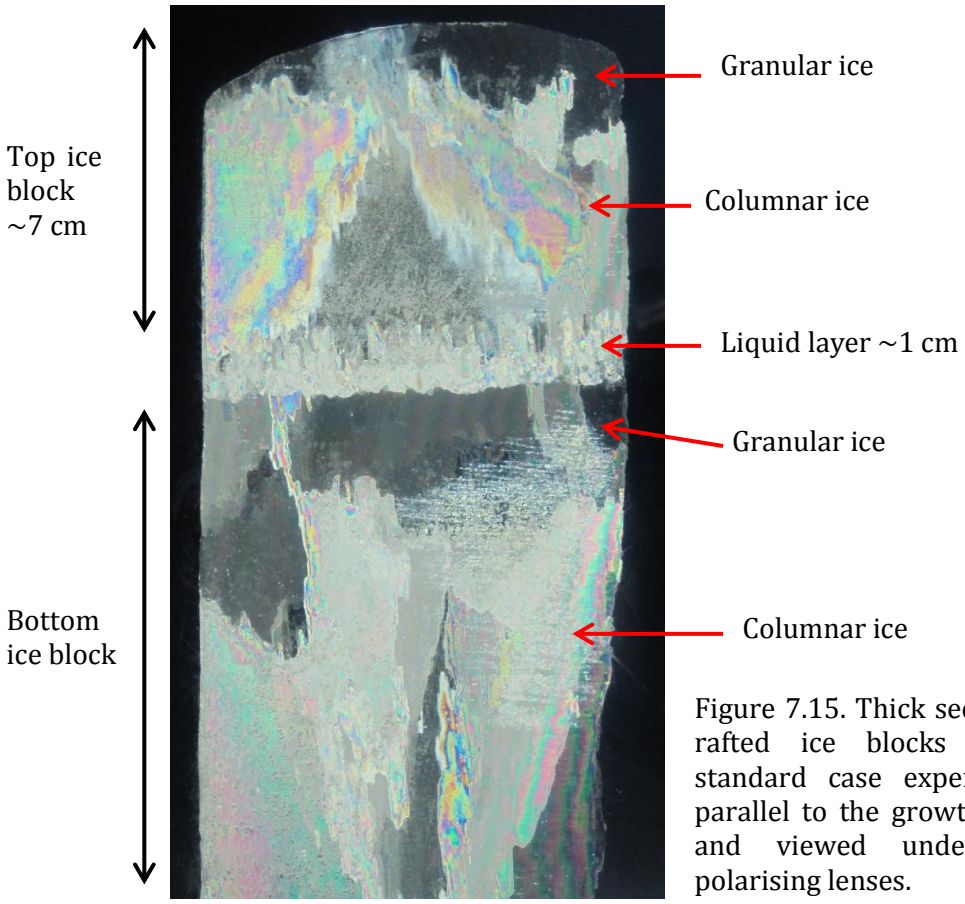

Figure 7.15. Thick section of the rafted ice blocks from the standard case experiment cut parallel to the growth direction and viewed under crossed polarising lenses.

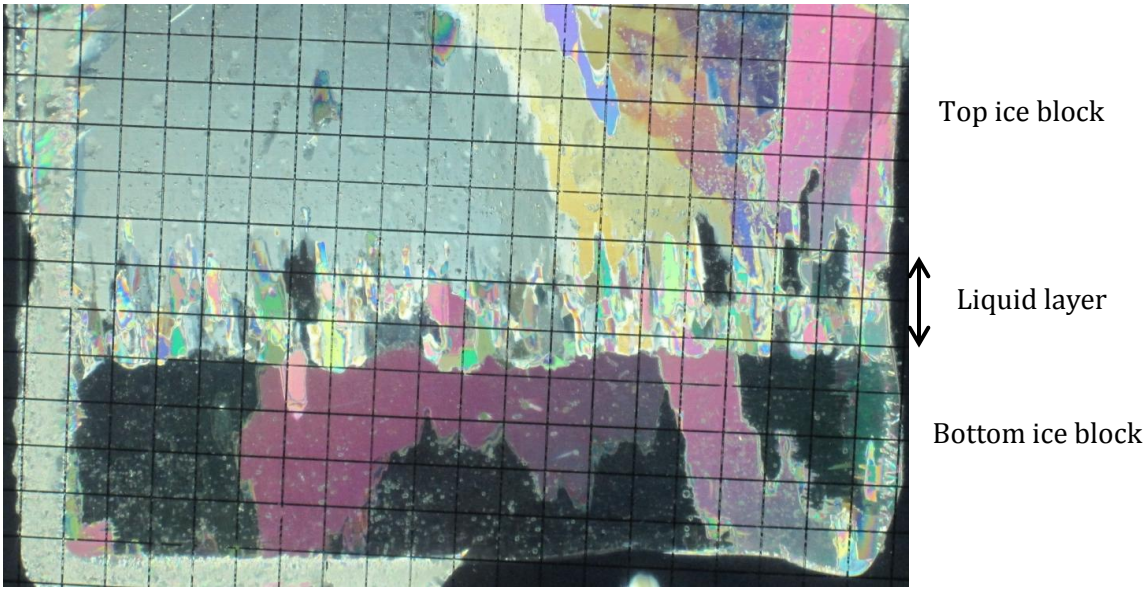

Figure 7.16. Thin section of liquid layer from the standard case rafted ice experiment, where the section was cut parallel to the growth direction. The photograph was taken through crossed polarising lenses, with a 0.5 cm^2 grid placed on top.

7.5 Discussion

The experiments presented in this chapter examine the temperature and salinity evolution during the consolidation of two saline ice blocks. The results show that in all the experiments (bar the freshwater case) the salinity of the liquid layer and the water below the rafted section gradually increased. The principal questions are where is this brine coming from and by what mechanism it is being released into the liquid layer and the water below? There are three possible scenarios: 1) brine is draining from the original ice blocks into the liquid layer and the water below via convective overturning, 2) brine is being 'flushed' out of the top ice block and into the liquid layer due to a positive hydraulic head which is produced as one ice block is lifted above the other during the rafting process, 3) brine is being rejected/drained from the newly forming ice in the liquid layer and at the base of the rafted section. As was shown in Chapter 6, for gravity drainage to take place the ice needs to be sufficiently permeable (brine volume $\gtrsim$ 5 %) and have sufficient buoyancy forcing ($Ra_c \gtrsim 10$). Using Figure 6.12, which shows the brine volume calculated for a variety of salinities and temperatures, we find that for salinities of 1.7-2 ppt and 10.1-10.8 ppt (see Table 5.1) the ice needs to be warmer than -2°C and -11°C to be sufficiently permeable for fluid transport to take place. In the 33ppt experiment, the whole rafted

section is warmer than -11°C therefore implying that it would indeed be sufficiently permeable for fluid transport to take place. Conversely, in the standard case experiment, the top 4 cm of the rafted section is below -2°C and therefore is, in principle, impermeable to fluid transport (see Figure 7.6). This means that even if a positive hydraulic head is produced during the rafting process, for the standard case experiment flushing will not occur. Using the temperatures recorded during the experiments and the bulk salinities measured for the ice pre-rafting, the local Rayleigh number (Eq.2.5) was calculated for the standard case and the 33 ppt experiments. Figure 7.17 shows the Rayleigh number profiles calculated for the standard case experiment up to the point of thermodynamic consolidation. The figure shows that during the consolidation process the Rayleigh number was significantly below 10. The same was true for the 33 ppt experiment. The reason for very low Rayleigh numbers is that before the ice blocks were rafted a large percentage of the brine had already drained out of the ice thus reducing the bulk salinity. This therefore allowed more freezing to take place on the walls of the brine pockets hence reducing the permeability of the ice and in turn lowering the Rayleigh number Ra. In nature, I expect that, unless the ice blocks are thin (i.e. less than 3-4 cm) some brine would have already drained out of the ice sheets before they are rafted. Out of interest I also calculated Ra assuming that no brine had been expelled from the ice blocks prior to rafting (i.e. $S_{bulk} = 6$ and 33 ppt). I found that in the 6 ppt case, Ra still did not exceed 2 in the upper ice block; however in the lower ice block it exceeded 10. Similarly, in the 33 ppt case, the Rayleigh number only exceeded 10 in the upper ice block when $S_{bulk} > 25$ ppt. This implies that unless the ice sheets are thin and salty it is unlikely that brine draining from the upper ice block would increase the salinity in the liquid layer. The fact that in the standard case experiment there was no significant change in the bulk salinity of the ice blocks implies that no brine drainage or flushing are likely to have taken place and therefore that the salinity of the liquid layer and the water below the rafted section increased due to brine being rejected/drained from the newly forming ice growing in the liquid layer and at the base of the rafted section. In the 33 ppt experiment, there was a 20-30% reduction in the salinity of the ice blocks indicating that brine either drained during the handling of the ice or during the rafting experiment itself. Since there was not sufficient buoyancy forcing (i.e. $Ra < 10$) it is unlikely that convective overturning caused a reduction in the salinity of the ice blocks. This therefore only leaves flushing as a possible mechanism. From studies of melt ponds we know that flushing is a rather quick process (i.e. it would take place in under

a couple of hours) therefore I would expect to see a rather sharp rise in salinity in the liquid layer during the initial stages of the consolidation. Since the salinity of the liquid layer was observed to remain roughly constant in the first 400 minutes of consolidation I believe that brine drained out of the ice either during the assembly process or during the coring and sampling of the ice at the end of the experiment. Without further controlled experiments, where the ice blocks do not have to be physically lifted out the water, I cannot be certain that no flushing would take place in the open ocean. However, since no flushing or brine drainage took place in the standard case experiment, I believe that the assumption made in the model that brine is only released from the newly growing ice in the liquid layer is correct for low salinity environments such as the Caspian Sea.

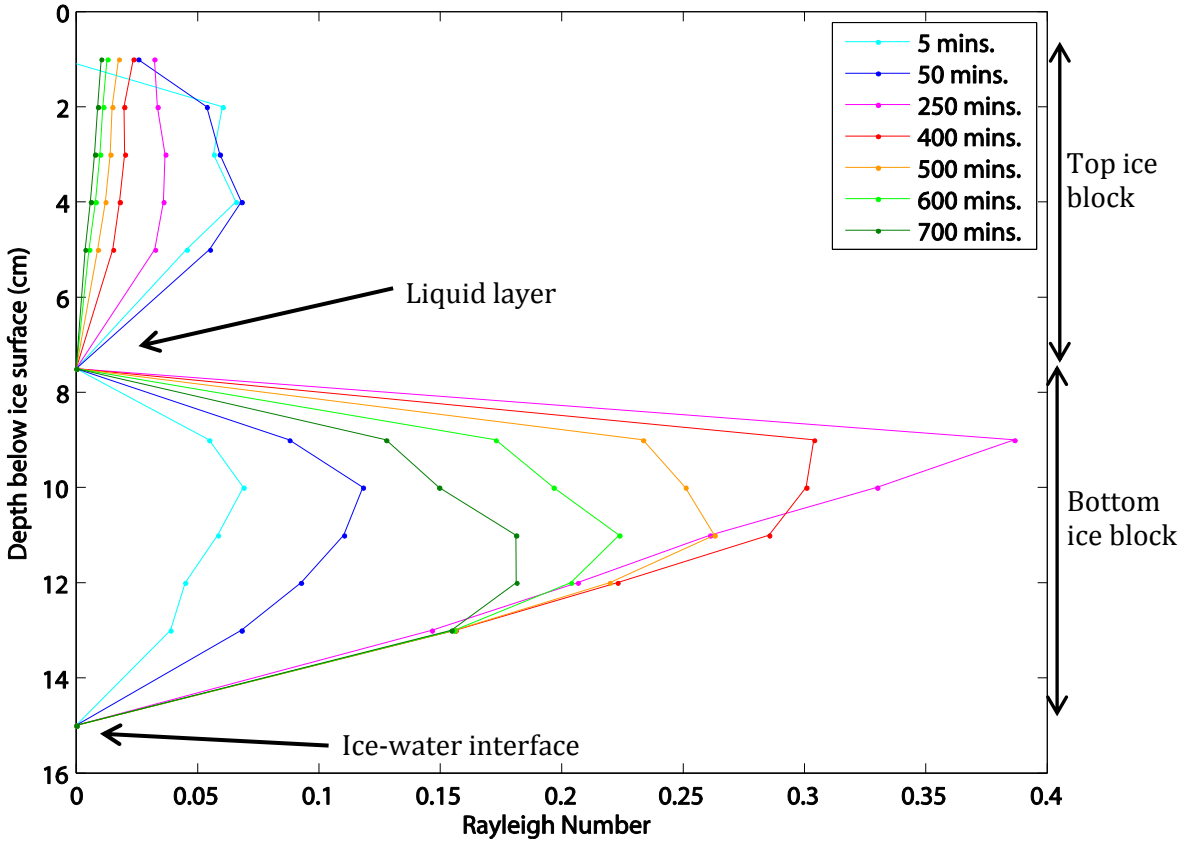

Figure 7.17. Rayleigh number profiles calculated at various stages during the consolidation process for the standard case experiment.

It should be noted that the experimental method used introduces some effects that may cause a departure from what might be observed in nature. These are either to do with the assembling of the ice blocks or are consequences of having a closed container.

To assemble the ice blocks, trace heating had to be used to remove the ice blocks from the acrylic cylinders which unavoidably caused the temperature of the ice blocks to increase by about 1°C. Sawing the ice blocks flat removes the fragile dendrites which may in nature get caught between rafting ice blocks thus making the liquid layer more slush than a region of pure liquid. However, it seems likely that even in the field most of the dendrites would be scraped off as one ice sheet rides up over the other. Finally, the process of physically transferring one block to another container could have, in the 33 ppt case, caused brine to drain out of the block.

The cylinder walls may have prevented the liquid layer from draining laterally, causing its salinity to increase more than it otherwise would have. Lending some support to our experiments, in the HSVA ice tank experiments, where the ice blocks were unconfined, a considerable rise in the salinity of the liquid layer was also observed (see Appendix F). This is also consistent with the model (Chapter 6) where it is assumed that the lateral extent of the ice sheets is so large that lateral drainage of the liquid layer is be neglected. The confinement of the cylinder also meant that brine that drained during the initial formation of the ice caused the salinity of the liquid layer between two rafted ice blocks to be initially ~10-15% higher than expected. In addition, this meant that during the course of the experiment the salinity increased from 7±0.5 ppt to 22±0.5ppt and from 37±0.5 ppt to 64±0.5 ppt. It is unlikely that this will affect the thermodynamic consolidation time as there was little ice growth at the base of the rafted ice blocks. Once ice growth starts it is likely that brine drains out of the newly forming ice thus reducing the temperature at the base of the rafted section. This would prolong the time taken for the rafted ice to reach mechanical consolidation.

Without large scale experiments with which to compare these results I cannot credibly estimate what effects these processes have on the consolidation times. In any case the main purpose of these experiments was to test the consolidation model and most of the limitations mentioned above can be accommodated by suitably constraining the model, as will be discussed in the following chapter.

7.6 Summary

In this chapter, I presented a series of experiments that were carried out in the Ice Physics Laboratory at UCL to investigate the consolidation of rafted sea ice. During each test the temperature in the ice blocks and temperature and salinity of the liquid layer were monitored continuously. Results showed that in all the saline tests, the salinity of the liquid layer increased over the course of the experiment. This is because as the liquid layer freezes, increasing amounts of salt are released into the remaining liquid layer. This in turn caused a reduction in the temperature of the liquid layer as it was cooled to its freezing temperature. By inverting the temperature using the non-linear liquidus curve, we saw that the inverted temperature readings are in good agreement with the salinity samples taken from the liquid layer demonstrating that the assumption made in the model that the liquid layer is held at its freezing temperature is reasonable.

In all experiments, it was observed that there was initially a period when there was little or no change in the temperature and the salinity of the liquid layer. During this period, the temperature in the upper ice block only decreased by a small amount and the temperature in the lower ice block gradually increased. This suggests that either there was no freezing of the liquid layer and the ice blocks were simply equilibrating to their surroundings, or freezing is predominately at the top of the lower ice block and the latent heat released on freezing moved up through the top ice block. After this initial period, the temperature in both ice blocks and the liquid layer started to decrease rapidly as freezing took over at the base of the upper ice block. This rapid decrease in temperature then continued until the ice blocks were physically bonded (which was confirmed by taking cores at specific times of interest). At this point the bond between both ice blocks was still physically weak because the consolidated liquid layer had a high liquid fraction. The strength of the bond then gradually increased as the as the temperature of the liquid layer and hence the liquid fraction decreased overtime. I therefore referred to two stages of consolidation: ‘thermodynamic’ and ‘mechanical’. Thermodynamic consolidation refers to the time that sheets had physically bonded, which I took to be the time that the temperature in the liquid layer stops decreasing rapidly and changed to a more gradual decrease. Mechanical consolidation refers to the time that the ice blocks had reached a stable strength, which occurs around the time that the salinity of the liquid layer became constant.

Results of the tests showed that all the experiments had thermodynamically consolidated in less than a day, however it took significantly longer for the ice sheets to reach mechanical consolidation. The time it took for the experiments to reach mechanical consolidation may have been prolonged by the increasing salinity of the water below the rafted section reducing the rate of cooling. Results of the sensitivity tests showed that the thickness of the ice blocks used in the experiment appeared to have the greatest effect on thermodynamic consolidation time, whereas the salinity of the solution used in the experiment appeared to have a greater effect on the mechanical consolidation time. Increasing the gap thickness caused the consolidation times to increase almost linearly, indicating that the rate of heat transfer through the ice must have remained roughly constant.

8 Testing the rafted ice consolidation model

8.1 Introduction

In this chapter, the rafted ice consolidation model (c.f. Chapter 6) is tested against laboratory data (c.f. Chapter 7) using input parameters to conform to those used in the standard case experiment. These are; the initial thickness of the ice sheets, $H_0 = 7$ cm; the initial thickness of the liquid layer, $h_0 = 10$ mm; the salinity of the ocean, $S_{ocean} = 7.5$ ppt[1] (i.e. the initial salinity of the liquid layer). It was not possible to estimate accurately the atmospheric and oceanic heat fluxes during the experiment therefore the boundary condition at the ice-atmosphere interface (Eq. 6.9) and the Stefan condition at the ice-ocean interface (Eq. 6.13) were constrained by using the temperature measured during the experiments at the ice-atmosphere surface and the growth rate inferred from laboratory experiments respectively.

There are two major uncertainties in the consolidation model, which are due to a poor understanding of the physical processes involved in the consolidation of rafted ice sheets. Firstly, model simulations showed that the liquid layer tended to migrate downwards when there was a negative temperature gradient in the lower ice block. This meant for simulations where the thickness of the liquid layer was greater than 0.6 cm the liquid layer did not freeze. The experiments showed that (i) liquid layers up to 2 cm can easily freeze and (ii) no downward migration of the liquid layer was observed. These suggest that downward migration of the liquid layer may be a consequence of assumptions and/or boundary conditions in the model. Secondly, the mechanism through which salt is released into the liquid layer is uncertain. As I argue in the previous chapter, it is unlikely that any brine drained or was flushed out of the upper ice block during the standard case experiment. Therefore the explanation for the salinity of the liquid layer to increase is from brine being rejected/draining from the new ice growing at the base of the upper ice block and at the top of the lower ice block. But this poses two questions as to where this salt is coming from and what quantity of salt is being rejected: Is it being rejected from both growing interfaces (as

[1] This salinity (7.5 ppt) is slightly higher than the initial salinity of the water (6 ppt) from which the ice was grown due to brine drainage that took place during the initial stage growth stage of the ice (c.f. Chapter 5).

assumed in the model)? Or is it only being rejected from the top interface? In this Chapter, these uncertainties will be investigated by constraining and varying some of the physical processes in the model and comparing the results to experimental data. In section 8.2, the temperature data that are used to force the model are described. The results of tests done to investigate these uncertainties are presented in section 8.3. A discussion of the results and implications for the model are then presented in section 8.4. A summary of the chapter is given in section 8.5.

8.2 Forcing data

The consolidation model was forced using the temperatures measured at the ice-atmosphere surface during the standard case experiment and the growth rate inferred from temperature measurements in the water below the rafted section. This means that the boundary condition at the ice-atmosphere interface (Eq. 6.9) reduces to $T = T_0$. The Stefan condition at the ice-water interface (Eq. 6.13) no longer needs to be solved and the amount of ice growth at the base of the rafted section can simply be updated every time step. I also assume that in the laboratory no shortwave radiation penetrates into the ice so that the last term in equation (6.1) is neglected. Temperatures at the ice-atmosphere surface were measured every 5 minutes using a single thermistor probe placed on the top of the rafted section. In Figure 8.1, the measured ice-surface temperature is shown with a polynomial fit to the data (red line in the plot). To use these data in the model, I evaluated the polynomial over intervals of 3 seconds so that the temperature could then be updated every timestep. The amount of growth at the base of the rafted section was estimated from temperatures measurements that were measured by a 20 cm probe, positioned in the water below the rafted section (c.f. Chapter 7). The position of the ice-water interface as a function of time (Figure 7.8) was estimated by finding the time that the temperature at a given thermistor decreased below the freezing temperature. This was -0.45°C for a 7.5 ppt solution of NaCl. Knowing the position of the individual thermistors as a function of depth (there was a 2cm separation between thermistors) the amount of ice growth at the base of the lower ice block could then be estimated. By fitting a quadratic to the data, I found that ice growth did not start until ~1400 minutes after the start of the consolidation experiment. I forced the growth rate to be zero up until 1400 minutes. After this time, the amount of ice growth at the base

of the lower ice block was updated at every time step using the quadratic fit to the data shown in Figure 7.8.

In some of the model tests, the temperature of the liquid layer was also constrained to values derived from experiments so that the uncertainty in the brine release process could be ignored while other processes involved in consolidation were investigated. This means that equations (6.14) and (6.16) no longer need to be solved and the temperature of the liquid layer can simply be updated at every time step. Figure 8.2 shows the temperatures that were recorded in the liquid layer using the single thermistor probe that was sandwiched between both ice blocks. By fitting a polynomial to the data (red line in the plot) and evaluating it over intervals of 3 seconds the liquid layer temperature can then be updated at every timestep.

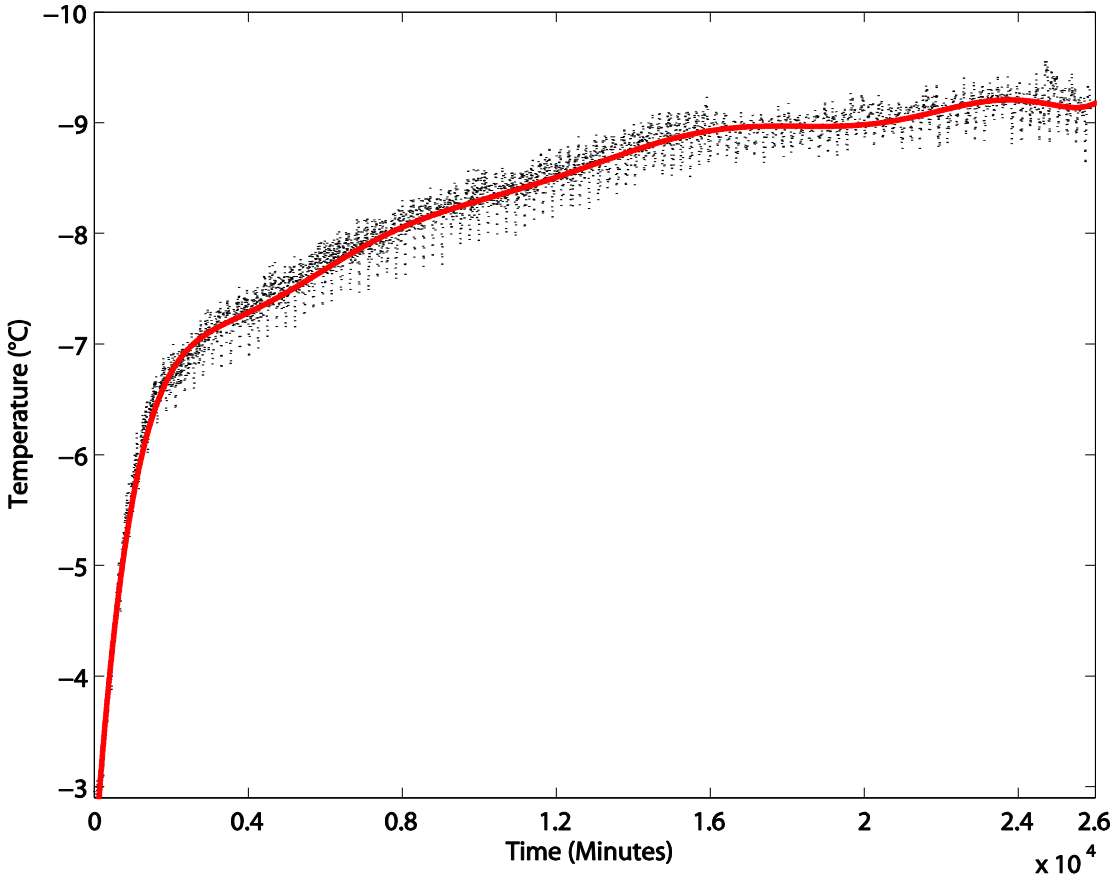

Figure 8.1. Temperature measured at the ice-atmosphere surface during the standard case rafting experiment, where the black dashed line shows the data measured by the thermistor and the red line a nine order polynomial fit to the data.

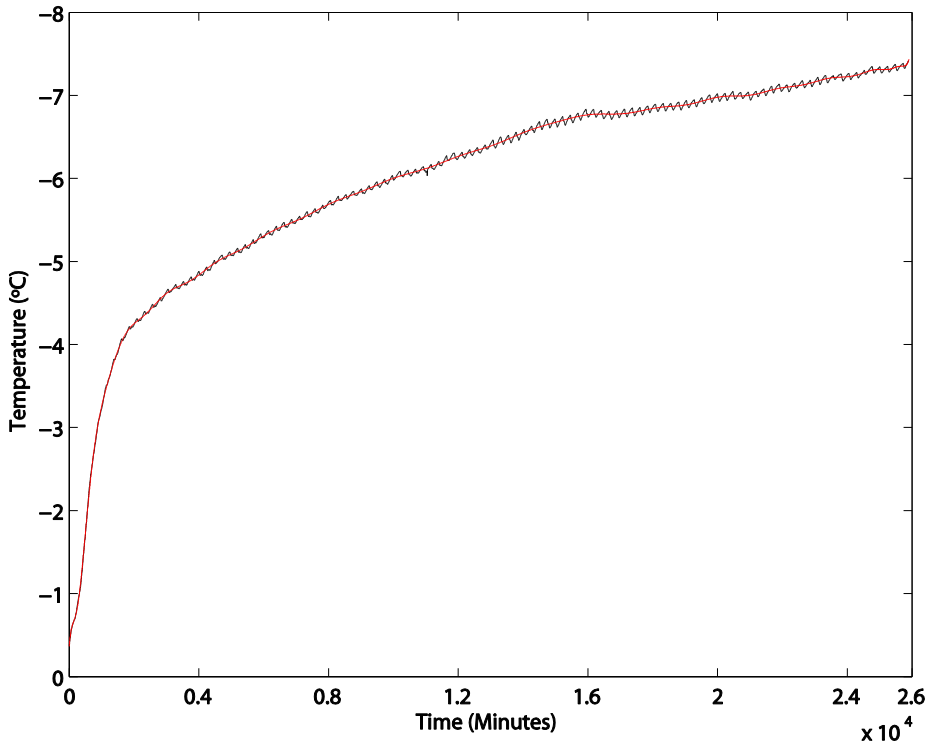

Figure 8.2. Temperature measured in the liquid layer during the standard case experiment, where the black line shows the readings recorded by the thermistor and the red line an eight order polynomial fit to the data.

8.3 Test and Results

To investigate the uncertainty in the migration of the liquid layer and the brine release process a number of model tests were done whilst varying some of the physical processes in the model. In this section, the conditions of each test and the results are presented. The results of each test are then compared to the experimental data and the implications for the model discussed.

Investigating the migration of the liquid layer

To investigate the uncertainty in the migration of the liquid layer, the model was first run allowing the liquid layer to migrate downwards. In the second test, the position of the growing interface at the top of the lower ice block was constrained so that no melting could take place thereby preventing the liquid layer from migrating downwards. In both tests the temperature of the liquid layer was forced using the values measured experimentally. This allowed the uncertainty in the brine release process to be ignored while the migration of the liquid layer was investigated.

Test 1: Allowing the liquid layer to migrate

The results of the test allowing the liquid layer to migrate showed that the ice sheets did not consolidate and that the thickness of the liquid layer started to increase after ~350 minutes (see Figure 8.3). This is because, as Figure 8.4 shows, the position of the freezing front located below the liquid layer (h_b), started to melt after ~250 minutes causing the liquid layer to migrate downwards. What causes the ice to melt is the fact that the temperature of the liquid layer, being at the liquidus temperature appropriate to its high salinity, is lower than the temperature in the lower ice sheet. This therefore promotes a negative temperature gradient in the lower ice block causing sensible heat to be extracted from the lower block and be converted into the latent heat of the liquid phase. Because the liquid layer is assumed to have a constant temperature heat cannot diffuse in the liquid layer and therefore causes melting at h_b.

Figure 8.5 shows the temperature profiles in the ice blocks for this test, where the profiles predicted by the model are shown by the solid lines and the values recorded by the thermistors in the experiment are shown by the circles. The figure shows that in the earlier part of the test, the two sets of data are in reasonable agreement. However, at later times the values predicted by the model for the lower ice block are ~0.9°C lower than those measured in the experiments. This is because in the model the top of the lower ice blocks is held at the temperature of the liquid layer and so once melting has initiated, the liquid layer migrates downwards thereby lowering the temperature in the top of the lower ice block.

The experiments show that the ice sheets do in fact consolidate and there was no evident downward migration of the liquid layer. Since the model does not replicate these conditions I believe that the migration of the liquid layer is not real and therefore should be constrained so that no melting can take place at h_b. This is now done in Test 2.

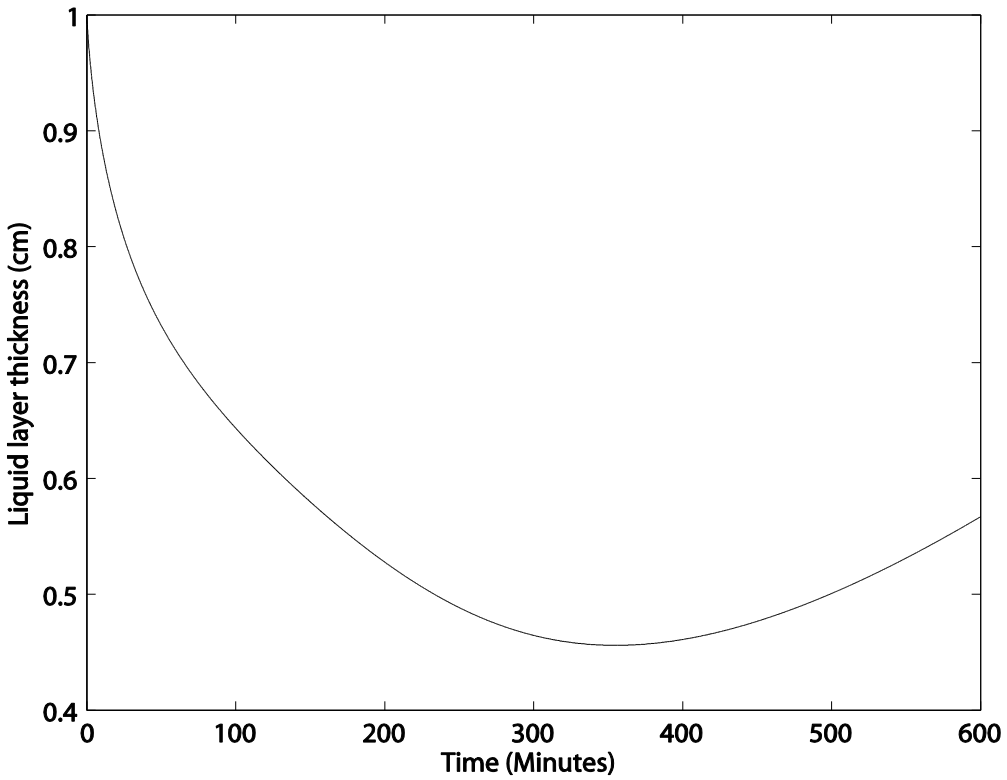

Figure 8.3. The thickness of the liquid layer as a function of time for Test 1.

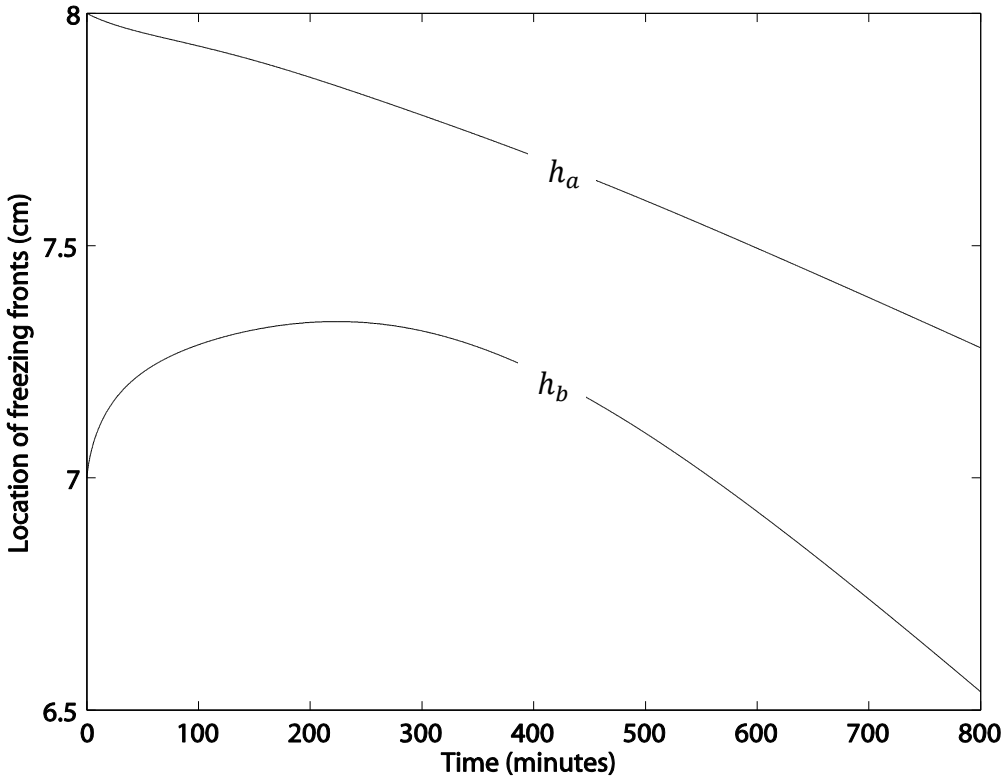

Figure 8.4. The location of the freezing interfaces above (h_a) and below (h_b) the liquid layer as a function of time for Test 1.

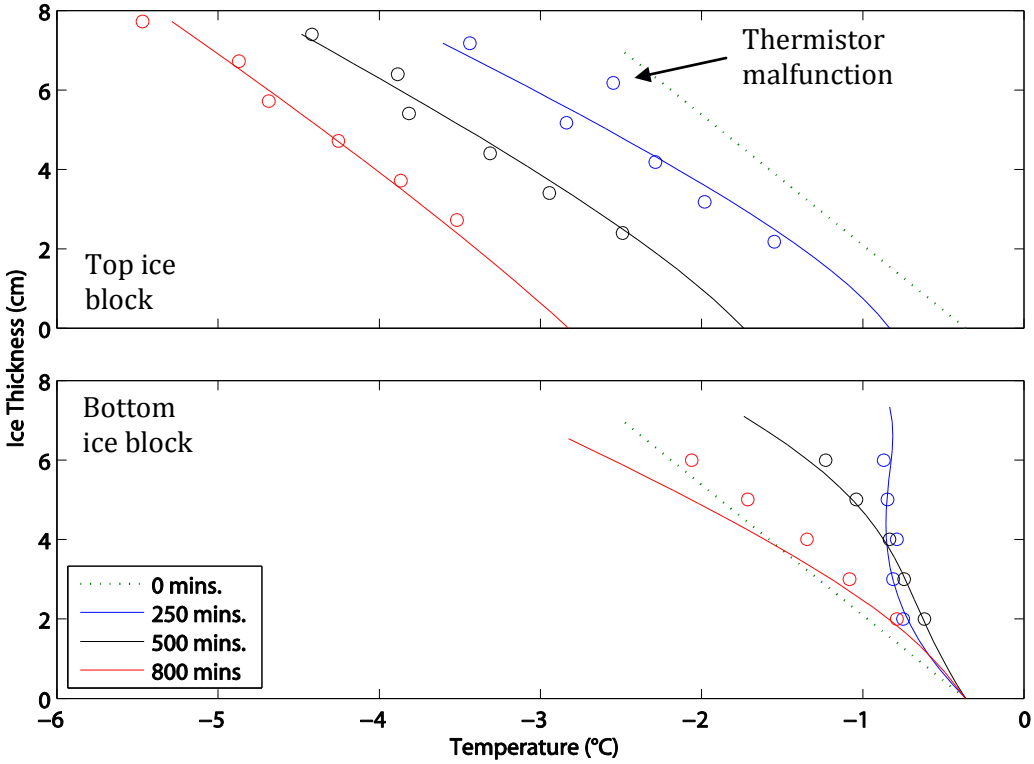

Figure 8.5. The temperature evolution in the ice blocks for Test 1. The values predicted by the model are shown by the solid lines and those recorded by the thermistors in the experiments are shown by the circles.

Test 2: No migration of the liquid layer

In this test, to prevent the liquid layer from migrating, the model was constrained so that no melting could take place at h_b. This was done by adding a line of code in the model which imposed the condition that when the growth rate of the ice sheet below the liquid layer is less than zero (i.e. $dh_b/dt < 0$), $dh_b/dt = 0$, so that that no melting can take place and h_b remains at the same position. This effect of this can be seen clearly in Figure 8.6, which shows the location of the freezing fronts for this test. The figure shows that initially ice growth is predominantly at h_b as heat was conducted from the liquid layer into the lower ice block. After ~200 minutes, ice growth ceased at h_b and the position of the interface remained constant. Ice growth then only took place at h_a and continued until the liquid layer completely froze, after 750 minutes. This is 50 minutes longer than the thermodynamic consolidation time (700 minutes) predicted by the experiments. Considering the error in the best fit line method used to determine consolidation in the experiments is at best ±50 minutes I believe that this is a good estimate by the model.

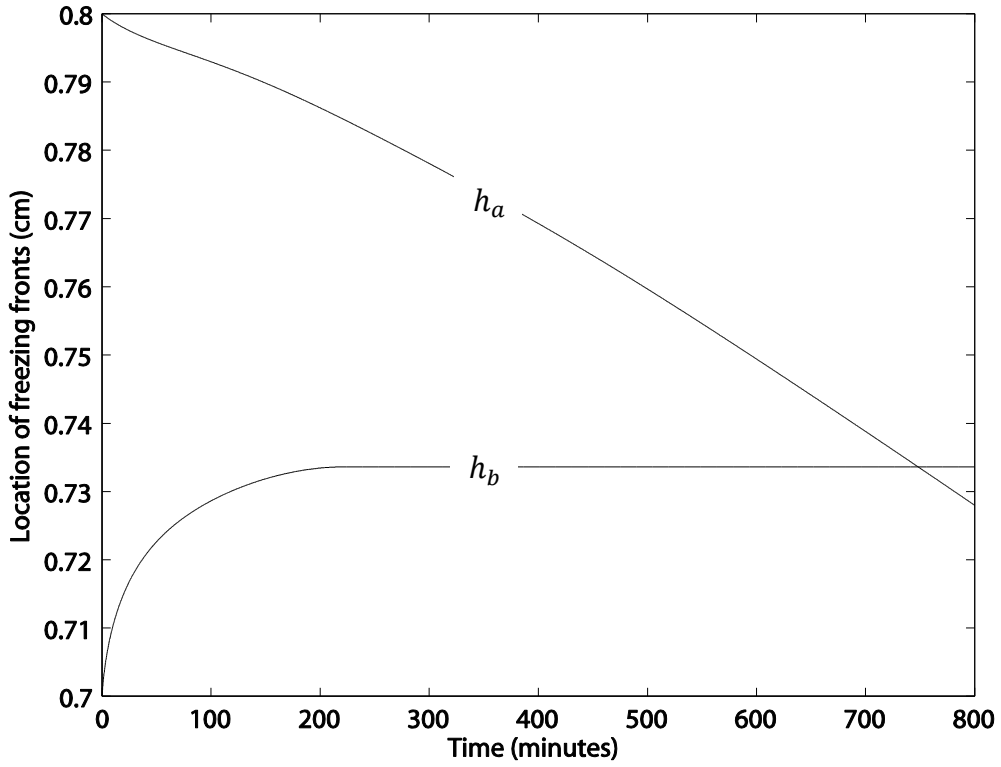

Figure 8.6. The location of the freezing interfaces above (h_a) and below (h_b) the liquid layer as a function of time for Test 2.

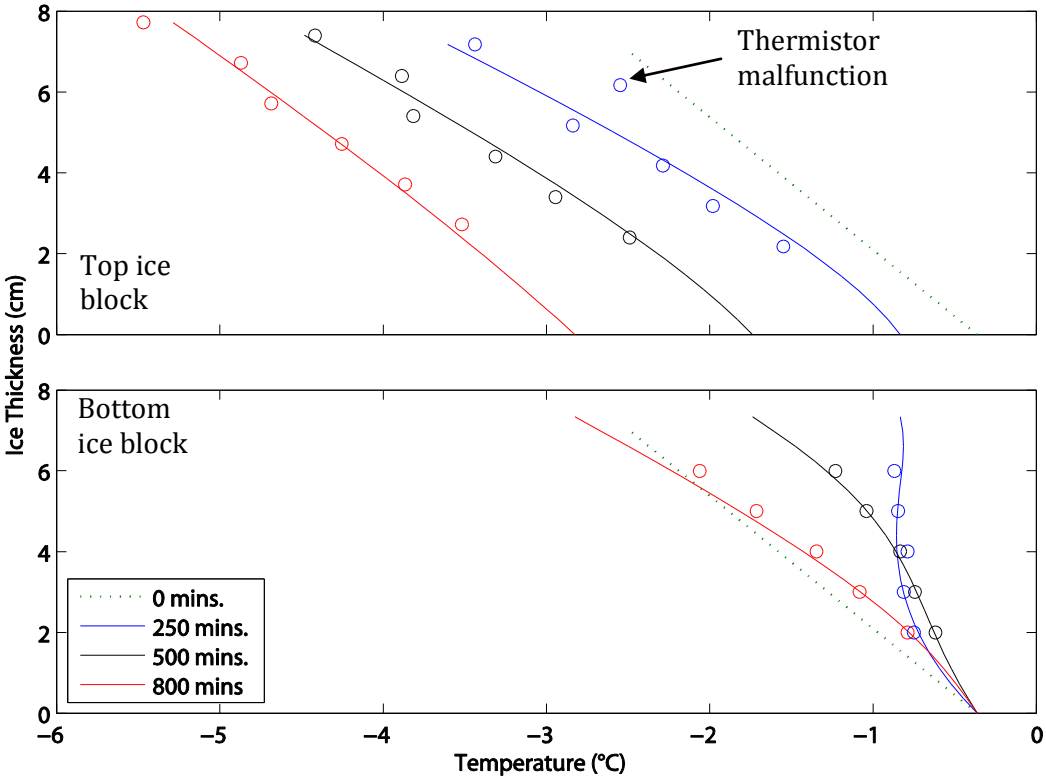

Figure 8.7. The temperature evolution in the ice blocks for Test 2. The values predicted by the model are shown by the solid lines and those recorded by the thermistors in the experiments are shown by the circles.

Figure 8.7 shows the temperature profiles predicted by the model and the values recorded by the thermistors in the experiment. The figure shows that the two sets of data are now in very good agreement. This demonstrates that the mushy layer equations accurately predict the temperature distribution in the ice. Therefore since the model is now able to predict a similar consolidation time to that found in the experiments and can accurately predict the temperature distribution in the ice, I believe that fixing the position of h_b so that no melting can take has significantly improved the model. Now that I am confident that the model predicts the rate of consolidation to a good degree of accuracy I shall investigate the uncertainty in the brine release process.

Investigating the uncertainty in the brine release process

To investigate the uncertainty in the brine release process, the model was first run only allowing the brine released from ice growing at the base of the upper ice sheet to contribute to the salinity of the liquid layer (Test 3). However, as will be shown this underestimated the rate at which the salinity of the liquid layer increased. Therefore in the subsequent test (Test 4), brine was released from both interfaces growing at the base of the upper ice sheet and at the top of the lower ice block. For comparison, I then repeated tests 2 and 4 for the 33 ppt experiment.

Test 3: Brine release only from ice growing at the base of the upper ice sheet.

In this test, brine was only released from the ice growing at the base of the upper ice sheet, so that the salinity of the liquid layer is given by (c.f. Chapter 6),

$$S_{liquid} = S_{ocean} + f\frac{\Delta h_a}{h_t}S_{ocean}, \qquad (8.1)$$

where S_{ocean} is the concentration of the tank water prior to commencing the experiment (which in this case is 7.5 ppt), Δh_a is the amount of freezing at the base of the upper ice sheet, f is the fraction of salt released and h_t is the thickness of the liquid layer at time *t*. Since I am uncertain about f during the laboratory experiments, I shall run the model for a number of different values. The selected values of 10, 30, 60 and 100 % give a wide range of outcomes.

In Figure 8.8, the positions of the freezing fronts for the different values of f are presented. The figure shows that the greater the value of f the slower the rate of freezing. This is as expected, since the more salt expelled into the liquid layer, the more heat that needs to be extracted for subsequent freezing to take place. For comparison the results from Test 2 (bold dashed line), where the temperature of the liquid layer was constrained using data measured in the experiments, are also plotted. The freezing fronts in Test 2 are advancing at slower rates than predicted by the simulations run for different values of f. This suggests that the salinity of the liquid layer in the simulations is not increasing at a quick enough rate. To investigate this I plot the liquid layer temperature predicted by the simulations along with those measured during the standard case experiment. Figure 8.9 shows that in the first 600 minutes the liquid layer temperatures predicted by the simulations are always fractionally warmer than those found in the experiments. This implies that, assuming the temperature of the liquid layer is always held at its freezing temperature, the salinity of the liquid layer is not increasing sufficiently in the simulations. Therefore in the next test I shall allow brine to be released into the liquid layer from interfaces growing both above and below the liquid layer. Note that in the temperature evolution plots, the temperatures plotted for the simulations after 600 minutes should be ignored for the time being and will be discussed later.

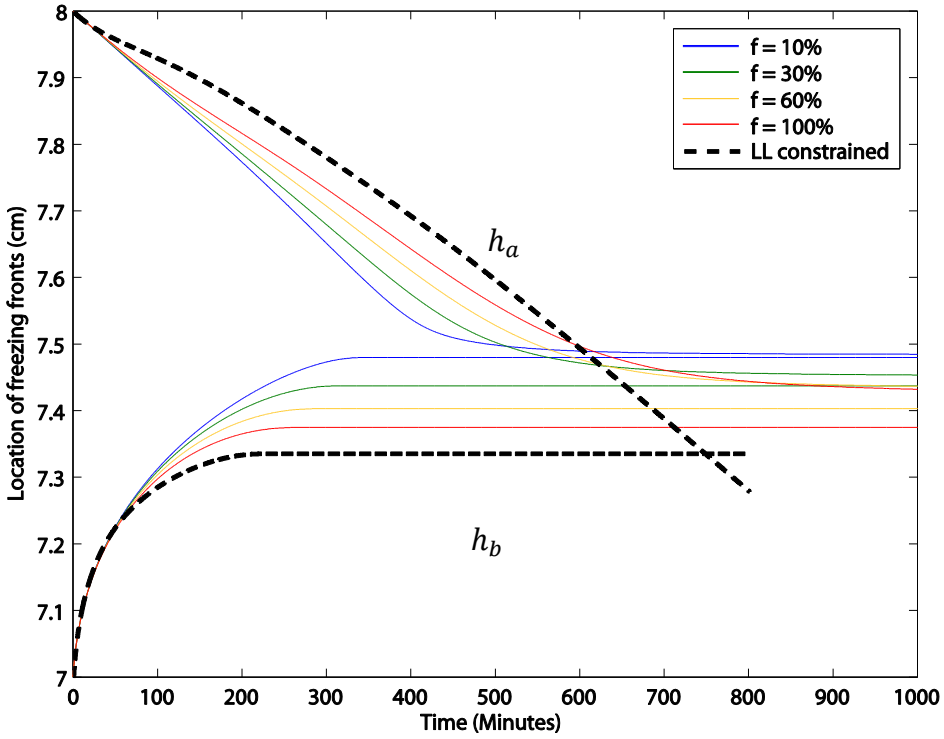

Figure 8.8. The location of the freezing interfaces above (h_a) and below (h_b) the liquid layer for Test 3, where the fraction of salt release (f) was set to 10 (blue line), 30 (green line), 60 (orange line) and 100 % (red line). Also included in this plot are the values obtained when the temperature of the liquid layer (LL) was constrained (i.e. Test 2).

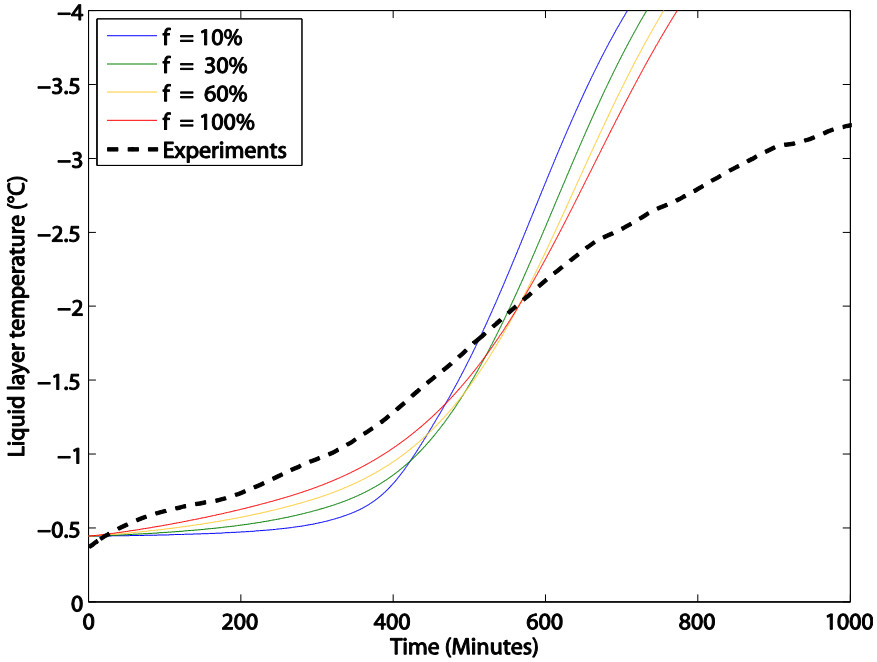

Figure 8.9.Temperature evolution in the liquid layer for Test 3 where the fraction of salt release (f) was set to 10 (blue line), 30 (green line), 60 (orange line) and 100 % (red line). Also included in this plot are the values that were measured during the standard case experiment.

Test 4: Brine release from both growing interfaces

In this test, brine was assumed to be released from interfaces growing both above and below the liquid layer, such that

$$S_{liquid} = S_{ocean} + fS_{ocean}\left(\frac{h_0}{h_t} - 1\right) \qquad (8.2)$$

where $h_0 = 10$ mm is the initial thickness of the liquid layer and f, the fraction of salt released, is now a function of the growth at both interfaces. As in the previous test the model was run for f = 10, 30, 60 and 100%.

In Figure 8.10, the positions of the freezing fronts for the respective tests are shown. The figure shows that this time the results from Test 2 are within the bounds of those predicted by the simulations. In fact, the rate of freezing at h_b in Test 2 is almost exactly the same as that found in the simulation run with $f = 60$ %. However, at h_a the growth rate found in Test 2 varies between those found in the 60 and 100% simulations. This suggests that the value of f lies in the range of 60 – 100 %.

Figure 8.11 shows the liquid layer temperatures for each value of f along with those measured during the standard case experiment. The figure shows that in the first ~200 minutes the temperatures measured during the experiments lie just above the temperatures predicted by the simulation run with $f = 60$ %. However, after this time, the temperature recorded in the experiments decreases at a marginally faster rate than predicted by all the model simulations. Perhaps this is because during the first ~200 minutes ice growth is predominately at h_b so that when brine is rejected from the growing ice it is denser than the liquid layer and therefore some of it accumulates between the advancing asperities. However, when ice growth stops at h_b and only takes place at h_a the brine being rejected is likely to convect with the liquid layer thus producing a zone of turbulent mixing. This might cause some of the brine originally trapped between the asperities to mix with the remaining liquid layer, therefore rapidly increasing the salinity and in turn reducing its temperature. This may explain why the rate of freezing in Test 2 is closer to the simulations

where $f = 60$ % in the first 200-300 minutes but at later times is nearer the simulations where $f = 100$ %. Figure 8.12 shows a schematic diagram illustrating this concept.

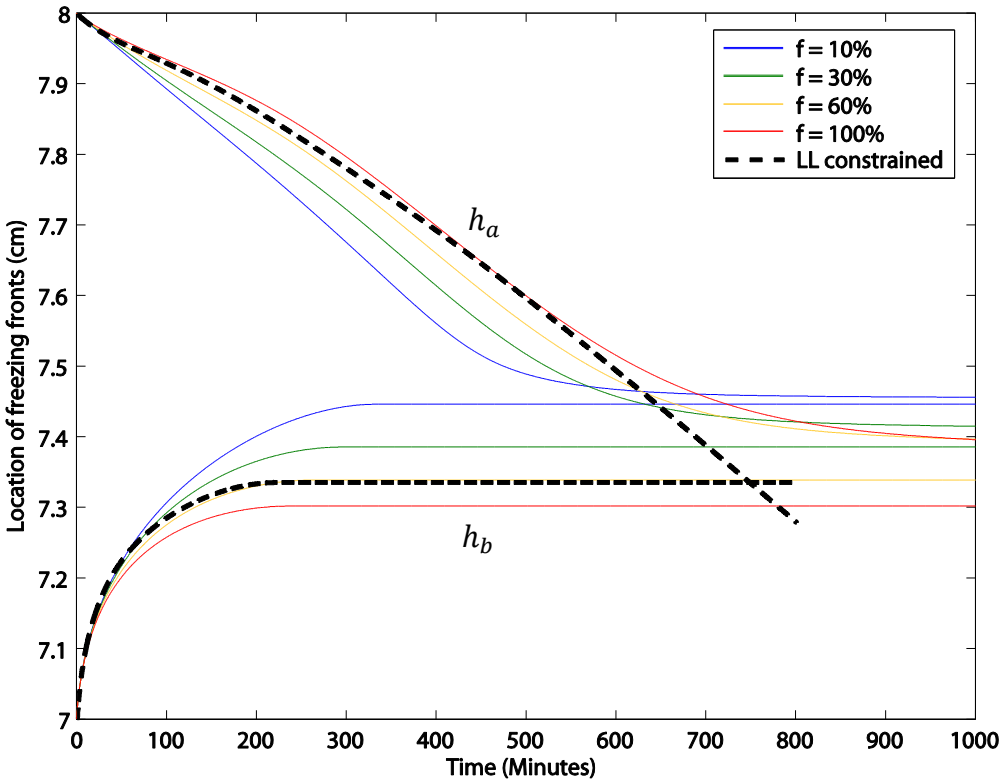

Figure 8.10. The location of the freezing interfaces above (h_a) and below (h_b) the liquid layer for Test 4, where simulations where the fraction of salt release (f) was set to 10 (blue line), 30 (green line), 60 (orange line) and 100 % (red line). Also included in this plot are the values obtained when the temperature of the liquid layer (LL) was constrained (i.e. Test 2).

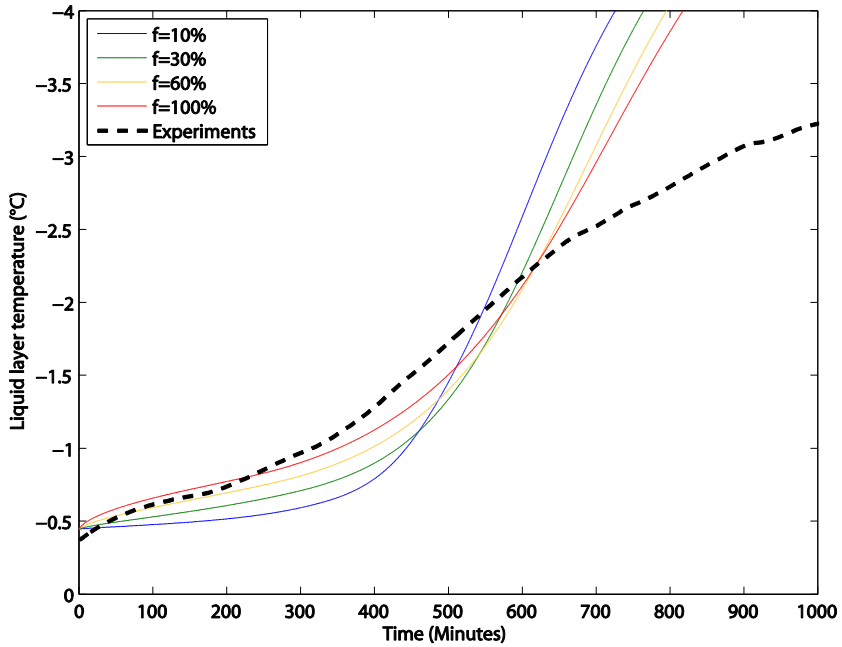

Figure 8.11. Temperature evolution in the liquid layer for test 4 where the fraction of salt release (f) was set to 10 (blue line), 30 (green line), 60 (orange line) and 100 % (red line). Included in this plot are the values that were measured during the standard case experiment.

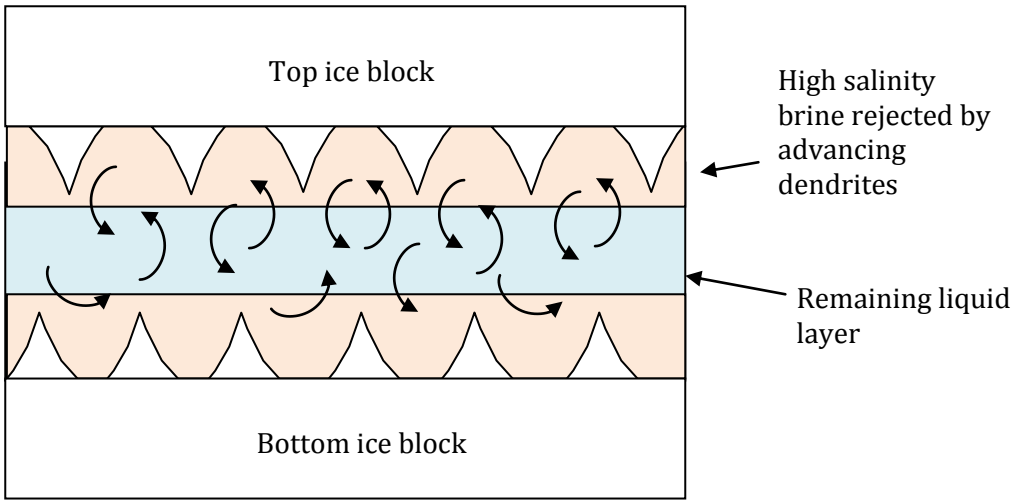

Figure 8.12. Schematic of the brine distribution in the liquid layer.

From Figure 8.10, it is evident that in the simulations the liquid layer will never completely freeze over (unless it reaches the Eutectic temperature). This is because as long as a fraction of salt is released into the liquid layer there will always be a liquid layer remaining even if it is infinitely thin. I therefore imposed a 'cut-off' in the program (c.f. Chapter 6) such that when the liquid layer reaches the size of the surface asperities (h_{sa}) (i.e. the surface roughness) the adjacent ice sheets can be considered consolidated. From conservation of salt h_{sa} can be estimated from

$$h_{sa} = \frac{h_0}{\frac{S_t - S_{ocean}}{f S_{ocean}} + 1}, \tag{8.3}$$

where S_t is the concentration of the liquid layer immediately prior to thermodynamic consolidation (which in this case is 42 ppt). A plot of h_{sa} versus f is shown in Figure 8.13. The plot shows that the surface asperity height lies in the range 0 to 1.79 mm.

The simulations run with f =10, 30, 60 and 100 %, correspond respectively to surface asperity heights of 0.21, 0.6, 1.15 and 1.79 mm. Employing these cut-offs reveal that the liquid layer consolidated at 599, 634, 649 and 653 minutes respectively. These are all within 100 minutes of the consolidation time found in the experiments. Therefore it seems no matter what value of f is chosen, a rough estimate of the consolidation time can be obtained. This is because f and h_{sa} are linked via the conservation of salt (Eq. 8.3) so the

greater the value of f the greater the cut-off thickness. The results of these simulations showed that it is likely that the value of f lies in the range of 60 – 100 %, which correspond to a consolidation time of 650 minutes. This is in good agreement with the thermodynamic consolidation time predicted in the laboratory experiments. I am therefore confident that employing the salt rejection factor can, at least in the lower salinity experiments, predict the rate of salt release to a reasonable degree of accuracy.

It is evident from Figure 8.11, that if the model run is continued beyond the cut-off point, the temperature of the liquid layer continues to decrease at a much greater rate than that observed in the experiment. This is because after thermodynamic consolidation the freezing interfaces have bonded sufficiently such that no continuous liquid layer remains, and rather there exists a series of brine pockets. Under these conditions the brine is confined to the pockets and no longer contributes to the salinity of the liquid layer. The fact that the model does not take account of this explains why an artificial cooling of the liquid layer is seen in the simulations. For this reason the model, as it stands, cannot predict the rate of mechanical consolidation.

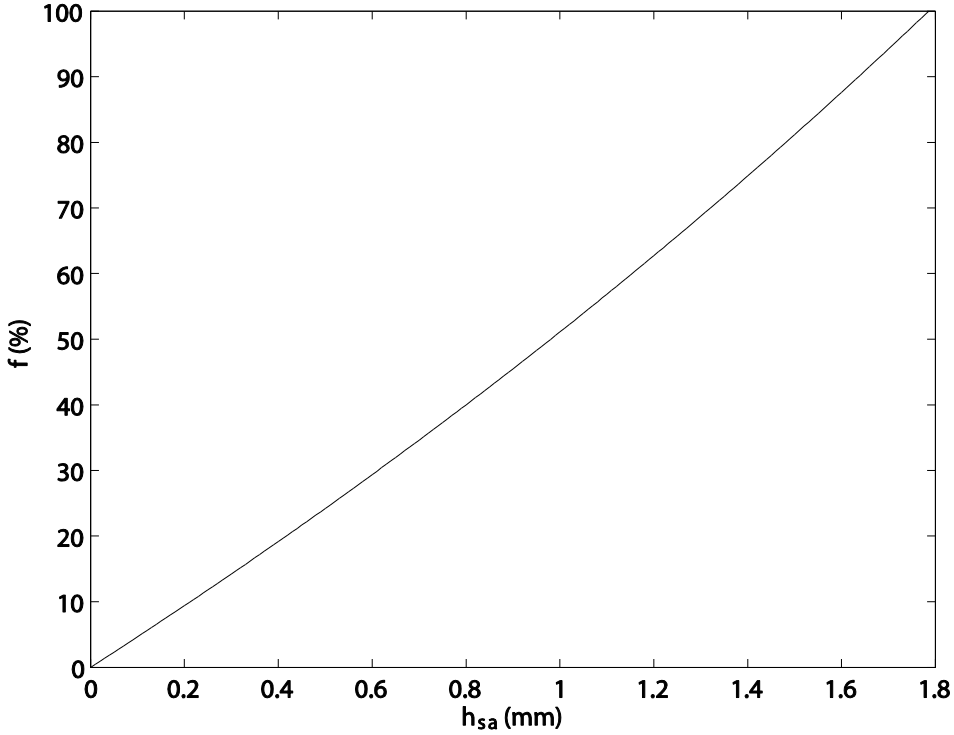

Figure 8.13. Dependence of the fraction of salt released (f) into the liquid layer on the surface asperity height (h_{sa}).

Test 5: Does this work for the 33 ppt case?

In this test, the model was run using forcing data collected from the 33 ppt laboratory experiment. As in the 6 ppt case, the model was first run constraining the temperature in the liquid layer using temperatures recorded during the experiment. The model was then run assuming salt is released from interfaces growing both above and below the liquid layer for the same values of f.

In Figure 8.14, the positions of the freezing fronts for the respective tests are shown. The figure shows that in the simulation run with the temperature of the liquid layer constrained, the model predicts a freezing time of 1150 minutes. This is approximately 150 minutes later than the consolidation times found in the experiments. The simulation data with $f =$ 10-20% are consistent with the constrained case. This is quite different from the 6 ppt case. Perhaps coincidentally, however, the absolute quantity of salt being released is of similar magnitude in each case (15% of 37 ppt = 5.5, while 80% of 7.5 ppt = 6).

Figure 8.15 shows the temperature evolution of the liquid layer for the simulations and the 33 ppt laboratory experiment. It is evident that the temperatures recorded in the experiment are in very good agreement with the simulation run with $f =$ 10%, up until around 700 minutes. After this time the simulations continue to deviate from the experimental data in much the same way as in the 6 ppt case. According to Eq. (8.3), with $S_t =$ 53 ppt and $S_{ocean} =$ 37 ppt, taking $f =$ 10% yields a value of h_{sa} = 1.9mm, which corresponds to a cut-off time of 860 minutes. This is some 150 minutes sooner than was found in the experiments.

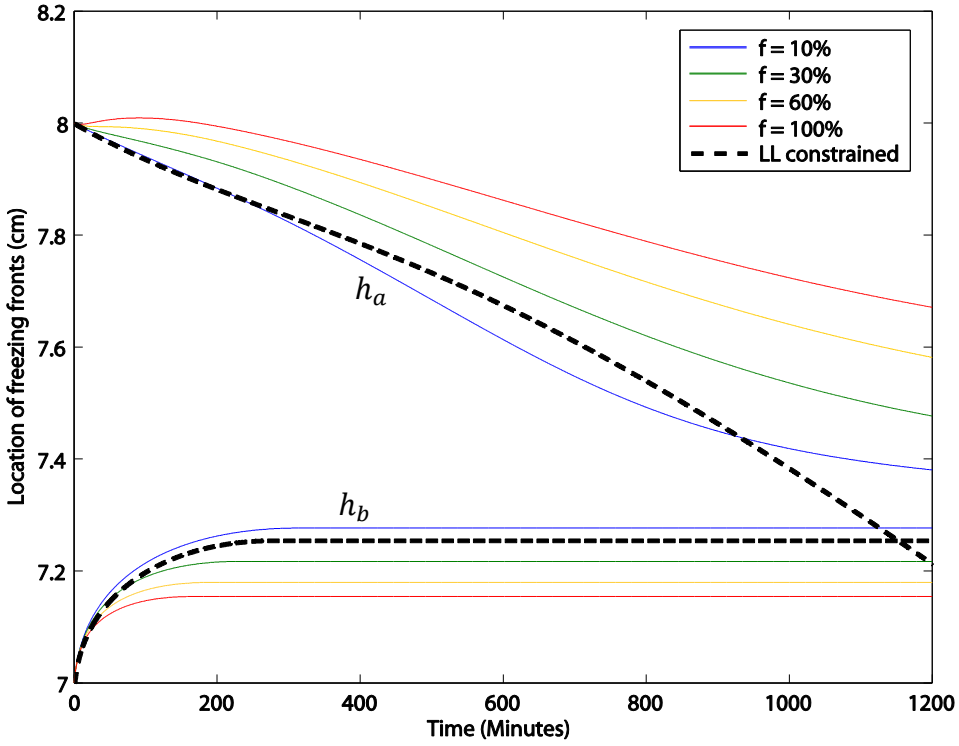

Figure 8.14. The location of the freezing interfaces above (h_a) and below (h_b) the liquid layer for Test 5, where simulations where the fraction of salt release (f) was set to 10 (blue line), 30 (green line), 60 (orange line) and 100 % (red line). Also included in this plot are the values obtained when the temperature of the liquid layer (LL) was constrained.

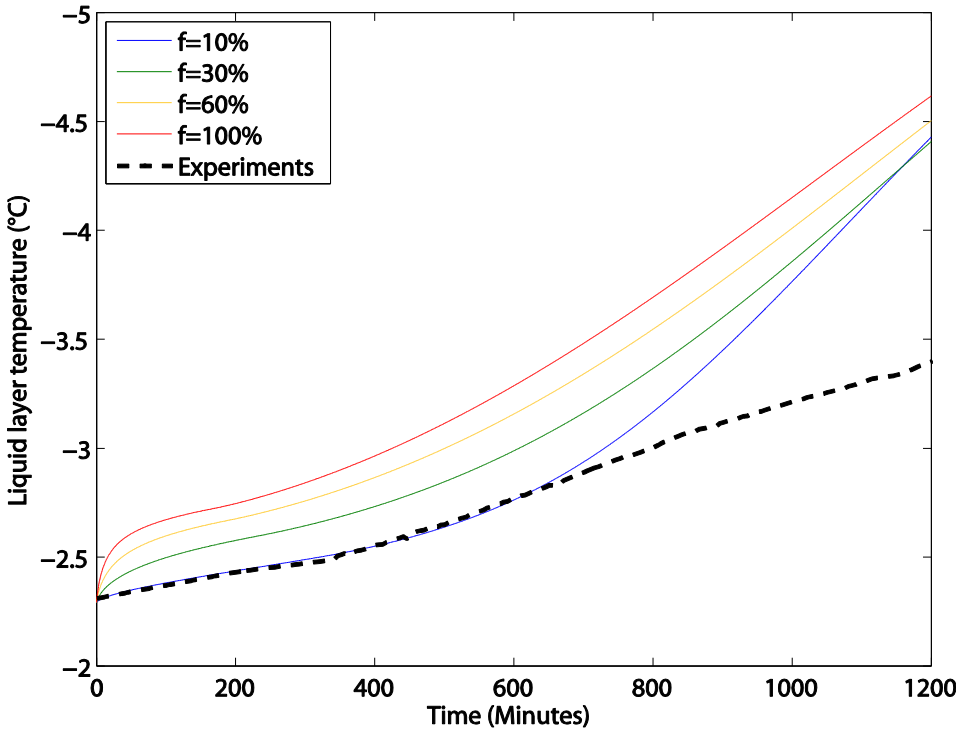

Figure 8.15. Temperature evolution in the liquid layer for Test 5 where the fraction of salt release (f) was set to 10 (blue line), 30 (green line), 60 (orange line) and 100 % (red line). Also included in this plot are the values that were measured during the 33 ppt experiment.

8.4 Discussion

Model simulations showed that the liquid layer tended to migrate downwards when there was a negative temperature gradient in the lower ice block. This is caused by the assumption that the liquid layer has a spatially uniform temperature and salinity, which only holds if the liquid layer is sufficiently narrow that diffusion homogenises the salt distribution within the layer. This is satisfied provided $(h/H)^2 \ll Le$, where h is the gap thickness, H is the thickness of the ice sheets and Le the Lewis number ~ 10^{-2} (c.f. Chapter 6). In the laboratory experiments the gap thickness was 1 cm and the ice sheets were 7 cm thick, resulting in $(h/H)^2 \simeq 0.02$. This implies that the salt may not be evenly distributed across the liquid layer. In order to compensate for this, the model was constrained so that no melting can take place at the top of the lower ice block, thereby preventing the liquid layer from migrating downwards. It is likely that this is only valid up to a certain gap thickness, beyond which the temperature and salinity distributions in the liquid layer need to be fully modelled. This is not trivial because the boundary conditions for salinity and temperature need to be solved simultaneously, in combination with the liquidus constraint at the interface.

In the model the increasing salinity of the liquid layer was accounted for using a salt rejection factor f. This simplistic approach produced reasonable results, but to describe accurately the evolution of the liquid layer it would be necessary to properly model the brine drainage into the liquid layer, which is beyond the scope of this work.

For both salinities (6 and 33 ppt), in the simulations where the liquid layer temperature was constrained, the consolidation time predicted was longer than found in the experiments, whereas when the fraction of salt release was estimated, it was systematically lower. For the latter case this is driven by the assumption that the liquid layer is held its freezing temperature, while in reality there could well be a time delay before it reaches freezing temperature. This would also explain why the discrepancy in the 33 ppt case is greater, because the more concentrated the solution; a) the higher the specific heat capacity and b) the lower the freezing temperature. This means that more heat needs to be extracted in order to cool the liquid layer down to its freezing temperature. This effect could also be accounted for by modelling the temperature and salinity distribution in the liquid layer.

8.5 Summary

In this chapter, the model was tested against the experiments described in Chapter 7. Results showed that the liquid layer migration is an artefact of the model imposed by assuming a constant salinity across the liquid layer. This was accounted for by constraining the model so that no melting occurred at the top of the lower ice block. By doing this, I was able to find thermodynamic consolidation times that were consistent to within 15% of the experimental data. To investigate the fraction f of salt that is released into the liquid layer, the model was run for a range of values of f. The results showed that in the 6 ppt case, the simulations with f between 60 and 100% gave results similar to the experimental data, while in the 33 ppt case f was found to lie between 10 and 20%. The model could be improved by accounting for temperature and salinity distributions in the liquid layer and brine drainage into the liquid layer.

9 Strength of the bond between two rafted ice blocks

9.1 Introduction

A key question for engineering safe structures in ice infested waters is the load rafted sea ice could exert and how it would deform. In a rafted section, the layers of sea ice are initially separated by thin layers of water. The bonds between the layers are at first weak but strengthen with time to produce a coherent ice sheet. At present most design loads assume that the strength of rafted ice is 10-20% less than that of level ice of the same thickness (Jizu et al., 1991). This is because it is believed that the bonds between layers in a rafted section may be weaker than solid ice. However, there is very little experimental data to back this theory.

In Chapter 7, I found that in all the tests the rafted ice had physically bonded in under a day. However the strength of the bond at this time was still very weak. When the ice was left to consolidate for greater time periods the strength of the bond gradually increased. In this chapter, I describe my investigation of the strength of the bond between two rafted ice sheets by shearing cores under increasing states of consolidation. The results are then compared with salinity and temperature data that were recorded during consolidation to establish if there is a relation between the two. I then present the results from shear tests that were done after every consolidation experiment (of Chapter 7) to establish the effects changes in the ice thickness, gap thickness and solution salinity have on the shear strength of the bond. The experimental method is described in section 9.2. The results of the shear experiments are presented in section 9.3. A discussion of the results is presented in section 9.4 and a summary of the chapter in presented in section 9.5.

9.2 Experimental method

To investigate the strength of the bond between two rafted ice sheets the standard case[2] experiment was repeated eight times with varying consolidation times. When the experiment had reached the specified time, cores were taken perpendicular to the ice surface

[2] For the standard case, ice was grown from a 6 ppt solution of NaCl and water to a thickness of 7cm and assembled so that there was a gap of 1cm between the rafted ice sheets (c.f. Chapter 7).

using a 9 cm corer. A total of three cores could be taken for each experiment: two were sheared in the asymmetric four-point bending rig (AFPB) and one cut into 1-2 cm sections in order to measure the salinity variation with depth. In some of the earlier tests only one core was sheared because the position of the thermistors probes obstructed coring.

During each test, temperature was recorded every 5 minutes in the ice blocks and the liquid layer. Temperature was measured in the ice blocks using 5 cm probes positioned such that the top thermistor in the probe was approximately 1 cm below the ice surface. In the liquid layer the temperature was recorded using a single thermistor positioned approximately midway between the two blocks. The salinity of the liquid layer was measured by taking samples using a hypodermic needle and syringe and measuring the salinity using a MISCO digital refractometer.

To shear the rafted ice the bottom end of the core was shortened so that the lower ice block in the rafted section was the same thickness as the upper ice block. Samples were tested directly after cutting to be able to determine the strength in a state as close to in situ as possible. The sample was then loaded between the two plates of the AFPB rig and positioned so that the liquid layer was between the inner loading bars (see Figure 9.1). The outer and inner loading bars were positioned at 5 cm and 0.5 cm, respectively, from the centre line (i.e. $\alpha = 0.1$). This configuration was chosen for the standard case rafted ice thickness (7 cm). However, I also kept these positions for the thicker rafted ice sheets so that I could make direct comparisons between the different ice thicknesses. Load was applied to the upper plate by a 200kN closed-loop servo-hydraulic universal testing machine, fitted with a temperature-controlled environmental chamber. During all tests, the environmental chamber was held at a nominal temperature of -10±1°C and the actuator displacement rate was set to 30 mm min^{-1}. Displacement, time and load were monitored in real time and logged using a National Instruments data acquisition card and LabView software. Figure 9.1 shows a before and after photograph of a rafted ice sample loaded in the AFPB rig.

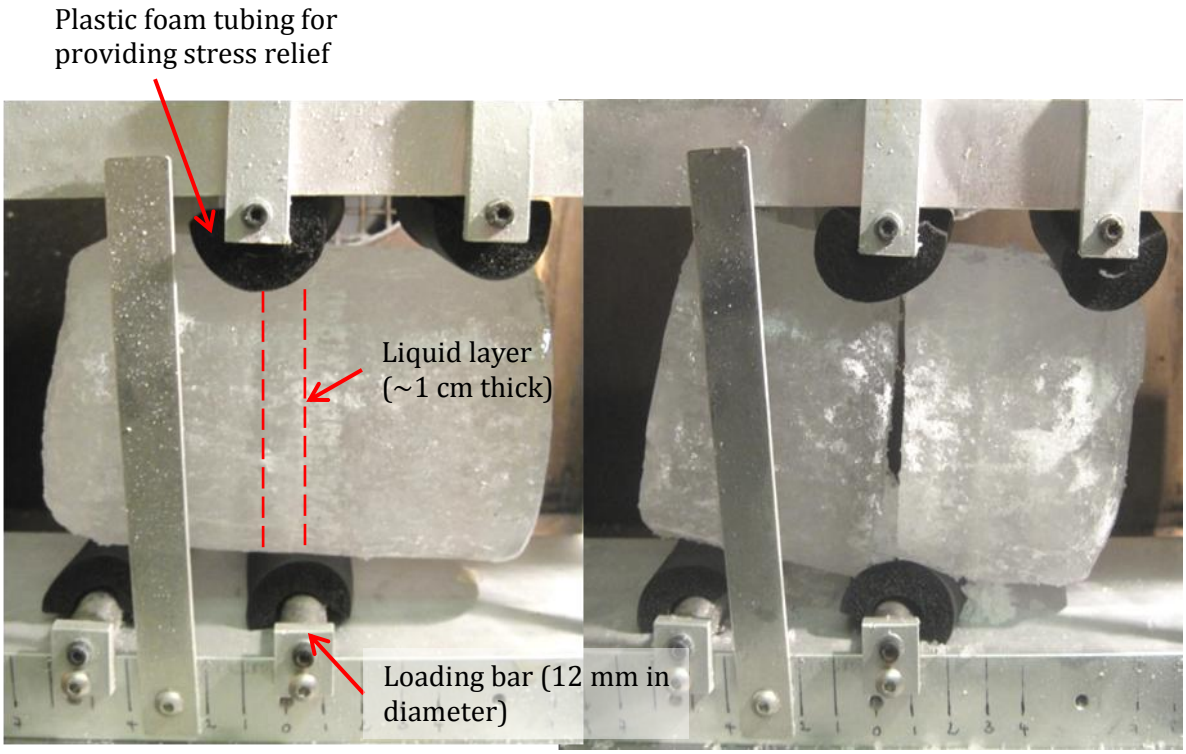

Figure 9.1. Photograph of a rafted ice sample loaded in the asymmetric four-point bending rig before (a) and after (b) the experiment. The position of the liquid layer is accentuated by the dashed red lines. The inner and outer loading pins are positioned 0.5 cm and 5 cm, respectively from the centre line. Notice that fracture plane extended between the two inner loading bars.

9.3 Results

Shear tests under increasing states of consolidation

In Table 9.1, the results of the shear tests are presented along with the bulk salinity of the sheared cores. The results show that in general the shear strength tended to increase with consolidation time (consolidation time is measured from when the ice blocks were assembled). This can be seen clearly in Figure 9.2, where the results are plotted as a function of time. There are two exceptions to this trend which are experiments no. 2 and 4 (shown in red) that have much greater strengths than expected. This is because, as Table 9.1 shows, the initial salinity of the solution from which the ice was grown was ~0.5ppt lower than in the other experiments. This reduced the initial salinity of the ice blocks and the liquid layer making them freeze faster and thus increase the bond strength. I have left these in the plot as I think it is interesting to note how a small change in the initial salinity of the

solution can change the strength by such a large amount. The results also show that when two cores were sheared in an experiment the strength of the second core was always fractionally higher than the first core. This is because, as mentioned in Chapter 5, once one core has been taken from the rafted section a void is left in the remaining ice thereby exposing it to the cool air of the cold room. This reduced the temperature of the remaining ice thereby making it stronger. Although the temperature of the cores was not measured after coring we know from chapter 5 that the second core tended to be ~1°C colder than the first.

In Figure 9.2 there are two different regimes present. Up to 15000 minutes, the shear strength of the bond increased linearly, while after this time the shear strength appears to stabilize at around 400 kPa. This corresponds to the time that the salinity of the liquid layer became constant (see Figure 7.5). This is no coincidence, since when the salinity stops changing the temperature of the liquid layer has essentially stabilised to that of the cold room. If the cold room temperature was further cooled, it is likely that the shear strength would increase. This is apparent in the data where the second cores, which were around 1°C colder, exhibit higher strengths.

Table 9.1. Results of the shear tests done under increasing degrees of consolidation.

Test no.	Time core was taken (Minutes)	Shear strength (kPa)	Bulk salinity of sheared core (ppt)	Initial water salinity (ppt)
1	1606	85±5	1.2	6
2	2826	216±12	1	5.5
3	2955	29±3	1.9	6.2
4	5802	470±26	1	5.6
5	8632	175±10[a] 242±14[b]	1.8	6
6	14325	300±17[a] 432±24[b]	1.7	6.2
7	25960	397±22[a] 506±28[b]	2.2	6.1
8	34440	365±20[a] 404±23[b]	1.6	6.3

'a' is the first of the two cores that was taken and sheared and 'b' is the second

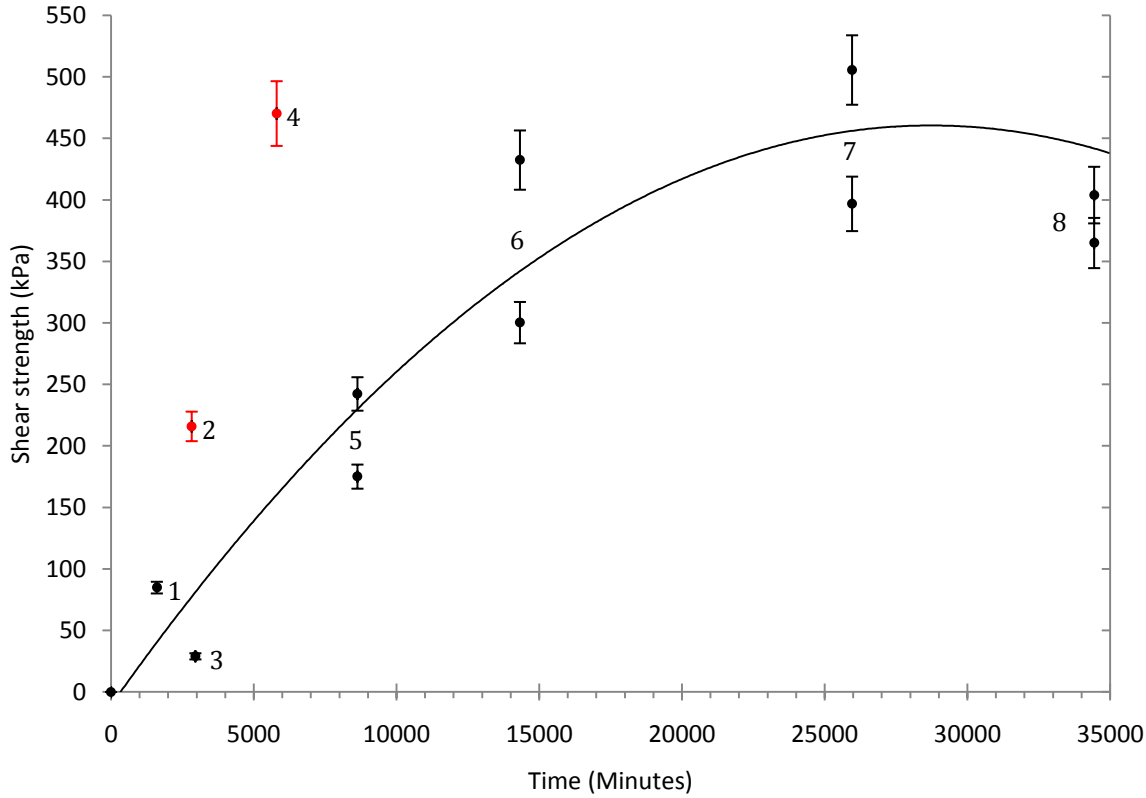

Figure 9.2. The strength of the bond between two rafted ice sheets as a function of time with a quadratic fit through the values found in tests 1, 3, 5, 6, 7 and 8. Time zero is when the blocks were assembled.

Shear tests on mechanically consolidated ice

In Table 9.2, the results of all the shear tests that were done after every consolidation experiment in Chapter 7 are presented. In two of the tests, the inner loading bars significantly indented into the ice. This caused indentation stresses to be created, which are not accounted for in calculation of shear strength, causing the measured loads to be artificially higher. This effect was particularly noticeable for the 33 ppt case.

The results show that the average shear strength of the ice grown from the 6 ppt solution was 417 kPa. Variations in the thickness of the ice blocks did not have any effect on the shear strength. This is as expected because the loading conditions on the consolidated liquid layer do not change and once mechanically consolidated, the salinity and temperature of the liquid layer should be similar for the different ice thicknesses. There was, however, a noticeable difference in the measured strength of the 0.5 cm gap, where it was some 50 to 100 kPa less than average. This is probably connected to the position of the loading pins

with respect to the liquid layer. In the 1 and 2 cm cases the inner loading pins are either on the boundaries of or within the liquid layer. In the 0.5 cm case they are positioned outside the liquid layer, which means that some of the load is applied to the columnar ice in the upper ice block. This could induce a strain jump at the interface between the columnar ice and the granular ice in the liquid layer causing the sample to fail prematurely, in much the same way that composite beams can delaminate (Patnaik and Hopkins, 2004). For this reason, the 0.5 cm case is not included in the average quoted above.

The average shear strength of the rafted ice in the 33 ppt case was 285 kPa, although this value may be high due to the indentation of the pins on the second core. Albeit, the shear strength is significantly lower than the average of the 6 ppt experiments, as expected due to the higher salinity and porosity of the ice.

It is worth noting that in most of the tests the actual failure plane tended to shear along the interface between the liquid layer and the lower ice block. This is probably because the top of the ice block was always smooth and flat, which meant that there was very little interlocking contact between the two surfaces, giving rise to a weak plane. In contrast, due to the platelet structure of the columnar crystals at the base of the upper ice block the liquid layer formed a strong interlocking bond as can be seen clearly in the thin section shown in Figure 7.16. This may not be the case in nature as the ice surface is likely to be uneven.

Table 9.2. Results of the shear tests that were done after every test in Chapter 7.

Test no.	Initial salinity of solution (ppt)	Ice thickness (cm)	Gap thickness (cm)	Shear strength (kPa)	Ice temperature (°C)	Ice Salinity (ppt)	Density (Mg m^{-3})	Porosity (%)
1	6	7	1	397±22 [a]	-4.2	2.2	-	-
				506±28 [b]	-5.3	2.2	-	-
3	33	7	1	224±12 [a]	-5.5	6.2	0.905	8.36
				346±19 [b,c]	-5.9	8.8	0.925	8.91
4	6	10	1	324±18 [a]	-4.5	2.3	0.917	3.2
				405±23 [b]	-5.4	2.4	0.914	3.2
5	6	14	1	396±22 [a]	-4.9	2.9	0.910	4.57
				439±25 [b]	-5.7	3.2	0.912	4.19
6	6	7	0.5	355±20 [a]	-4.8	1.5	0.912	2.63
				383±21 [b]	-5.2	1.6	0.910	2.81
7	6	7	2	379±21 [a]	-4.7	1.9	0.920	2.33
				490±27 [b,c]	-4.9	2	0.918	2.54

[a] First core that was taken and sheared
[b] Second core that was taken and sheared
[c] Significant indentation of the specimen at the location of the inner loading bars

9.4 Discussion

The average shear strength of the bond between rafted ice blocks in the 6 ppt experiments was 417 kPa, which is some 30% weaker than the average value found for level ice in Chapter 5 (612 kPa). At first sight this appears to contradict the findings of Poplin and Wang (1994) who found that the horizontal compressive strength of rafted ice was in some cases greater than level ice. However it should be noted that in their tests the blocks on either side of the liquid layer would support the applied load, so that in essence the strength of the liquid layer is not being examined. While these results are valid in conditions where the ice is loaded uniformly on a vertical structure, the outcome would be different if the ice encountered a sloping structure. For example if the lower sheet would come into contact with the structure before the upper sheet, the strength of the liquid layer itself becomes important. The implication of this is that in a region where rafted ice is predominant, it would be advisable to build conical or similar structures.

In the 33 ppt case it was not possible to compare the rafted ice and level ice shear strengths as the level ice samples would not fail in shear under the same loading conditions. The values obtained in the 33 ppt rafted ice tests were however noticeably lower than those for the 6 ppt case. This would imply that rafted ice in the Polar Regions is weaker than in the north Caspian Sea under similar atmospheric conditions. However, the considerably colder temperatures of the Arctic and Antarctic are likely to strengthen the liquid layer. Further experiments would need to be performed under varying temperatures to investigate this.

The absolute strengths measured in the laboratory experiments cannot be used directly in calculations of ice loads on offshore structures. This is because ice contains natural flaws so that the larger the sample, the larger the number of natural flaws. This leads to large scale ice strengths being lower than those measured on small samples. Nevertheless, the results may serve as a strength index between level and rafted ice which could be applied to large scale data.

9.5 Summary

In this chapter, a series of experiments were described that investigated the strength of the bond between two rafted ice blocks. This was done by performing shear tests under increasing states of consolidation. Results showed that the strength of the bond between two rafted ice sheets increased with time. This suggests that when thermodynamically consolidated, the liquid layer still had a high liquid fraction, which gradually decreased as the temperature of the liquid layer cooled with time. For the standard case the strength of the liquid layer stabilized after ~ 12 days (17500 minutes). Variations in the thickness of the ice blocks and the gap between them appeared to have little effect on the strength of the liquid layer. On the other hand, the salinity of the solution used in the experiment clearly had an impact. The maximum shear strength attained in the 6 ppt experiments was 30% less than that of level ice. This result may help in estimating the contribution that rafted ice makes to loads on offshore structures.

10 Conclusions and recommendations

Conclusions

The research presented in this thesis was motivated by the prevalence of rafted sea ice in the Caspian Sea, where massive reserves of oil and gas have been discovered. The sea ice conditions in the region are unique due the low salinity of the water, which causes seasonal sea ice to form quickly at the onset of winter. The newly formed ice is readily moved by strong winds, causing the ice sheets to raft multiple times, producing thick sea ice features. The strength of the rafted sea ice varies considerably depending on the degree of consolidation. Hence understanding the consolidation process is of importance in assessing the risk to offshore structures.

A thermodynamic model of sea ice has been developed, using the mushy layer equations and the Stefan condition to predict the rate of ice growth in a variety of environments. When applied to conditions prevalent in the Arctic and Antarctic, the model was found to predict growth rates similar to those observed in the field. Growth rates and temperature distributions simulated by the model are also in good agreement with laboratory data recorded during the growth of saline ice. With these verifications established, this thermodynamic model was developed into a consolidation model for rafted sea ice.

The rafted ice consolidation model calculates the time taken for the layers of ice in a rafted section to bond effectively into a coherent ice sheet. The rafted ice is assumed to be composed of layers of sea ice of equal thickness, separated by thin layers of ocean water. Model simulations showed that the consolidation process is sensitive to changes in the initial thickness of the liquid layer h_0, the ice thickness, the salinity of the ocean, the fraction of salt release during freezing f, the surface asperity height h_{sa} and the downward radiative fluxes. Most of these parameters can be quite well constrained because they have been widely researched, however h_0, f and h_{sa} are not well known. Therefore laboratory experiments were conducted to investigate further these parameters.

Results from laboratory and larger scale ice tank experiments showed that the salinity of the liquid layer increased over the course of the experiment. As the liquid layer freezes, increasing amounts of salt are released into the remaining liquid layer. This in turn causes a reduction in the temperature of the liquid layer as it cools to its freezing temperature. The salinities obtained by inverting the temperature using the non-linear liquidus curve are in good agreement with the direct salinity measurements, demonstrating that the assumption made in the model that the liquid layer is held at its freezing temperature is reasonable. The temperature in the liquid layer decreased at first rapidly and continued until the rafted ice was physically bonded. At this point the bond was still physically weak because the consolidated liquid layer had a high liquid fraction. The strength of the bond then gradually increased as the temperature and the liquid fraction decreased. I therefore referred to two stages of consolidation: 'thermodynamic' and 'mechanical'. Thermodynamic consolidation referred to the time that sheets have physically bonded, which I took to be the time that the temperature in the liquid layer changes from a rapid decrease to a gradual one. Mechanical consolidation referred to the time that the strength of the rafted ice stabilised, which occurred around the time that the salinity of liquid layer became constant.

In all laboratory experiments, the rafted ice thermodynamically consolidated in less than a day. Increasing the thickness of the ice, the salinity of the solution and the gap size all increased the consolidation time. From cores taken under increasing states of consolidation, it was discovered that at the time of thermodynamic consolidation the ice sheets were far from their maximum strength. Mechanical consolidation required many more days (6 to 30 depending on the conditions). The time period between thermodynamic and mechanical consolidation could provide an important window where the rafted ice could be broken up before it becomes a hazard to offshore structures.

The comparison of results from laboratory experiments and model tests showed some notable differences. Most importantly, the consolidation model predicts that when the gap thickness is greater than 6mm the liquid layer would not freeze. This was clearly not the case experimentally. This led to investigations into why the model predicts that the liquid layer migrates down rather than freezes which turned out to be an artefact of the model imposed by assuming a constant salinity across the liquid layer. While this assumption holds for small gaps it clearly does not for larger gaps sizes. Consequently, the model was

constrained so that no melting took place at the top of the lower block, thereby preventing liquid layer migration. This constraint significantly improved the predictions of the model, finding thermodynamic consolidation times that were consistent to within 15% of the experimental data. Investigation into the salt release process revealed that when brine release was limited to ice growing at the base of the upper ice sheet the salinity increase in the liquid layer was underestimated. However, when brine was released from interfaces growing both above and below the liquid layer, model simulations were comparable to laboratory data. The fraction of salt released into the liquid layer was found in the 6 ppt case to lie between 60 and 100%, while in the 33 ppt case a value of 10 and 20% was found. Having made these changes, the model can be used to find the rate of thermodynamic consolidation given a range of ice thicknesses in a variety of environments. However, as it stands, the model cannot be used to predict the rate of mechanical consolidation.

Measurements on the mechanically consolidated rafted ice showed that for the 6 ppt case (corresponding to the Caspian Sea) the average shear strength of the bond between two rafted blocks was 417 kPa. Variations in the thickness of the ice and the gap appeared to have little effect on the rafted ice bond. On the other hand, the salinity of the solution used in the experiment clearly had an impact. The maximum shear strength attained in the 6 ppt experiments was 30% less than that of level ice. This is lower than the 10-20% assumed to date in the literature. The varying conditions in the field could account for this discrepancy.

The absolute strengths measured in laboratory experiments cannot be used directly in calculations of ice loads on offshore structures. This is because ice contains natural flaws so that the larger the sample, the larger the number and size of the natural flaws. This leads to large scale ice strengths being lower than those measured on small samples. Nevertheless, the results may serve as a strength index between level and rafted ice which could be applied to large scale data. This result may help in estimating the contribution that rafted ice makes to loads on offshore structures.

In conclusion, a consolidation model has been developed that can be used to predict rates of thermodynamic consolidation of rafted ice in a variety of environments. This does not, however, provide the engineering data needed in the field since at the time of

thermodynamic consolidation the rafted ice has not reached maximum strength. This is achieved some considerable time later, and when this has happened the data shows that the shear strength attained remains lower than that of level ice.

Recommendations for further work

Improvements to be made to the rafted ice consolidation model:

- The next step in the development of the model would be to incorporate the salinity and temperature distribution in the liquid layer. To do this the diffusion equations describing the transport of solute and heat would need to be solved. The difficulty here lies in the solutal boundary conditions, where the concentrations at the boundaries of the liquid layer are dependent on the rate of freezing which in turn depends on the temperature distribution in the ice and the liquid layer. This would require the diffusion equations to be solved simultaneously.
- To describe accurately the salinity evolution of the liquid layer it would be necessary to model brine drainage into the liquid layer. This would effectively mean extending into a two-dimensional model. Oertling and Watts (2004) and Vancoppenolle et al. (2007; 2010) have recently suggested such models for the desalination of level ice. It is worth investigating if these models, or at least the concept therein, could be applied to rafted sea ice.
- Extend the model so that it can be used to predict mechanical consolidation. This could be quite straightforward, by merging the ice sheets and the consolidated liquid layer into a single ice block and running the simulation until the salinity in the liquid layer becomes constant.

Suggested improvements to laboratory experiments:

- Investigate the influence of air temperature on the consolidation process.
- Measure the surface roughness and its influence on the consolidation process.
- Perform experiments in a larger tank to minimise the effect of brine drainage.

- Develop an experimental method that does not involve lifting the ice out of the water from which it was grown, thus limiting brine drainage. Again a larger tank would help, allowing ice blocks to be assembled in situ.

Field experiments

- Perform field experiments to validate the small scale laboratory tests.
- Large scale shear experiments would be of particular interest to investigate the size effect.

Despite the experimental and modelling limitations I believe that my work represents a humble advancement towards understanding the consolidation and strength of rafted sea ice.

Appendix A: MATLAB code for the thermodynamic model of sea ice growth

The thermodynamic model for sea ice growth was coded in MATLAB version 9. The model code consists of a driver program 'level_ice.m' (Figure A.1) and 3 additional modules containing functions that are called from the main program (Figures A.2 to A.4). In the main programme, the forcing parameters (atmospheric, salinity, thermophysical and initial ice thickness), the grid size, the time step and the equations for the liquidus curve and solid fraction are first specified. The boundary condition at the ice surface is then solved to find the initial temperature at the ice surface using the 'solve' function. This is then used along with the liquidus temperature and ice thickness to define the initial condition in the ice. After this, the 'for' loop starts, where the heat diffusion equation is solved using the 'pdepe' function which calls the functions layerfun.m (Figure A.2), layeric1.m (Figure A.3) and layerbc.m (Figure A.4) which define respectively, the components of the pde, the initial condition and the boundary conditions. The pdepe function outputs a temperature for every timestep at each point specified on the grid. In this set-up, a mesh of 11 nodes and a time step of 3 seconds were used. The solution from the 3rd time step is then used to determine the temperature gradient in the ice and the thermal conductivity, which are used along with the volumetric latent heat, solid fraction and oceanic heat flux to calculate the rate of ice growth using the Stefan condition. The new time, ice thickness and initial condition are then specified for the next iteration of the loop. The loop then continues the number of times specified and outputs the results on a plot that shows the temperature evolution in the ice sheet as a function of depth. Each step in the programme is explained in greater detail by the comment fields marked in green after the percentage sign (%).

```
%--------------------------------------------------
% FORCING PARAMETERS
%--------------------------------------------------

% ATMOSPHERIC
F_LW=154.52; % downward longwave radiation
F_SW=0; % downward shortwave radiation
F_sens=5.7; % sensible heat flux
F_lat=3; % latent heat flux
E=0.99; % emissivity (Ebert & Curry, 1993)
sigma=5.67e-8; % Stefan-Boltzmann constant
alpha=0.6; % varies from 0.5-0.7 for bare ice (Perovich, summer school)
```

```
io=0.4; % fraction of radiation absorbed at suface (Feltham & Taylor,
2007)
K=1.5; %shortwave bulk extinction coefficient of sea ice (1/m)
F_ocean=3; % oceanic heat flux

% SALINITY
C0=33; % initial salinity of gap-taken to be that of sea water (ppt)
Cb=5; % bBulk concentration of sea ice.

% THERMOPHYSICAL
k_a=0.03; % conductivity of air (W/mK)-Weeks & Ackley (1982)
Va=0.025; % volume of air in sea ice- Timco & Frederking (1996)
L=3.014e8; % volumetric heat of fusion for sea ice (J/m^3)
c_i=1.883e6; % volumetric heat capacity of pure ice at 273K (J/m^3K)
r=1.09; % density ratio of brine to ice

% INTIAL SEA ICE THICKNESS (m)
H0=0.01;
H=H0;
ho=0;
%--------------------------------------------------

%--------------------------------------------------
% GRID AND TIME STEP SPACING
m = 0; % parameter corresponding to the symmetry of the problem. m can be
a slab=0, cylindrical=1, or spherical=2.
t = 1:1:3; % time step in seconds
x=0:0.001:H; % spatial grid size in meters
n=length(x);
t3=t(:,3)-0;
%--------------------------------------------------

%--------------------------------------------------
% Non-linear liquidus curve for NaCl
TL=273.15+((-5.33e-7*C0^3)-(9.37e-6*C0^2)-(0.0592*C0));
% Solid fraction at the ice ocean boundary
sf0=1-(Cb/C0);
%--------------------------------------------------

%--------------------------------------------------
% Finds the initial temp at ice surface using prescribed heat fluxes
syms T
Ta0=solve(E*(F_LW-(sigma*T.^4))+((1-alpha)*(1-io)*F_SW)-F_sens-
F_lat+(2.2*(TL-T)/H0));
Ta=Ta0(1)
%--------------------------------------------------

%--------------------------------------------------
% INITIAL CONDITION FOR THE HEAT EQUATION
IC=[((Ta-TL)/H) TL];
% IC is then updated in the loop by using polyfit to get the coefficients
% of a best-fit curve.
%--------------------------------------------------

%--------------------------------------------------------------------------
% Runs the loop every 3 secs what you put for t controls this
%--------------------------------------------------------------------------
ti0=280000; % no of times you want to run code (time(seconds)=ti0*3)
```

```
% pre-allocating space for arrays.
x=zeros(1,n,ti0);
u=zeros(1,n,ti0);

for ti=ti0;

% Solves the non-linear heat diffusion equation where u is the
temperature in degrees Kelvin
x(:,:,ti)=linspace(0,H,n);
sol(:,:,ti)=pdepe(m,@layerfun,@layeric1,@layerbc,x(:,:,ti),t,[],H,Ta,
TL,Cb,IC,k_a,Va,L,c_i,K,io,alpha,F_SW,E,F_LW,sigma,F_sens,F_lat);
u(:,:,ti)=sol(3,:,ti); % Takes the third solution of the pde
clear sol

% To get dT/dx at the moving interfaces.
Dx=x(:,n,ti)-x(:,n-1,ti);
Duo=u(:,2,ti)-u(:,1,ti);
DuDxo=Duo./Dx; % du/dx at the ocean-ice interface

% k_eff: thermal conductivity
theta=u(:,:,ti)-273.15;
k_i=1.16*(1.91-(8.66e-3.*theta)+(2.97e-5.*theta.^2));
k_b=0.4184.*(1.25+0.030.*theta+0.00014.*theta.^2);
k_bi=((2*k_i+k_a-(2*Va)*(k_i-k_a))./(2*k_i+k_a+Va*(k_i-k_a))).*k_i;
k_eff=k_bi+(k_bi-k_b).*(((5.33e-7*Cb^3)+(9.37e-
6*Cb^2)+(0.0592*Cb))./theta);

% To get the rate at which the ice-ocean boundary
% is moving at using Stefan Condition
DhDto=((DuDxo*k_eff(1))+F_ocean)/(L*sf0*r);
ho=ho+(DhDto*t3); %growth after 3 seconds

%--------------------------------------------------------------------------
% SPECIFY VALUES FOR THE NEXT LOOP
%--------------------------------------------------------------------------

% This gives the next time steps
tf=t;
a=t(3)+(t(2)-t(1)); b=a+(t(3)-t(1));
t=[a:t(2)-t(1):b];

% This calculates the new thickness of the ice sheet
delta_ho=0-ho;
H=H0+delta_ho;


% This calculates the coeff. of the Eq. of the line of the last u output
% for the new initial condition.
y=u(end,:,ti);
IC=polyfit(x(:,:,ti),y,10);

end

%--------------------------------------------------------------------------
% PLOT
%--------------------------------------------------------------------------

%Plot of how the heat is distributed in the slabs of ice.
```

```
U=[TL Ta]-273.15;
X=[0 H0]*100;
figure; plot(U,X,'k-',u(:,:,ti)-273.15,x(:,:,ti)*100,'r-');
grid on
legend('Initial Condition','1 day.')
ylabel('Ice Thickness (cm)');
xlabel('Temperature (C)');
```

Figure A.1. Driver program entitled 'level_ice.m'

```
% Function that defines the components of the pdepe.

function [c,f,s] =layerfun(x,t,u,DuDx,H,Ta,TL,Cb,IC,k_a,Va,L,c_i,K,io,
alpha,F_SW,E,F_LW,sigma,F_sens,F_lat)

%-------------------------------------------------------------------------
% To calculate the effective thermal conductivity
%-------------------------------------------------------------------------

theta=u-273.15;
k_i=1.16*(1.91-(8.66e-3.*theta)+(2.97e-5.*theta.^2)); % conductivity of
pure ice (W/mK)- pure polycrystalline ice Sakazume and Seki (1978)
k_bi=((2*k_i+k_a-(2*Va)*(k_i-k_a))./(2*k_i+k_a+Va*(k_i-k_a))).*k_i;
% conductivity of bubbly ice - Schwerdtfeger (1963)
k_b=0.4184.*(1.25+0.030.*theta+0.00014.*theta.^2);% conductivity of brine
k_eff=k_bi+(k_bi-k_b).*(((5.33e-7*Cb^3)+(9.37e-
6*Cb^2)+(0.0592*Cb))./theta);

%-------------------------------------------------------------------------
% To calculate the effective specific heat capacity
%-------------------------------------------------------------------------

c_eff=c_i+(L.*(((5.33e-7*Cb^3)+(9.37e-6*Cb^2)+(0.0592*Cb))./(theta.^2)));
% J/m3K

c = c_eff;
f = k_eff*DuDx;
s =(K*io*(1-alpha)*F_SW*exp(-K*(H-x)));
```

Figure A.2. layerfun.m

```
% Defines the initial condition, where intially u(x,0)=(((Ta-TL)*x)/H)-TL

function u0 = layeric1(x,H,Ta,TL,Cb,IC,k_a,Va,L,...
c_i,K,io,alpha,F_SW,E,F_LW,sigma,F_sens,F_lat)

Sz=size(IC,2);
for k=1:Sz
    X(k)=x^(Sz-k);
end

X=X(:);
u0 = IC*X;
```

Figure A.3. layeric1.m

```
% Defines the boundary condition

 function [pl,ql,pr,qr] = layerbc(xl,ul,xr,ur,t,H,Ta,TL,Cb,IC,k_a,Va,L,
c_i,K,io,alpha,F_SW,E,F_LW,sigma,F_sens,F_lat)
%-------------------------------------------------------------------------

pl = ul-TL;
ql = 0;
pr=(E*(F_LW-(sigma*ur.^4))+((1-alpha)*(1-io)*F_SW)-F_sens-F_lat);
qr = -1;
```

Figure A.4. layerbc.m

Appendix B: Thermistor probe design and fabrication

All temperature measurements in this research were made using thermistor probes that I designed and constructed with the help of Steve Boon, an electrical technician at UCL. In total, three sets of thermistor probes 5, 10 and 20 cm in length were constructed to measure the temperature in ice of different thicknesses and 5 single thermistors to measure the temperature of the air and water (see Figure B.1 for photographs of each type of probe). In this Appendix, I describe the types of thermistors used, the construction and assembly of the thermistor probes, and the details of the data logging system.

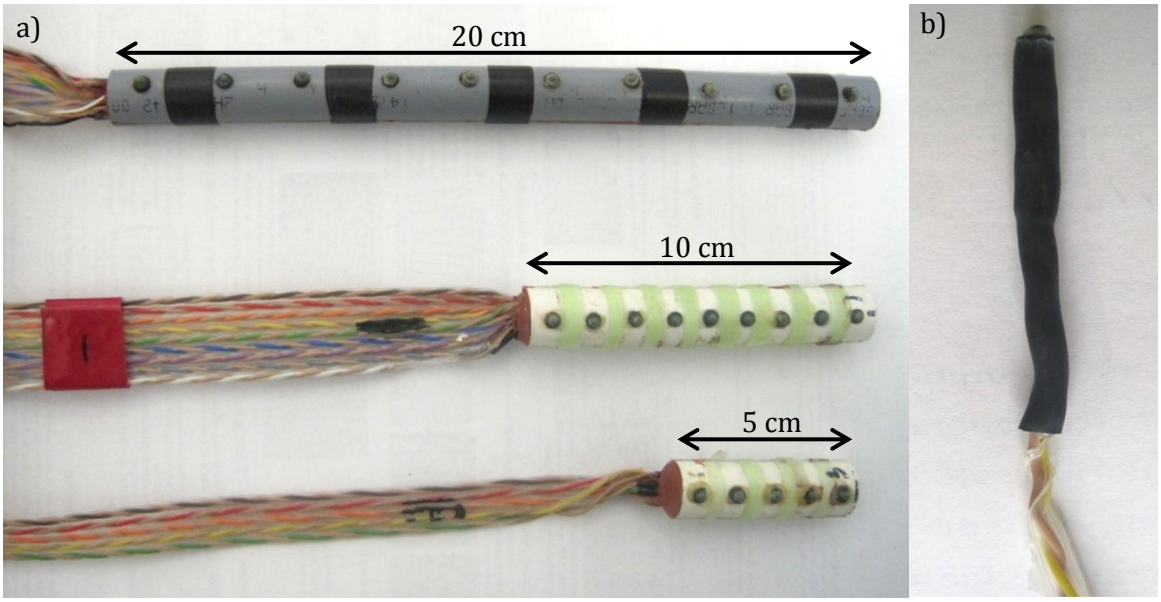

Figure B.1. Photograph of (a) the 5, 10 and 20 cm thermistor probes and, (b) one of the single thermistors used to measured temperature in the ice and air and water. The 5, 10 and 20 cm probes contain respectively, 5, 9 and 10 thermistors spread evenly over 1 cm intervals for the 5 and 10 cm probes and 2 cm intervals for the 20 cm probes.

Thermistors

A thermistor is a temperature sensor composed of sintered semiconducting material which exhibits a large change in resistance proportional to a small change in temperature. Thermistors were chosen as they are very sensitive and accurate for a reasonable price. In addition they are also rugged and come in a wide variety of physical forms. In our probes we used the YSI 55006 Glass-Encapsulated Material (GEM) thermistor (see Figure B.2),

which has an interchangeability tolerance of ±0.2ºC between 0 and 70ºC, and was purchased from Variohm. The GEM also provides a hermetic seal, eliminating moisture from entering the sensor. The thermistor works by passing a small, direct current through the thermistor and measuring the drop in voltage. Specification for this thermistor is a direct current of less than 30 µA.

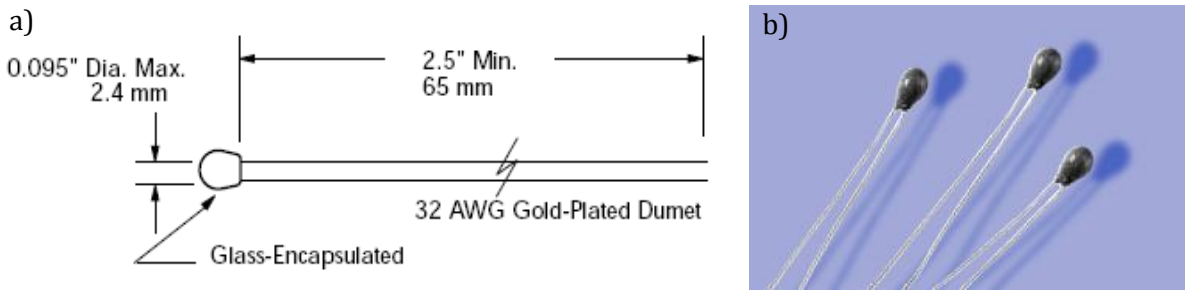

Figure B.2. Schematic (a) and photograph (b) of the YS1 550066 GEM thermistor (courtesy of www.YSI.com).

Thermistor probes

To construct the thermistor probes the thermistors were first soldered to twisted pairs of ribbon cable and insulated/sealed with glue-lined heat shrink (both ordered from RS components). Holes were then drilled in a 150 mm diameter PVC plumbing pipe and the thermistors inserted. The pipe and thermistors were then potted using a RS potting compound. The thermistors were then sealed once more with marine epoxy to ensure they were water tight. The opposite end of the ribbon cable was then fitted with connectors, which slotted directly into a custom made circuit board that supplied the thermistors with a direct current of 18.2±0.2 µA. In Figure B.3 a schematic of the circuit board is given.

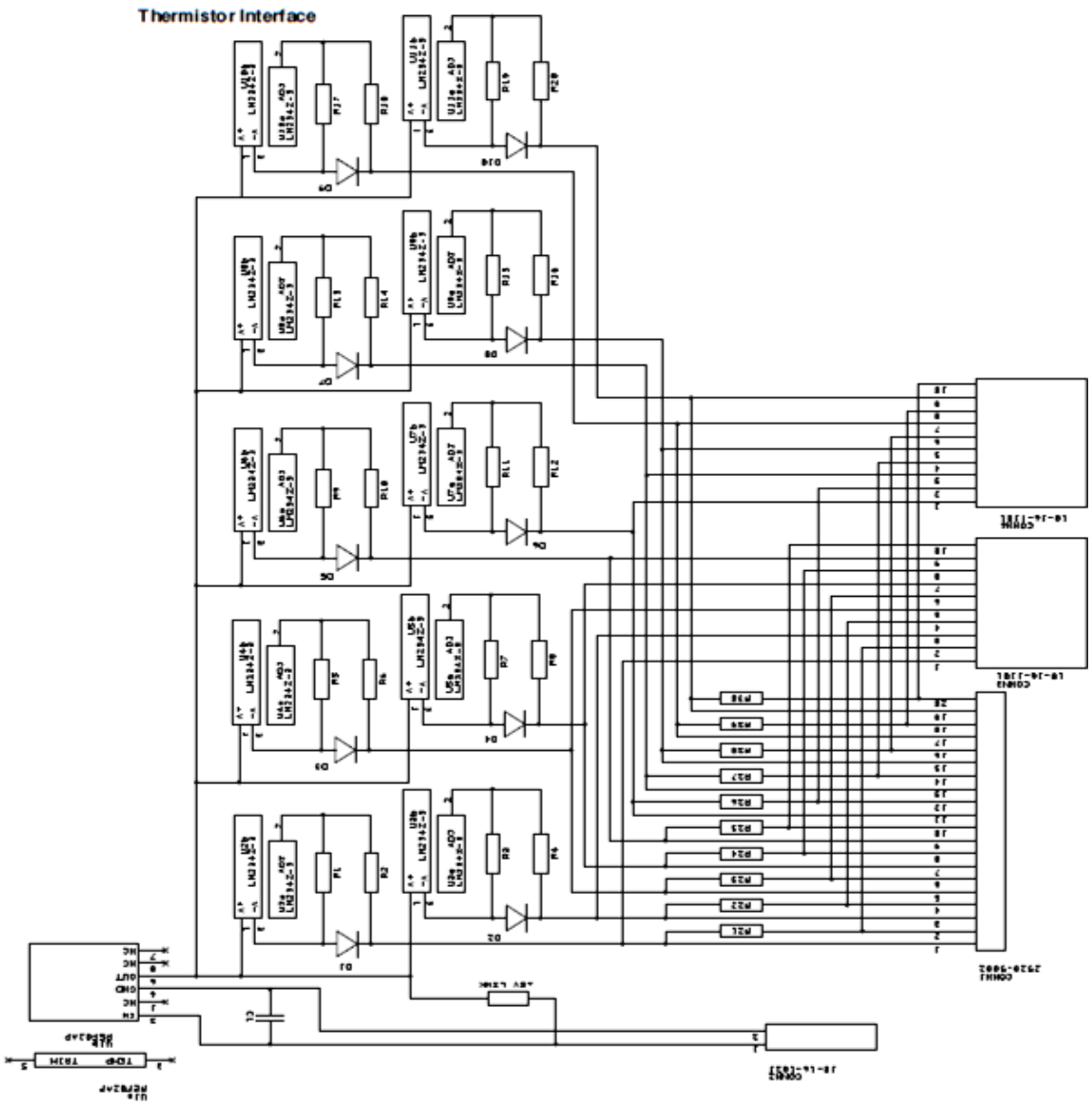

Figure B.3. Schematic of the circuit board interface.

The resistances were recorded every 5 minutes (although this time can easy can easily be changed) using the National Instruments Compact Fieldpoint data logger and LabView control software. In LabView, the resistances were converted into temperatures using the Steinhart-Hart equation,

$$\frac{1}{T} = A + Bln(R) + C[\ln(R)]^3, \qquad \text{(B.1)}$$

where T is the temperature in Kelvin, R is the resistance in Ohms and $A = 1.030697 \times 10^{-3}$, $B = 2.38896 \times 10^{-4}$, and $C = 1.57 \times 10^{-7}$ are the Steinhart-Hart coefficients which depend upon the type and model of thermistor and the temperature range of interest.

To find A, B, and C, the resistance of the thermistor at three temperatures was determined from the Resistance versus Temperature tables provided by the manufacturer (see Figure B.4). I chose these temperatures to be -15, 0 and 5°C, which corresponded to resistance of 61020, 29490 and 23460 Ω. These resistances and temperatures are then used to solve three simultaneous equations:

$$\frac{1}{T_{-15}} = \frac{1}{258} = A + B[\ln(R_{-15})] + C[\ln(R_{-15})]^3 \quad \text{(B.2)}$$

$$\frac{1}{T_0} = \frac{1}{273} = A + B[\ln(R_0)] + C[\ln(R_0)]^3 \quad \text{(B.3)}$$

$$\frac{1}{T_5} = \frac{1}{278} = A + B[\ln(R_5)] + C[\ln(R_5)]^3 \quad \text{(B.4)}$$

for the values of A, B and C. In Table B.1 the excel spreadsheet that was used to calculate the coefficients for the Steinhart-Hart equation is given.

YSI *Precision Temperature Group*
2670 Indian Ripple Road
Dayton, Ohio 45440-3605 USA
937 427 1231 fax 937 427 1640

Resistance Data for YSI Thermistors

Thermistor Mix		"L"	"L"	"L"	"B"	"B"	"B"	"B"	"B"	"H"	"H"	"H"	"H"	"H"
Ohms @ 25°C		100	300	1000	2252	3000	5000	6000	10,000	10,000	30,000	100 K	300 K	1 M
Temperature														
°F	°C													
-112.0	-80	14,470	67,660	278,800	1,660,000	2,211,000	3,685,000	4,423,000	7,371,000	3,558,000				
-110.2	-79	13,510	62,780	258,100	1,518,000	2,022,000	3,371,000	4,044,000	6,741,000	3,296,000				
-108.4	-78	12,620	58,290	239,100	1,390,000	1,851,000	3,086,000	3,703,000	6,172,000	3,055,000				
-106.6	-77	11,800	54,150	221,700	1,273,000	1,696,000	2,827,000	3,392,000	5,653,000	2,833,000				
-104.8	-76	11,040	50,340	205,600	1,167,000	1,555,000	2,592,000	3,109,000	5,182,000	2,629,000				
-103.0	-75	10,330	46,830	190,800	1,071,000	1,426,000	2,378,000	2,853,000	4,756,000	2,440,000				
-101.2	-74	9672	43,580	177,200	982,800	1,309,000	2,182,000	2,618,000	4,364,000	2,266,000				
-99.4	-73	9061	40,590	164,700	902,700	1,202,000	2,005,000	2,405,000	4,008,000	2,106,000				
-97.6	-72	8494	37,820	153,100	829,700	1,105,000	1,843,000	2,211,000	3,684,000	1,957,000				
-95.8	-71	7966	35,260	142,500	763,100	1,016,000	1,695,000	2,033,000	3,389,000	1,821,000				
-94.0	-70	7475	32,900	132,600	702,300	935,400	1,560,000	1,871,000	3,119,000	1,694,000				
-92.2	-69	7018	30,710	123,500	646,700	861,400	1,436,000	1,723,000	2,872,000	1,577,000				
-90.4	-68	6592	28,680	115,100	595,900	793,700	1,323,000	1,588,000	2,646,000	1,469,000				
-88.6	-67	6195	26,800	107,300	549,400	731,800	1,220,000	1,464,000	2,440,000	1,369,000				
-86.8	-66	5825	25,060	100,100	506,900	675,200	1,126,000	1,351,000	2,251,000	1,276,000				
-85.0	-65	5479	23,450	93,480	467,900	623,300	1,039,000	1,247,000	2,078,000	1,190,000				
-83.2	-64	5157	21,950	87,300	432,200	575,700	959,900	1,152,000	1,919,000	1,111,000				
-81.4	-63	4856	20,550	81,580	399,500	532,100	887,200	1,064,000	1,774,000	1,037,000				
-79.6	-62	4575	19,260	76,280	369,400	492,100	820,500	984,200	1,640,000	968,400				
-77.8	-61	4312	18,050	71,350	341,800	455,300	759,200	910,700	1,518,000	904,900				
-76.0	-60	4066	16,930	66,780	316,500	421,500	702,900	843,300	1,405,000	845,900				
-74.2	-59	3835	15,890	62,530	293,200	390,500	651,100	781,200	1,302,000	791,100				
-72.4	-58	3620	14,920	58,590	271,700	361,900	603,500	723,900	1,206,000	740,200				
-70.6	-57	3418	14,020	54,920	252,000	335,700	559,700	671,400	1,119,000	692,800				
-68.8	-56	3229	13,170	51,500	233,800	311,500	519,400	622,900	1,038,000	648,800				
-67.0	-55	3051	12,390	48,320	217,100	289,200	482,200	578,400	964,000	607,800				
-65.2	-54	2885	11,650	45,360	201,700	268,600	447,900	537,400	895,600	569,600				
-63.4	-53	2729	10,970	42,600	187,400	249,700	416,300	499,300	832,100	534,100				
-61.6	-52	2582	10,330	40,030	174,300	232,200	387,100	464,400	774,000	501,000				
-59.8	-51	2445	9730	37,630	162,200	216,000	360,200	432,100	720,200	470,100				
-58.0	-50	2315	9171	35,390	151,000	201,100	335,300	402,300	670,500	441,300				
-56.2	-49	2194	8647	33,300	140,600	187,300	312,300	374,600	624,300	414,500				
-54.4	-48	2079	8158	31,350	131,000	174,500	291,000	349,000	581,700	389,400				
-52.6	-47	1972	7699	29,520	122,100	162,700	271,300	325,300	542,200	366,000				
-50.8	-46	1870	7270	27,810	113,900	151,700	253,000	303,500	505,800	344,100				
-49.0	-45	1775	6867	26,220	106,300	141,600	236,200	283,200	472,000	323,700				
-47.2	-44	1685	6489	24,720	99,260	132,200	220,500	264,500	440,800	304,600				
-45.4	-43	1600	6135	23,320	92,720	123,500	205,900	247,000	411,700	286,700				
-43.6	-42	1521	5803	22,010	86,650	115,400	192,500	230,900	384,800	270,000				
-41.8	-41	1445	5491	20,790	81,020	107,900	180,000	215,900	359,800	254,400				
-40.0	-40	1374	5198	19,640	75,790	101,000	168,300	201,900	336,500	239,800	884,600	3,356,000		
-38.2	-39	1307	4922	18,560	70,930	94,480	157,500	189,000	315,000	226,000	830,900	3,147,000		
-36.4	-38	1244	4663	17,540	66,410	88,460	147,500	176,900	294,900	213,200	780,800	2,951,000		
-34.6	-37	1184	4420	16,590	62,210	82,870	138,200	165,700	276,200	201,100	733,900	2,769,000		
-32.8	-36	1127	4191	15,700	58,300	77,660	129,500	155,300	258,900	189,800	690,200	2,599,000		
-31.0	-35	1073	3975	14,860	54,660	72,810	121,400	145,600	242,700	179,200	649,300	2,440,000		
-29.2	-34	1023	3772	14,070	51,270	68,300	113,900	136,600	227,700	169,300	611,000	2,292,000		
-27.4	-33	974.9	3580	13,330	48,110	64,090	106,900	128,200	213,600	160,000	575,200	2,154,000		
-25.6	-32	929.6	3400	12,630	45,170	60,170	100,300	120,300	200,600	151,200	541,700	2,025,000		
-23.8	-31	886.6	3230	11,970	42,420	56,510	94,220	113,000	188,400	143,000	510,400	1,904,000		
-22.0	-30	846.0	3069	11,350	39,860	53,100	88,530	106,200	177,000	135,200	481,000	1,791,000		
-20.2	-29	807.5	2918	10,770	37,470	49,910	83,220	99,830	166,400	127,900	453,500	1,685,000		
-18.4	-28	771.0	2775	10,220	35,240	46,940	78,260	93,890	156,500	121,100	427,700	1,586,000		
-16.6	-27	736.4	2640	9705	33,150	44,160	73,620	88,320	147,200	114,600	403,500	1,494,000		
-14.8	-26	703.6	2512	9218	31,200	41,560	69,290	83,130	138,500	108,600	380,900	1,407,000		
-13.0	-25	672.5	2392	8758	29,380	39,130	65,240	78,280	130,500	102,900	359,600	1,326,000		
-11.2	-24	643.0	2278	8323	27,670	36,860	61,450	73,720	122,900	97,490	339,600	1,250,000		
-9.4	-23	614.9	2170	7914	26,070	34,730	57,900	69,460	115,800	92,430	320,900	1,178,000		
-7.6	-22	588.3	2068	7527	24,580	32,740	54,580	65,490	109,100	87,660	303,300	1,111,000		
-5.8	-21	563.0	1972	7161	23,180	30,870	51,470	61,760	102,900	83,160	286,700	1,049,000		
-4.0	-20	538.9	1880	6815	21,870	29,130	48,560	58,270	97,110	78,910	271,200	989,800		
-2.2	-19	516.1	1794	6489	20,640	27,490	45,830	54,990	91,650	74,910	256,500	934,600		
-0.4	-18	494.3	1712	6180	19,480	25,950	43,270	51,900	86,500	71,130	242,800	882,700		
1.4	-17	473.6	1634	5887	18,400	24,510	40,860	49,020	81,710	67,570	229,800	834,000		
3.2	-16	454.0	1561	5611	17,390	23,160	38,610	46,330	77,220	64,200	217,600	788,200		
5.0	-15	435.2	1491	5349	16,430	21,890	36,490	43,770	72,960	61,020	206,200	745,200		
6.8	-14	417.4	1424	5101	15,540	20,700	34,500	41,400	69,010	58,010	195,400	704,700		
8.6	-13	400.4	1361	4866	14,700	19,580	32,630	39,170	65,280	55,170	185,200	666,700		
10.4	-12	384.2	1302	4643	13,910	18,520	30,880	37,060	61,770	52,480	175,600	630,900		
12.2	-11	368.8	1245	4432	13,160	17,530	29,230	35,060	58,440	49,940	166,600	597,200		
14.0	-10	354.1	1191	4232	12,460	16,600	27,670	33,200	55,330	47,540	158,000	565,500		
15.8	-9	340.0	1140	4042	11,810	15,720	26,210	31,470	52,440	45,270	150,000	535,600		
17.6	-8	326.7	1091	3862	11,190	14,900	24,830	29,810	49,690	43,110	142,400	507,500		
19.4	-7	313.9	1045	3691	10,600	14,120	23,540	28,240	47,070	41,070	135,200	481,000		
21.2	-6	301.7	1001	3529	10,050	13,390	22,320	26,780	44,630	39,140	128,500	456,000		
23.0	-5	290.1	958.9	3374	9534	12,700	21,170	25,400	42,340	37,310	122,100	432,400		
24.8	-4	278.9	919.0	3228	9046	12,050	20,080	24,100	40,170	35,570	116,000	410,200		
26.6	-3	268.3	881.0	3088	8586	11,440	19,060	22,880	38,130	33,930	110,300	389,200		
28.4	-2	258.2	844.8	2956	8151	10,860	18,100	21,720	36,190	32,370	104,900	369,400		
30.2	-1	248.5	810.3	2830	7741	10,310	17,190	20,620	34,370	30,890	99,800	350,700		
32.0	0	239.2	777.5	2710	7355	9796	16,330	19,600	32,660	29,490	94,980	333,100	1,088,000	3,966,000
33.8	1	230.3	746.2	2596	6989	9310	15,520	18,620	31,030	28,150	90,410	316,400	1,030,000	3,740,000
35.6	2	221.9	716.3	2487	6644	8851	14,750	17,700	29,500	26,890	86,090	300,600	975,300	3,529,000
37.4	3	213.8	687.8	2384	6319	8417	14,030	16,840	28,060	25,690	81,990	285,700	923,800	3,330,000
39.2	4	206.0	660.6	2286	6011	8006	13,340	16,020	26,690	24,550	78,110	271,600	875,200	3,144,000
41.0	5	198.6	634.6	2192	5719	7618	12,700	15,240	25,400	23,460	74,440	258,300	829,500	2,969,000
42.8	6	191.5	609.9	2102	5444	7252	12,090	14,500	24,170	22,430	70,960	245,700	786,300	2,804,000
44.6	7	184.6	586.2	2017	5183	6905	11,510	13,810	23,020	21,450	67,660	233,800	745,600	2,649,000
46.4	8	178.1	563.6	1936	4937	6576	10,960	13,150	21,920	20,520	64,530	222,500	707,200	2,504,000
48.2	9	171.9	542.1	1859	4703	6265	10,440	12,530	20,880	19,630	61,560	211,900	671,000	2,367,000
50.0	10	165.9	521.5	1785	4482	5971	9951	11,940	19,900	18,790	58,750	201,700	636,800	2,238,000
51.8	11	160.1	501.7	1714	4273	5692	9486	11,380	18,970	17,980	56,070	192,200	604,500	2,117,000

Figure B.4. Resistance versus temperature table for the YSI thermistors, where the values for the thermistors used in this experiment are boxed in red.

Table B.1. The spreadsheet used to calculate the coefficients for the Steinhart and Hart equation courtesy of YSI temperature.

A1	'SPREADSHEET METHOD FOR SOLVING STEINHART & HART EQUATION.
A2	'1/T = a + b(lnR) + c(lnR)^3
A4	'Input temperature and resistance
B5	'Temp (C)
C5	'Resistance
D5	'T(K)
E5	'ln(R)
A6	'Low
B6	0
C6	7355
D6	+B6+273.15
E6	@LN(C6)
A7	'Mid
B7	40
C7	1199
D7	+B7+273.15
E7	@LN(C7)
A8	'High
B8	70
C8	394.5
D8	+B8+273.15
E8	@LN(C8)
A10	'Solve three simultaneous equations to obtain coefficients a,b,c:
A12	'ln(R1) - ln(R2)
B12	+E6 -E7
C12	'Coefficients:
A13	'ln(R1) - ln(R3)
B13	+E6-E8
C13	'a=
D13	1/D6-D15*E6^3-D14*E6
A14	'(1/T1)-(1/T2)
B14	1/D6 - 1/D7
C14	'b=
D14	(B14-D15*(E6^3-E7^3))/B12
A15	'(1/T1) - (1/T3)
B15	1/D/6-1/D8
C15	'c=
D15	(B14-B12*B15/B13)/((E6^3-E7^3)-B12*(E6^3-E8^3)/B13)
A17	'Solving for R, given T:
A19	'For T (Deg C) =
B19	25
C19	+B19+273.15
D19	'=T (K)
A21	'R = exp{[A^2/4 + B^3/27)^(1/2) - (A/2]^(1/3)
A22	' - [(A^2/4 + B^3/27)^(1/2) + A/2]^(1/3)}
A24	'A =(a -1/T)/c
B24	(D13 - (1/C19))/D15
D24	'A squared =
E24	+B24^2

A25	'B = b/c
B25	+D14/D15
D25	'B cubed=
E25	+B25^3
A27	'R =
B27	@EXP((@SQRT(E24/4+E25/27)-B24/2)^(1/3)-(@SQRT(E24/4+E25/27)+B24/2) ^(1/3))
C27	'Ohms
A28	'dR/dT=
B28	-1*B27/(C19^2*(D14+3*D15*(@LN(B27))^2))
A29	'%dR/dt=
B29	+B28/B27*100
A31	'Solving for Temperature given R:
A32	'Ohms =
B32	2252
A34	'Temperature (C) =
B34	1/(D13+D14*@LN(B32)+D15*(LN(B32))^3)-273.15

Note: Cells that start with an apostrophe ' are labels. Boxed cells indicate data you must enter. Other cells are formulas.

Appendix C: A model for the consolidation of rafted sea ice (JGR paper)

A model for the consolidation of rafted sea ice

E. Bailey,[1] D. L. Feltham,[2,3] and P. R. Sammonds[1,2]

Received 2 September 2008; revised 21 September 2009; accepted 27 October 2009; published 9 April 2010.

[1] Rafting is one of the important deformation mechanisms of sea ice. This process is widespread in the north Caspian Sea, where multiple rafting produces thick sea ice features, which are a hazard to offshore operations. Here we present a one-dimensional, thermal consolidation model for rafted sea ice. We consider the consolidation between the layers of both a two-layer and a three-layer section of rafted sea ice. The rafted ice is assumed to be composed of layers of sea ice of equal thickness, separated by thin layers of ocean water. Results show that the thickness of the liquid layer reduced asymptotically with time, such that there always remained a thin saline liquid layer. We propose that when the liquid layer is equal to the surface roughness the adjacent layers can be considered consolidated. Using parameters representative of the north Caspian, the Arctic, and the Antarctic, our results show that for a choice of standard parameters it took under 15 h for two layers of rafted sea ice to consolidate. Sensitivity studies showed that the consolidation model is highly sensitive to the initial thickness of the liquid layer, the fraction of salt release during freezing, and the height of the surface asperities. We believe that further investigation of these parameters is needed before any concrete conclusions can be drawn about rate of consolidation of rafted sea ice features.

Citation: Bailey, E., D. L. Feltham, and P. R. Sammonds (2010), A model for the consolidation of rafted sea ice, *J. Geophys. Res.*, *115*, C04015, doi:10.1029/2008JC005103.

1. Introduction

[2] Driving forces such as offshore winds and ocean currents can cause ice floes to collide, forming ridges or rafted sea ice. Ridges are elongated piles of rubble, and rafting is the overriding of one sheet by another. Various studies have investigated what conditions are favorable for rafting to take place as opposed to ridging [*Hopkins et al.*, 1999; *Parmerter*, 1975; *Tuhkuri and Lensu*, 2002; *Weeks and Kovacs*, 1970]. These studies have shown that rafting is most common between thin ice sheets (<0.3 m) of uniform thickness. Two types of rafting have been identified: (1) simple rafting, where the two ice sheets interact along a straight edge and one sheet "simply" overrides the other, and (2) finger rafting, where the interacting sheets fracture along lines perpendicular to their interacting edge and form fingers. Alternate fingers are then overthrust and underthrust, leaving an interlocked structure [*Vella and Wettlaufer*, 2007; *Vella and Wettlaufer*, 2008; *Weeks and Kovacs*, 1970].

[3] Multiple rafting is also known to occur in some regions, where ice floes override one another multiple times to produce thick sea ice features [*Babko et al.*, 2002]. This process is particularly common in the north Caspian Sea, an area of particular interest because of its oil and gas reserves. Multiply rafted sections have been observed to contain up to 13 layers, all of roughly equal thickness, producing structures that are greater than 4 m in thickness (D. Mayne, personal communication, 2007). This phenomenon is also common in the Southern Ocean, where the sea ice thickness is usually less than a meter [*Babko et al.*, 2002]. For example, *Worby et al.* [1996] analyzed 62 ice cores retrieved from 50 ice floes in the Bellinghausen and Amundsen seas and found that the floes with an average thickness of 0.9 m contained around eight distinct layers. In the Arctic, *Melling et al.* [1993] also observed that as many as four layers of ice were rafted in the southeastern Beaufort Sea to produce a total thickness of ~6 m.

[4] To date, rafting has not received as much attention in the literature as ridging. This is perhaps because ridge keels have been a greater concern for engineers [*Hopkins et al.*, 1999], or perhaps it is due to the difficulties in identifying rafted ice thicker than 0.15–0.20 m in aerial imagery or of any other thickness in laser profiles or under ice sonar records [*Babko et al.*, 2002].

[5] An ice feature can represent a zone of either weakness or strength in the ice pack depending on the degree of consolidation [*Hoyland*, 2002]. In a rafted section, the layers of sea ice are initially separated by thin layers of ocean water. The bonds between the layers are at first weak but may strengthen with time to produce a coherent ice sheet. Rafted sea ice is important from both a geophysical and an

[1]Rock and Ice Physics Laboratory, Department of Earth Sciences, University College London, London, UK.
[2]Centre for Polar Observation and Modelling, National Centre for Earth Observation, Department of Earth Sciences, University College London, London, UK.
[3]British Antarctic Survey, Cambridge, UK.

0148-0227/10/2008JC005103

engineering point of view. From a geophysical perspective, rafted sea ice accounts for a significant fraction of the ice volume and may help determine the large-scale strength of the pack ice. In addition, it seems that rafting plays an important part in the mechanical redistribution of the sea ice thickness distribution [*Babko et al.*, 2002; *Toyota et al.*, 2004]. *Poplin and Wang* [1994] carried out extensive uniaxial compression tests on rafted ice samples collected in Norton Sound, Alaska. Their results showed that on ice samples cut horizontal to the crystal growth direction, at strain rates of 10^{-4} and 10^{-5} s^{-1}, the mean strengths of consolidated rafted ice were actually larger (1.55 and 1.06 MPa) than the corresponding landfast samples (1.25 and 0.64 MPa). Since rafted ice loads are usually applied horizontally to offshore structures, this result implies that once consolidated, rafted ice may be a significant ice hazard. Therefore, the strength and thickness of rafted ice is also important in the design and operation of Arctic vessels and offshore structures [*Hopkins et al.*, 1999].

[6] In this paper we present a one-dimensional, thermal consolidation model for rafted sea ice. We first consider the consolidation of two layers of rafted sea ice and then three layers of multiply rafted sea ice. The mathematical formulation of the consolidation model and the method of solution are described in section 2. In section 3, we present the parameters that are to be used in our simulations that are specific to the environments of the north Caspian Sea, the Arctic, and the Antarctic. In section 4, the results of the numerical simulations are presented, and the sensitivity of the model to certain parameters is examined. A discussion of the results and concluding remarks are presented in section 5.

2. Model Description

[7] The consolidation model for rafted sea ice calculates how long it will take for the layers in a rafted section of sea ice to effectively bond into a coherent ice sheet. We consider the consolidation between the layers of both a two-layer and a three-layer section of rafted sea ice. The model is one-dimensional, and we confine our attention to regions of rafted ice that extend over large enough distances that horizontal effects need not be taken into account. The rafted ice is assumed to be composed of layers of sea ice of equal thickness, separated by thin layers of ocean water. The thin layers of ocean water between the ice sheets are observed to initially form because large surface asperities or fragments of snow and ice caught between the ice sheets act as spacers, allowing seawater to flood in. Most samples collected of multiply rafted sea ice show that the layers in a rafted section are of roughly equal thickness. This suggests that the ice sheets rafted in quick enough succession that thermodynamic growth of the adjacent level ice could not have taken place during the same rafting event. Therefore, from the perspective of the model presented in section 2.1, multiple rafting took place simultaneously. In this section we describe the mathematical formulation and the method of solution of the consolidation model.

2.1. Mathematical Formulation

[8] We consider the situation where two identical ice sheets of initial thickness H_0 have rafted, such that there is a liquid layer of initial thickness h_0 located between adjacent sheets (Figure 1). The sea ice is described as a mushy layer, a rigid matrix of pure ice immersed in its brine [*Feltham et al.*, 2006], and the liquid layer is a thin layer of ocean water, trapped between the asperities of the ice sheets. The internal temperature of each ice sheet is determined from the nonlinear one-dimensional heat diffusion equation,

$$c_{\text{eff}}\frac{\partial T}{\partial t}=\frac{\partial}{\partial z}\left(k_{\text{eff}}\frac{\partial T}{\partial z}\right)+A_R, \tag{1}$$

where c_{eff} and k_{eff} are the effective volumetric specific heat capacity and the thermal conductivity of sea ice (both functions of temperature), respectively, T is the temperature within the ice sheet, t is time, and z is the vertical spatial coordinate, which is taken to be positive upward. The final term, A_R, describes the absorption of solar radiation that penetrates through the upper sea ice surface, which we take to be

$$A_R=\kappa_i I_0(1-\alpha)F_{\text{SW}}e^{-\kappa_i z}, \tag{2}$$

where $\kappa_i = 1.5\ \text{m}^{-1}$ is Beer's extinction coefficient, $I_0 = 0.4$ is the fraction of incident radiation that passes through the surface into the interior of the ice, $\alpha = 0.6$ is the albedo for bare ice, and F_{SW} is the flux of incoming shortwave radiation [*Ebert and Curry*, 1993; *Maykut and Untersteiner*, 1971].

[9] The effective volumetric heat capacity and thermal conductivity of sea ice are given by [*Bitz and Lipscomb*, 1999; *Feltham et al.*, 2006]

$$c_{\text{eff}}=c_i-\frac{T_L(S_{\text{bulk}})-T_L(0)}{\theta^2}L \tag{3}$$

and

$$k_{\text{eff}}=k_{\text{bi}}-(k_{\text{bi}}-k_{\text{b}})\frac{T_L(S_{\text{bulk}})-T_L(0)}{\theta}, \tag{4}$$

where $T_{\text{L}}(S_{\text{bulk}})$ is the liquidus (freezing) temperature of sea ice with a bulk salinity S_{bulk}, which we take to be uniform across the sheet, $T_{\text{L}}(0)$ is the liquidus temperature of pure water, $\theta = T - T_{\text{L}}(0)$, $L = 3.014 \times 10^8\ \text{J m}^{-3}$ is the volumetric heat of fusion of pure ice, $c_i = 1.883 \times 10^6\ \text{J (m}^3\ \text{K)}^{-1}$ is the volumetric heat capacity of pure ice [*Ebert and Curry*, 1993], and k_{bi} and k_{b} are the conductivities of bubbly ice and brine, respectively.

[10] After *Schwerdtfeger* [1963], we take k_{bi} and k_{b} to be

$$k_{\text{bi}}=\frac{2k_{\text{i}}+k_{\text{a}}-2V_{\text{a}}(k_{\text{i}}-k_{\text{a}})}{2k_{\text{i}}+k_{\text{a}}+V_{\text{a}}(k_{\text{i}}-k_{\text{a}})}k_{\text{i}}\ \text{W(m K)}^{-1} \tag{5}$$

and

$$k_{\text{b}}=0.4184\left(1.25+0.030\ \text{K}^{-1}\theta+0.00014\ \text{K}^{-2}\theta^2\right)\text{W(m K)}^{-1}, \tag{6}$$

where $k_{\text{i}} = 1.16(1.91 - 8.66 \times 10^{-3}\ \text{K}^{-1}\ \theta + 2.97 \times 10^{-5}\ \text{K}^{-2}\ \theta^2)\ \text{W (m K)}^{-1}$ is the conductivity of pure ice [*Sakazume and Seki*, 1978], $k_{\text{a}} = 0.03\ \text{W (m K)}^{-1}$ is the conductivity of air [*Weeks and Ackley*, 1986], and $V_{\text{a}} = 0.025$ is the fractional volume of air in sea ice [*Timco and Frederking*, 1996].

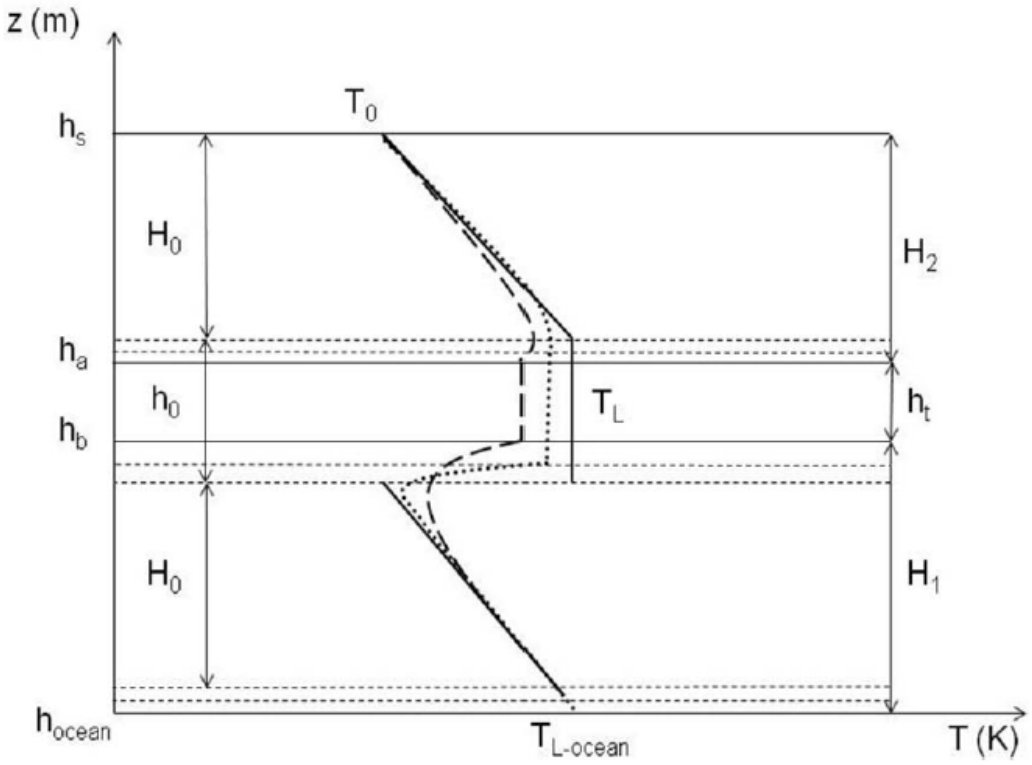

Figure 1. Schematic of the consolidation model illustrating how the temperature profiles, the thickness of the ice sheets, and the liquid layer evolve with time. H_0 and h_0 are the initial thicknesses of the ice sheets and the liquid layer, respectively, and $H_{1,2}$ and h_t are the thicknesses at a later time t. T_0 is the initial temperature at the ice-atmosphere interface, T_L is the liquidus temperatures in the liquid layer (and is also a function of time), and $T_{L\text{-ocean}}$ is the liquidus temperature of the ocean. The dashed lines at the interfaces between the ice sheets and the liquid layer and the lower ice sheet and the ocean indicate the movement of these interfaces due to freezing, where h_a is the location of the freezing front above the liquid layer, h_b is the location of the freezing front below the liquid layer, and h_{ocean} is the location of the freezing front at the ice-ocean interface. The bolder lines denote the temperature profiles in the ice sheets and the liquid layer: the solid line depicts the initial temperature in the ice sheets and the liquid layer, and the dotted and dashed lines depict the temperature at later times.

[11] The sea ice is assumed to be in local thermodynamic equilibrium, which implies that the temperature T and brine concentration S_{brine} lie on the liquidus curve in the phase diagram for sea ice, i.e., $T = T_L(S_{brine})$. The liquidus curve can be approximated by the liquidus curve for sodium chloride solution [*Notz et al.*, 2005; *Weast*, 1971],

$$T_L(S) = -5.33 \times 10^{-7} S^3 - 9.37 \times 10^{-6} S^2 - 0.0592 S + 273.15 \text{ K}. \quad (7)$$

We consider the ice sheets to initially have identical linear temperature profiles on the basis of the air and sea temperatures at the upper and lower boundaries (Figure 1), giving the following initial condition:

$$T = \frac{T_0 - T_L(S_{ocean})}{H_0} z + T_L(S_{ocean}) (t = 0), \quad (8)$$

where T_0 is the temperature at the upper surface, $T_L(S_{ocean})$ is the freezing temperature at the salinity of the ocean S_{ocean}, and H_0 is the initial thickness of the ice slabs.

[12] In the absence of surface melting, the net flux, $(F_{net})_0$, at the upper surface of the rafted ice ($x = h_s$), must balance the conductive flux, $-k_{eff}\,\partial T/\partial x$, at the surface, such that

$$(F_{net})_0 \equiv \varepsilon_i (F_{LW} - \sigma T_0^4) + (1 - \alpha)(1 - I_0) F_{SW} - F_{sens} - F_{lat} = -k_{eff} \frac{\partial T}{\partial z} (z = h_s), \quad (9)$$

where $\varepsilon_i = 0.99$ is the emissivity of bare ice, F_{LW} is the flux of downward longwave radiation, $\sigma = 5.67 \times 10^{-8}$ J (K^4 m^2 s)$^{-1}$ is the Stefan-Boltzmann constant, and F_{sens} and F_{lat} are the sensible and latent heat fluxes [*Ebert and Curry*, 1993; *Maykut and Untersteiner*, 1971; *Taylor and Feltham*, 2004].

[13] At the interior interfaces ($z = h_a$, h_b), i.e., the interfaces above and below the liquid layer, the boundary conditions are

$$T = T_L(S_{liquid}) (z = h_a, h_b) \quad (10)$$

and

$$L\phi\left(\frac{\rho_{\text{brine}}}{\rho_{\text{ice}}}\right)\frac{dh}{dt} = k_{\text{eff}}\frac{\partial T}{\partial z}(z = h_a, h_b), \tag{11}$$

where S_{liquid} is the salinity of the liquid layer, $\phi = 1 - S_{\text{bulk}}/S_{\text{liquid}}$ is the local solid fraction per unit volume of the sea ice, dh/dt is the velocity of the respective boundary, and $\partial T/\partial z$ is the temperature gradient in the ice at the boundary.

[14] At the sea ice–ocean boundary ($z = h_{\text{ocean}}$), the sea ice is held constant at the freezing temperature of the ocean,

$$T = T_L(S_{\text{ocean}})(z = h_{\text{ocean}}). \tag{12}$$

The ice growth rate at the ice-ocean boundary is given by the Stefan condition,

$$L\phi\left(\frac{\rho_{\text{brine}}}{\rho_{\text{ice}}}\right)\frac{dh_{\text{ocean}}}{dt} = k_{\text{eff}}\frac{\partial T}{\partial z} + F_{\text{ocean}}(z = h_{\text{ocean}}), \tag{13}$$

where F_{ocean} is the heat flux from the ocean directed into the base of the ice sheet. The adoption of a nonzero solid fraction at the sea ice–ocean interface, $\phi(z = h_{\text{ocean}}) = 1 - S_{\text{bulk}}/S_{\text{ocean}}$, where S_{bulk} is a constant, is an approximation in that S_{bulk} will vary throughout the interface region [*Notz and Worster*, 2008]. Here the approximation implies we are tracking the location of the "consolidated" ice-ocean interface. This approximation conveys the mathematical advantage that the interface location can be determined explicitly (rather than using an implicit numerical technique) and leads to little numerical error [*Feltham*, 1998]. We have assumed that upon freezing, the liquid expanded by 9%, i.e., $\rho_{\text{brine}}/\rho_{\text{ice}} = 1.09$ [*Pounder*, 1965].

[15] Since the liquid layer is narrow, salt diffusion maintains a uniform salinity inside the liquid layer on the time scale of changes in diffusive heat flux in the surrounding ice sheets provided that $(h/H)^2 \ll Le$, where h is the liquid layer thickness, H is the ice layer thickness, and Le is the Lewis number, defined as the diffusion rate of salt divided by the effective thermal diffusivity of sea ice and equal to approximately 10^{-2} [*Feltham*, 1998]. For the calculations presented here, this condition is satisfied, and therefore, the temperature of the liquid layer T_{liquid} is uniform and equal to the local liquidus temperature,

$$T_{\text{liquid}} = T_L(S_{\text{liquid}}). \tag{14}$$

[16] We assume that the liquid layer initially consists of ocean water, and as it freezes, a fraction f' of the salt originally contained in the seawater is released into the liquid layer. This assumption is based upon the observation that the liquid layer becomes increasingly salty as freezing progresses (see section 3). We believe that brine is released only from the freezing at the upper layer, so that conservation of salt implies

$$S_{\text{liquid}} = S_{\text{ocean}} + f'\frac{\Delta h_a}{h_t}S_{\text{ocean}}, \tag{15}$$

where Δh_a is the amount of freezing at the upper layer and h_t is the thickness of the liquid layer at time t. In the experiments described in section 3 it was impractical to measure Δh_a, but the liquid layer thickness could be measured. Therefore, for the purposes of comparison with observations, and because the error it introduces is small compared with uncertainty in the measurement of the liquid layer salinity, we assume that $\Delta h_a = f''\Delta h_b$, where f'' is a constant and Δh_b is the amount of freezing at the lower layer. Then, since $\Delta h_a = h_0 - h_t - \Delta h_b$, we can rewrite conservation of salt as

$$S_{\text{liquid}} = S_{\text{ocean}} + fS_{\text{ocean}}\left(\frac{h_0}{h_t} - 1\right), \tag{16}$$

where $f = f'/(1 + f'')$. The rate of change of h_t can be deduced from the difference in the Stefan conditions at the boundaries above and below the liquid layer, so that

$$\frac{dh_t}{dt} = \frac{k_{\text{eff}}}{\phi L}\frac{\rho_{\text{ice}}}{\rho_{\text{brine}}}\left(\frac{\partial T_a}{\partial z} - \frac{\partial T_b}{\partial z}\right), \tag{17}$$

where $\partial T_a/\partial z$ and $\partial T_b/\partial z$ are the temperature gradients at the boundaries above ($z = h_a$) and below ($z = h_b$) the liquid layer, respectively. The system of equations (1)–(17) comprises a closed partial differential, initial boundary value problem.

[17] When considering the consolidation of three layers of rafted sea ice, we assume that the three layers are separated by two thin layers of ocean water that are initially of equal thickness. The mushy layer equations described above are used to determine the vertical heat transport within the ice sheets (equations (1)–(7)) and are subject to the same initial condition (equation (8)) and boundary conditions that describe the heat fluxes at the ice-atmosphere interface (equation (9)), the ice-liquid layer interfaces (equations (10) and (11)), and the ice-ocean interface (equations (12) and (13)). The rate at which the liquid layers reduce with time is then determined from the difference in the Stefan conditions at the respective interfaces (equation (17)).

2.2. Method of Solution

[18] The model described in section 2.1 was coded in MATLAB. The heat diffusion equation (equation (1)) was solved for each ice sheet using a grid spacing of 2 mm and a time step of 1 s. Every 3 s the thickness of the liquid layers was calculated (equation (17)), and the local liquidus temperature (equation (14)), the solid fraction, and the thickness of the ice slabs were updated.

[19] Initial runs revealed that when the fraction of salt released into the liquid layer (f) is greater than zero, the thickness of the liquid layers reduced asymptotically with time, such that there always remained a thin saline liquid layer. Complete solidification of the liquid layer will occur only if the temperature reaches the eutectic temperature of the seawater. We know from field observations that the layers of ice do, in fact, consolidate. Our model assumes that the surfaces of the ice slabs are smooth, whereas, in reality, they are rough. At some stage the surface asperities will grow sufficient in size to effectively bond the slabs together. We therefore imposed a "cutoff" in the program such that when the liquid layer reaches the size of the surface

Table 1. Parameters Used for Our Model Calculation

Forcing Data	North Caspian Sea	Arctic	Antarctic
F_{LW} (W m^{-2})	205[a]	154.52[b]	158[c]
F_{SW} (W m^{-2})	76[a]	0[b]	0[c]
F_{sens} (W m^{-2})	3[a]	5.7[b]	43[c]
F_{lat} (W m^{-2})	−1[a]	0.5[b]	−3[c]
F_{ocean} (W m^{-2})	9.7	3[d]	3[d]
S_{ocean} (ppt)	6	33	35
S_{bulk} (ppt)	1	5	5
f (%)	27	27	27
h_{sa} (mm)	0.5	0.5	0.5
h_0 (mm)	5	5	5
H_0 (m)	0.2	0.2	0.2

[a]Mean for January 2008 provided by the National Centers for Environmental Prediction (NCEP).
[b]Mean for December 1998 taken from atmospheric SHEBA data.
[c]Mean for July 2007 provided by NCEP.
[d]*Perovich and Elder* [2002].

asperities (h_{sa}), the adjacent ice sheets can be considered consolidated.

3. Model Parameters

[20] The model was run using parameters typical to the environments of the north Caspian Sea, the Arctic, and the Antarctic (see Table 1). Constant values were used for the forcing data (F_{LW}, F_{SW}, F_{sens}, F_{lat}, F_{ocean}), the ocean salinity (S_{ocean}), and the bulk salinity of the sea ice (S_{bulk}). The atmospheric data (F_{LW}, F_{SW}, F_{sens}, F_{lat}) were calculated from averages of the coldest months in the respective locations, using data collected during the Surface Heat Budget of the Arctic Ocean (SHEBA) experiment for the Arctic and the National Centers for Environmental Prediction for the north Caspian and the Antarctic. The oceanic heat flux (F_{ocean}) was set to 3 W m^{-2} for the Arctic and the Antarctic and 9.7 W m^{-2} for the north Caspian. These values were based on data collected over first-year sea ice in the Arctic between November 1997 and February 1998 as part of the SHEBA project [*Perovich and Elder*, 2002] and data collected in the north Caspian Sea.

[21] The fraction of salt (f) that is released into the liquid layer from the freezing interfaces was calculated from a series of consolidation experiments that were carried out on rafted sea ice in the Hamburg Ship Model Basin (HSVA). Salinity measurements were made of the upper liquid layer of a three-layer section of multiply rafted sea ice by drilling a hole down to the layer and sampling the liquid with a pipette. The salinity and temperature of the sample were then recorded using the WTW conductometer (LF191). The results of this experiment showed that as the thickness of the liquid layer decreased, the salinity of the layer gradually increased. From conservation of salt, f was calculated from

$$f = \frac{S_t - S_{ocean}}{S_{ocean}} \frac{1}{h_0/h_{sa} - 1}, \tag{18}$$

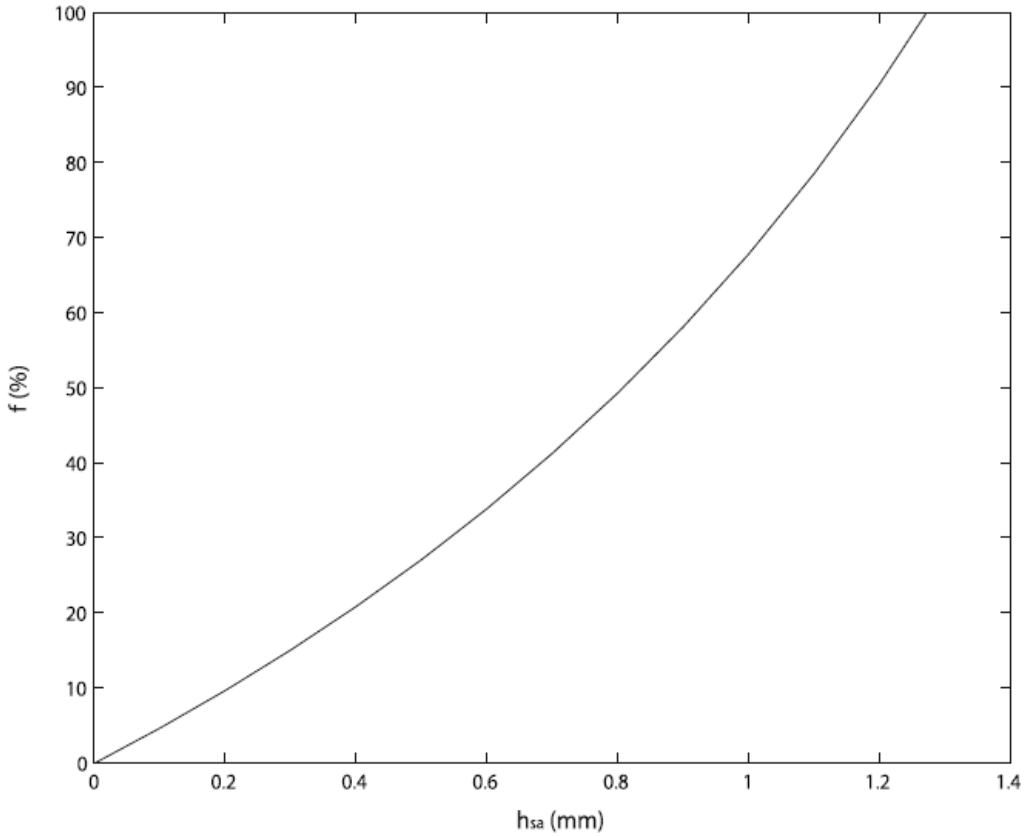

Figure 2. Dependence of the fraction of salt released (f) into the liquid layer on the surface asperity height (h_{as}), based on data collected during the HSVA ice tank experiments.

Table 2. Results for the Rate of Consolidation of Two Layers of Rafted Sea Ice

Location	Rate of Consolidation (min)
Caspian Sea	80
Arctic	891
Antarctic	542

where S_t = 77.3 parts per thousand (ppt) is the concentration of the liquid layer immediately prior to the upper two layers of ice becoming consolidated, S_{ocean} = 32.8 ppt is the concentration of the tank water prior to commencing the experiment, h_0 = 3 mm is the initial thickness of the liquid layer, and h_{sa} is the surface asperity height. The mechanism by which a fraction of the salt is released from the sea ice formed as the liquid layer freezes is not entirely clear. We speculate that the mechanism involved is brine convection highly localized to the vicinity of the interface between the ice and liquid layer, probably at a length scale of the order of the crystal spacing itself. Brine convection is discussed in more detail by *Notz and Worster* [2008].

[22] A plot of h_{sa} versus f is shown in Figure 2. The plot shows that on the basis of equation (18) the surface asperity height lies in the range of 0 to 1.27 mm. For our simulations, h_{sa} was set to 0.5 mm, making the fraction of salt released f equal to 27% (f' is approximately twice this value if one considers salt release only from freezing at the upper surface of the liquid layer and roughly equal freezing rates at the upper and lower interfaces).

4. Numerical Simulations

[23] In this section we present the results of our simulations. First, we describe the results for simple rafting and then multiple rafting. After this we present a series of sensitivity tests that were performed in order to test the model's sensitivity to certain parameters.

4.1. Simple Rafting

[24] The model was run for two layers of simply rafted sea ice using parameters typical of the environments of the north Caspian, the Arctic, and the Antarctic (see Table 2). The results show that the ice sheets all consolidated in under 15 h (900 min). The quickest rate was by far the north Caspian, followed by the Antarctic, and then, finally, the Arctic.

[25] Figure 3 shows the variation in the thickness of the liquid layer and its temperature with time. Figure 3 shows that as the thickness of the liquid layers reduces, so does the temperature of the liquid layer. This is because as the liquid layer freezes, increasing amounts of salt are released into the liquid layer, therefore reducing its freezing temperature. Figure 3b shows that prior to consolidation, the temperature of the liquid layer reduced to 265.5 K (−7.65°C), which

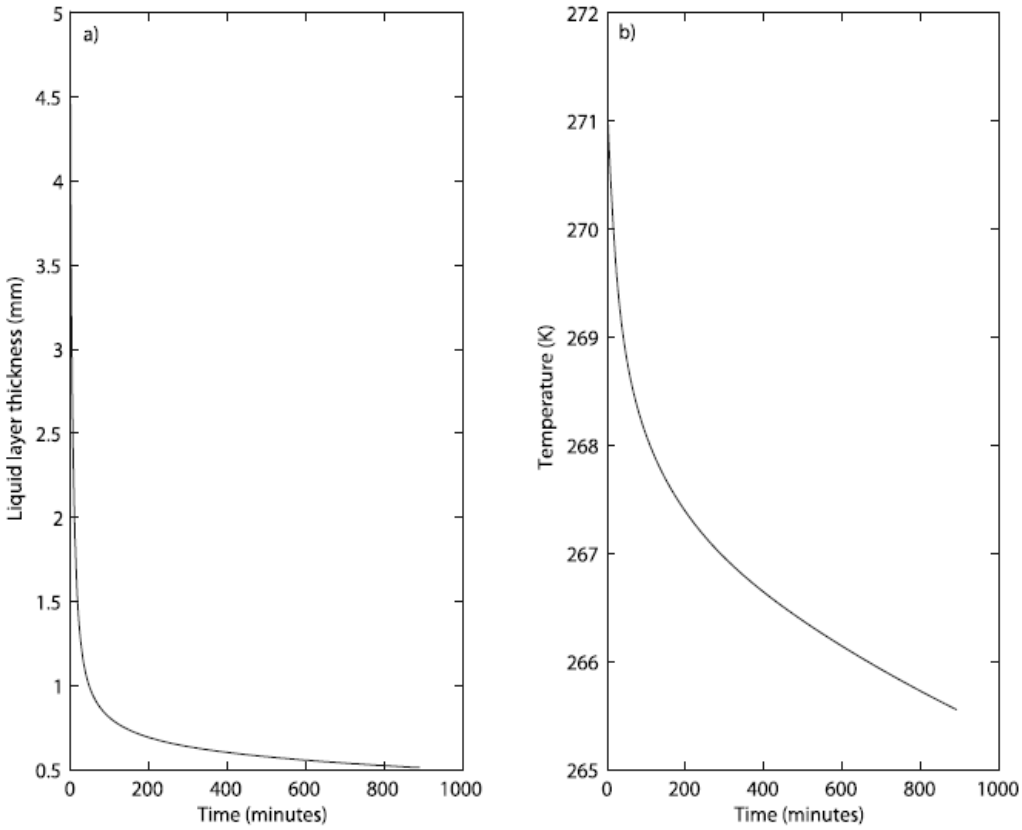

Figure 3. The evolution of (a) the thickness of the liquid layer and (b) the temperature in the liquid layer with time, using parameters representative of the Arctic.

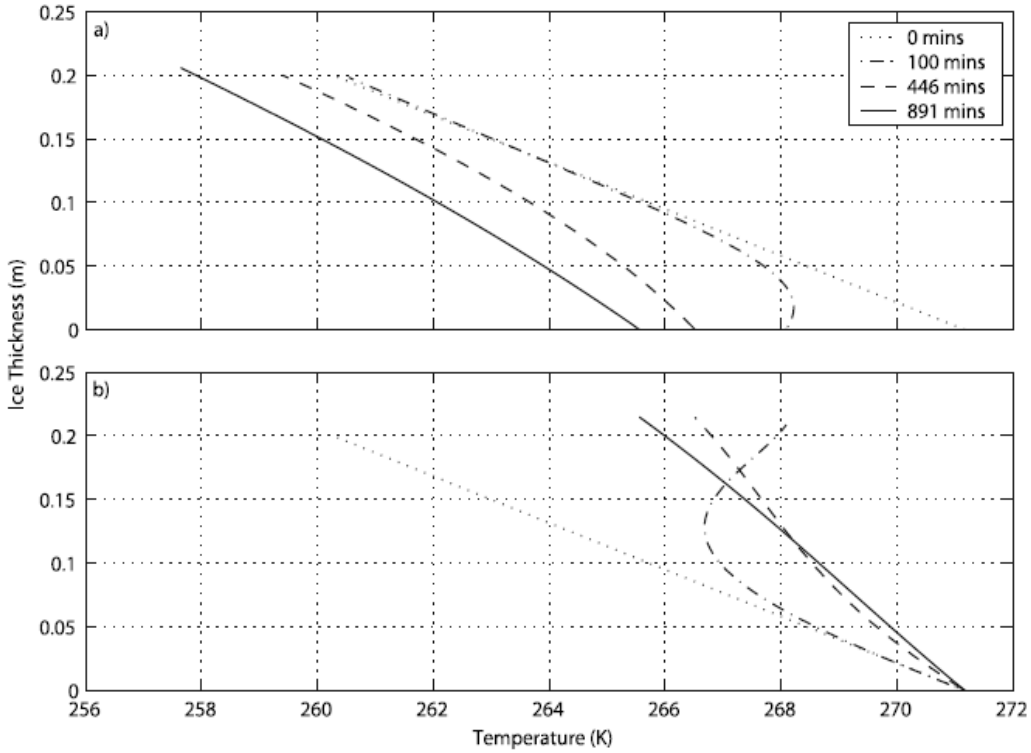

Figure 4. The evolution of the temperature profiles in a two-layer rafted section of sea ice using parameters representative of the Arctic: (a) the ice sheet that is in contact with the atmosphere and (b) the ice sheet that is in contact with the ocean. The dotted line shows the initial condition, the dashed-dotted line shows the temperature at 100 min, the dashed line shows the temperature at 446 min, and the solid line shows the temperature profile when the liquid layer has consolidated (at 891 min).

corresponds to salinity of 113 ppt (calculated by inverting equation (7)).

[26] Figure 4 shows the evolution of the temperature profiles in each ice sheet for the Arctic. This is of interest because the rate of consolidation is dependent on the temperature gradient on either side of the liquid layer (equation (17)). Figure 4a represents the ice sheet that is in contact with the atmosphere, and Figure 4b represents the ice sheet that is in contact with the ocean. The dotted line shows the initial condition, and the solid line shows the temperature profile when the upper layer has consolidated. Figure 4 shows that the temperature in the ice sheets is initially linear and then gradually evolves to reestablish an almost linear temperature profile throughout the two ice sheets.

4.2. Multiple Rafting

[27] In this section we present the results for a three-layer, multiply rafted section of sea ice (see Table 3). The results show that using parameters representative of the north Caspian Sea, it took 80 min for the ice sheets to consolidate, whereas when using Arctic and Antarctic parameters it took significantly longer to freeze. This is principally due to the differences in the salinity of the ocean and the sea ice. In each case the upper liquid layer froze faster than the lower layer did, which is as we would expect as the upper layer is close to the colder temperatures of the atmosphere. The time difference in the case of the north Caspian is, however, very small, indicating that there are enough cold reserves within the ice sheets to freeze both liquid layers almost simultaneously, which might explain why multiple rafting is a predominant ice hazard in the region. It is also interesting to note that in the cases of the Arctic and the Antarctic the consolidation time for the upper liquid layer was ~0.7 times shorter than the consolidation time for two layers of rafted ice (comparing Tables 2 and 3), indicating the effect that the oceanic heat flux and ocean temperature have on the consolidation process.

[28] Figure 5 shows the evolution of the temperature profiles in three layers of multiply rafted sea ice using parameters representative of the Arctic. Figure 5a represents the ice sheet that is in contact with the atmosphere, Figure 5b represents the ice sheet that is in the center of the rafted section, and Figure 5c represents the ice sheet that is in

Table 3. Results for the Rate of Consolidation of Three Layers of Multiply Rafted Sea Ice

	Rate of Consolidation (min)	
Model Run	Upper Liquid Layer	Lower Liquid Layer
Caspian Sea	78	80
Arctic	640	2198
Antarctic	423	1783

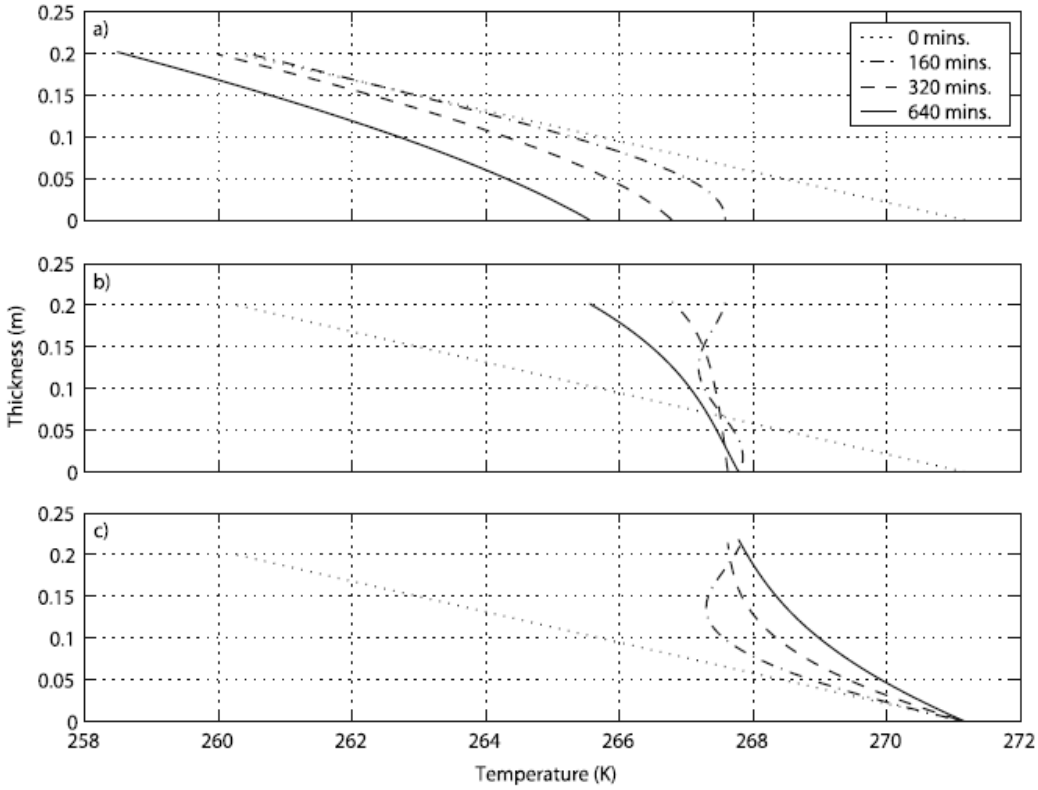

Figure 5. The evolution of the temperature profiles in a three-layer section of rafted sea ice using parameters specific to the Arctic: (a) the ice sheet that is in contact with the atmosphere, (b) the ice sheet that is in the center of the rafted section, and (c) the ice sheet that is in contact with the ocean. The dotted line shows the initial condition, the dashed-dotted line shows the temperature at 160 min, the dashed line shows the temperature at 320 min, and the solid line shows the temperature profile when the upper layer has consolidated (at 640 min).

contact with the ocean. The dotted line shows the initial condition, and the solid line shows the temperature profile when the upper layer consolidated. Figure 5 shows that the temperature at the upper liquid layer decreases with time until it consolidates at 640 min. The adjacent ice sheets were then merged, and the program continued until the lower liquid layer consolidated (see Figure 6). Figure 6 shows that the temperature of the lower liquid layer is now decreasing with time until it freezes after 2198 min.

4.3. Sensitivity Studies

[29] Since it is the first time that the consolidation of rafted sea ice has been investigated numerically, it is important to investigate the model's sensitivity to certain parameters that are not well known. To do such an analysis, a standard case must first be chosen, which we take to be the parameters for the Arctic listed in Table 1. In each sensitivity study, multiple runs were made, varying one parameter at a time, within a conceivable range, while holding the others constant at the standard case values. The parameters we examine are the initial liquid layer thickness h_0, the initial ice thickness H_0, the bulk salinity of the sea ice S_{bulk}, the salinity of the ocean S_{ocean}, the fraction of salt released into the liquid layer f, the surface asperity height h_{sa}, and the forcing data (F_{LW}, F_{SW}, F_{sens}, F_{lat}, F_{ocean}).

[30] The dependence of the consolidation time (C_{time}) on h_0, H_0, S_{bulk}, S_{ocean}, f, and h_{sa} is shown in Figure 7. Figure 7a shows the dependence of C_{time} on h_0. Figure 7a shows that the larger h_0 is, the longer C_{time} is. When h_0 is below 3 mm, C_{time} is very rapid, and for thicknesses greater than 4 mm, C_{time} increases by almost a factor of 3 for every millimeter increase in h_0. For values greater than 6 mm, model runs showed the liquid layer did not consolidate and started to rise after about 6000 min (see Figure 8). Figure 9 shows the temperature profiles for when h_0 was set to 7 mm. The solid lines show the temperature profiles in the ice sheets when the liquid layer thickness started to increase (at 5847 min). At this point, the temperature profiles are linear and of negative gradient, which promotes "melting" at the top of the lower ice sheet and freezing at the base of the upper ice sheet. We put the term melting in quotation marks because what is driving the phase change is the difference in salinity of the liquid layer and ice sheet; technically, the lower ice layer is said to dissolve, rather than melt [*Woods*, 1992]. What drives the heat transport into the liquid layer is the fact that the temperature of the liquid layer, being at the liquidus temperature appropriate to its high salinity, is lower than the temperature in the lower ice sheet. Sensible heat is extracted from the lower ice layer and converted into the latent heat of the liquid phase. Since the base of the ice sheet

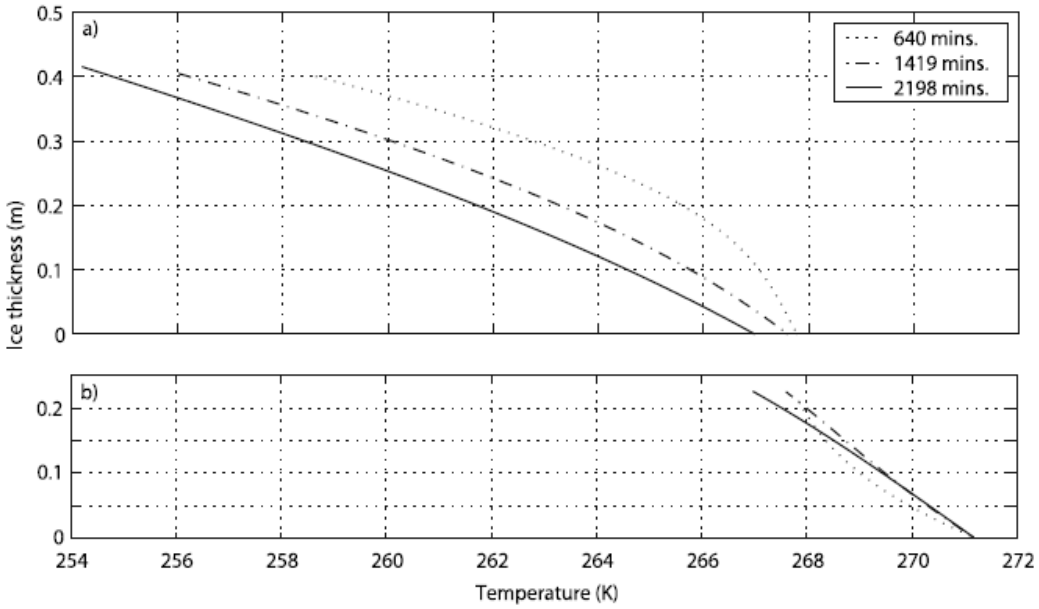

Figure 6. The evolution of the temperature profiles after the top two ice sheets shown in Figure 4 have frozen together: (a) the consolidated top two ice sheets and (b) the remaining ice sheet that is in contact with the ocean. The dotted line shows the temperature profile when the upper liquid layer consolidated (640 min), the solid line shows the temperature when the bottom liquid layer consolidated (2198 min), and the dashed line is midway between these two points (1419 min).

above the liquid layer is freezing and the top of the ice sheet below the liquid layer is melting, the liquid layer is migrating downward. To investigate this, we plotted the location of the freezing fronts with time (see Figure 10). Figure 10 shows that after an initial rise both liquid layers have migrated downward by ~0.1 m in about 6000 min.

[31] Figure 7b shows the dependence of C_{time} on H_0. Figure 7b shows that at both large and small ice layer thicknesses, the consolidation time increases. At large H_0 this is due to the reduced extraction of heat from the liquid layer to the atmosphere through the upper ice layer. At low H_0, the rate of diffusion of heat from the ocean into the

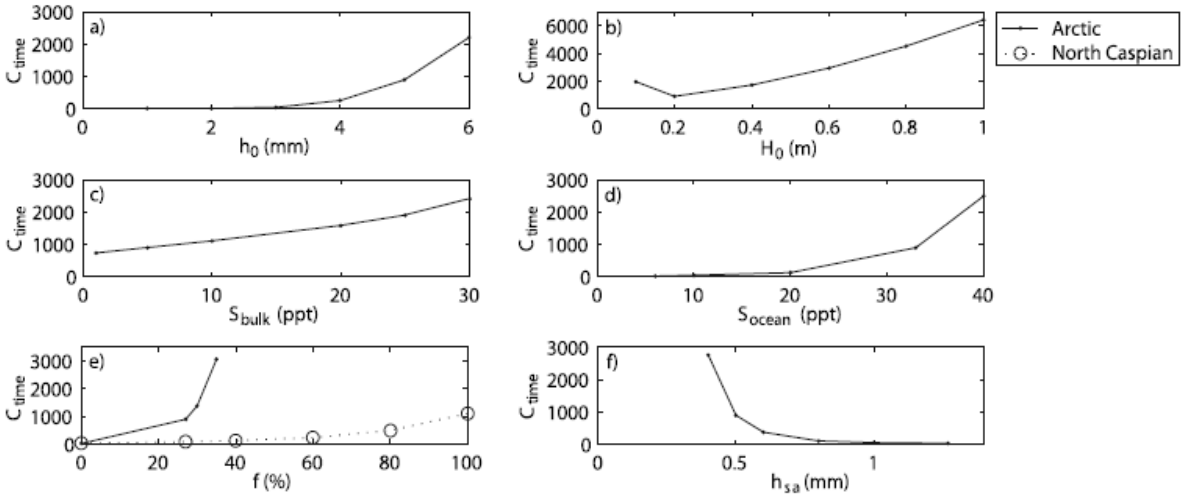

Figure 7. Dependence of the consolidation time (C_{time}) in minutes on (a) the initial liquid layer thickness h_0, (b) the initial ice thickness H_0, (c) the bulk salinity of the sea ice S_{bulk}, (d) the salinity of the ocean S_{ocean}, (e) the fraction of salt released into the liquid layer f, and (f) the surface asperity height h_{sa}. The solid line and the dashed line show the simulations run with parameters specific to the Arctic and the north Caspian, respectively.

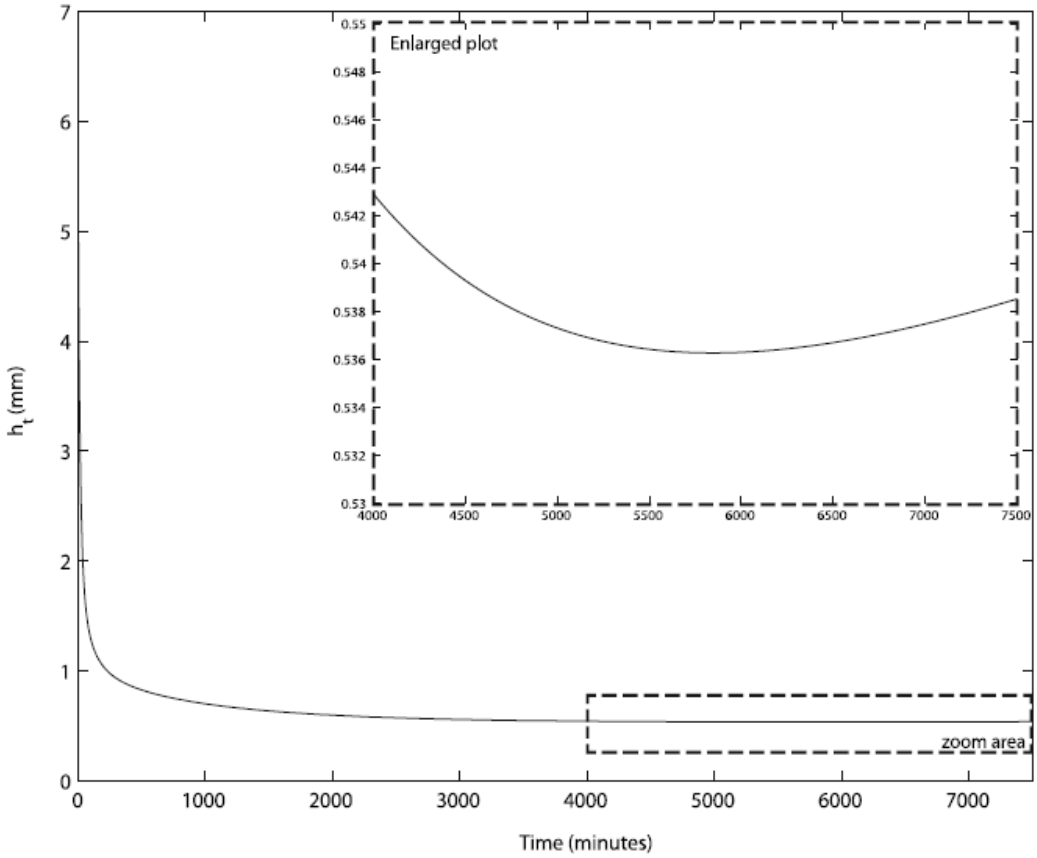

Figure 8. The rate at which the thickness of the liquid layer (h_t) is reducing with time in minutes when h_0 = 7 mm. The enlarged plot shows a zoom of the area in the dashed box.

liquid layer through the lower layer ice sheet is enhanced, slowing down consolidation.

[32] Figure 7c shows the model's sensitivity to S_{bulk}. The plot shows that the higher S_{bulk} is, the larger C_{time} is. This is because an increase in S_{bulk} lowers the thermal conductivity of the sea ice and increases its specific heat capacity, which reduces the ability of the sea ice to conduct heat away to the atmosphere, thus retarding the consolidation time.

[33] Figure 7d shows that the greater S_{ocean} is, the greater C_{time} is. This is because an increase in S_{ocean} lowers the freezing temperature of the ocean, thereby decreasing the initial temperature gradients in the ice sheets and thus the diffusional heat fluxes through them, so that C_{time} is increased. In addition, an increase in S_{ocean} also increases the initial salinity of the liquid layer, such that as consolidation proceeds, the liquid layer gets increasingly salty. At the high salinities reached just prior to the consolidation (~110 ppt using standard case parameters) the nonlinearity of the liquidus curve causes a greater than linear decrease in the freezing temperature of the liquid layer, which acts to further retard the consolidation time. This is why in Figure 7d we see a greater than linear increase in C_{time} for salinities higher than ~20 ppt, despite the fact that it has little effect on the freezing temperature of the ocean.

[34] To explore the uncertainty in the brine release process, the dependence of C_{time} on f for both the Arctic and north Caspian parameters was investigated while h_{sa} was held constant at 0.5 mm (see Figure 7e). As the fraction of salt released into the liquid layer during freezing f increases, the consolidation time increases because the freezing temperature of the liquid layer decreases. Figure 6e shows that for f greater than 35%, there are no points for the Arctic; this is because under these conditions the liquid layer did not consolidate. Conversely, for the north Caspian the effect of varying f from 0% to 100% varied the consolidation time between 30 and 1000 min. This is due to the differences in the salinity of the seawater.

[35] Figure 7f shows the sensitivity of the model to the surface asperity height h_{sa}. Figure 7f shows that the smaller h_{sa} is, the greater C_{time} is. This makes sense since the smaller the surface roughness, the greater the quantity of liquid that has to freeze before the asperities can effectively bond.

[36] The sensitivity of the model to the forcing data is shown in Figure 11. Figure 11 shows that C_{time} is sensitive to the incoming longwave, F_{LW}, and shortwave, F_{SW}, radiation and the sensible F_{sens} and the latent heat F_{lat} fluxes and rather insensitive to changes in the oceanic heat flux F_{ocean}. Since the variation in the radiative fluxes tends to be larger than the variation in the sensible and latent heat fluxes, changes in the radiative fluxes will tend to have a greater influence on the consolidation time. Note that in Figure 11b, F_{SW} is varied only from 0 to 125 W m^{-2}. This is

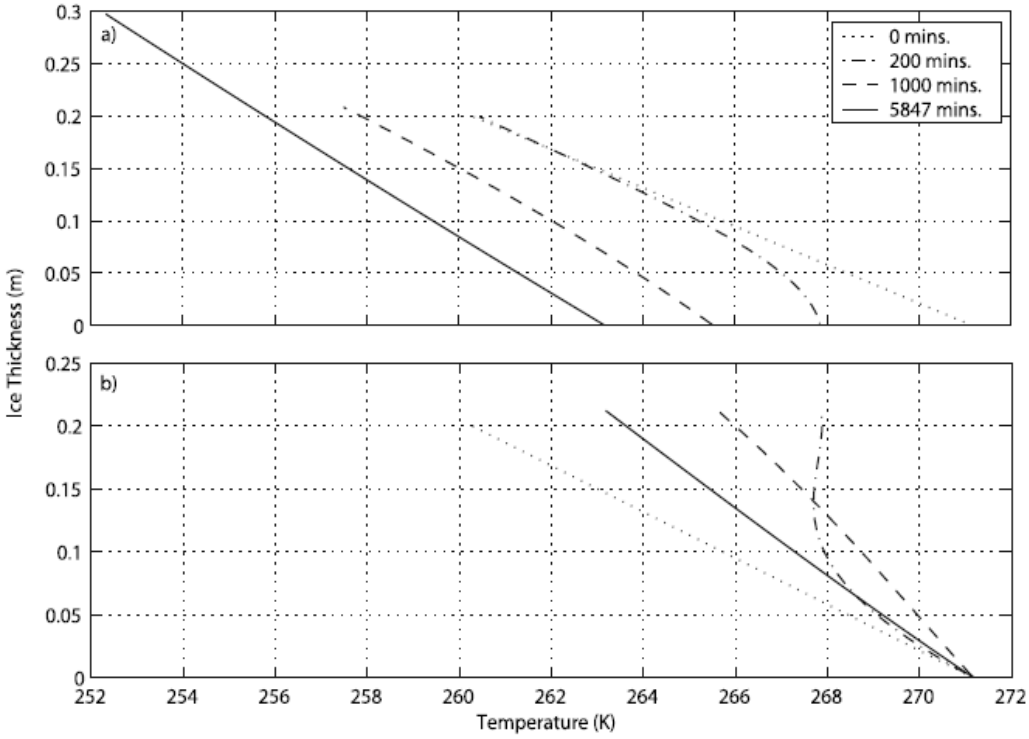

Figure 9. The temperature profiles in the ice sheets when $h_0 = 7$ mm. The dotted line shows the initial condition, and the solid line shows the temperature distribution when the liquid layer started to rise.

because for values higher than 125 W m^{-2} the ice sheets did not freeze.

5. Discussion and Concluding Remarks

[37] We have presented a one-dimensional, thermal consolidation model for rafted sea ice. Initial runs revealed that when f was greater than zero, the thickness of the liquid layers between the ice sheets reduced asymptotically with time, such that there always remained a thin saline liquid layer. Under these circumstances the ice sheets will never freeze. We therefore proposed a cutoff, such that when the liquid layer reached the size of the surface asperities the adjacent ice sheets could be considered consolidated.

[38] On the basis of our consolidation experiments that were carried out at the HSVA ice basin the surface asperity height was calculated to be between 0 and 1.27 mm. The experiments showed that the salinity of the liquid layer gradually increased with time, therefore indicating that there was a fraction of salt being released into the liquid layer. The fraction of salt that is being released, however, is somewhat uncertain because of the logistics of sampling such a tiny quantity of liquid. Our experimental results showed that prior to the top two layers of a three-layer stack becoming consolidated the salinity had reached 77.3 ppt. This therefore shows that brine is being released from the newly forming sea ice and/or that brine is draining out from the ice sheet above into the liquid layer. We speculate that the mechanism responsible for removing salt from the sea ice is highly localized brine convection at the ice-liquid layer interface.

[39] We considered the consolidation of both two layers and three layers of rafted sea ice. The results showed, using the parameters representative of the north Caspian, Antarctic, and Arctic, that it took about 1, 9, and 15 h, respectively, for two layers of rafted sea ice to consolidate. The consolidation time for three layers of ice in the north Caspian was the same as that for two layers of ice, indicating that there are enough cold reserves within the ice sheets to freeze the liquid layers. Conversely, it took significantly longer for three layers of rafted ice to freeze in the Antarctic (30 h) and the Arctic (37 h). The rapid consolidation of rafted ice in the Caspian Sea is due to the low salinity (6 ppt) of the water. Rapid consolidation might also permit subsequent rafting of the consolidated layers and may help to explain the prevalence of multiply rafted ice in the region.

[40] A number of sensitivity studies were conducted to determine the effect variations in model parameters and forcing fluxes had on the consolidation time for simply rafted Arctic sea ice. The results showed that typical variations in the oceanic heat flux and the sensible and latent heat fluxes had little effect on the consolidation time. However, the model was highly sensitive to changes in the initial thickness of the liquid layer h_0, the ice thickness, the salinity of the ocean, the fraction of salt release during freezing f, the surface asperity height h_{sa}, and the downward radiative fluxes. Most of these parameters can be quite well constrained because they have been widely researched; however, h_0, f, and h_{sa} are not well known. Therefore, we believe that further investigation of these parameters is needed before any concrete conclusions can be drawn about the rate of consolidation of rafted sea ice features.

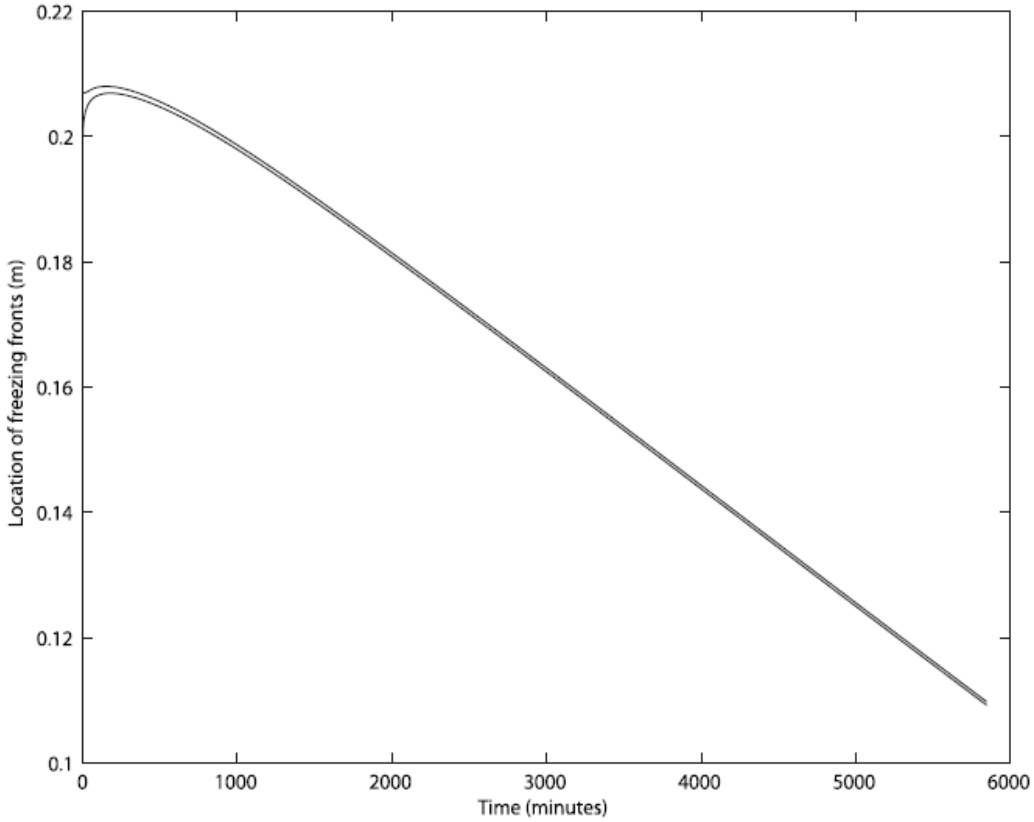

Figure 10. Location of the freezing fronts with time when $h_0 = 7$ mm.

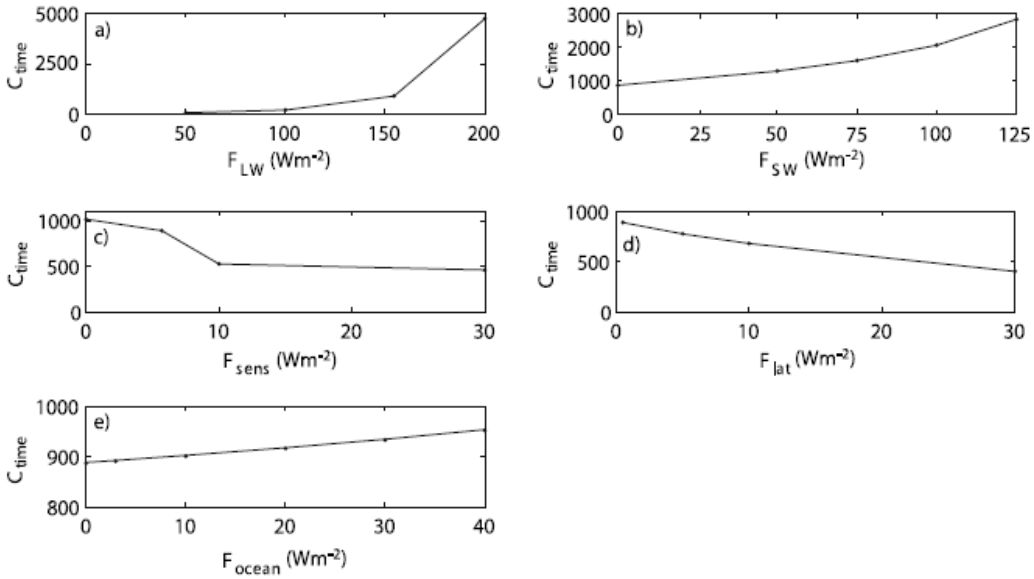

Figure 11. Dependence of the consolidation time (C_{time}) in minutes on (a) the downward longwave radiation flux F_{LW}, (b) the downward shortwave radiation flux F_{SW}, (c) the sensible heat flux F_{sens}, (d) the latent heat flux F_{lat}, and (e) the oceanic heat flux F_{ocean}.

[41] To our knowledge, there is no published experimental work on the consolidation of rafted sea ice, which is surprising considering it is one of the important deformation mechanisms in sea ice. *Marchenko and Chenot* [2009] carried out some consolidation experiments on drifting ice in the Barents Sea in April 2006. They measured the cohesion between two submerged ice disks that were ~15 cm in diameter and 3–4 cm thick and found that after a period of 2 days the disks had not frozen together. They also submerged an ice beam that had dimensions of 3 × 0.5 × 0.5 m below level ice and found that after a day it was still possible to move the beam using a shovel. While these results are inconclusive, they suggest that in some circumstances the ice sheets will never consolidate or will take a long time to consolidate.

[42] One of the questions that keeps coming up in discussions on the consolidation process of rafted sea ice is, does brine drainage occur throughout the ice layer? Brine drainage is the name given to density-driven convective overturning of brine within the sea ice and/or the ocean water immediately below the sea ice layer. The effect of brine drainage could be to replace the concentrated brine within the liquid layer with less saline brine, which would allow the liquid layers to freeze at a faster rate.

[43] For brine drainage to occur there needs to be sufficient forcing (e.g., buoyancy forcing), and the ice needs to be sufficiently permeable. The "law of fives" states that if the brine volume of sea ice is greater than 5%, the ice is sufficiently permeable for brine to travel through the ice given sufficient forcing [*Golden et al.*, 1998]. This brine volume corresponds to a temperature warmer than −5°C at a salinity of 5 ppt [*Frankenstein and Garner*, 1967]. In our model calculations for the Arctic and Antarctic we used a bulk salinity of 5 ppt, and the respective temperature plots (Figures 3, 4, and 5) show that the temperature exceeds −5°C only directly above and below the liquid layer and at the ice-ocean interface. Therefore, on the basis of this law, the ice would only be sufficiently permeable in these regions for brine drainage to occur. (In the case of the north Caspian the low salinity of sea ice means that the ice would not be sufficiently permeable for brine drainage to occur.) In particular, this means that even if a positive hydraulic head is produced during the rafting process, flushing will not occur in the winter cases we consider.

[44] Theoretical and experimental studies on the convection of mushy layers have shown that for convective overturning or gravity drainage to occur in sea ice, the local Rayleigh number must exceed a critical value $Ra_c \sim 10$ [*Worster*, 1992, 2000; *Wettlaufer et al.*, 1997; *Notz and Worster*, 2008]. We therefore calculated the Rayleigh number at different stages during the consolidation process for the Arctic, the Antarctic, and the north Caspian. The results showed that the Rayleigh number did not exceed Ra_c at any point. Therefore, on the basis of our calculations of the law of fives and the Rayleigh number we believe that there would be no brine drainage during the consolidation process and if there were it would take place only in localized regions directly above and below the liquid layer and at the ice-ocean interface. Certainly, there was no evidence of brine drainage throughout the ice sheets in our experiments in the HSVA. Salinity measurements of sail blocks from an ice ridge in the Barents Sea lend some support to our calculations [*Bonnemaire et al.*, 2003]. The sail blocks consisted of four layers of rafted ice, each 0.3 m in thickness, and had C-shaped salinity profiles repeating over the thickness of each layer, suggesting that layers of ice had consolidated without brine drainage taking place.

[45] Despite the importance of rafting, it has drawn very little attention in comparison to ridging over the past decade. Given that with the effects of global warming there is expected to be an overall thinning of sea ice in the Arctic [*Solomon et al.*, 2007], rafting and ridging events are likely to increase. Therefore, we believe that a greater understanding of rafted sea ice is going to be of importance in the years to come. We hope that this paper encourages future modeling, experiments, and fieldwork on rafted sea ice to help improve understanding of the consolidation process.

[46] **Acknowledgments.** We would like to thank Derek Mayne for many useful discussions. Support for this research was provided by the UK Natural Environment Research Council. D. L. Feltham would like to thank the Leverhulme Trust for financial support.

References

Babko, O., D. A. Rothrock, and G. A. Maykut (2002), Role of rafting in the mechanical redistribution of sea ice thickness, *J. Geophys. Res.*, *107*(C8), 3113, doi:10.1029/1999JC000190.

Bitz, C. M., and W. H. Lipscomb (1999), An energy-conserving thermodynamic model of sea ice, *J. Geophys. Res.*, *104*(C7), 15,669–15,677, doi:10.1029/1999JC900100.

Bonnemaire, B., K. V. Hoyland, P. Liferov, and P. O. Moslet (2003), An ice ridge in the Barents Sea. Part 1: Morphology and physical parameters in-situ, paper presented at 17th International Conference on Port and Ocean Engineering Under Arctic Conditions, Univ. of Sci. Technol., Trondheim, Norway.

Ebert, E. E., and J. A. Curry (1993), An intermediate one-dimensional thermodynamic sea ice model for investigating ice-atmosphere interactions, *J. Geophys. Res.*, *98*(C6), 10,085–10,109, doi:10.1029/93JC00656.

Feltham, D. (1998), Fluid dynamics and thermodynamics of sea ice., Ph.D. thesis, Univ. of Cambridge, Cambridge, U. K.

Feltham, D. L., N. Untersteiner, J. S. Wettlaufer, and M. G. Worster (2006), Sea ice is a mushy layer, *Geophys. Res. Lett.*, *33*, L14501, doi:10.1029/2006GL026290.

Frankenstein, G., and R. Garner (1967), Equations for determining the brine volume of sea ice from −0.5°C to −22.9°C, *J. Glaciol.*, *6*(48), 943–944.

Golden, K. M., S. F. Ackley, and V. I. Lytle (1998), The percolation phase transition in sea ice, *Science*, *282*, 2238–2241, doi:10.1126/science.282.5397.2238.

Hopkins, M. A., J. Tuhkuri, and M. Lensu (1999), Rafting and ridging of thin ice sheets, *J. Geophys. Res.*, *104*(C6), 13,605–13,613, doi:10.1029/1999JC900031.

Hoyland, K. V. (2002), Consolidation of first-year sea ice ridges, *J. Geophys. Res.*, *107*(C6), 3062, doi:10.1029/2000JC000526.

Marchenko, A., and C. Chenot (2009), Regelation of ice blocks in the water and the air, paper presented at 20th International Conference on Port and Ocean Engineering Under Arctic Conditions, Luleå Univ. of Technol., Luleå, Sweden.

Maykut, G. A., and N. Untersteiner (1971), Some results from a time-dependent thermodynamic model of sea ice, *J. Geophys. Res.*, *76*(6), 1550–1575, doi:10.1029/JC076i006p01550.

Melling, H., D. R. Topham, and D. A. Riedel (1993), Topography of the upper and lower surfaces of 10 hectares of deformed ice, *Cold Reg. Sci. Technol.*, *21*, 349–369, doi:10.1016/0165-232X(93)90012-W.

Notz, D., and M. G. Worster (2008), In situ measurements of the evolution of young sea ice, *J. Geophys. Res.*, *113*, C03001, doi:10.1029/2007JC004333.

Notz, D., J. S. Wettlaufer, and M. G. Worster (2005), A non-destructive method for measuring the salinity and solid fraction of growing sea ice in situ, *J. Glaciol.*, *51*(172), 159–166, doi:10.3189/172756505781829548.

Parmerter, R. R. (1975), A model of simple rafting in sea ice, *J. Geophys. Res.*, *80*(15), 1948–1952, doi:10.1029/JC080i015p01948.

Perovich, D. K., and B. Elder (2002), Estimates of oceanic heat flux at SHEBA, *Geophys. Res. Lett.*, *29*(9), 1344, doi:10.1029/2001GL014171.

Appendix D: MATLAB code for the consolidation model of rafted sea ice

The consolidation model of rafted sea ice was coded in MATLAB version 9. The model code comprises of a driver program 'two_layer.m' (Figure D.1) and 6 additional modules containing functions that are called from the main program (Figures D.2 to D.7). In the main programme, the forcing parameters (atmospheric, salinity, thermophysical, initial ice and liquid layer thicknesses), the grid size, the time step and the equations for the liquidus curve and solid fraction are first specified. The boundary condition at the ice surface is then solved to find the initial temperature at the ice surface using the 'solve' function. This is then used along with the liquidus temperature and ice thickness to define the initial condition in both ice sheets (Eq. 6.8). After this, arrays are pre-allocated for the parameters that are to be saved by the model, which helps to improve the performance and speed of the programme. The 'for' loop is then started, where the heat diffusion equation (Eq. 6.1) is solved for both ice sheets using the 'pdepe' function which calls the functions layerfun.m (Figure D.2), layeric1.m (Figure D.3) and layerbc.m (Figure D.4) for the upper ice sheet and layerfun2.m (Figure D.5), layeric2.m (Figure D.6) and layerbc2.m (Figure D.7) for the lower ice sheet. These functions define respectively, the components of the pde, the initial condition and the boundary conditions. The pdepe function outputs a temperature for every timestep at each point specified on the grid. In this set-up, a mesh of 11 nodes and a time step of 3 seconds were used. The solution from the 3rd time step is then used to determine the temperature gradient and the thermal conductivity (Eq. 6.4) at the growing ice interfaces. These are used, along with the volumetric latent heat, the solid fraction and the density ratio in the Stefan condition (Eqs. 6.11 & 6.13) to calculate the rate of ice growth at the respective interfaces. The amount of growth was then used to determine the concentration of the liquid layer (Eq. 6.15) and the thickness of the liquid layer (Eq. 6.16). The temperature of the liquid layer (Eq. 6.14), the thickness of the ice slabs and the initial condition are then updated for the next time step. The loop then continues for the number of times specified and outputs the results on three plots which show the thickness of the liquid layer as a function of time, the temperature evolution in the ice sheets and the concentration in the liquid layer. Each step in the programme is explained in greater detail by the comment fields marked in green after the percentage sign (%).

```
%-------------------------------------------------
% FORCING PARAMETERS
%-------------------------------------------------

% ATMOSPHERIC
F_LW=205; % downward longwave radiation
F_SW=76; % downward shortwave radiation
F_sens=3; % sensible heat flux
F_lat=-1; % latent heat flux
E=0.99; % emissivity [Ebert & Curry, 1993]
sigma=5.67e-8; % Stefan-Boltzmann constant
alpha=0.6; % varies from 0.5-0.7 for bare ice [Perovich, summer school]
io=0.4; % fraction of radiation absorbed at surface [Feltham & Taylor,
2007]
K=1.5; %shortwave bulk extinction coefficient of sea ice (1/m)
F_ocean=9.7; %oceanic heat flux

% SALINITY
C0=6; % initial salinity of gap-taken to be that of sea water (ppt)
Cb=1.7; % bulk concentration of sea ice.
F=0.1; % fraction of salt released into the liquid layer (LL)

% THERMOPHYSICAL
k_a=0.03; % conductivity of air (W/mK)-Weeks & Ackley (1982)
Va=0.025; % volume of air in sea ice- Timco & Frederking (1996)
L=3.014e8; % volumetric heat of fusion for sea ice (J/m^3)
c_i=1.883e6; % volumetric heat capacity of pure ice at 273K (J/m^3.K)
r=1.09; % density ratio of brine to ice

% ICE & LIQUID LAYER THICKNESSES
H0=0.1;
H=H0; % initial thickness of upper ice block (m)
H2=H0; % initial thickness of lower ice block (m)
h0=0.05; % initial thickness of liquid layer between two ice blocks (m)
ha=H0+h0; % position of boundary above LL
hb=H0; % position of boundary below LL
ho=0; % position of boundary at ice-ocean interface
h=h0;
%-------------------------------------------------

%-------------------------------------------------
% GRID AND TIME STEP SPACING
m = 0; % parameter corresponding to the symmetry of the problem. m can be
a slab=0, cylindrical=1, or spherical=2.
t = 1:1:3; % time step in seconds
x=0:0.01:H; % spatial grid size in meters
n=length(x);
t3=t(:,3)-0;
%-------------------------------------------------

%-------------------------------------------------
% Non-linear liquidus curve for NaCl
TL0=273.15+((-5.33e-7*C0^3)-(9.37e-6*C0^2)-(0.0592*C0));
TL=TL0;
%-------------------------------------------------
```

```
%-------------------------------------------------
% Finds the initial temp at ice surface using prescribed heat fluxes
syms T
Ta0=solve(E*(F_LW-(sigma*T.^4))+((1-alpha)*(1-io)*F_SW)-F_sens-
F_lat+(2.2*(TL-T)/H0));
Ta=Ta0(1);
%-------------------------------------------------

%-------------------------------------------------
% SOLID FRACTIONS
sf0=1-(Cb/C0); % at the ice_ocean boundary
sf_1=1-(Cb/C0);  % at the ice-liquid layer boundaries
%-------------------------------------------------

%-------------------------------------------------
% INITIAL CONDITIONS FOR THE ICE SHEETS
IC=[((Ta-TL)/H) TL];
IC2=[((Ta-TL)/H) TL];
% IC is then updated in the loop by using polyfit to get the coefficients
% of a best-fit curve.
%-------------------------------------------------------------------------

%-------------------------------------------------------------------------
ti0=10000; % no of times you want to run code (time(seconds)=ti0*3)

% pre-allocating space for arrays.
x=zeros(1,n,ti0);
x2=zeros(1,n,ti0);
u=zeros(1,n,ti0);
u2=zeros(1,n,ti0);
delta_h=zeros(1,ti0);
h1=zeros(1,ti0);
h2=zeros(1,ti0);
C=zeros(1,ti0);

for ti=1:ti0;

% Specifies the grid
x(:,:,ti)=linspace(0,H,n);
x2(:,:,ti)=linspace(0,H2,n);

% Solves the non-linear heat diffusion equations where u is the
temperature in degrees Kelvin
sol(:,:,ti)=pdepe(m,@layerfun,@layeric1,@layerbc,x(:,:,ti),t,[],H,Ta,...
TL,Cb,IC,k_a,Va,L,c_i,K,io,alpha,F_SW,E,F_LW,sigma,F_sens,F_lat);
sol2(:,:,ti)=pdepe(m,@layerfun2,@layeric2,@layerbc2,x2(:,:,ti),t,[],...
H,H2,Ta,TL,TL0,Cb,IC2,L,k_a,Va,c_i,K,io,alpha,F_SW,h);
% takes the third solution (i.e. time 3 seconds)
u(:,:,ti)=sol(3,:,ti); % temperature distribution in upper ice block
u2(:,:,ti)=sol2(3,:,ti); % temperature distribution in upper ice block
clear sol sol2

% To get du/dx at the moving interfaces.
Dx=x(:,n,ti)-x(:,n-1,ti);
Dx2=x2(:,n,ti)-x2(:,n-1,ti);
Dua=u(:,2,ti)-u(:,1,ti);
DuDxa=Dua./Dx; %du/dx above the gap.
Dub=u2(:,n,ti)-u2(:,n-1,ti);
DuDxb=Dub./Dx2; % du/dx below the gap
```

```
Duo=u2(:,2,ti)-u2(:,1,ti);
DuDxo=Duo./Dx2; % du/dx at the ocean-ice interface

% thermal conductivity (k_eff) for upper ice block
theta=u(:,:,ti)-273.15;
k_i=1.16*(1.91-(8.66e-3.*theta)+(2.97e-5.*theta.^2));
k_b=0.4184.*(1.25+0.030.*theta+0.00014.*theta.^2);
k_bi=((2*k_i+k_a-(2*Va)*(k_i-k_a))./(2*k_i+k_a+Va*(k_i-k_a))).*k_i;
k_eff=k_bi+(k_bi-k_b).*(((5.33e-7*Cb^3)+(9.37e-
6*Cb^2)+(0.0592*Cb))./theta);

% thermal conductivity (k_eff) for lower ice block
theta2=u2(:,:,ti)-273.15;
k_i2=1.16*(1.91-(8.66e-3.*theta2)+(2.97e-5.*theta2.^2));
k_b2=0.4184.*(1.25+0.030.*theta2+0.00014.*theta2.^2);
k_bi2=((2*k_i2+k_a-(2*Va)*(k_i2-k_a))./(2*k_i2+k_a+Va*(k_i2-k_a))).*k_i2;
k_eff2=k_bi2+(k_bi2-k_b2).*(((5.33e-7*Cb^3)+(9.37e-
6*Cb^2)+(0.0592*Cb))./theta2);

% To get the rate at which the boundaries are moving using Stefan
conditions
DhDta=(DuDxa*k_eff(1))/(L*sf_1*r); %above LL
DhDtb=(DuDxb*k_eff2(n))/(L*sf_1*r); %below LL
DhDto=((DuDxo*k_eff2(1))+F_ocean)/(L*sf0*r); %at ice-ocean interface

ha=ha+(DhDta*t3); %growth after 3 seconds
h1(ti)=ha; % new position of interface above LL
hb=hb+(DhDtb*t3);
h2(ti)=hb;
ho=ho+(DhDto*t3); % new position of interface above LL

% Gives the rate at which the gap is closing with time.
delta_h(ti)=ha-hb;
h=delta_h(ti);

%-------------------------------------------------------------------------
% SPECIFY VALUES FOR THE NEXT LOOP
%-------------------------------------------------------------------------

% Calculates the new concentration of LL
C(ti,:)=C0+(C0*F*((h0/delta_h(ti))-1));

% Calculates new freezing temp. of LL
TL=273.15+((-5.33e-7*C(ti)^3)-(9.37e-6*C(ti)^2)-(0.0592*C(ti)));

sf_1=1-(Cb/C(ti)); % new solid fraction

% This gives the next time step
tf=t;
a=t(3)+(t(2)-t(1)); b=a+(t(3)-t(1));
t=a:t(2)-t(1):b;

% Calculates the new thickness of ice blocks
delta_ha=(H0+h0)-ha; %amount of growth above LL
H=H0+delta_ha;
delta_hb=hb-H0; %amount of growth below LL
delta_ho=0-ho; %amount of growth at ice-ocean interface
```

```
H2=H0+delta_hb+delta_ho;

% Calculates the coeff. of the Eq. of the line of the last u output
% for the new initial condition.
IC=polyfit(x(:,:,ti),u(:,:,ti),7); % for upper ice block
IC2=polyfit(x2(:,:,ti),u2(:,:,ti),9); % for lower ice block

end

%-------------------------------------------------------------------------
% PLOTS
%-------------------------------------------------------------------------
% plot of how the thickness of the LL changes with time
time=0:3/60:tf(:,3)/60;
HH=[h0 delta_h(1:ti)]*100;
figure; plot(time,HH);
xlabel('Time (minutes)');
ylabel(Thickness of the liquid layer (cm)');

% plot of how the heat is distributed in the ice sheets.
U=[TL0 Ta]-273.15;
X=[0 H0]*100;
figure; subplot(2,1,1);
plot(U,X,'k:',u(:,:,ti/2)-273.15,x(:,:,ti/2)*100,'k-.',u(:,:,ti)-
273.15,x(:,:,ti)*100,'k-');
subplot(2,1,2)
plot(U,X,'k:',u2(:,:,ti/2)-273.15,x2(:,:,ti/2)*100,'k-.',u2(:,:,ti)-
273.15,x2(:,:,ti)*100,'k-');
ylabel('Ice Thickness (cm)');
xlabel('Temperature (°C)');

% plot of how the concentration in the LL changes with time
C=[C0 C(1:ti)];
plot(time,C);
xlabel('Time (minutes)');
ylabel('Concentration of the liquid layer (ppt)');
```

Figure D.1. Driver program entitled 'two_layer.m'

```
% Define the components of the pdepe for the upper ice sheet.
function [c,f,s] =layerfun(x,t,u,DuDx,H,Ta,TL,Cb,IC,k_a,Va,L,c_i,K,io,
alpha,F_SW,E,F_LW,sigma,F_sens,F_lat)
%-------------------------------------------------------------------------
% To calculate the effective thermal conductivity
%-------------------------------------------------------------------------
theta=u-273.15;
k_i=1.16*(1.91-(8.66e-3.*theta)+(2.97e-5.*theta.^2)); % Conductivity of
pure ice (W/mK)- pure polycrystalline ice Sakazume and Seki (1978)
k_bi=((2*k_i+k_a-(2*Va)*(k_i-k_a))./(2*k_i+k_a+Va*(k_i-k_a))).*k_i;
% Conductivity of bubbly ice - Schwerdtfeger (1963)
k_b=0.4184.*(1.25+0.030.*theta+0.00014.*theta.^2); %Conductivity of brine
k_eff=k_bi+(k_bi-k_b).*(((5.33e-7*Cb^3)+(9.37e-
6*Cb^2)+(0.0592*Cb))./theta);
%-------------------------------------------------------------------------
% To calculate the effective specific heat capacity
%-------------------------------------------------------------------------
c_eff=c_i+(L.*(((5.33e-7*Cb^3)+(9.37e-6*Cb^2)+(0.0592*Cb))./(theta.^2)));
% J/m3K
```

```
c = c_eff;
f = k_eff*DuDx;
s =(K*io*(1-alpha)*F_SW*exp(-K*(H-x)));
```

Figure D.2. layerfun.m

```
% Defines the initial condition for the upper ice sheet where initially
% u(x,0)=(((Ta-TL)*x)/H)-TL

function u0 = layeric1(x,H,Ta,TL,Cb,IC,k_a,Va,L,...
c_i,K,io,alpha,F_SW,E,F_LW,sigma,F_sens,F_lat)

Sz=size(IC,2);
for k=1:Sz
    X(k)=x^(Sz-k);
end
X=X(:);
u0 = IC*X;
```

Figure D.3. layeric1.m

```
% Defines the boundary condition for the upper ice sheet

function [pl,ql,pr,qr] = layerbc(xl,ul,xr,ur,t,H,Ta,TL,Cb,IC,k_a,Va,L,
c_i,K,io,alpha,F_SW,E,F_LW,sigma,F_sens,F_lat)
%-------------------------------------------------------------------------

pl = ul-TL; % base of ice sheet held at freezing temp. of liquid layer
ql = 0;
pr=(E*(F_LW-(sigma*ur.^4))+((1-alpha)*(1-io)*F_SW)-F_sens-F_lat);
qr = -1;
```

Figure D.4. layerbc.m

```
% Defines the components of the pde for the lower ice sheet to use pdepe.

function [c,f,s] = layerfun2(x2,t,u2,DuDx2,H,H2,Ta,...
TL,TL0,Cb,IC2,L,k_a,Va,c_i,K,io,alpha,F_SW,h)

%-------------------------------------------------------------------------
% To calculate the effective thermal conductivity
%-------------------------------------------------------------------------
theta2=u2-273.15;
k_i2=1.16*(1.91-(8.66e-3.*theta2)+(2.97e-5.*theta2.^2)); % Conductivity
of solid ice
% (W/mK)- pure polycrystalline ice Sakazume and Seki (1978)
k_bi2=((2*k_i2+k_a-(2*Va)*(k_i2-k_a))./(2*k_i2+k_a+Va*(k_i2-k_a))).*k_i2;
% Conductivity of bubbly ice-Schwerdtfeger (1963)
k_b2=0.4184.*(1.25+0.030.*theta2+0.00014.*theta2.^2);
% %Conductivity of brine (Lange & Forke, 1952)
k_eff2=k_bi2+(k_bi2-k_b2).*(((5.33e-7*Cb^3)+(9.37e-
6*Cb^2)+(0.0592*Cb))./theta2); % W/mK



%-------------------------------------------------------------------------
% To calculate the effective specific heat capacity
```

```
%-------------------------------------------------------------------------
c_eff2=c_i+(L.*(((5.33e-7*Cb^3)+(9.37e-
6*Cb^2)+(0.0592*Cb))./(theta2.^2))); % J/m3K

c = c_eff2;
f = k_eff2*DuDx2;
s =(K*io*(1-alpha)*F_SW*exp(-K*(H+h+(H2-x2))));
```

Figure D.5. layerfun2.m

```
% Defines the initial condition for the lower ice sheet where initially
% u(x,0)=(((Ta-TL)*x)/H)-TL

function u20 =
layeric2(x2,H,H2,Ta,TL,TL0,Cb,IC2,L,k_a,Va,c_i,K,io,alpha,F_SW,h)
Sz=size(IC2,2);
for i=1:Sz
    X2(i)=x2^(Sz-i);
end
X2=X2(:);
u20 = IC2*X2;
```

Figure D.6. layeric2.m

```
% Defines the boundary condition for the lower ice sheet
% u(0,t)= u(h,t) = TL.

function [pl,ql,pr,qr] = layerbc2(x2l,u2l,x2r,u2r,...
t,H,H2,Ta,TL,TL0,Cb,IC2,L,k_a,Va,c_i,K,io,alpha,...
F_SW,h)

pl = u2l-TL0; % base of ice sheet kept at its freezing temp.
ql = 0;
pr = u2r-TL; % top of ice sheet held a freezing temp. of liquid layer
qr = 0;
```

Figure D.7. layerbc2.m

Appendix E: Additional plots from the laboratory experiments on the consolidation of rafted sea ice

In this appendix, I present the plots of all the consolidation experiments that were used to determine the times that the ice blocks had consolidated. 'Thermodynamic' consolidation was taken as the time that the temperature in the liquid layer ceased to decrease rapidly and changed to a more gradual decrease. This was estimated by fitting a best fit line to the temperature data recorded during rapid decrease and finding the time that the readings started to deviate from this trend. 'Mechanical' consolidation was taken as the time that the salinity of the samples extracted from the liquid layer with a needle and syringe became constant. This I estimate by fitting a best fit line to the data recorded just prior to the salinity becoming constant and finding the crossover point with the constant salinity values. These times have been indicted on the plots by superimposing lines on the graphs. Greater explanations are given in the figure captions. The approximate times that the ice blocks had consolidated, along with the test parameters are presented in Table E.1.

Table E.1. The thermodynamic and mechanical consolidation times for each test.

Test no.	Initial salinity of solution (ppt)	Nominal ice thickness (cm)	Nominal gap thickness (cm)	Approximate times that the ice had consolidated (minutes)	
				Thermodynamic	Mechanical
1*	6	7	1	700 (11hrs, 40mins)	17500 (12days, 3hrs, 40mins)
2	0	7	1	430 (7hrs, 10mins)	5000 (3day, 11hrs, 20mins)
3	33	7	1	1000 (16hrs, 40mins)	50000 (34days, 17hrs, 20mins)
4	6	10	1	1620 (1day, 3hrs)	21400 (14days, 21hrs)
5	6	14	1	2200 (1day, 12hrs, 40mins)	28600 (19days, 20hrs)
6	6	7	0.5	420 (7hrs)	10000 (6days, 22hrs, 40mins)
7	6	7	2	1120 (18hrs, 40min)	32900 (22 days, 20hrs)

*standard case

Test 1: The standard case experiment

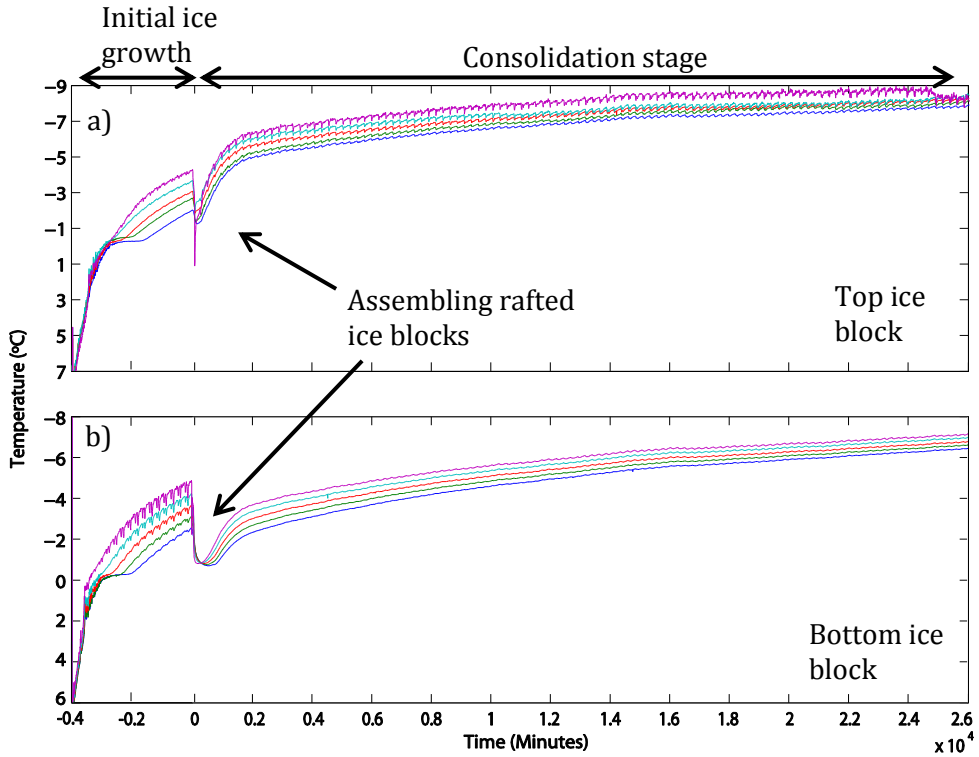

Figure E.1. Temperature-time traces for the standard case experiment (test 1), where plot a) shows the temperatures recorded by the thermistor probe in the top ice block and plot b) shows the temperatures recorded in the bottom ice block. Negative time refers to the 'initial ice growth' stage and positive time refers to the 'consolidation stage'.

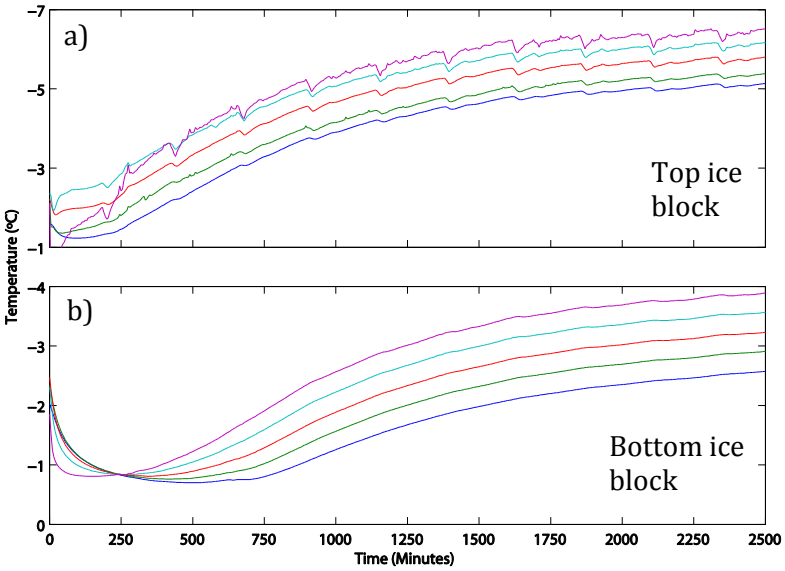

Figure E.2. Enlarged plot of the first 2500 minutes of consolidation.

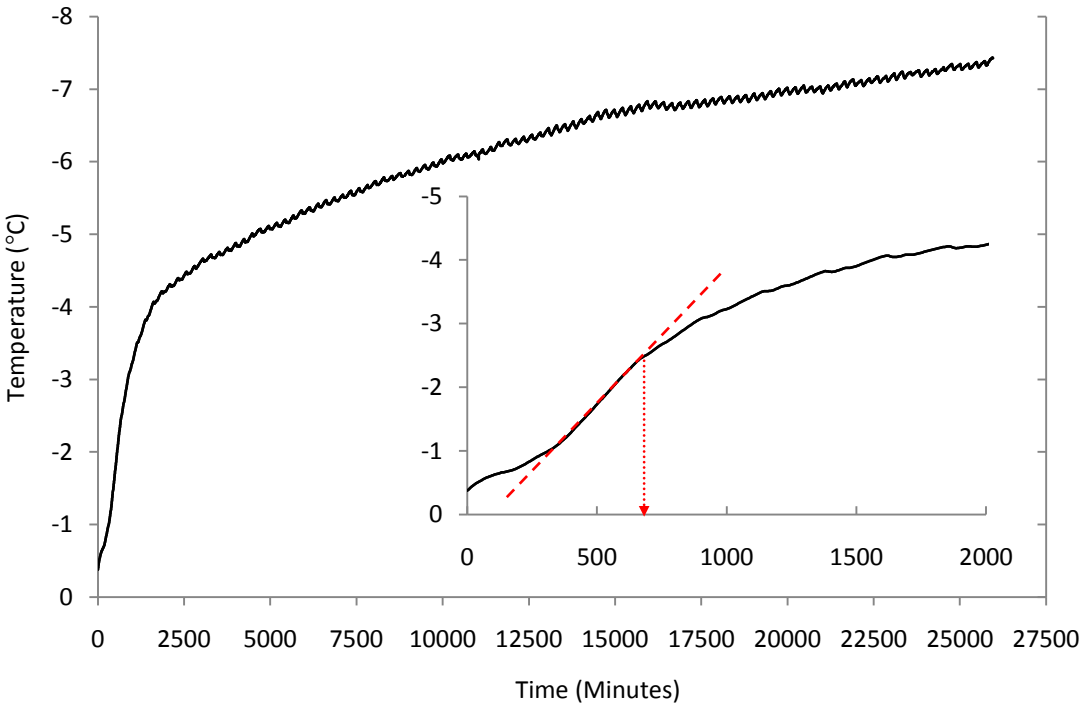

Figure E.3. Temperature evolution of the liquid layer for the standard case experiment (test 1). The enlarged plot shows a zoom of the first 2000 minutes of consolidation. By fitting a best fit line to the data recorded during the rapid decrease in temperature and finding the time that the temperature started to deviated from this trend I estimate that the ice sheet thermodynamically consolidated at ~700 minutes.

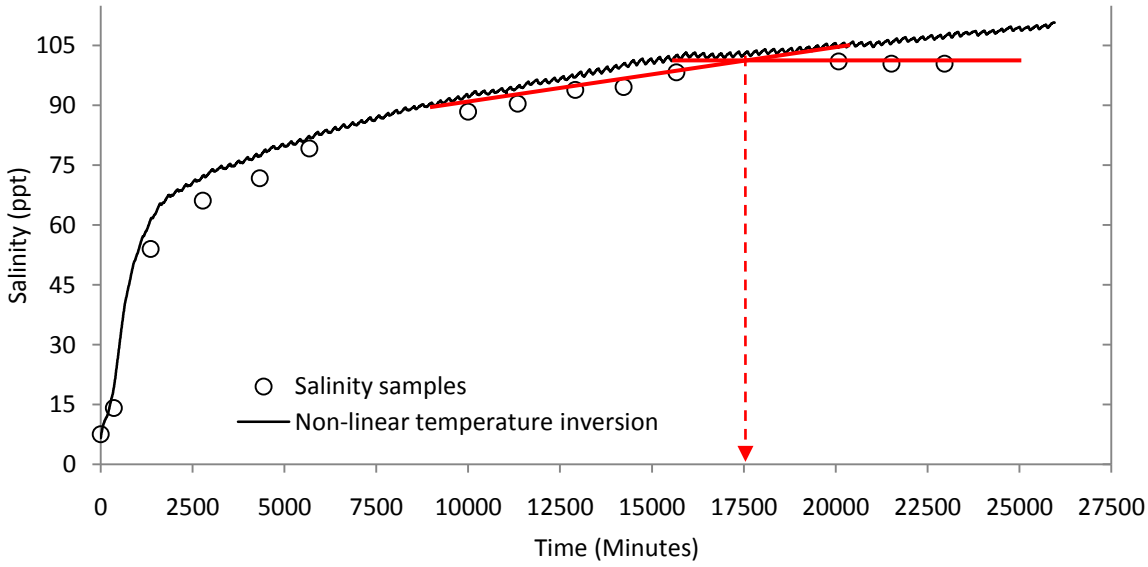

Figure E.4. Salinity evolution in the liquid layer for the standard case experiment (test 1). The circles represent the samples that were taken with a needle and syringe and the black line the temperature readings that were inverted using the non-linear liquidus curve (Eq. 7.2). Mechanical consolidation was taken as the time that the salinity of the samples extracted from the liquid layer became constant, which took place at ~17500 minutes.

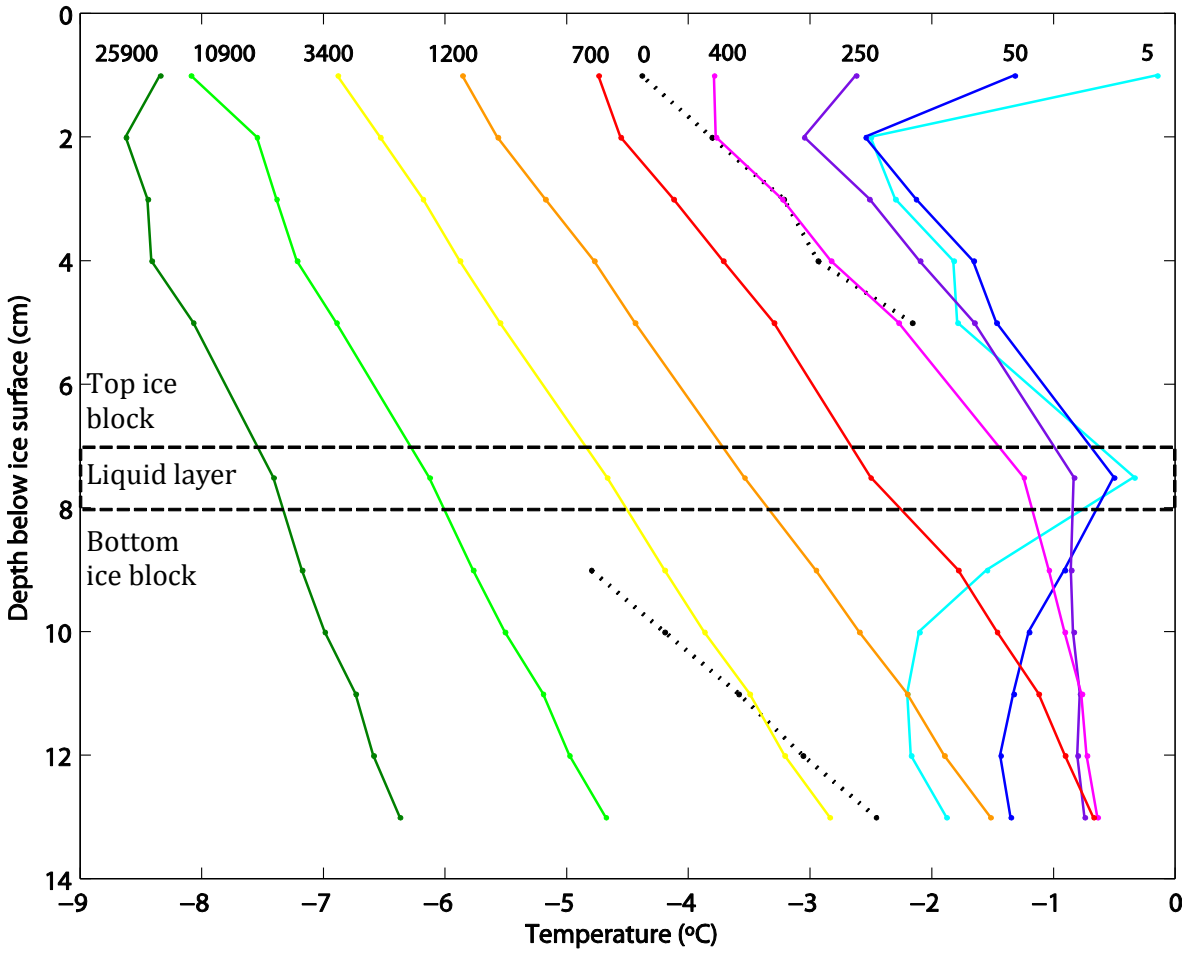

Figure E.5. The temperature evolution in the ice sheets and the liquid layer as a function of depth and time for the standard case experiment (test 1). The dotted line shows the temperature in the ice blocks prior to when the trace heating had been turned on and the solid lines the temperature profiles at different times of interest.

Test 2: The freshwater experiment

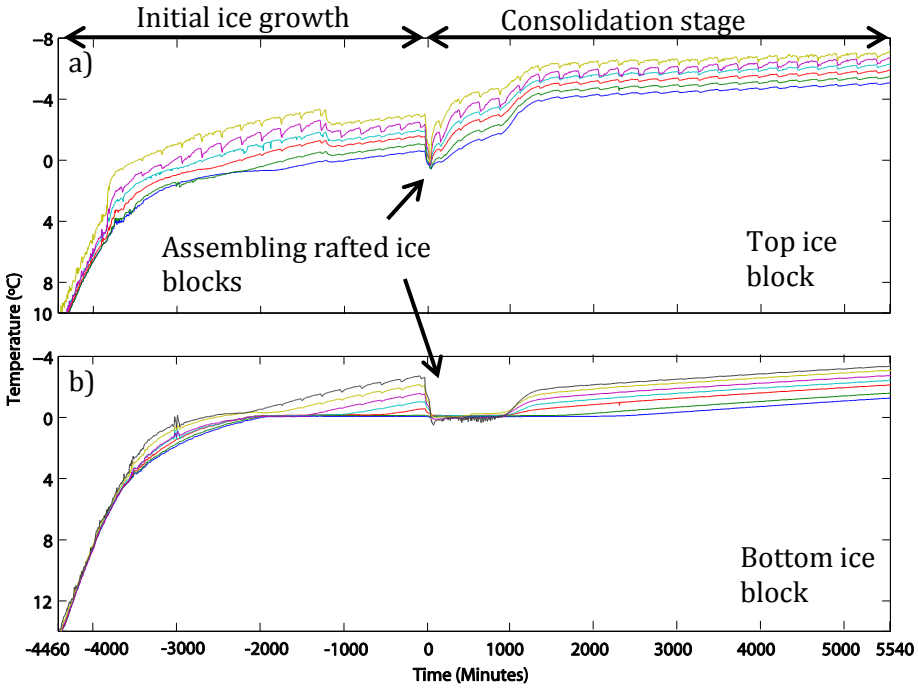

Figure E.6. Temperature-time traces for the freshwater experiment (test 2), where plot a) shows the temperatures recorded by the thermistor probe in the top ice block and plot b) shows the temperatures recorded in the bottom ice block. Negative time refers to the 'initial ice growth' stage and positive time refers to the 'consolidation stage'.

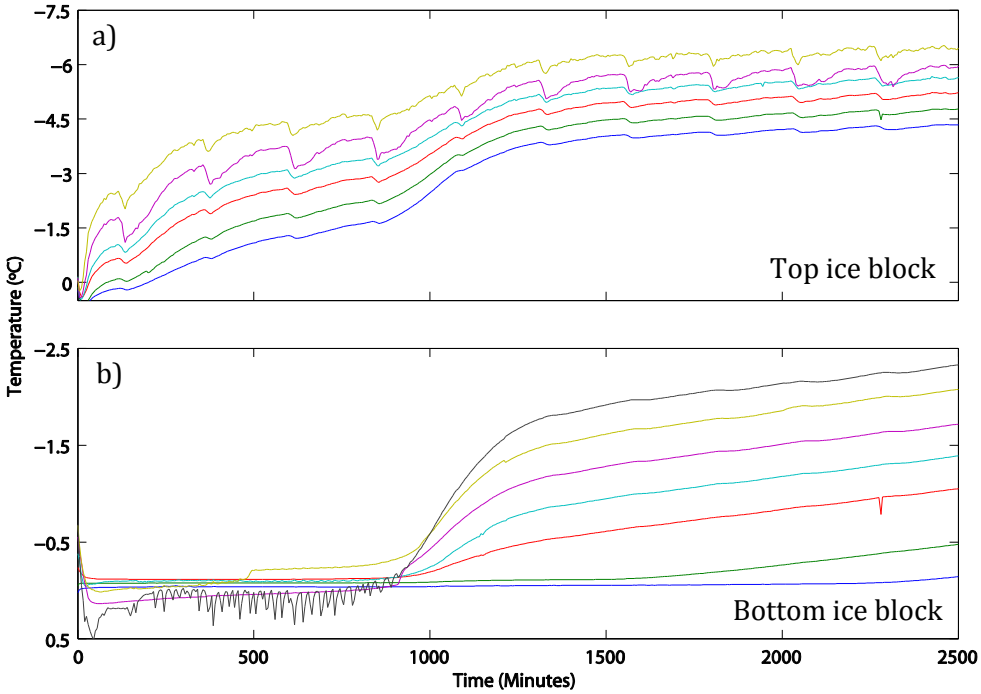

Figure E.7. Enlarged plot of the first 2500 minutes of consolidation.

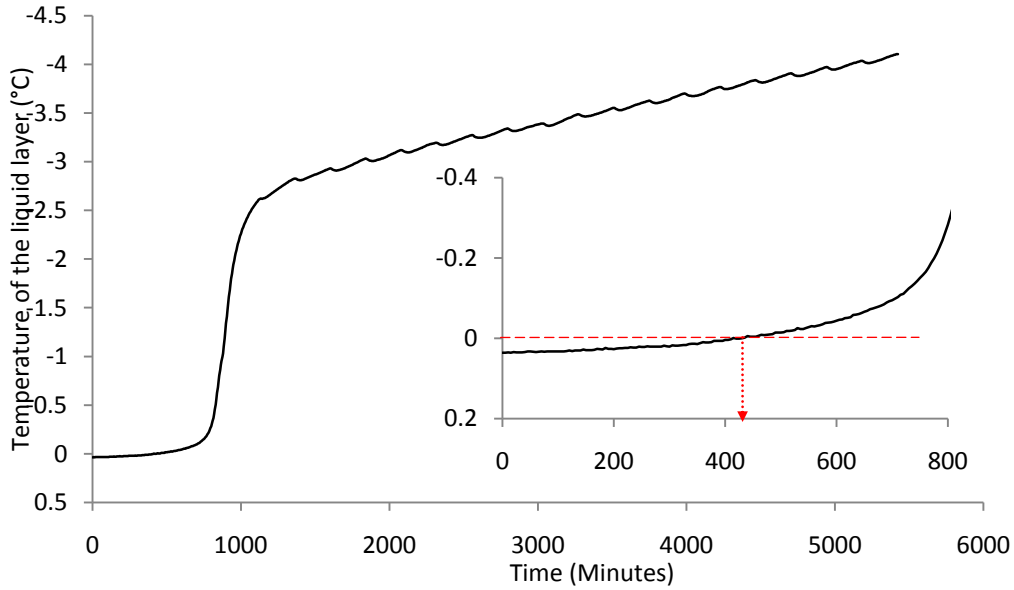

Figure E.8. Temperature evolution of the liquid layer for the freshwater experiment (test 2). The enlarged plot shows a zoom of the first 800 minutes of consolidation. Can see that the temperature starts to decrease below zero after ~430 minutes.

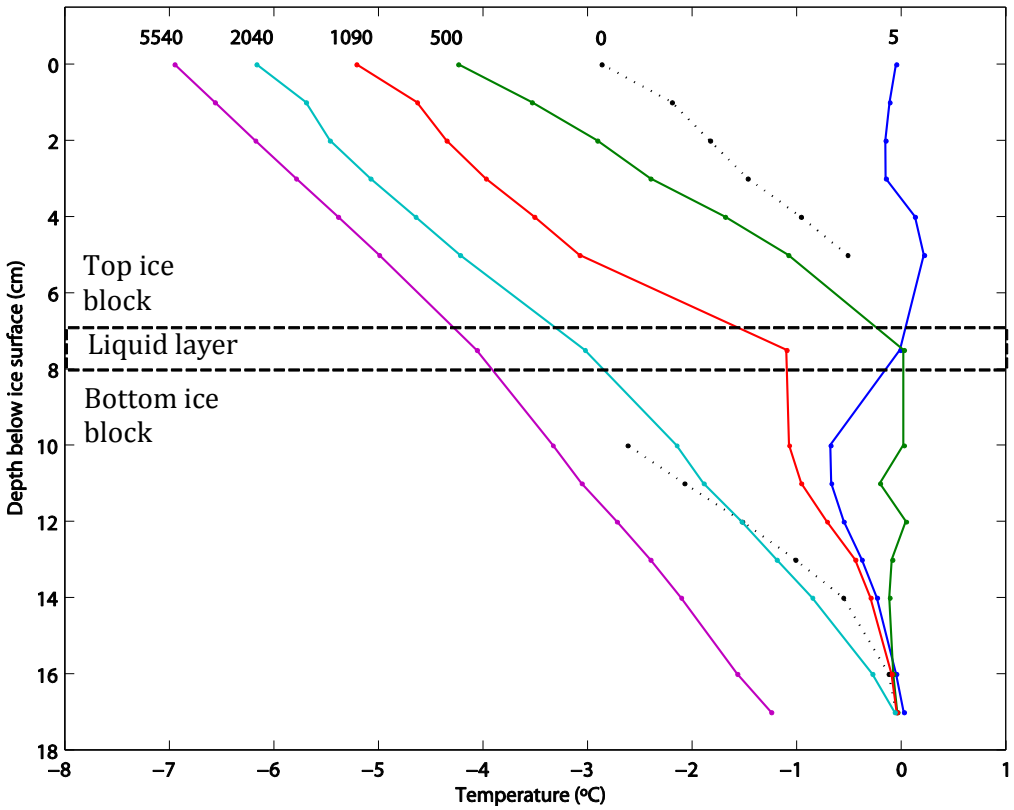

Figure E.9. The temperature evolution in the ice sheets and the liquid layer as a function of depth and time for the freshwater experiment (test 2). The dotted line shows the temperature in the ice blocks prior to when the trace heating had been turned on and the solid lines the temperature profiles at different times of interest.

Test 3: The 33 ppt experiment

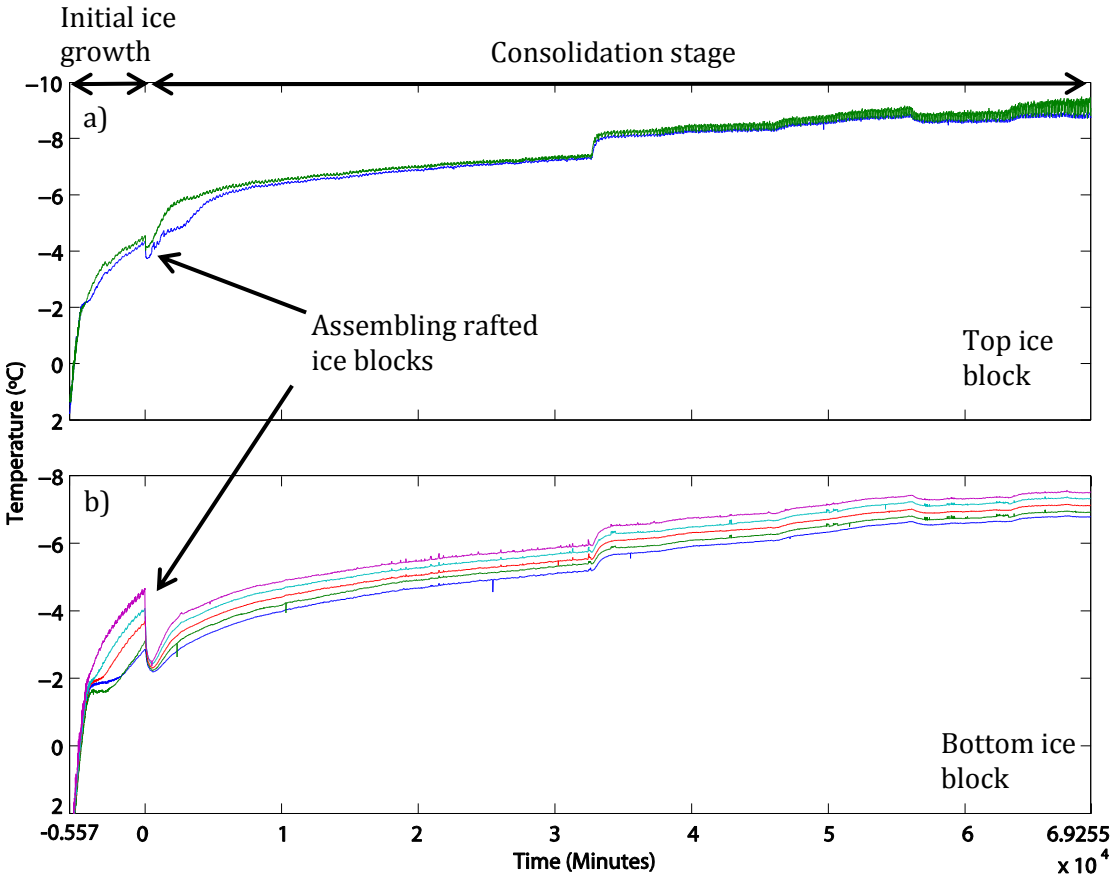

Figure E.10. Temperature-time traces for the 33 ppt experiment (test 3), where plot a) shows the temperatures recorded by the thermistor probe in the top ice block and plot b) shows the temperatures recorded in the bottom ice block. Negative time refers to the 'initial ice growth' stage and positive time refers to the 'consolidation stage'. Note that by this stage in the experimental program the probe in the top block was badly corroded and I was only able to get reliable readings from 2 of the thermistors.

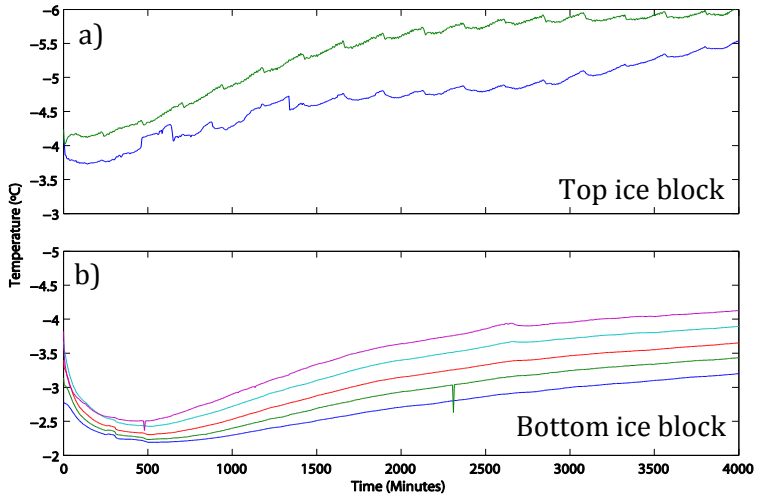

Figure E.11. Enlarged plot of the first 4000 minutes of consolidation.

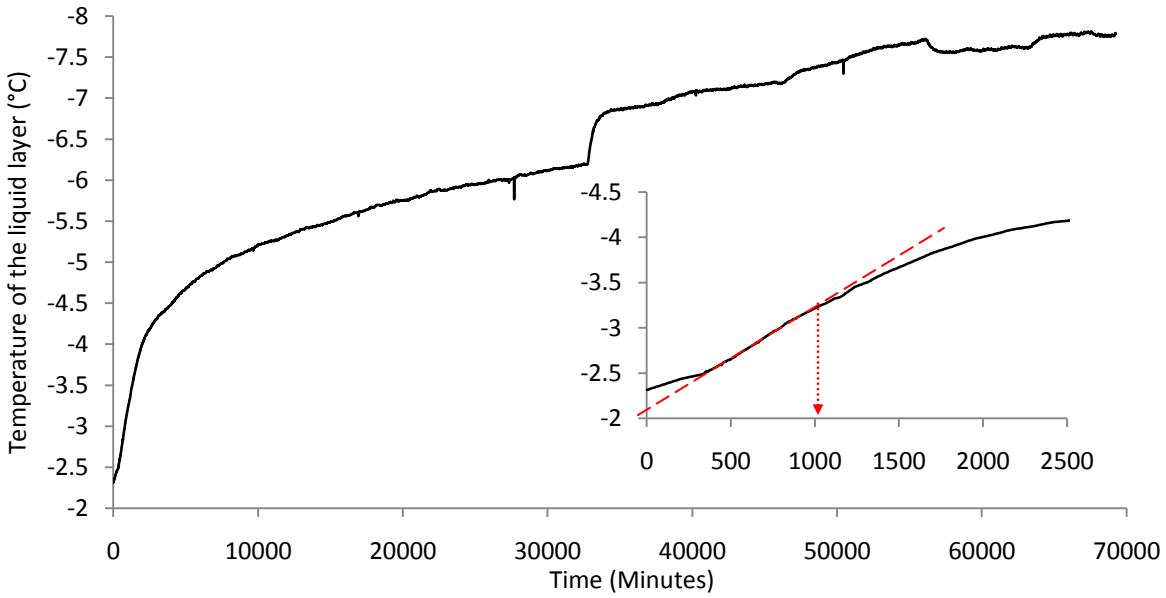

Figure E.12. Temperature evolution of the liquid layer for the 33 ppt experiment (test 3). The enlarged plot shows a zoom of the first 2500 minutes of consolidation. By fitting a best fit line to the data recorded during the rapid decrease in temperature and finding the time that the temperature started to deviated from this trend I estimate that the ice sheet thermodynamically consolidated at ~1000 minutes.

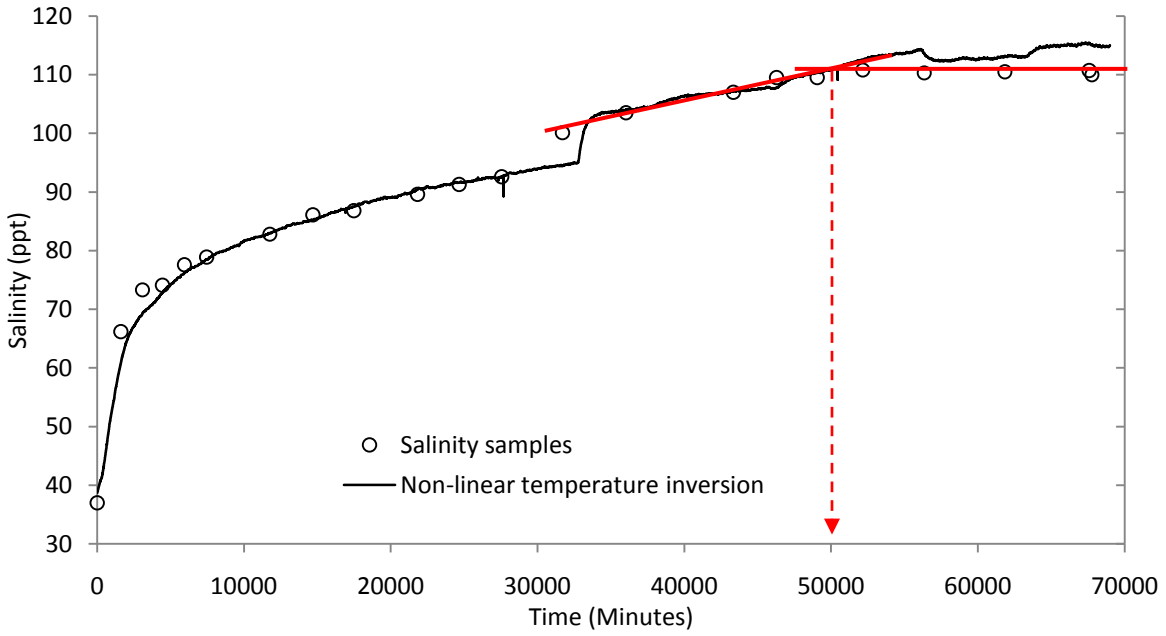

Figure E.13. Salinity evolution in the liquid layer for the 33 ppt experiment (test 3). The circles represent the samples that were taken with a needle and syringe and the black line the temperature readings that were inverted using the non-linear liquidus curve (Eq. 7.2). Mechanical consolidation was taken as the time that the salinity of the samples extracted from the liquid layer became constant, which took place at ~50000 minutes.

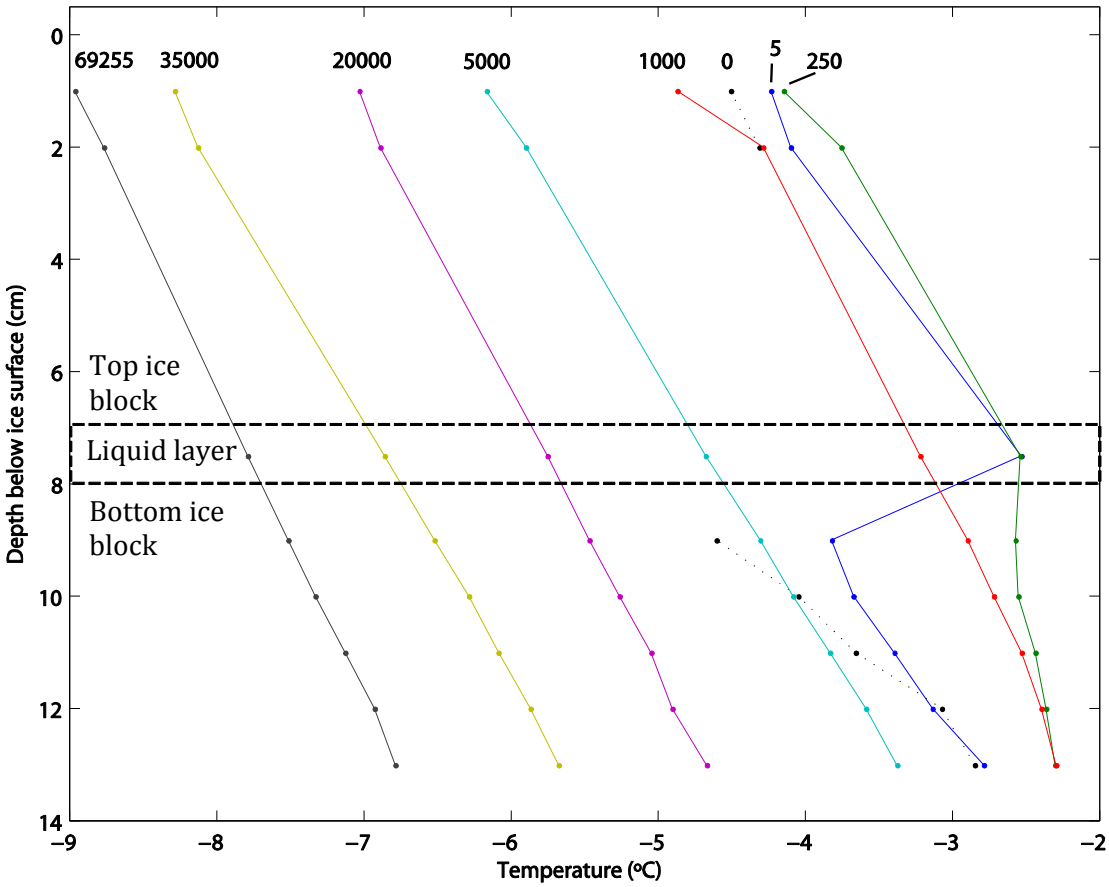

Figure E.14. The temperature evolution in the ice sheets and the liquid layer as a function of depth and time for the 33 ppt experiment (test 3). The dotted line shows the temperature in the ice blocks prior to when the trace heating had been turned on and the solid lines the temperature profiles at different times of interest.

Test 4: The 10 cm thick ice experiment

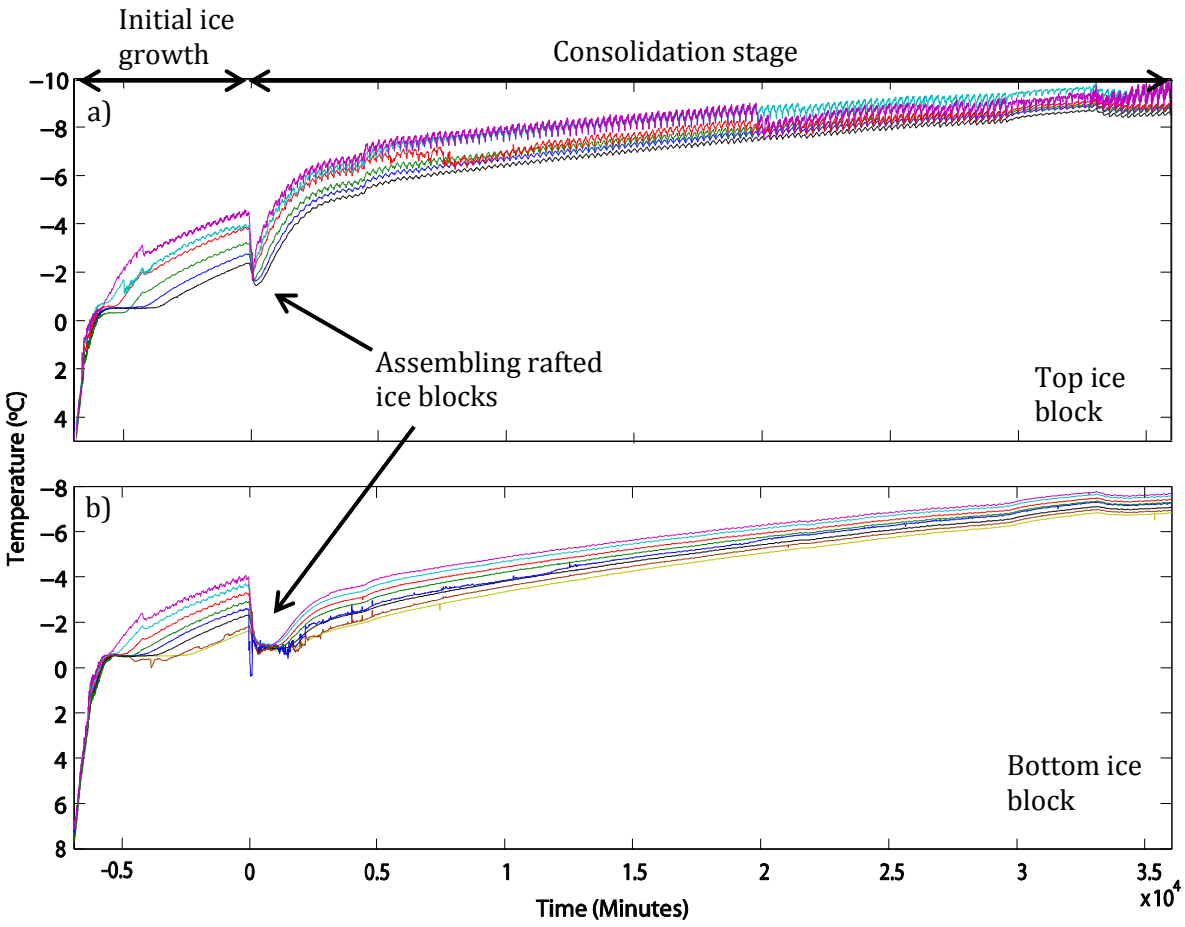

Figure E.15. Temperature-time traces for the 10 cm thick experiment (test 4), where plot a) shows the temperatures recorded by the thermistor probe in the top ice block and plot b) shows the temperatures recorded in the bottom ice block. Negative time refers to the 'initial ice growth' stage and positive time refers to the 'consolidation stage'. Note that in this plot there are only 6 reading in the top ice block and 8 in the bottom ice block. This is because in the top ice block two thermistors had frozen into place above the ice surface as the probe had accidentally slipped during set-up. In addition, the 3rd thermistor down from the ice surface and the top thermistor in the top and bottom ice blocks, respectively, had corroded and therefore were not functioning correctly.

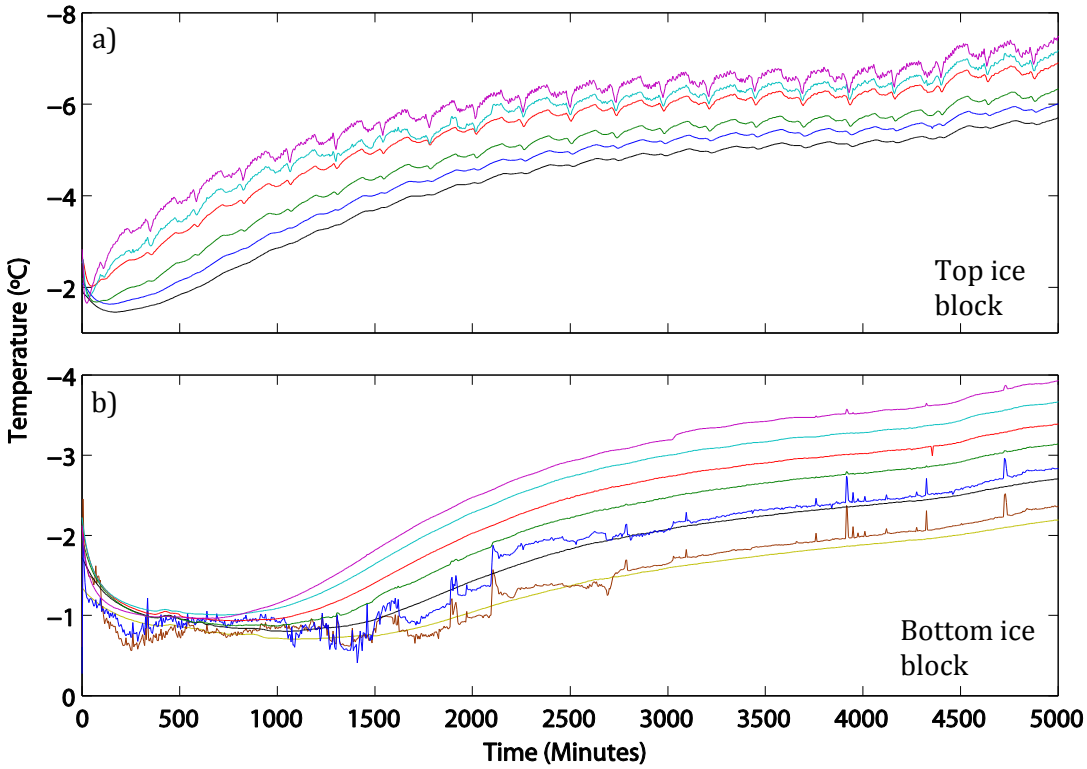

Figure E.16. Enlarged plot of the first 5000 minutes of consolidation.

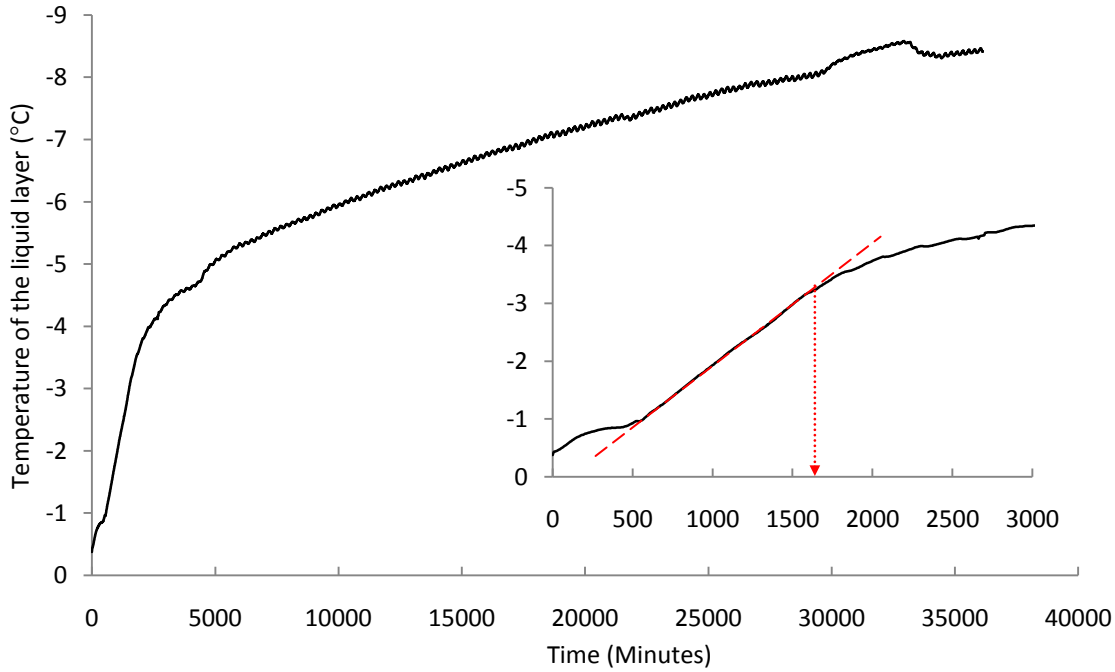

Figure E.17. Temperature evolution of the liquid layer for the 10 cm thick ice experiment (test 4). The enlarged plot shows a zoom of the first 3000 minutes of consolidation. By fitting a best fit line to the data recorded during the rapid decrease in temperature and finding the time that the temperature started to deviated from this trend I estimate that the ice blocks thermodynamically consolidated at ~1620 minutes.

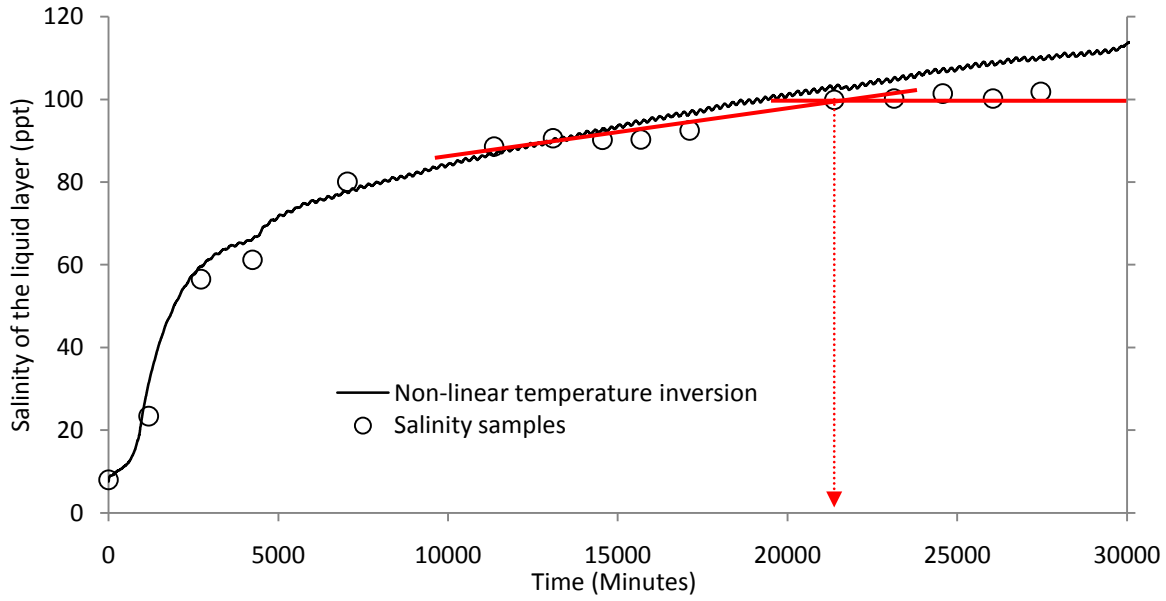

Figure E.18. Salinity evolution in the liquid layer for the 10 cm thick ice experiment (test 4). The circles represent the samples that were taken with a needle and syringe and the black line represents the temperature readings that were inverted using the non-linear liquidus curve (Eq. 7.2). The salinity of the samples extracted from the liquid layer became constant around 21400 minutes.

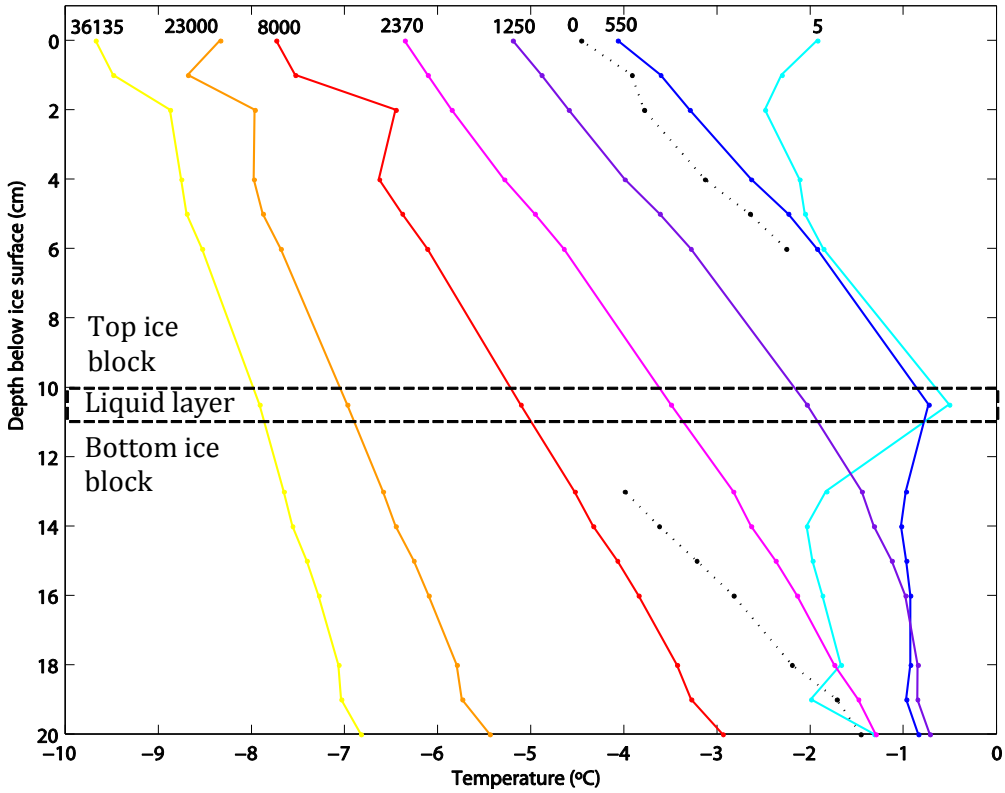

Figure E.19. The temperature evolution in the ice sheets and the liquid layer as a function of depth and time for the 10 cm thick ice experiment (test 4). The dotted line shows the temperature in the ice blocks prior to when the trace heating had been turned on and the solid lines the temperature profiles at different times of interest.

Test 5: The 14 cm thick ice experiment

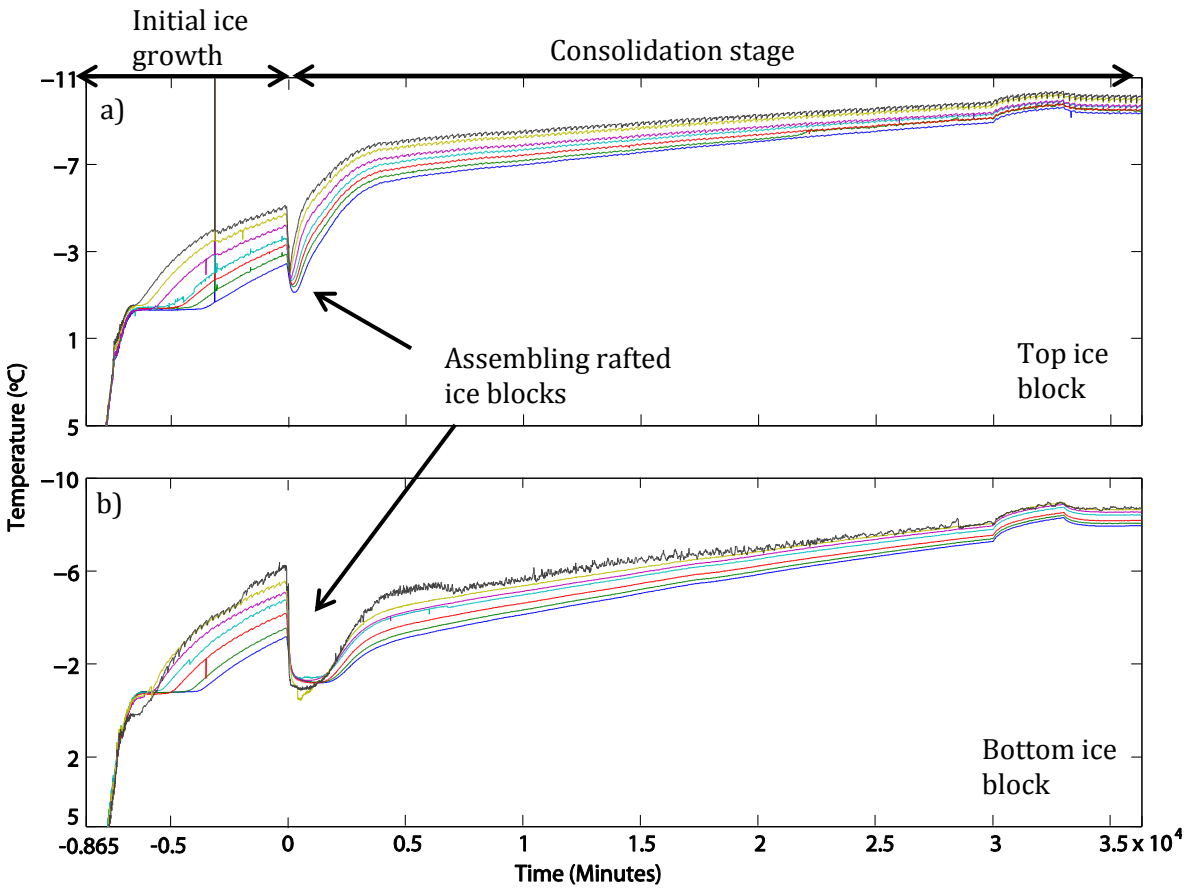

Figure E.20. Temperature-time traces for the 14 cm thick rafted ice experiment (test 5), where plot a) shows the temperatures recorded by the thermistor probe in the top ice block and plot b) shows the temperatures recorded in the bottom ice block. Negative time refers to the 'initial ice growth' stage and positive time refers to the 'consolidation stage'.

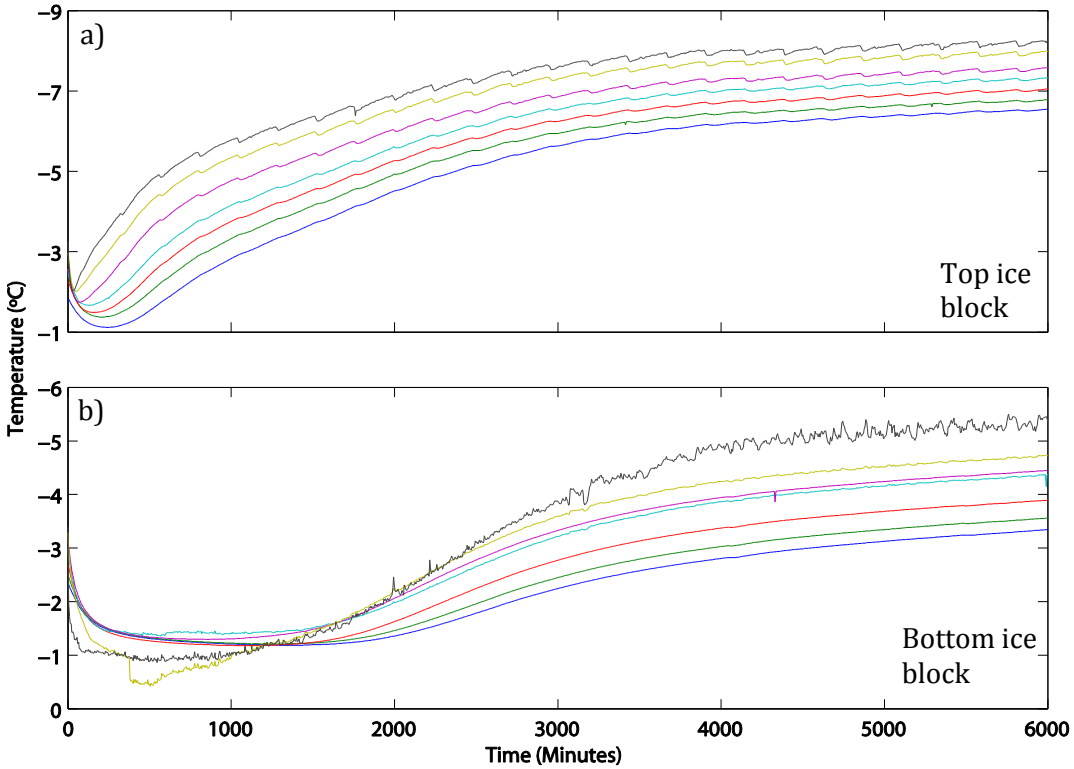

Figure E.21. Enlarged plot of the first 6000 minutes of consolidation.

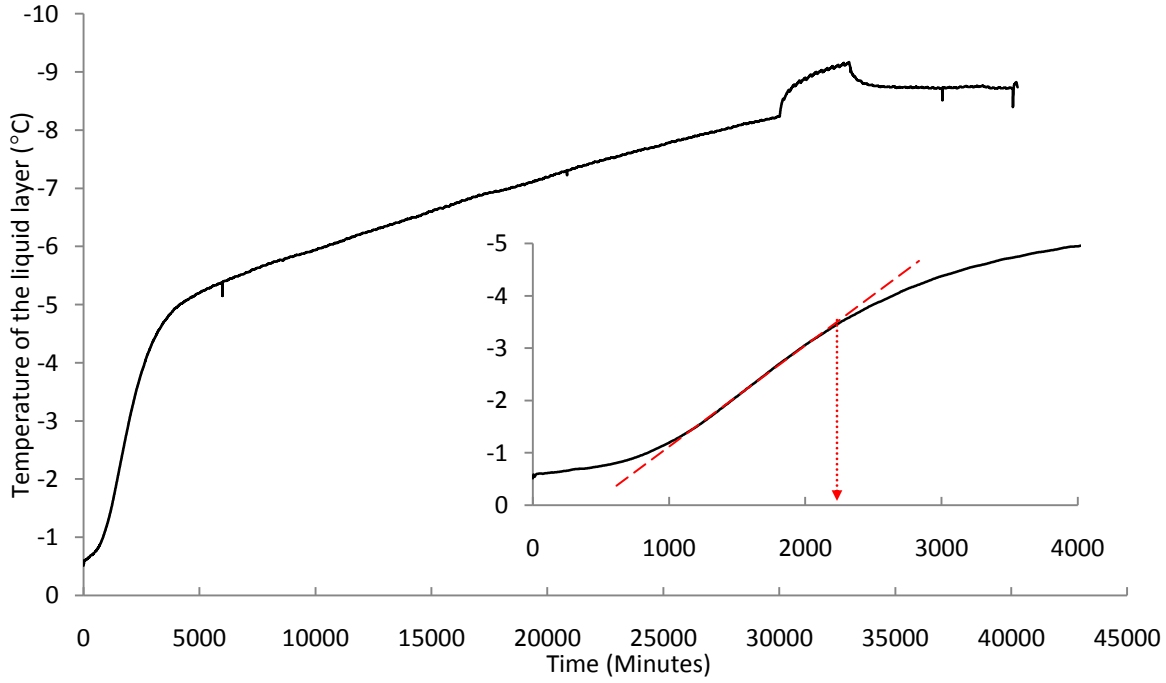

Figure E.22. Temperature evolution of the liquid layer for the 14 cm thick ice experiment (test 5). The enlarged plot shows a zoom of the first 4000 minutes of consolidation. By fitting a best fit line to the data recorded during the rapid decrease in temperature and finding the time that the temperature started to deviated from this trend I estimate that the ice blocks thermodynamically consolidated at ~2200 minutes.

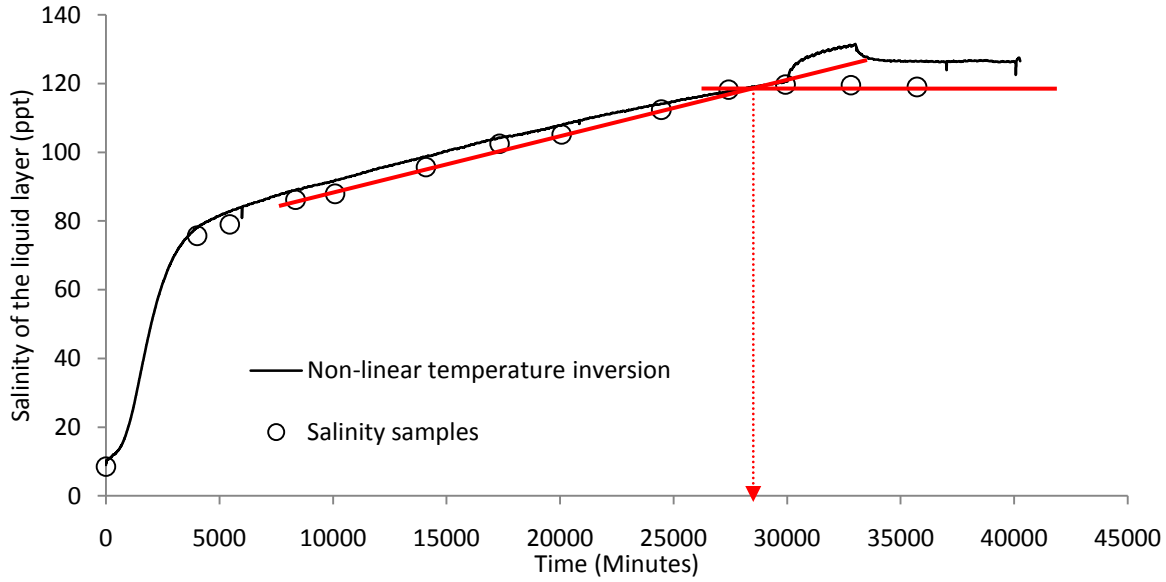

Figure E.23. Salinity evolution in the liquid layer for the 14 cm thick ice experiment (test 5). The circles represent the samples that were taken with a needle and syringe and the black line represents the temperature readings that were inverted using the non-linear liquidus curve (Eq. 7.2). The salinity of the samples extracted from the liquid layer became constant around 28600 minutes.

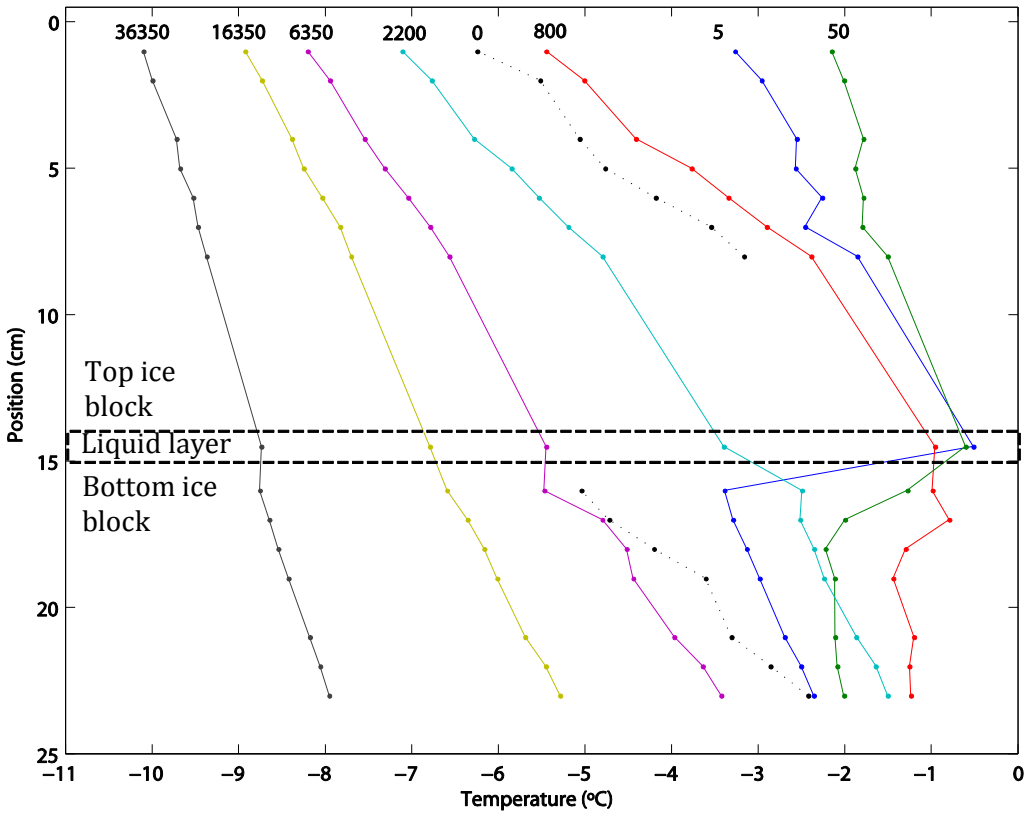

Figure E.24. The temperature evolution in the ice sheets and the liquid layer as a function of depth and time for the 14 cm thick ice experiment (test 5). The dotted line shows the temperature in the ice blocks prior to when the trace heating had been turned on and the solid lines the temperature profiles at different times of interest.

Test 6: The 0.5 cm thick gap experiment

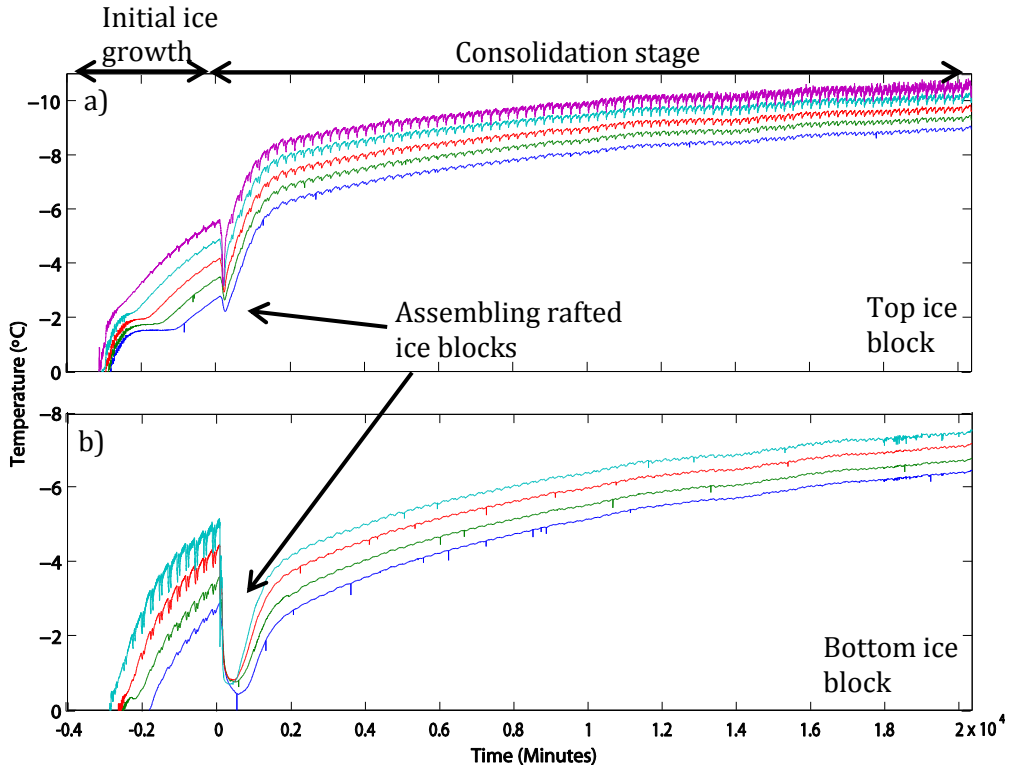

Figure E.25. Temperature-time traces for the 0.5 cm thick gap experiment (test 6), where plot a) shows the temperatures recorded by the thermistor probe in the top ice block and plot b) shows the temperatures recorded in the bottom ice block. Negative time refers to the 'initial ice growth' stage and positive time refers to the 'consolidation stage'. In the bottom ice block there are only 4 thermistors as the bottom thermistor had corroded by this stage in the experimental program.

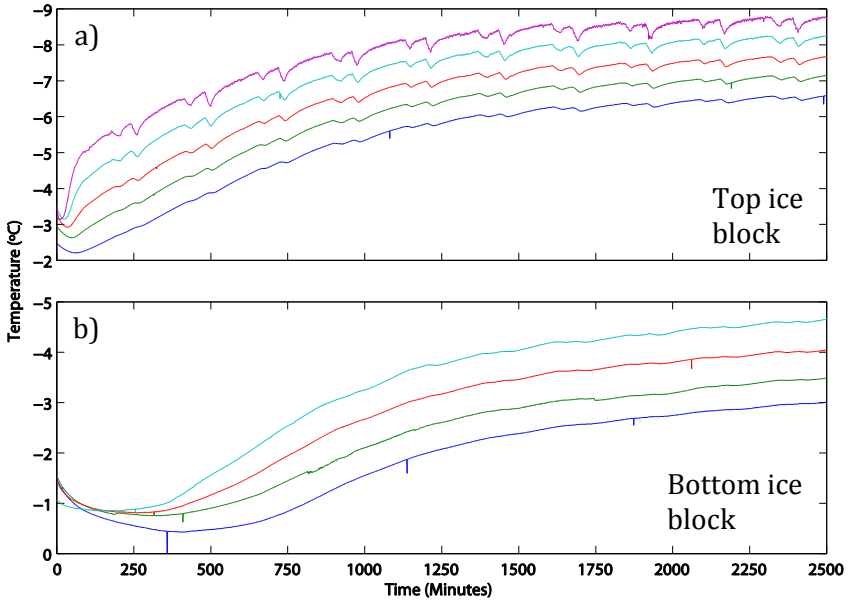

Figure E.26. Enlarged plot of the first 2500 minutes of consolidation.

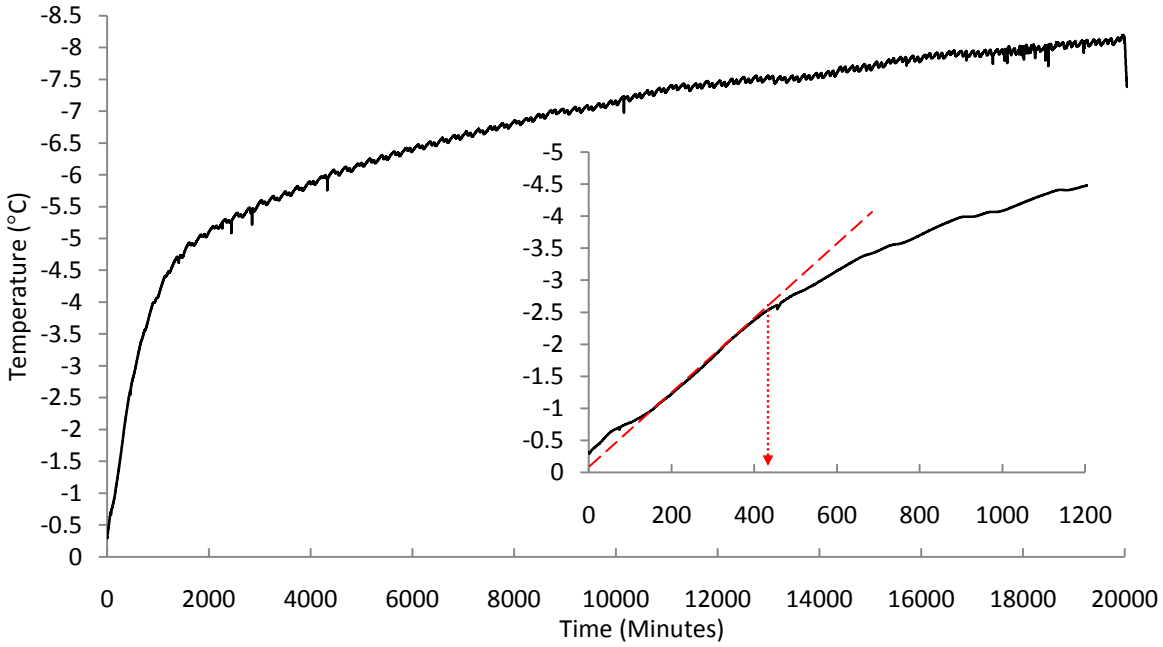

Figure E.27.Temperature evolution of the liquid layer for the 0.5 cm thick gap experiment (test 6). The enlarged plot shows a zoom of the first 1200 minutes of consolidation. By fitting a best fit line to the data recorded during the rapid decrease in temperature and finding the time that the temperature started to deviated from this trend I estimate that the ice blocks thermodynamically consolidated at ~420 minutes.

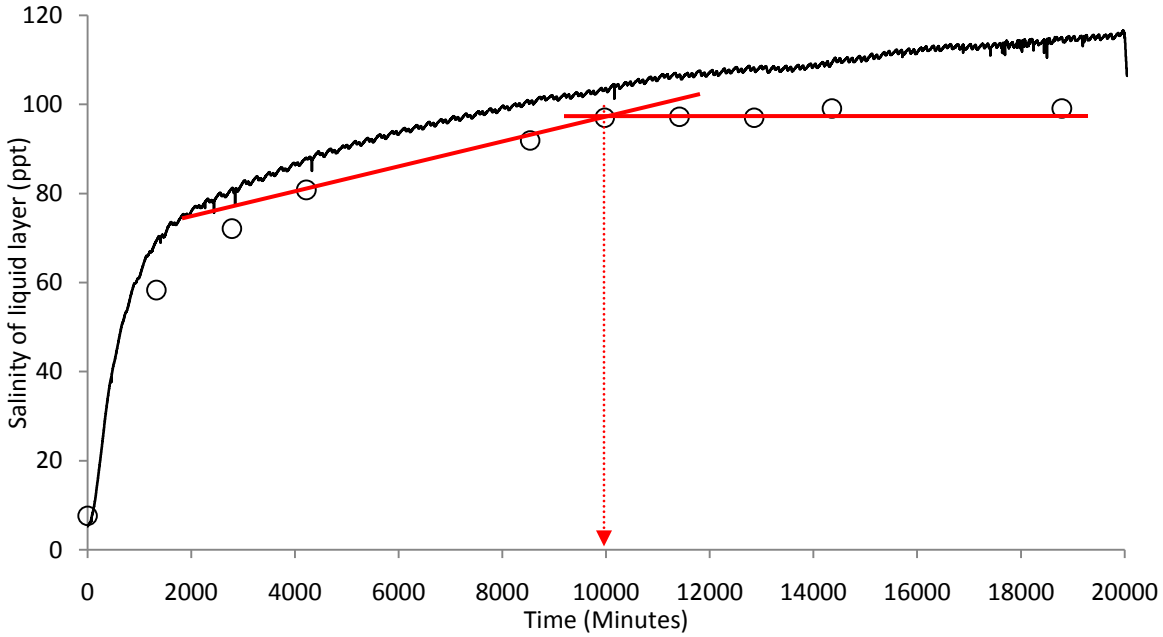

Figure E.28. Salinity evolution in the liquid layer for the 0.5 cm thick gap experiment (test 6). The circles represent the samples that were taken with a needle and syringe and the black line represents the temperature readings that were inverted using the non-linear liquidus curve (Eq. 7.2). The salinity of the samples of the liquid layer became constant ~ 10000 minutes.

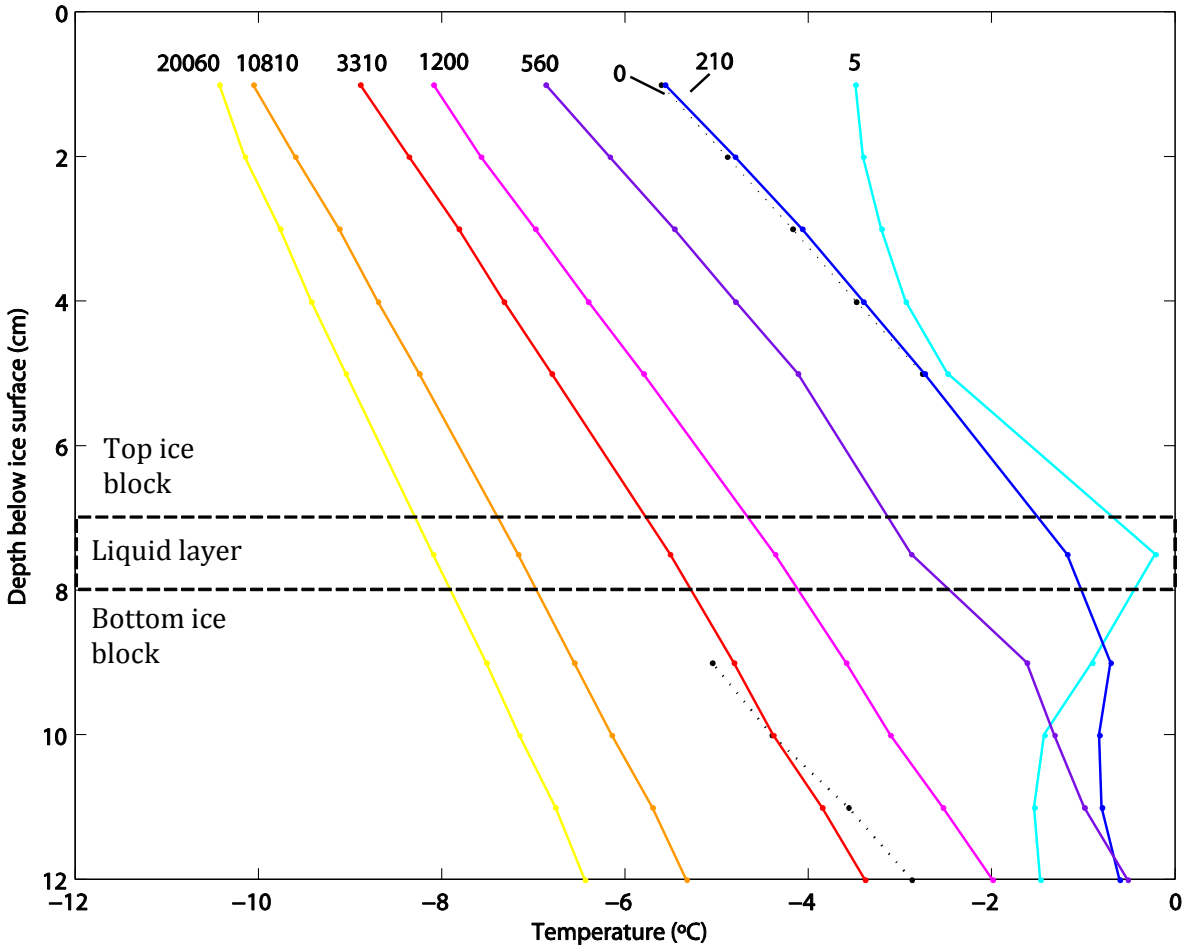

Figure E.29. The temperature evolution in the ice sheets and the liquid layer as a function of depth and time for the 0.5 cm thick gap experiment (test 6). The dotted line shows the temperature in the ice blocks prior to when the trace heating had been turned on and the solid lines the temperature profiles at different times of interest.

Test 7: The 2 cm thick gap experiment

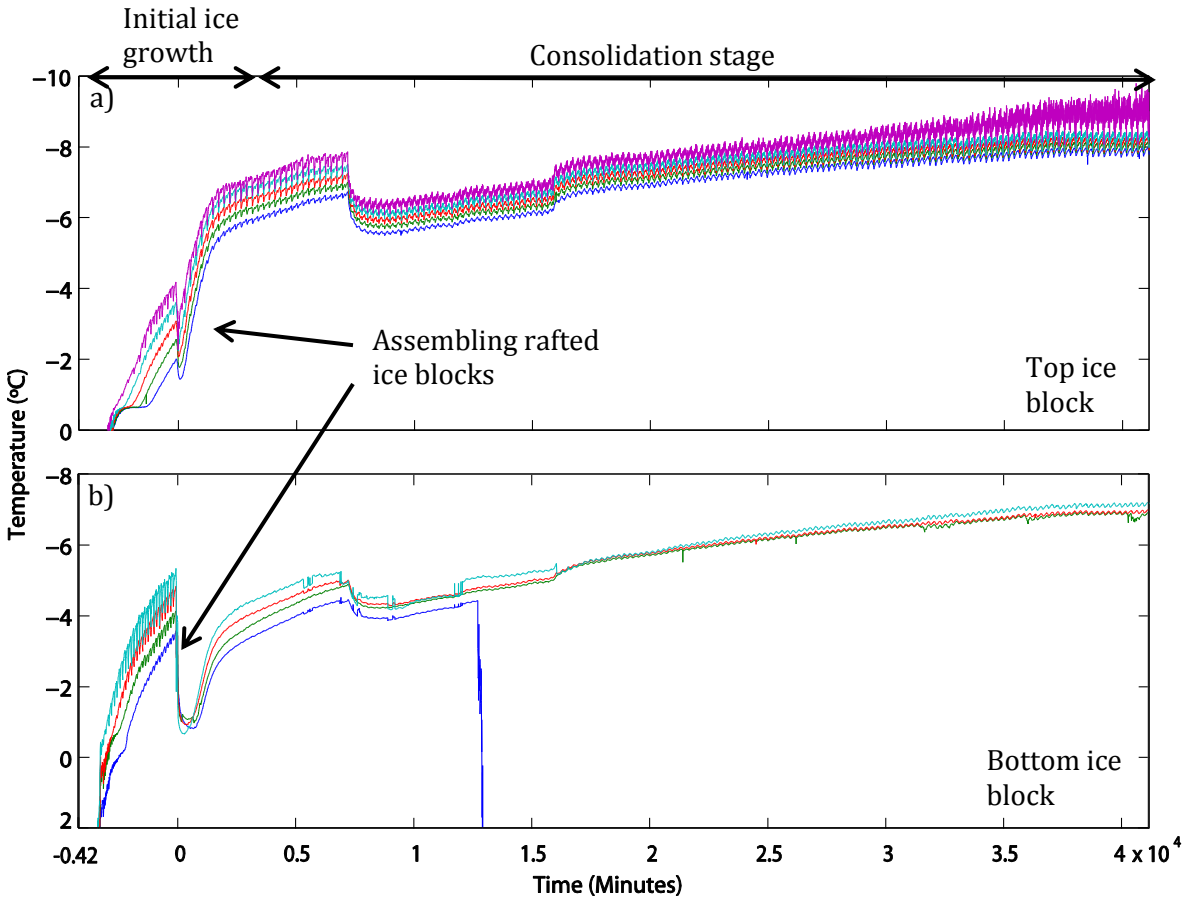

Figure E.30. Temperature-time traces for the 2 cm thick gap experiment (test 7), where plot a) shows the temperatures recorded by the thermistor probe in the top ice block and plot b) shows the temperatures recorded in the bottom ice block. Negative time refers to the 'initial ice growth' stage and positive time refers to the 'consolidation stage'. In the bottom ice block there are initially 4 thermistors working. However after ~7000 minutes there appears to be a sudden rise in temperature which also affects another one of the thermistors in the bottom ice block. Thus bringing the number of temperature traces down to 3.

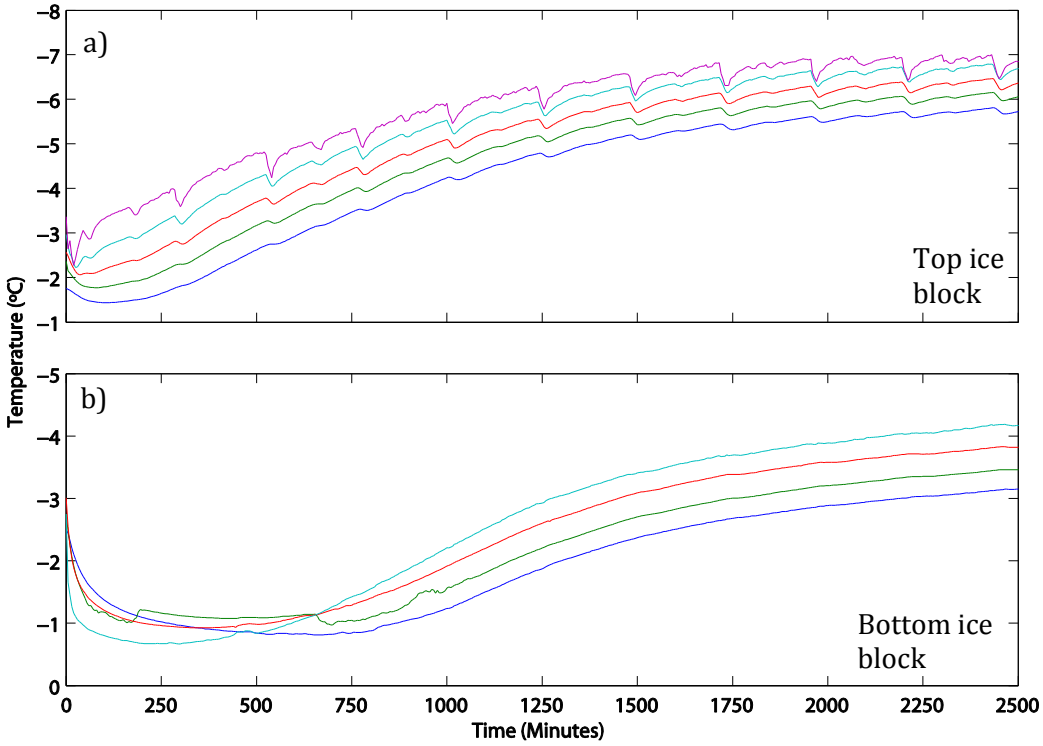

Figure E.31. Enlarged plot of the first 2500 minutes of consolidation.

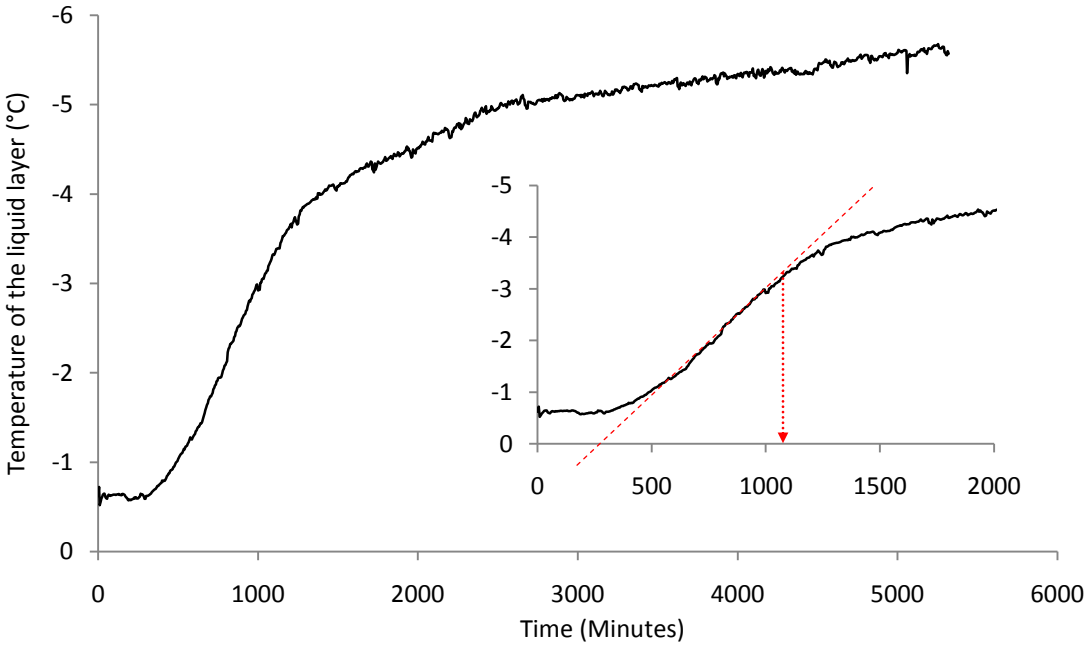

Figure E.32. Temperature evolution of the liquid layer for the 2 cm thick gap experiment (test 7). The enlarged plot shows a zoom of the first 2000 minutes of consolidation. By fitting a best fit line to the data recorded during the rapid decrease in temperature and finding the time that the temperature started to deviated from this trend I estimate that the ice blocks thermodynamically consolidated at ~1120 minutes.

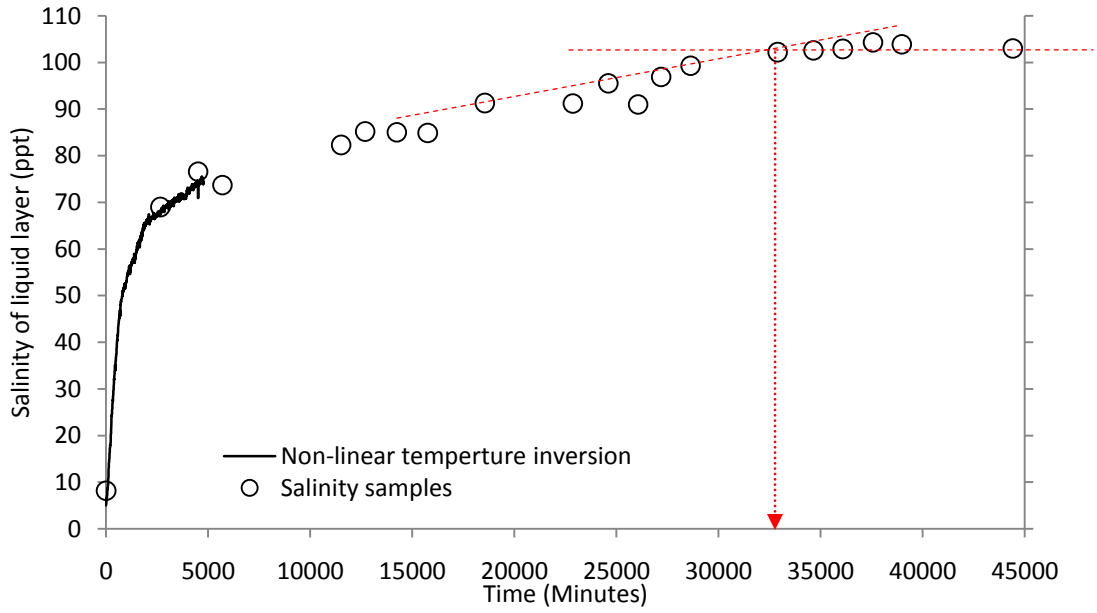

Figure E.33. Salinity evolution in the liquid layer for the 2 cm thick gap experiment (test 7). The circles represent the samples that were taken with a needle and syringe and the black line represents the temperature readings that were inverted using the non-linear liquidus curve (Eq. 7.2). There are no readings from the temperature inversion after 5000 minutes as unfortunately the thermistor in the liquid layer malfunctioned after the point. The time that the salinity of the samples extracted from the liquid layer became constant was ~32900 minutes.

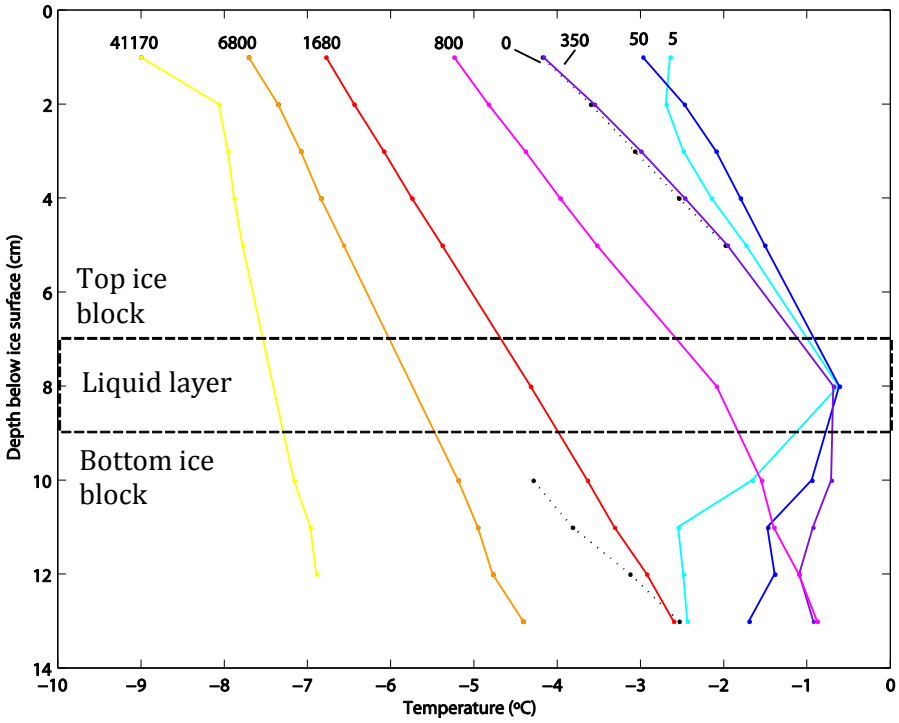

Figure E.34. The temperature evolution in the ice sheets and the liquid layer as a function of depth and time for the 2 cm thick gap experiment (test 7). The dotted line shows the temperature in the ice blocks prior to when the trace heating had been turned on and the solid lines the temperature profiles at different times of interest.

Appendix F: Ice tank experiments on the consolidation of rafted sea ice

F.1 Introduction

The consolidation and strength of rafted sea ice was investigated experimentally in the Arctic Environmental Test Basin (AETB) at the Hamburgische Schiffbau-Versuchsanstalt (HSVA) in Germany. The purpose of these experiments was to perform larger scale experiments to compliment the laboratory work carried out in the Ice Physics laboratory at UCL, described in chapter 7. Initially these experiments were to be performed in the north Caspian Sea as part of the AgipKCO ice field programme, however due to insufficient ice cover in the winter of 2006-07 and inadequate helicopter time in 2007-08, I was unable to. Fortunately, I was able to incorporate two experiments into a larger project that was investigating sea ice friction and rheology in the AETB (Lishman et al., 2009).

The AETB is a 30 m long, 6 m wide and 1.2 m deep water basin equipped with a refrigeration system that can bring the room temperature down to about -20°C, enabling the simulation of Arctic conditions. Conducting the experiments in the AETB enabled us not only to perform larger scale experiments than would be possible in the laboratory, but also to impose more controlled conditions than would be possible in the field. Ice tanks have been used successfully to investigate many sea ice processes, such as sea ice formation (Wilkinson, 2009), friction (Sammonds et al., 2005) and the mechanics of rafting (Tuhkuri and Lensu, 1997; 1998).

In this Appendix, I present two experiments that were set up to investigate the consolidation and strength of rafted sea ice. During an experiment, equally sized portions of level ice were manually piled on top of one another to produce a section of rafted sea ice. The rate of consolidation was then monitored using a combination of coring and drilling. Once consolidated, the physical properties of the rafted ice were measured. The experimental set up is described in section F.2. The physical properties of the level ice and rafted ice are presented in section F.3. The results of the consolidation experiments are described in section F.4. A brief discussion and summary of the appendix is presented in section F.5.

F.2 Experimental set up

Two experiments were set up in the AETB to investigate the consolidation and strength of rafted sea ice. The first experiment was set up to simulate the consolidation between 3-layers of multiply rafted sea ice assembled from 20 cm thick level ice. The second experiment was set up to simulate the consolidation between 2-layers of rafted and 3-layers of multiply rafted sea ice assembled from 10 cm thick level ice. To set-up an experiment, an ice sheet of the required thickness was grown from a 33 ppt solution of sodium chloride and water to match the concentrations found in the Arctic oceans. The ice sheet was then cut into blocks of equal size using a pneumatic chain saw, which were then manually piled on top of one another to simulate a section of rafted ice. The rate of consolidation was then monitored using a combination of coring and drilling. Once consolidated, the physical properties of the rafted ice were measured and compared with those of level ice.

During the experiments the air temperature was set to -10ºC. The temperatures of the air and water in the ice basin were recorded every minute for the duration of the experiments. Four temperature sensors were located 2 m above the ice surface and three in the water, below the ice surface, at different depths (see Figure F.1 for details). Figure F.2 shows the air temperatures measured at each senor during the consolidation experiments. The figure shows that the mean air temperature in the ice basin was -9ºC and deviated between -6ºC to -12ºC. The readings also show that there was about a 2ºC temperature difference across the length of the basin and a 1ºC difference across the width. Figure F.3 shows the water temperatures recorded during the experiments. Here we see that the temperature in the water increased with depth and that over the course of the experiments the temperature dropped by about 0.3ºC at each sensor, indicating that the water temperature was relatively stable.

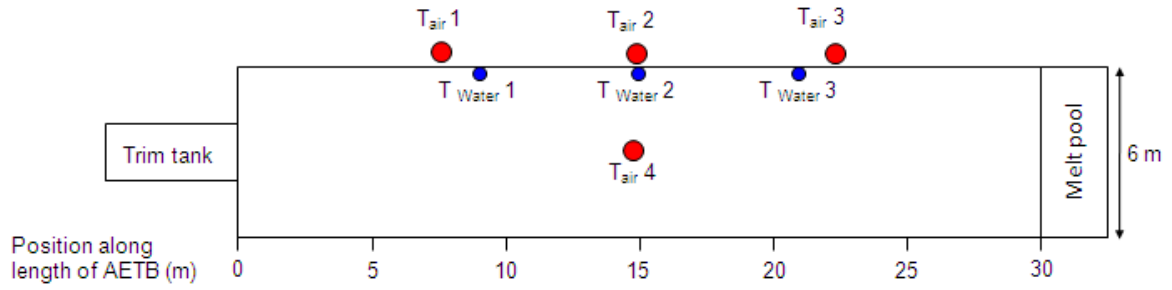

	Channel Number	Length Position (m)	Vertical Position (m)	
T_{air} 1	1	7.5	2	
T_{air} 2	2	15	2	
T_{air} 3	3	22.5	2	
T_{air} 4	4	15	2	
T_{Water} 1	6	8	0.3	above tank bottom
T_{Water} 2	7	15	0.5	above tank bottom
T_{Water} 3	8	21.5	0.7	above tank bottom

Figure F.1. Schematic of the Arctic Environmental Test Basin (AETB) showing the location of the temperature sensors (courtesy of HSVA laboratories).

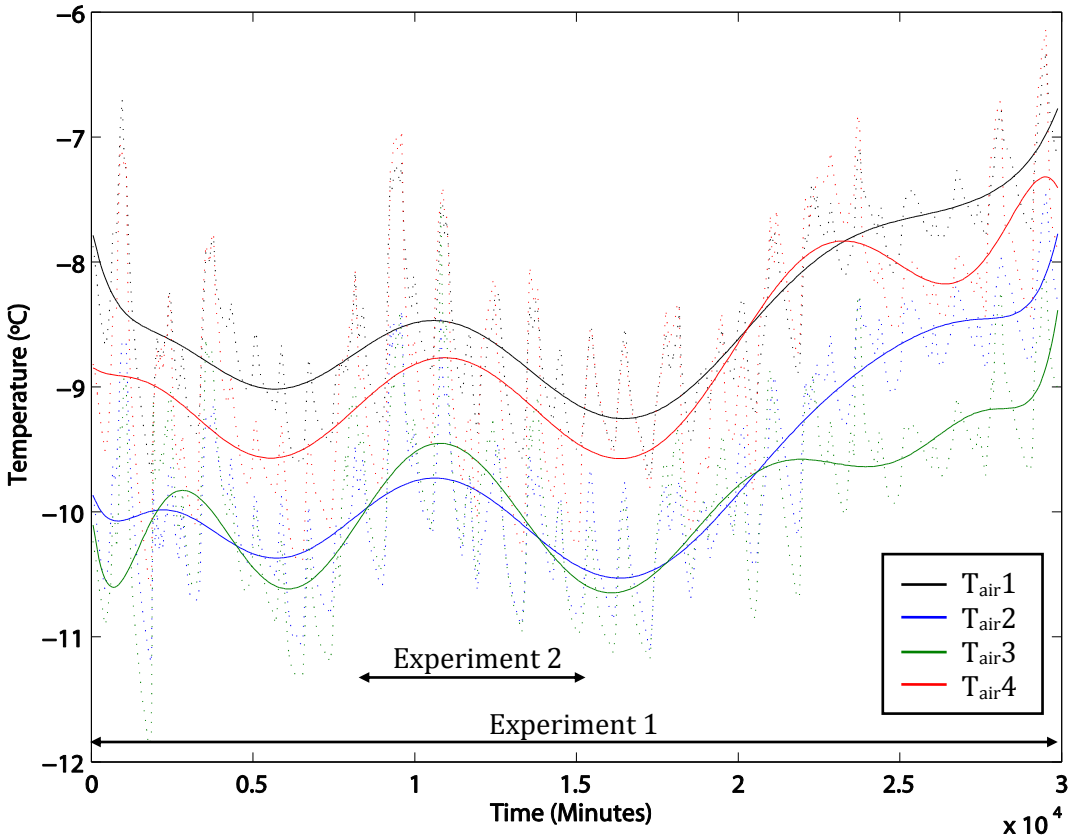

Figure F.2. Air temperatures recorded at the four sensors during Experiments 1 and 2, where the dotted lines show the hourly averaged values and the solid line a 10th order polynomial fit to the data.

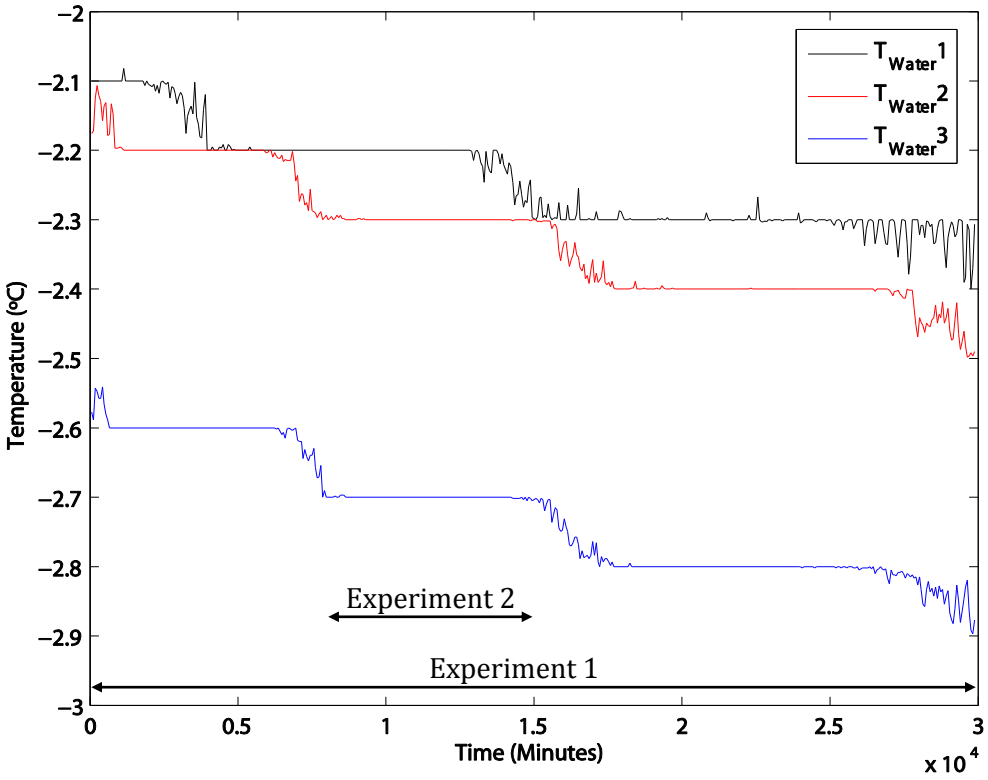

Figure F.3. Water temperatures recorded during Experiments 1 and 2, where $T_{water}1$, $T_{water}2$ and $T_{water}3$ are located respectively 0.3 m, 0.5 m and 0.7 m above the tank bottom.

Experiment 1

The purpose of Experiment 1 was to determine the time it takes for three layers of 20 cm thick sea ice, separated by 3 mm thick liquid layers, to consolidate. When the ice had reached a nominal ice thickness of 20 cm, three 1 m^2 blocks were cut from the ice sheet using a pneumatic chain saw. On the ice blocks that were to be in the middle and the bottom of the 3-layer stack, three wooden strips, 3mm in thickness, were frozen onto the surface to act as spacers between adjacent ice blocks (see Figure F.4). To build the rafted section, the first ice block was pushed into the wooden frame and tied down to the base of the frame (see Figure F.5). The purpose of the frame was to prevent lateral movement and also to help with the assembly process. The ice block and the frame were then submerged and the second block pushed into place. These two blocks were then attached to the frame and submerged whilst the third block was moved into position. The rate of consolidation was monitored using a combination of coring, drilling and temperature readings recorded in the ice blocks and the liquid layers. Figure F.6 shows a schematic and photograph of the assembled 3-layer section of rafted sea ice.

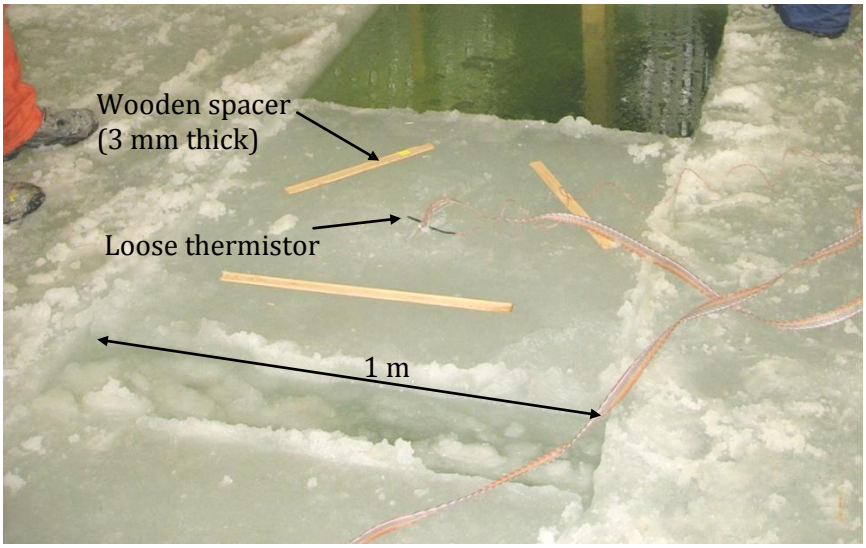

Figure F.4. Picture showing the 1m² ice block used in Experiment 1, with a thermistor probe frozen in to the centre, a loose thermistor attached to the top of the probe and wooden strips frozen onto the surface.

Figure F.5. Image showing the wooden frame with the first ice block attached to it.

Cores were taken using either 5 cm diameter by 30 cm long core barrel or a 9 cm by 1 m core barrel depending on the ice thickness. The drilling method came about as it was noted that when the first 5cm core was taken, the top two layers of ice had not consolidated and the remnant hole flooded with water rather quickly (see Figure F.7). To minimise the sample area and the affects of coring, we decided that we would also use drilling as a method of telling when the ice layers had consolidated. Therefore a rafted section was considered consolidated either (i) when the layers of ice had sufficiently bonded to take a core or (ii) when we drilled down to the liquid layer the drill hole no longer flooded with water. This also gave the added advantage that every time a drill hole was made a sample of the liquid layer could be taken using a pipette (Figure F.8) and its salinity measured. Salinity measurements were made using a temperature compensated WTW conductometer (model - LF191), which is accurate to ±0.1 ppt.

Temperature was recorded every minute in the ice blocks and the liquid layers using the 20 cm thermistor probes and single thermistors probes respectively (see Figure F.6a). The probes were frozen into the ice blocks prior to rafting and the loose thermistor attached to the top using string (see Figure F.4). As a backup, manual resistance readings were also taken at least once a day using a handheld multimeter, which were converted into temperatures using the Steinhart-Hart Eq. 5.1 (c.f. Chapter 5).

a)

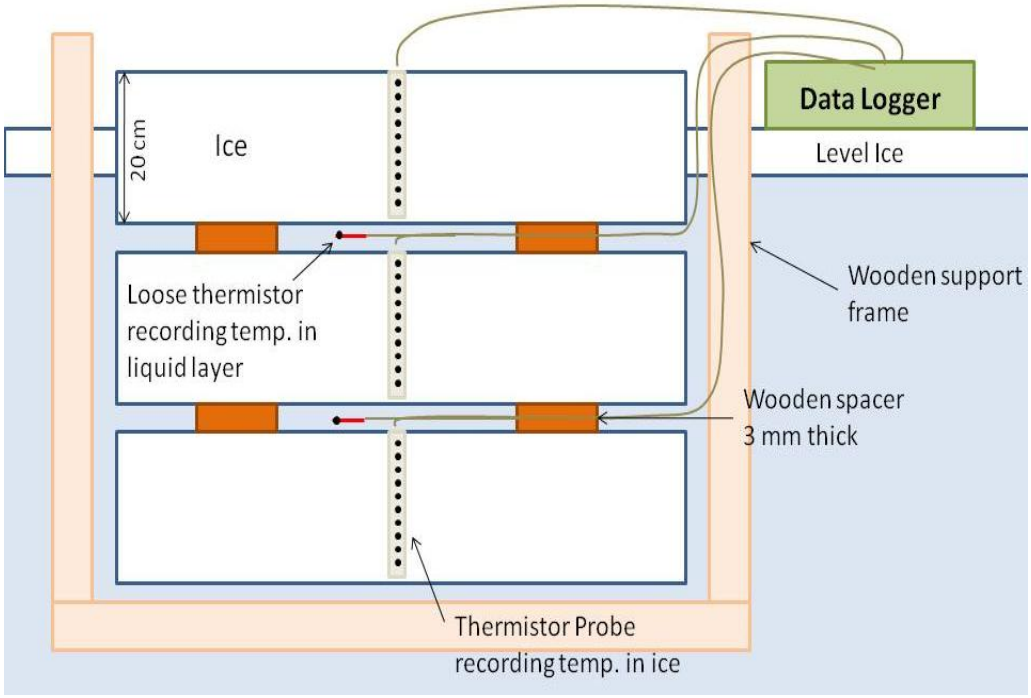

b)

Figure F.6. a) Two-dimensional schematic and b) photograph of the assembled 3-layer section of multiply-rafted sea ice.

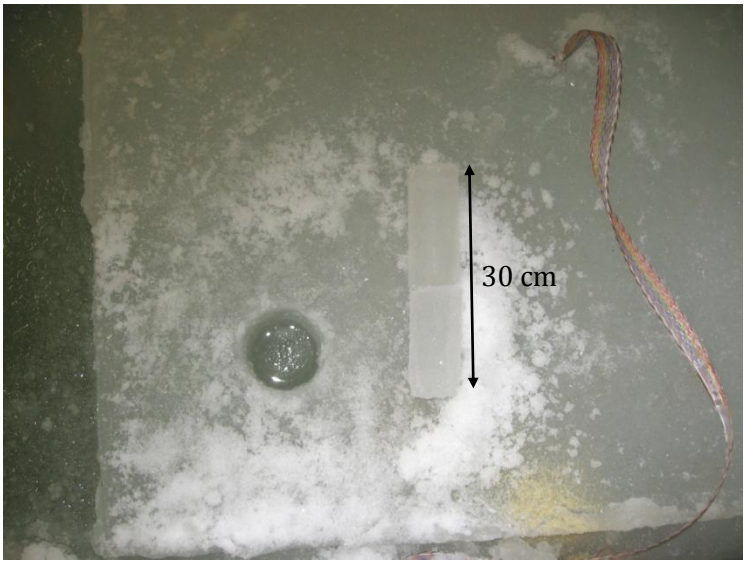

Figure F.7. Showing the first core taken with a 2 inch auger.

Figure F.8. Taking a sample of the liquid layer using a pipette.

Experiment 2

The purpose of Experiment 2 was to simulate the consolidation between both a 2-layer and a 3-layer section of rafted ice assembled from level ice 10 cm thick. To set up the experiment five blocks were cut from the level ice with dimensions 50 x 70 cm. Wooden spacers, 3 mm in thickness, were frozen to the top of three of the ice floes to act as spacers (see Figure F.9). The ice blocks were then manually assembled to produce 2 and 3-layer sections of rafted ice (see Figure F.10). The rates of consolidation of these sections were then monitored by coring and drilling. Temperature measurements were not made as the 10 cm thermistor probes had not been constructed by this stage in my research.

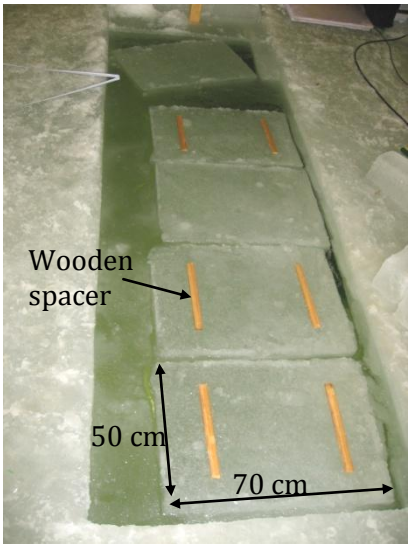

Figure F.9. Shows the 10 cm thick ice blocks used in Experiment 2 with wooden spacers frozen to the ice surface.

a) b)

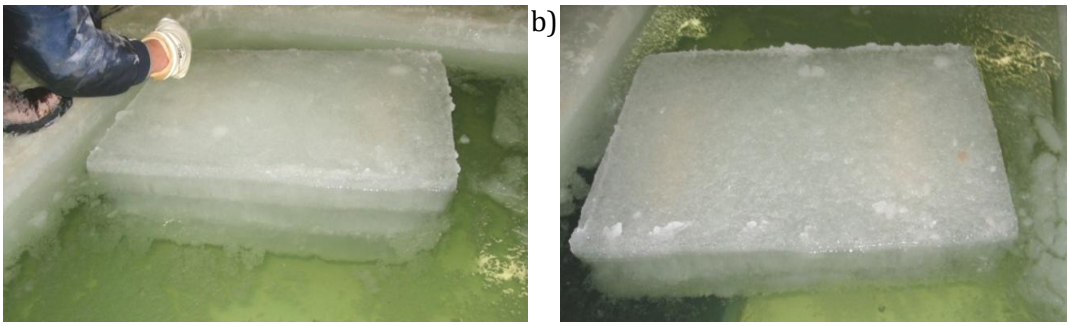

Figure F.10. Images showing a) the 3-layer and b) the 2-layer stacks of rafted ice that were made using ice blocks with dimensions 50 x 70 x 10 cm.

F.3 Physical properties of the ice

Level ice

To gain a better understanding of the physical properties of the level ice grown in the AETB I measured the salinity, density, crystal texture and fabric of the level ice.

The salinity of the ice was measured by taking a core of the ice, melting it down, and taking a reading using a WTW conductometer. A total of 6 cores were taken for salinity measurements. Four of the cores were melted down whole and two were cut up into sections to give the salinity at different depths. Table F.1 shows the salinity and thickness of the four cores that were melted down whole. The results show that the average salinity of the tank ice was 7.2 ppt. In Figure F.11 the salinity variation with depth is shown and exhibits classic C-shaped profiles.

Table F.1. The salinity, thickness and temperature of the four ice cores that were melted down whole.

Sample no.	Salinity (ppt)	Ice thickness (cm)
1	7.1	18
2	7.3	20.5
3	6.7	-
4	7.5	30

The density of the level ice was measured via the displacement method. A core of the ice was placed into a graduated cylinder containing cooking oil and the displacement of the oil measured. The mass of the core was then divided by the displacement to give the density. Three cores were taken when the ice was 30 cm thick and their densities measured: 862.7, 931.8 and 930.8 Kg m^{-3}. The first reading was discounted because at the time the sample was taken the temperature in the ice basin was just below freezing, which meant that the ice was relatively warm causing brine to drain out rapidly. When the next two samples were taken the air temperature was about -10°C and there was limited brine drainage. In addition, care was taken to keep the core upside down at all times to prevent the loss of brine.

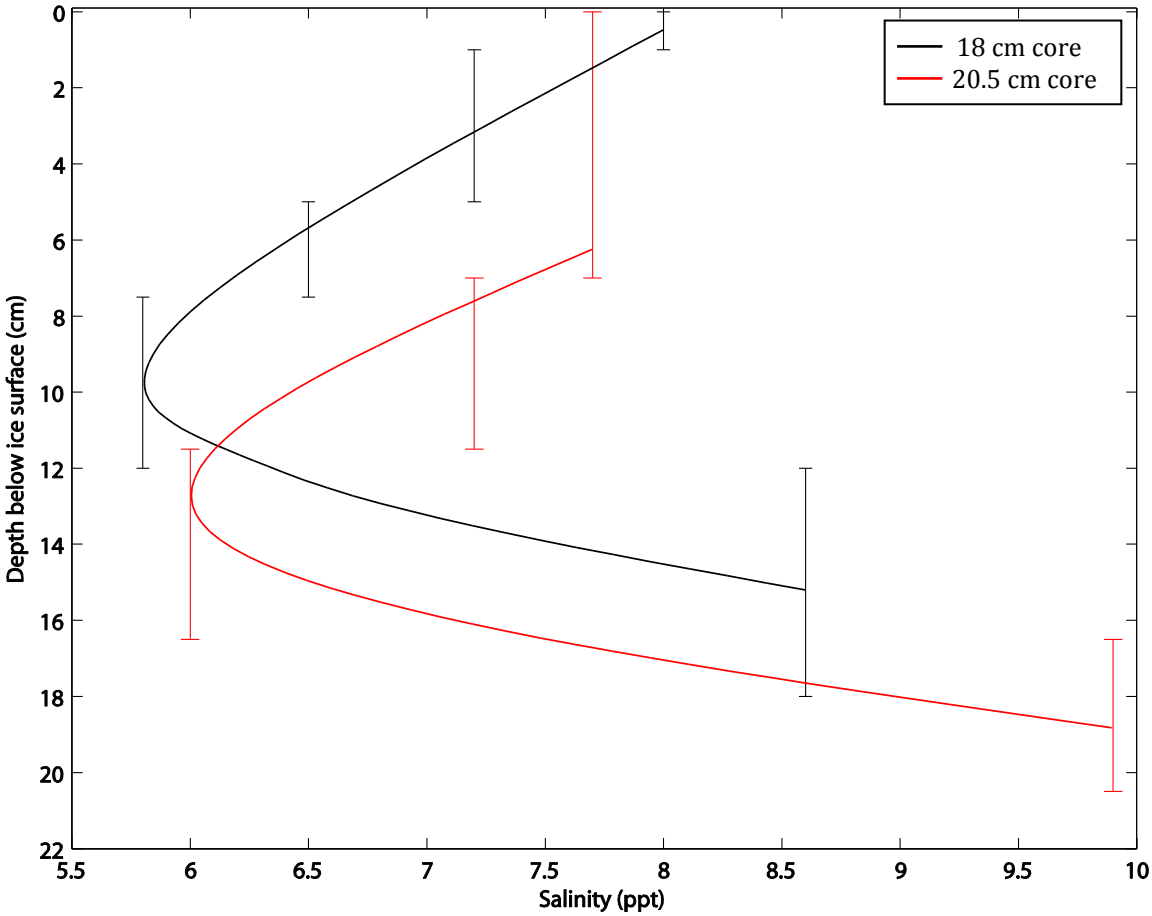

Figure F.11. Plot showing how the salinity of the level ice varied with depth when the ice was 18 cm (black line) and 20.5 cm (red line) thick. The error bars show the thickness of the section melted down and the solid line is a best fit through the data.

The crystal texture and fabric of the level ice was observed by cutting a block from the ice sheet, making thick (~5mm thick) and thin (~1mm thick) sections and viewing them under crossed polarising lenses. The thin sections were then analysed using an Automatic Ice Fabric Analyser (AIFA) in Bremerhaven to determine the orientation of the c-axes [for details of the AIFA see (Wang and Azuma, 1999)]. The thick section of the level ice (Figure F.12) shows that there is ~2 cm of granular ice followed by 26 cm of columnar ice. This columnar structure is a key identifier of congelation ice, typical in Arctic sea ice. Figure F.13 shows two thin sections of the columnar ice, with their respective fabric diagrams, that were cut horizontal (a) and vertical (b) to the ice growth. The figure shows that the c-axes of the crystals are randomly oriented in the horizontal plane and are about 2-3 cm wide. In the vertical, the crystals are long (~7-8 cm in length) and columnar.

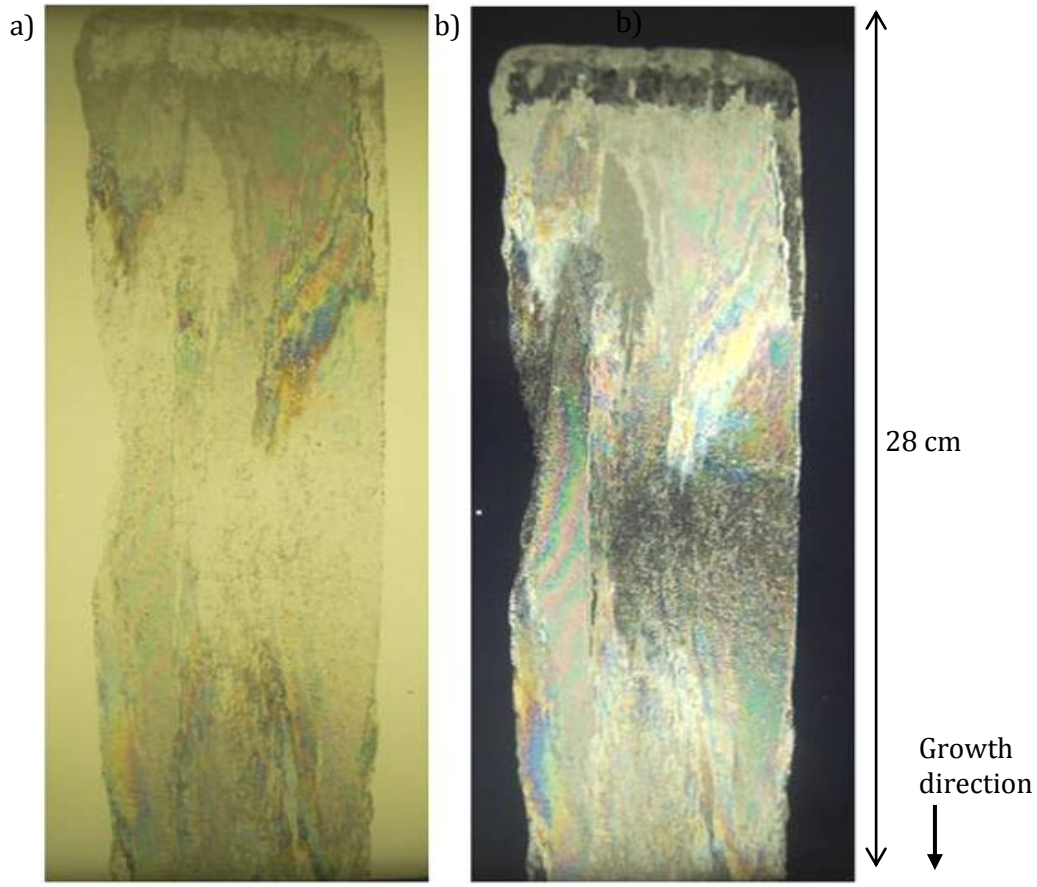

Figure F.12. Thick sections of the level ice cut parallel to the growth direction. Photograph a) shows the sample under plane polarising lenses and b) under crossed polarising lenses.

	Thin section	*Fabric diagram*
a)	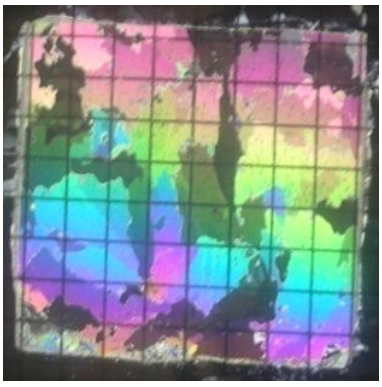	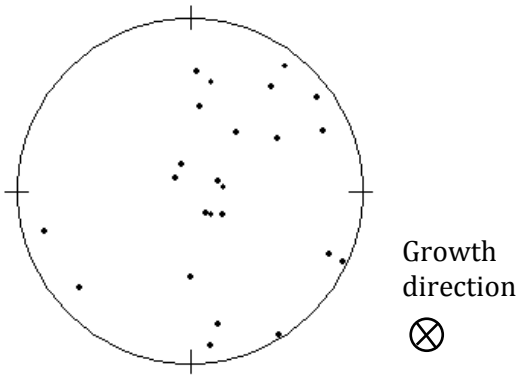

b)

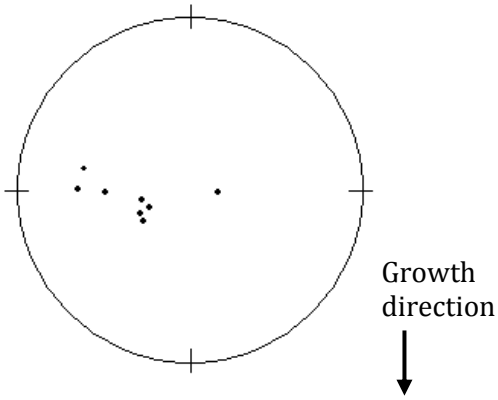

Figure F.13. Thin sections and fabric diagrams of columnar ice that was cut horizontal (a) and vertical (b) to the growth direction. The photographs of the thin sections were taken through crossed polarising lenses, with a 1 cm^2 grid on top. Fabric diagrams were produced of the thin sections shown using the Automatic Ice Fabric Analyser (AIFA) in Bremerhaven. Each point on the fabric diagram represents the c-axis of the crystal.

Rafted ice

Once the consolidation experiments were complete, cores of the rafted ice were taken and immediately stored in a cold room at -25°C. These were then shipped back to UCL in dry ice for examination. Back at UCL, salinity profiles and thick and thin sections were made of the consolidated rafted ice.

In Figure F.14 the salinity profiles from the 3 x 20 cm (Experiment 1) and the 3 x 10 cm (Experiment 2) are plotted. The plots show that the salinity of the rafted ice from both experiments varied between 3 and 6 ppt. This is about 3-4 ppt lower than was found for the level ice indicating that brine either drained during the consolidation process or the shipping and storage of the cores. Unfortunately due to a cold room breakdown the temperatures in the freezers reached close to 0°C, which is likely to have caused a large percentage of the brine to drain out of the samples. Therefore I cannot be sure when this reduction in salinity took place. The salinity profiles, however, seem to have kept their initial C-shaped profiles, which repeat over the three layers.

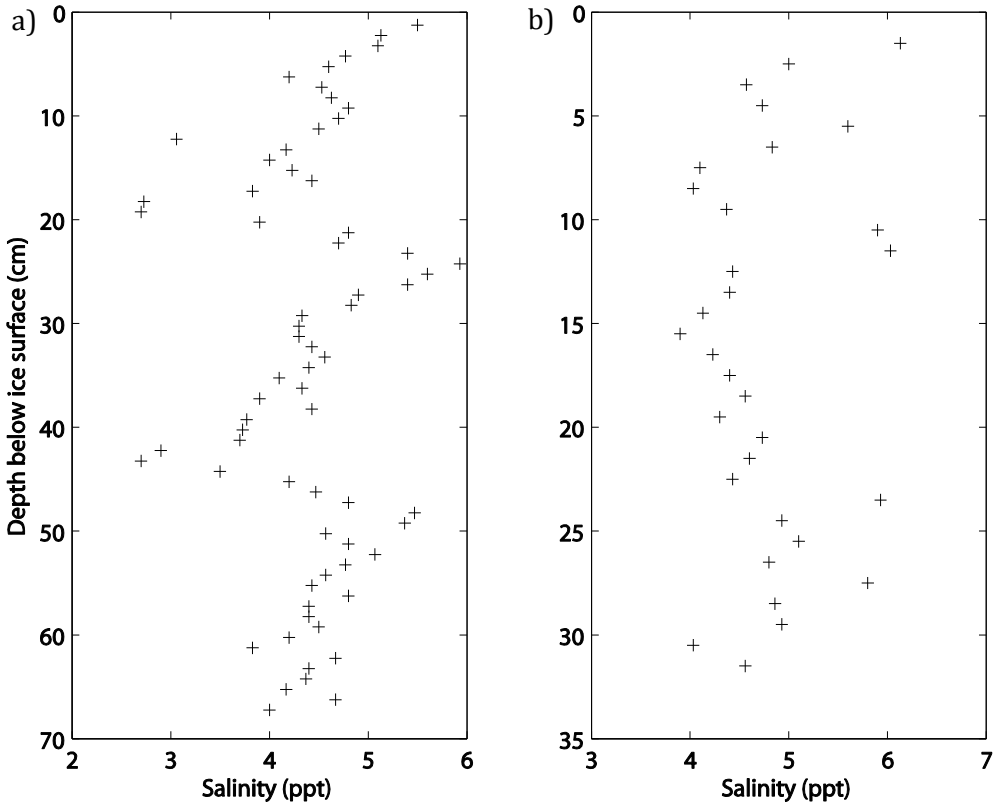

Figure F.14. Salinity profiles of the 3-layer rafted ice from Experiment 1 (a) and Experiment 2 (b).

The crystal texture of the rafted ice was observed by making thick (~5mm thick) and thin (~1mm thick) sections and viewing them under crossed polarising lenses. In Figure F.15, a thick section of the ice from the 3 x 20 cm (Experiment 1) is shown. The figure shows that in each of the layers there is 1-2 cm of granular ice, followed by ~18 cm of columnar ice growth and then the consolidated liquid layer. It is evident that in each level ice layer there is a thin layer of bubbles present at roughly the same depth. I am not sure what caused this bubble layer. However, the fact that it is present in every layer at the same depth seems to suggest it was related to a process taking place during the initial growth of the level ice rather than the rafted ice consolidation process.

Figure F.16 shows the thin sections that were made from the 3-layer section of rafted ice described in Experiment 1. The sections were cut parallel to the ice growth direction and viewed under crossed polarising lenses. Figures F.16a, c and e are of the level ice in the rafted section, while, Figures F.16 b and d are of the frozen liquid layers between adjacent ice blocks. If we examine Figures F.16b and d from top to bottom, there is 1.5-2 cm of columnar ice from the upper ice block, followed by a ~2 cm thick consolidated liquid layer,

and then the granular and columnar ice from the ice block below. This liquid layer thickness is considerably more than the 3 mm spacer that was used in the set up indicating that the wires from the thermistors must have got twisted during assembly thus making the size of the liquid layer larger than expected. The crystal structure in the liquid layer is composed of granular ice with randomly orientated crystals about 2-4 mm in diameter.

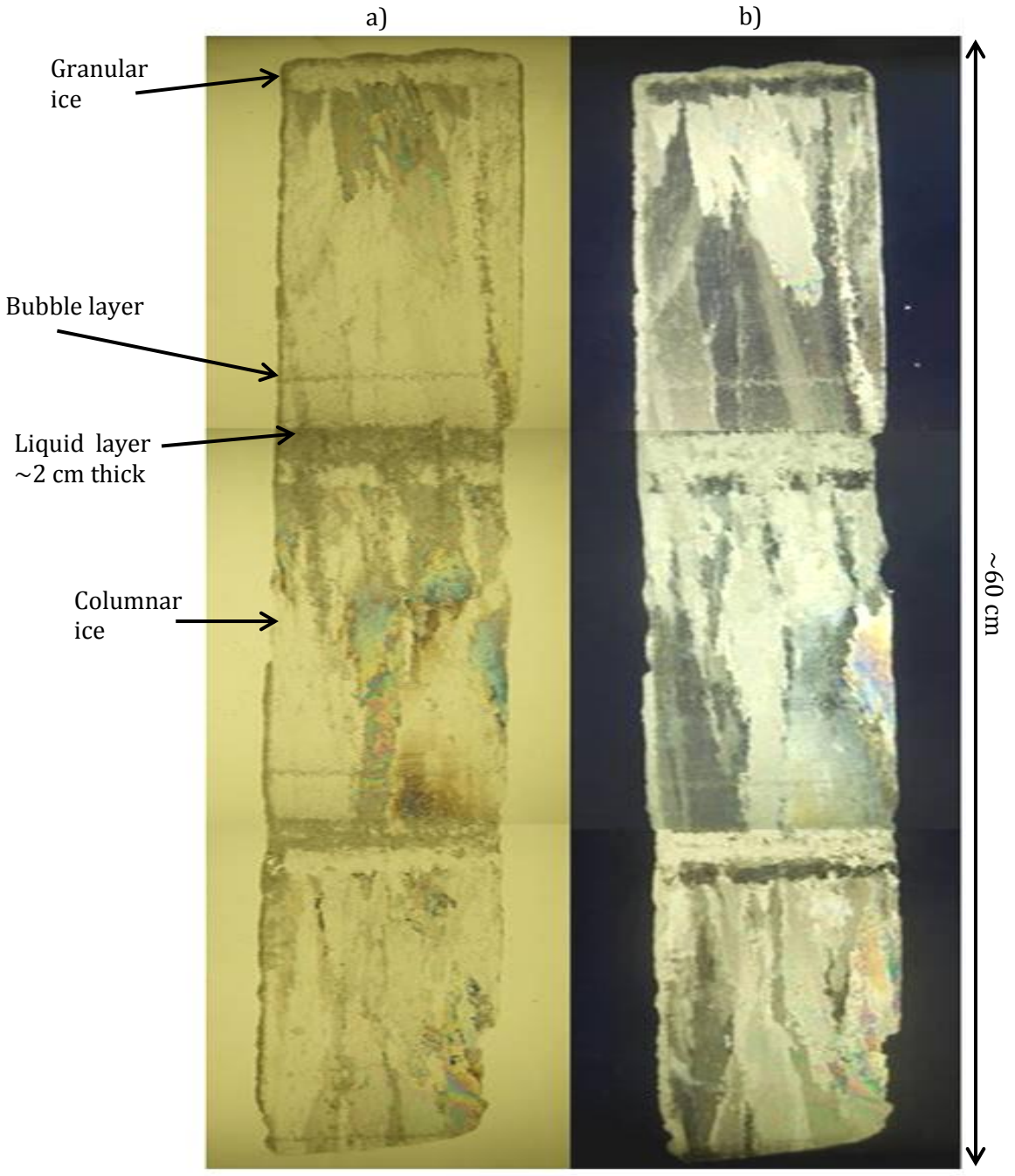

Figure F.15. Photographs of a thick section of the consolidated 3-layer section of rafted ice described in Experiment 1 viewed under a) plane polarised light and b) crossed polarising lenses.

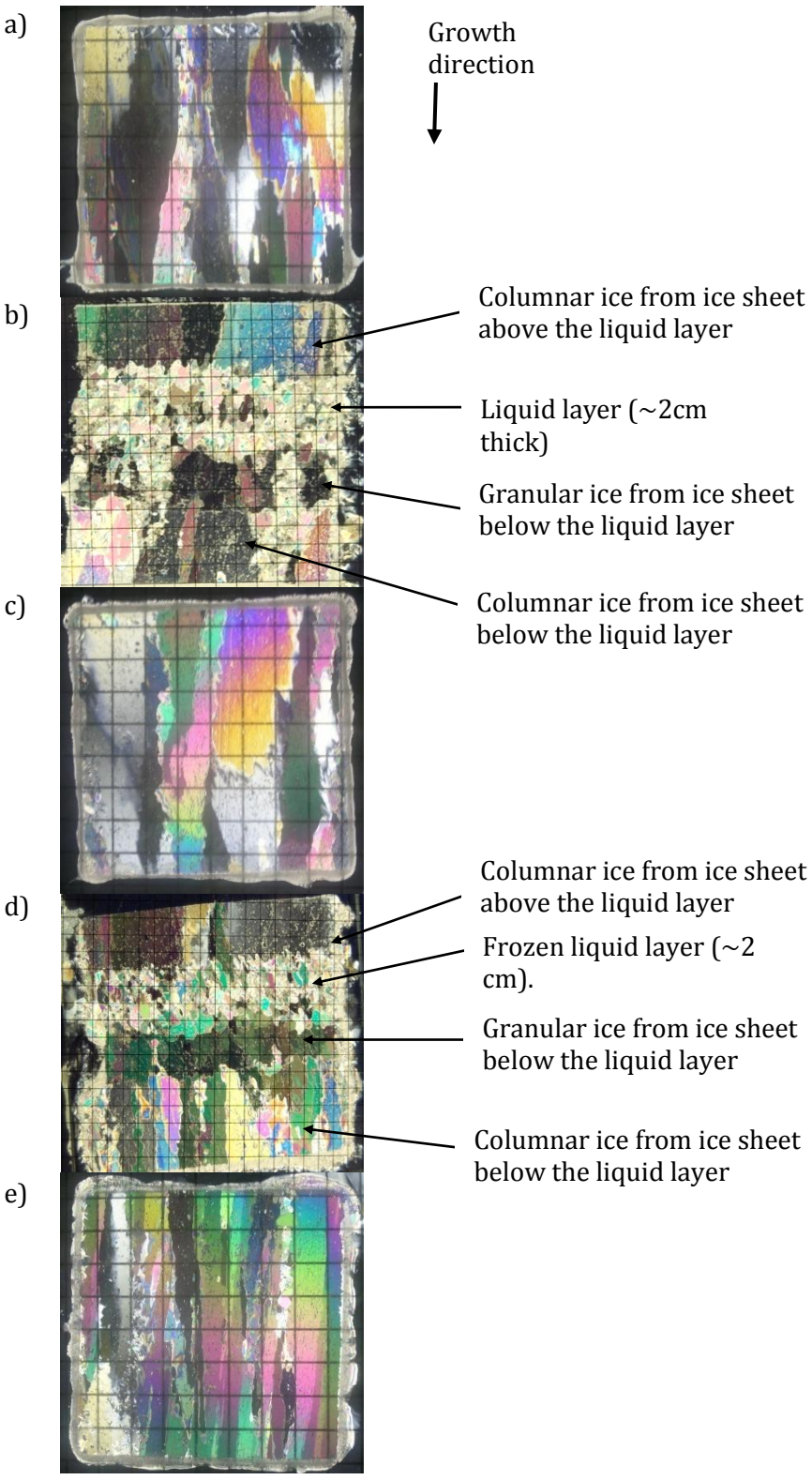

Figure F.16. Five thin sections made from the consolidated 3-layer section of ice used in Experiment 1 viewed under crossed polarising lenses. Thin sections were made of: a) the top ice block that is in contact with the air, b) the upper liquid layer, c) the ice block in the centre of the rafted section, d) the lower liquid layer, e) the bottom ice block that is in contact with the water. The grid size on figures a, c, and e is 1 cm^2, whereas those in figures b and d are 0.5 cm^2.

F.4 Results

Experiment 1

The rate of consolidation of the three-layer section of rafted ice was monitored using a combination of drilling and coring. Table F.2 shows the time in hours since the start of the experiment that a core was taken or the stack was drilled. The results show that it took between 2760 and 6900 minutes (~2-5 days) and 17520 and 28920 minutes (~12-19 days) for the upper and lower liquid layers to consolidate respectively. Unfortunately, the rate of freezing could not be determined with higher precision because firstly, we were unable to gain access to the ice basin on weekends and secondly, we ran out of space to core.

Table F.2. Times that cores were taken for Experiment 1.

Time core taken (Minutes)	Method	Notes
1260 (21hrs)	2 inch core	Hole flooded – upper liquid layer not consolidated
2760 (1day, 22hrs)	Drilling	Hole flooded – upper liquid layer not consolidated
6900 (4days 19hrs)	Drilling	No Flooding – upper layer consolidated
7320 (5 days 2hrs)	4 inch core	Upper layer consolidated and lower not consolidated
10260 (7days 3hrs)	4 inch core	Lower layer not consolidated
11880 (8days 6hrs)	4 inch core	Lower layer not consolidated
17520 (12 days 4hrs)	4 inch core	Lower layer not consolidated
28920 (20 days 2hrs)	4 inch core	Both liquid layers consolidated

Figure F.17a shows the evolution of the temperature in the 3-layer stack of ice at times of interest. The top plot represents the ice block that is in contact with the air, the middle plot the ice block that is in the centre of the rafted section and the bottom plot the ice block that is in contact with the basin water. Unfortunately fifteen of the thermistors, nine of which were in the bottom block and one in the upper liquid layer, were not functioning correctly.

This meant there was only one thermistor recording the temperature in the bottom ice block; therefore I included the temperatures recorded in the lower liquid layer into the same plot for interpretation. The black solid line shows the temperature in the ice blocks prior to when the ice blocks were rafted (0 minutes), the red dotted line the last temperature readings taken prior to when the upper liquid layer consolidated (2760 minutes), the solid blue line the temperature when the upper liquid layer had consolidated (6900 minutes), the solid green line the temperature just after the last core was taken before the lower layer consolidated (17520 minutes) and the dotted green line the temperature when all three layers had consolidated (28920 minutes). In this figure we see that the temperature in the ice blocks prior to rafting is linear and then gradually evolves to re-establish an almost linear profile throughout the 3 ice blocks.

Figure F.17b shows a close up of the temperature in the ice blocks at the boundaries of the upper liquid layer. The figure shows that prior to rafting the temperature at the base of the ice block above the liquid layer is about -2.5ºC, then an hour after rafting the temperature has risen to about -1.9ºC. This is due to warmer water from the basin flooding in between the ice blocks when they were assembled. The temperature then, at first rather rapidly, reduces with time until it becomes almost constant. There are two exceptions to this trend, the first at 1320 minutes and the second at 17520 minutes. At 1320 minutes, the temperature rises to -2ºC. This is because a core was taken (using the 2 inch auger) an hour prior to when these readings were taken causing warmer, fresher water to flood into the remnant hole therefore raising the temperature at the base of the ice block. At 17520 minutes, the temperature drops to -6ºC, which is caused by an overall drop in the temperature in the ice basin.

Figure F.17c shows the evolution of the temperature in the ice blocks at the boundaries of the lower liquid layer. As mentioned previously the lower plot also includes the temperature recorded in the lower liquid layer (points located at 0.2 m). At the base of the ice block above the lower liquid layer (top plot) we see that the temperature initially reduces with time, but then after 240 minutes it starts to rise until 2760 minutes, where it then commences to reduce once again until it has consolidated. In ice block below the liquid layer we also see a similar trend.

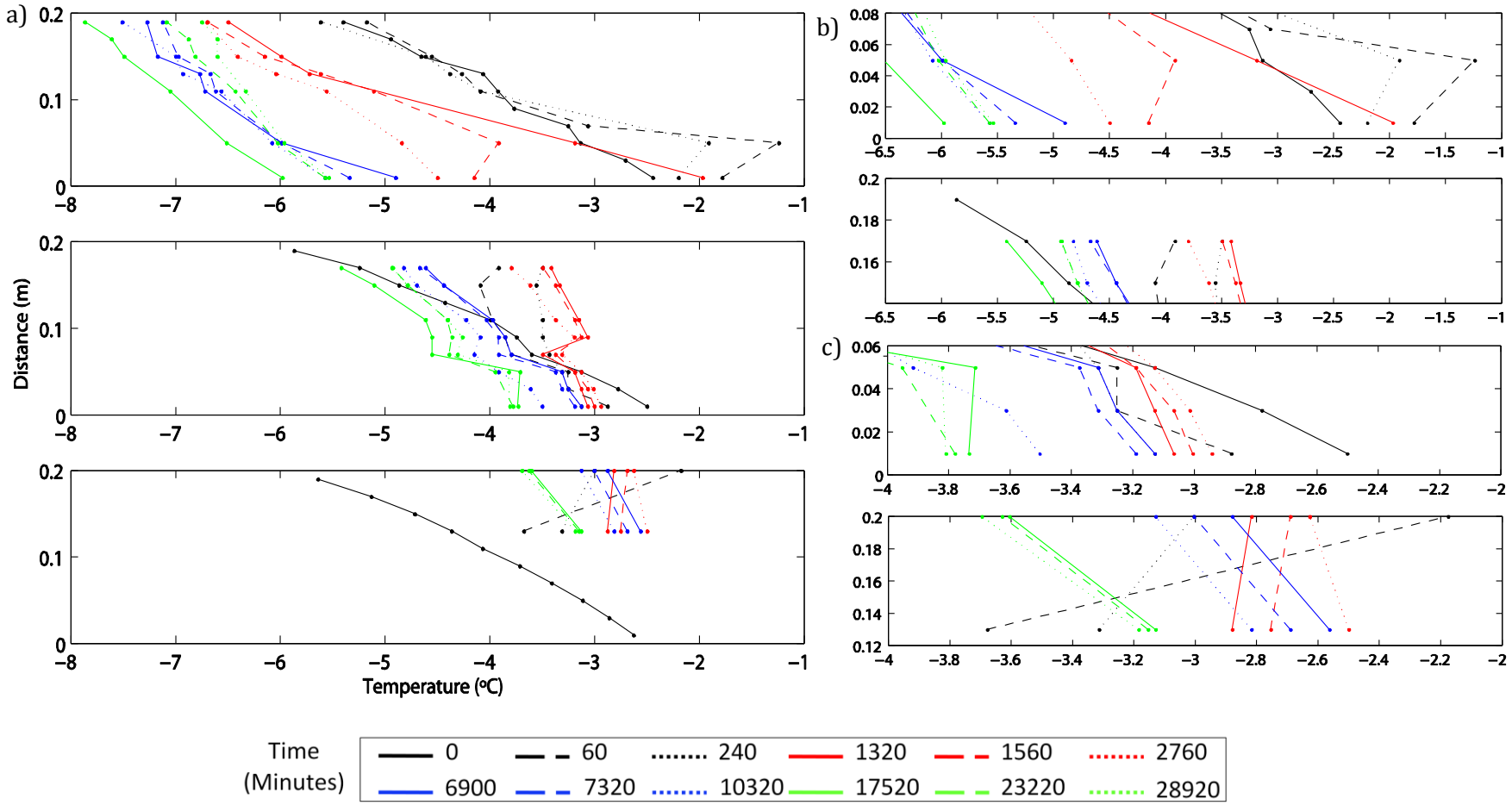

Figure F.17. The plots show a) the evolution of the temperature profiles in the 3-layer rafted section where the top ice block is in contact with the air, the bottom ice block is in contact with the water and the middle ice block is between the two. Plots b) and c) show zoomed in sections about the upper and lower liquid layer respectively.

Figure F.18 shows all of the temperatures recorded in the lower liquid layer. The figure shows that the temperature initially reduces rapidly with time, then after 1140 minutes it rises until 2580 minutes, and then starts to reduce once again until it eventually becomes almost constant after 21600 minutes. The initial cooling is likely due to freezing which took place as heat was conducted from the lower liquid layer into the ice block below. However, once all of the cold reserves in the lower ice block have been used up no more cooling can take place until heat is conducted out to the atmosphere. Unfortunately, no such data exists for the upper liquid layer because as mentioned previously the thermistor had corroded. I was however able to record the salinity and temperature on two occasions when I drilled down to the liquid layer and took samples using a pipette. These data are presented in Table F.3.

The results in Table F.3 show that the salinity in the upper liquid layer increased with time whilst the temperature reduced with time. This indicates that either brine is draining from the ice block above into the liquid layer, or from the newly forming ice growing in the liquid layer. A decrease in the temperature of the liquid layer is expected as the addition of salt lowers its freezing temperature. The sample taken at 6900 minutes is similar to the salinity of the liquid layer when the ice blocks had just consolidated, which I believe is because when the hole was drilled it no longer flooded and when a core was taken 420 minutes later (i.e. 7320 minutes from start of experiment) it had indeed consolidated. This value of 77.3 ppt was the value used in the rafted ice consolidation model (c.f. Chapter 6) to estimate the fraction of salt release and the surface asperity height.

Table F.3. Salinity and temperature of the samples taken with the pipette from the upper liquid layer in Experiment 1.

Time (Minutes)	Salinity (ppt)	Temperature (°C)
2760 (1day, 22hrs)	60.5	-3.91
6900 (4days 19hrs)	77.3	-4.98

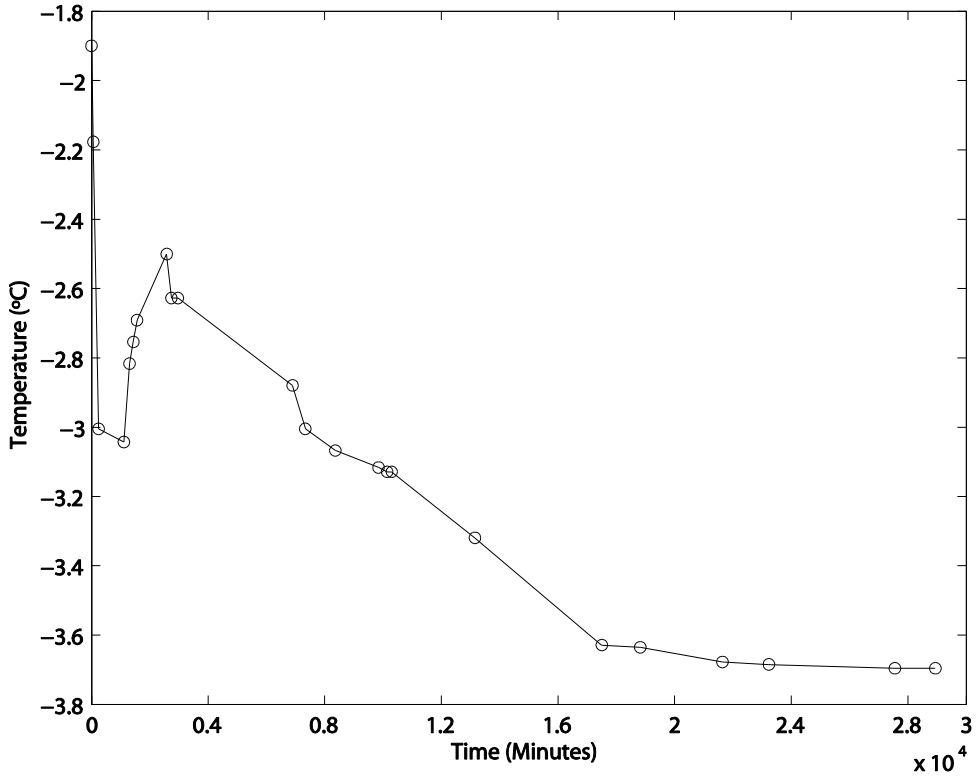

Figure F.18. Plot showing the changes in temperature in the lower liquid layer.

Experiment 2

Experiment 2 consisted of assembling a 2-layer and a 3-layer section of rafted ice and monitoring the rate of consolidation through a combination of drilling and coring. Table F.4 shows the time in hours since the start of the experiment that a core was taken or the stack was drilled. The results show that it took between 1800 and 2820 minutes (~1-2 days) for the 2-layer stack to consolidate and the top two layers in the 3-layer stack to consolidate and that it took between 2820 and 7200 minutes (~2-5 days) for the remaining two layers to consolidate.

Table F.4. Times that cores were taken for Experiment 2.

Time core taken (Minutes)	Method	2-layer section	3-layer section
1800 (1day, 6hrs)	Drilling	Not consolidated	Not consolidated
2820 (1day, 23hrs)	4 inch core	Consolidated	Upper LL consolidated
7200 (5 days)	4 inch core	-	Lower LL consolidated

F.5 Discussion and Summary

Experiment 1:

- The results show that it took respectively between 2760 and 6900 minutes (~2-5 days) and 17520 and 28920 minutes (~12-19 days) for the upper and lower liquid layers to in a 3 x 20 cm rafted section to consolidate.
- The thickness of the liquid layers between the blocks was ~2 cm thick because thermistor cables got twisted making the gap larger than the anticipated 3 mm.
- The temperature of lower liquid layer rose before freezing probably due to an initial freezing period.
- The temperature of lower liquid layer became constant after ~21600 minutes (15 days). This is within the time period that the lower liquid layer was observed to consolidate suggesting that constant temperature may signify consolidation.

Experiment 2:

- The results show that it took between 1800 and 2820 minutes (~1-2 days) for the 2-layers of 10 cm ice to consolidate.
- It took between 2820 and 7200 minutes (~2-5 days) for the layers in a 3 x 10 cm rafted section to consolidate. This is considerably quicker than the 3 x 20 cm section suggesting that the thicker the gap and liquid layer the longer the consolidation time.

References

Ackley, S. F. (1981), Sea-ice atmosphere interaction in the Weddell sea using drifting buoys, Proc. of Sea Level, Ice, Climate Change, Int. Assoc. of Hydrol. Sci. , Oxford, U.K.

AgipKCO (2010), Kashagan Project, http://www.agipkco.com.

Allison, I. (1979), Antarctic sea ice growth and oceanic heat flux, Proc. of Canberra Symposium on sea level, ice and climatic changes, IAHS Publ., No. 131, 161-170.

Ashton, G. D. (1986), Ice physics, in *River and Lake Ice Engineering*, edited by G. D. Ashton, Water Resource Publications, Littleton, Colorado.

Assur, A. (1958), Composition of sea ice and its tensile strength, *in Arctic Sea Ice, U.S. Nat. Acad. of Sci. Pub. , 598*, 106-138.

Atlas (1997), Atlas of the Astrakhan region, Federal service of geodesy and kartography, 15-16, Moscow.

Babko, O., D. A. Rothrock, and G. A. Maykut (2002), Role of rafting in the mechanical redistribution of sea ice thickness, *J. Geophys. Res.*, *107*(C8), 3113, doi:10.1029/1999JC 000190.

Bailey, E., D. L. Feltham, and P. R. Sammonds (2010), A model for the consolidation of rafted sea ice, *J. Geophys. Res.*, *115*(C04015), doi:10.1029/2008JC005103.

Barnes, H. T. (1928), *Ice Engineering*, 364 pp., Renoulf, Montreal.

Barnes, P., D. Tabor, and J. C. F. Walker (1971), The friction and creep of polycrystalline ice, Proc. of Roy. Soc., London.

Bitz, C. M., and W. H. Lipscomb (1999), An energy-conserving thermodynamic model of sea ice, *J. Geophys. Res.*, *104*(C7), 15669-15677.

Bowden, F. P., and T. P. Hughes (1939), The mechanism of sliding on ice and snow, *Proc. R. Soc., A 172*, 280-298.

BP (2010), Statistical Review of World Energy June 2010, London.

Butkovitch, T. R. (1956), Strength studies of sea ice, Snow, Ice and Permafrost Establishment. Res. rep. RR-20, Willamette, Illinois.

Butkovitch, T. R. (1959), On the mechanical properties of sea ice, Research Report 54, 11 pp, U. S. Army Cold Regions Research and Engineering Laboratory, Thule, Greenland.

Colony, R., and A. S. Thorndike (1984), An estimate of the mean field of Arctic sea ice motion, *J. Geophys. Res., 89*, 10623-10629.

Comiso, J. C. (2003), Large-scale characteristics and variablility of the global sea ice cover, in *In Sea Ice – An Introduction to its Physics, Chemistry, Biology and Geology*, edited by D. Thomas and G. S. Dieckmann, pp. 112-142, Blackwell Science, London.

Cox, G. F. N., and W. F. Weeks (1974), Salinity variations in sea ice, *J. Glaciol.*, *13*(67), 109-120.

Cox, G. F. N., and W. F. weeks (1975), Brine drainage and initial salt entrapment in sodium chloride ice, *CRRELL Research Report*, *345*.

Cox, G. F. N., and W. F. Weeks (1983), Equations for determining the gas and brine volumes in sea-ice samples, *J. Glaciol.*, *29*(102), 306-316.

Dykins, J. E. (1971), Ice Engineering - Material properties of saline ice for a limited range of conditions, Naval Civ. Eng. Lab., Tech. Rep. R720, Port Hueneme, California.

Ebert, E. E., and J. A. Curry (1993), An intermediate one-dimensional thermodynamic sea ice model for investigating ice-atmosphere interactions, *J. Geophys. Res.*, *98*, 10085-10109.

Eicken, H. (2003), From the Microscopic, to the Macroscopic, the Regional Scale: Growth, Microstructure and Properties of Sea Ice, in *Sea Ice - An Introduction to its physics, chemistry, biology and geology*, edited by D. N. Thomas and G. S. Dieckmann, pp. 22-81, Blackwell Science, Oxford.

Eicken, H., T. C. Grenfell, D. K. Perovich, J. A. Richter-Menge, and K. Frey (2004), Hydraulic controls of summer Arctic pack ice albedo, *J. Geophys. Res.*, *109*(C08007), doi:10.1029/2003JC001989.

Fedotov, V. I. (1973), Studies of Antarctic fast ice in *Studies in Ice Physics and Ice Engineering*, edited by G. N. Iakovlev, pp. 95-111, Arctic and Antractic Scientific Research Institute.

Feltham, D. (1998), Fluid dynamics and thermodynamis of sea ice., Ph.D. thesis, University of Cambridge, Cambridge, U.K.

Feltham, D. L., and M. G. Worster (1999), Flow-induced morphological instability of a mushy layer, *J. Fluid. Mech.*, *391*, 337-357.

Feltham, D. L., N. Untersteiner, J. S. Wettlaufer, and M. G. Worster (2006), Sea Ice is a mushy layer, *Geophys. Res. Lett.*, *33*, L14501, doi:10.1029/2006GL026290.

Frankenstein, G., and R. Garner (1967), Equations for determining the brine volume of sea ice from -0.5 C to -22.9 C, *J. Glaciol.*, *6*(48), 943-944.

Frederking, R. M. W., and G. W. Timco (1983), Uni-axial compressive strength and deformation of Beaufort Sea ice, in *International Conference on Port and Ocean Engineering under Arctic Conditions, POAC83*, edited, pp. 89-99, Helsink, Finland.

Frederking, R. M. W., and G. W. Timco (1984a), Measurement of shear strength of granular/discontinous-columnar sea ice, *Cold Reg. Sci. Technol.*, *9*, 215-220.

Frederking, R. M. W., and G. W. Timco (1984b), Compressive behaviour of Beaufort Sea ice under vertical and horizontal loading, Proc. of 3rd International Mechanics and Arctic Engineering (OMAE), New Orleans, USA.

Frederking, R. M. W., and G. W. Timco (1986), Field measurements of the shear strength of columnar-grained sea ice, Proc. of IAHR Ice Symposium 18-22 August 1986, Iowa City, Iowa.

Frederking, R. M. W., O. J. Svec, and G. W. Timco (1988), On measuring the shear strength of ice, in *9th International Symposium on Ice*, edited, pp. 76-88, IAHR Committee on Ice Problems, Sapporo, Japan.

Freitag, D. R., and T. McFadden (1997), *Introduction to Cold Regions Engineering*, ASCE press, New York.

Freitag, J. (1999), Untersuchungen zur Hydrologie des arkischen Meereises - Kosequenzen fur den kleinskaligen Strfftransport (in German), Berichte zur Polarforscung 325, Alfred-Wegener Institut fur Polar- und Meeresforschung, Bremehaven, Germany.

Giles, K. A., S. W. Laxon, and A. P. Worby (2008a), Antarctic sea ice elevation from satellite radar altimetry, *Geophys. Res. Lett.*, *35*(L03503), doi:10.1029/2007GL031572.

Giles, K. A., S. W. Laxon, and A. P. Worby (2008b), Circumpolar thinning of Arctic sea ice following the 2007 record ice extent minimum, *Geophys. Res. Lett.*, *35*(L22502), doi:10.1029/2008GL035710.

Gilpin, R. R., T. Hirata, and K. G. Cheng (1980), wave formation and heat transfer at an ice-water interface in the presence of a turbulent flow, *J. Fluid. Mech.*, *99*, 619-640.

Golden, K. M., S. F. Ackley, and V. I. Lytle (1998), The percolation phase transition in sea ice, *Science, 282*, 2238-2241.

Goodman, D. J., H. J. Frost, and M. F. Ashby (1981), The plasticity of polycrystalline ice, *Phil. Mag.*, *A43*(3), 665-695.

Gow, A. J., and W. B. Tucker (1990), Sea ice in the Polar regions, in *Polar Oceanography, Part A: Physical Science*, edited by W. O. Smith Jr., pp. 47-122, Academic Press Inc., San Diego.

Haas, C. (2003), Dynamics versus thermodynamics: The sea ice thickness distribution, in *In Sea Ice – An Introduction to its Physics, Chemistry, Biology and Geology*, edited by D. Thomas and G. S. Dieckmann, pp. 82-111, Blackwell Science, London.

Hatton, D. C., P. R. Sammonds, and D. L. Feltham (2009), *Philos. Mag.*, *89*(31), 2771-2799, doi:10.1080/14786430903113769.

Häusler, F. U. (1989), Formulae for total porosity evaluation on sodium chloride ice and urea-doped ice, *Cold Reg. Sci. Technol.*, *16*, 83-87.

Hoekstra, P., T. E. Osterkamp, and W. F. Weeks (1965), The migration of liquid inclusions in single ice crystals, *J. Geophys. Res.*, *70*(20), 4922-4931.

Hopkins, M. A., J. Tuhkuri, and M. Lensu (1999), Rafting and ridging of thin ice sheets, *J. Geophys. Res.*, *104*(C6), 13605 -13613.

Hoyland, K. V. (2002), Consolidation of first-year sea ice ridges, *J. Geophys. Res.*, *107*(C6), 3062, doi:10.1029/2000JC000526.

ISO/FDIS_19906 (in preparation), Petroleum and Natural Gas Industries - Arctic Offshore Structures, ISO TC 67/SC 7, International Organization for Standardization.

Jizu, X., S. Qingzeng, S. An, F. Yunlin, and L. Tongkui (1991), Sea Ice Engineering in China, *Journal of Coastal Research*, *7*(3), 759-770.

Johannessen, O. M., L. Bengtsson, M. W. Miles, S. I. Kuzmina, V. A. Semenov, G. V. Aledseev, A. P. Nagumyi, V. F. Zakharov, L. P. Bobylev, L. H. Pettersson, K. Hasselmann, and H. P. Cattle (2004), Arctic climate change: observed and modelled temperature and sea-ice variability, *Tellus*, *56*(A), 328-341.

Jones, J. S. (1997), High strain-rate compression tests on ice, *J. Phys. Chem. B.*, *101*, 6099-6101.

Kankaanpää, P. (1997), Distribution, morphology and structure of sea ice pressure ridges in the Baltic Sea, Fennia, *Fennia*, *175*, 139-240.

Kingery, W. D., and W. H. Goodnow (1963), Brine migration in salt ice, in *Ice and Snow: Properties, Processes and Applications*, edited by W. D. Kingery, pp. 237-347, MIT Press, Cambridge, Maas.

Kovacs, A. (1970), On the structure of pressured sea ice, Report prepared for the U. S. Coast Guards by U.S. Army Cold Regions Research and Engineering Laboratory, Hanover, New Hampshire.

Kovacs, A., and M. Mellor (1974), Sea ice morphology and ice as a geologic agent in the Southern Beaufort Sea, in *The Coast and Shelf of the Beaufort Sea*, edited by J. C. R. a. J. E. Sater, pp. pp. 113-161, Arlington.

Kwok, R., G. F. Cunningham, M. Wensnahan, I. Rigor, H. J. Zwally, and D. Yi (2009), Thinning and volume loss of the Arctic Ocean sea ice cover: 2003-2008, *J. Geophys. Res.*, *114*(C7), C07005, 10.1029/2009jc005312.

Kwok, R., and D. A. Rothrock (2009), Decline in Arctic sea ice thickness from submarine and ICESat records: 1958–2008, *Geophys. Res. Lett.*, *36*(L15501), doi:10.1029/2009GL039035.

Lange, M. A., S. F. Ackley, P. Wadhams, G. S. Dieckmann, and H. Eicken (1989), Development of the sea ice in the Weddell Sea, *Ann. Glaciol.*, *12*, 92-96.

Lemke, P. (1987), A coupled one-dimensional sea-ice ocean model, *J. Geophys. Res.*, *92*(C12), 13164-13172.

Leppäranta, M. (1993), A review of analytical models of sea-ice growth, *Atmosphere-Ocean*, *31*(1), 123-138.

Li, C., and H. Sun (2009), Ice rafting in the Bohai Sea, in *20th International Conference on Port and Ocean Engineering under Arctic Conditions*, edited by L. Fransson, Luleå University of Technology, Luleå, Sweden.

Lishman, B., P. R. Sammonds, D. L. Feltham, and A. Wilchinski (2009), The rate- and state- dependence of sea ice friction, in *20th International Conference on Port and Ocean Engineering under Arctic Conditions*, edited by L. Fransson, Luleå University of Technology, Luleå, Sweden.

Marchenko, A., and A. Makshtas (2005), A dynamic model of ridge build up, *Cold Reg. Sci. Technol.*, *41*, 175-188.

Marchenko, A., and C. Chenot (2009), Regelation of ice blocks in the water and the air, Proc. of 20th International Conference on Port and Ocean Engineering under Arctic Conditions, Luleå University of Technology, Luleå, Sweden.

Martin, S. (1979), A field study of brine drainage and oil entrainment in first year sea ice, *J. Glaciol.*, *22*, 473-502.

Massom, R. A., H. Eicken, C. Hass, M. O. Jeffries, M. R. Drinkwater, M. Sturm, P. Worby, X. Wu, V. I. Lytle, S. U. K. Morris, P. A. Reid, S. Warren, and I. Allison (2001), Snow on Antarctic sea ice, *Rev. Geophys.*, *39*, 413-445.

Maykut, G. A., and N. Untersteiner (1971), Some results from a time-dependent thermodynamic model of sea ice, *J. Geophys. Res.*, *76*(6), 1550-1575.

Maykut, G. A., and B. Light (1995), Refractive-index measurements in freezing in freezing sea ice and sodium chloride brines, *Appl. Opt.*, *34*(6), 950-961.

Melnikov, I. A. (1998), Winter production of sea ice algae in the western Weddell Sea, *Journal of Marine Systems*, *17*(1-4), 195-205.

Moslet, P. O. (2007), Field testing of uniaxial compression strength of columnar sea ice, *Cold Reg. Sci. Technol.*, *48*, 1-14, doi:10.1016/j.coldregions.2006.08.025.

Notz, D. (2005), Thermodynamic and fluid-dynamical processes in sea ice, Ph.D. thesis, 238 pp, University of Cambridge, Cambridge, United Kingdom.

Notz, D., and M. G. Worster (2008), In situ measurements of the evolution of young sea ice, *J. Geophys. Res.*, *113*, C03001, doi:10.1029/2007JC004333.

Notz, D., and M. G. Worster (2009), Desalination processes of sea ice revisited, *J. Geophys. Res.*, *114*, C05006, doi:10.1029/2008JC004885.

Oertling, A. B., and R. G. Watts (2004), Growth of and brine drainage from NaCl-H20 freezing: A simulation of young sea ice, *J. Geophys. Res.*, *109*(C04013), doi:10.1029/2001JC001109.

Oksanen, P., and J. Keinonen (1982), The mechanism of friction of ice, *Wear*, *78*, 315-324.

Ono, N. (1965), Thermal properties of sea ice 2. A method for determining the K/c value of a non-continous ice sheet. , *Low Temp. Sci.*, *A23*, 177-183.

Paige, R. A., and C. W. Lee (1967), Preliminary studies on sea ice in McMurdo Sound, Antractica, during "Deep Freeze 65", *J. Glaciol.*, *6*(46), 515-528.

Parmerter, R. R. (1975), A model of simple rafting in sea ice, *J. Geophys. Res.*, *80*, 1948-1952.

Patnaik, S., and D. Hopkins (2004), *Strength of Materials: A New Unified Theory for the 21st Century*, Elsevier, Boston, MA.

Perey, F. G. J., and E. R. Pounder (1958), Crystal orientation in ice sheets, *Can. J. Phys.*, *36*, 494-502.

Perovich, D. K., and B. Elder (2002), Estimates of oceanic heat flux at SHEBA, *Geophys. Res. Lett.*, *29*(9), 1344, doi:10.1029/2001GL014171.

Peyton, H. R. (1966), Sea ice strength, R-182, 285 pp, Geophysical Institute, University of Alaska, Alaska.

POAC (2009), Proceedings of the 20th International Conference on Port and Ocean Engineering under Arctic Conditions, Luleå University of Technology, Luleå, Sweden.

Poplin, J. P., and A. T. Wang (1994), Mechanical properties of rafted annual sea ice, *Cold Reg. Sci. Technol.*, *23*, 41-67.

Pounder, E. R. (1965), *The Physics of Ice*, 151 pp., Pergamon Press, Oxford.

Repetto-Llamazares, A. H. V., P. Jochmann, K. Evers, and K. V. Hoyland (2009a), Model testing of ridge reel loads on structures. Part 4: Preliminary results of freeze bond shear strength experiments, in *20th International Conference on Port and Ocean Engineering under Arctic Conditions*, edited by L. Fransson, Luleå, Sweden.

Repetto-Llamazares, A. H. V., N. Serré, K. Evers, P. Jochmann, and K. V. Hoyland (2009b), Model testing of ridge reel loads on structures. Part 2: Ridge building and physical properties, in *20th International Conference on Port and Ocean Engineering under Arctic Conditions*, edited by L. Fransson, Luleå, Sweden.

Sakazume, S., and N. Seki (1978), Thermal properties of ice and snow at low temperature region, *JSME*, *44*(382), 2059 - 2069.

Sammonds, P. R., S. A. F. Murrell, and M. A. Rist (1998), Fracture of multiyear sea ice, *J. Geophys. Res.*, *103*(21), 795–721,815.

Sammonds, P. R., D. C. Hatton, D. L. Feltham, and P. D. Taylor (2005), Experimental study of sliding friction and stick-slip on faults in floating ice sheets, in *18th International Conference on Port and Ocean Engineering Under Arctic Conditions*, edited by J. Dempsey, Potsdam, New York.

Sanderson, T. J. O. (1988), *Ice mechanics : risks to offshore structures*, 253p. pp., Graham & Trotman, London.

Schulson, E. M., and P. Duval (2009), *Creep and Fracture of Ice*, 401 pp., Cambridge University Press, ISBN 978-0-521-80620-6.

Schwartz, J., and W. F. Weeks (1977), Engineering properties of ice, *J. Glaciol.*, *19*(8), 499-530.

Schwartz, J., R. Frederking, V. Gavrillo, I. G. Petrov, K. I. Hirayama, M. Mellor, P. Tryde, and K. D. Vaudrey (1981), Standardized testing methods for measuring the mechanical properties of ice, *Cold Reg. Sci. Technol.*, *4*, 245-253.

Schwarzacher, W. (1959), Pack ice studies in the Arctic Ocean, *J. Geophys. Res.*, *64*, 2357-2367.

Schwerdtfeger, P. (1963), The thermal properties of sea ice, *J. Glaciol.*, *4*, 789 - 807.

Semtner, A. J. (1976), A model for the thermodynamic growth of sea ice in numerical investigation of climate, *J. Phys. Oceanogr.*, *6*, 379-389.

Semtner, A. J. (1984), On modelling the seasonal thermodynamic cycle of sea ice in studies of climatic change, *Clim. Change*, *6*(27-37).

Shafrova, S., and K. V. Hoyland (2008), The freeze-bond strength in first-year ice ridges. Small-scale field and laboratory experiments, *Cold Reg. Sci. Technol.*, *54*(1), 54-71, doi:10.1016/j.coldregions.2007.11.005.

Sinha, N. K. (1983a), Field tests on rate sensitivity of vertical strength and deformation of first-year columnar-grained sea ice, Proc. of POAC83, Helsinki, Finland.

Sinha, N. K. (1983b), Field test 1 of compressive strength of first year sea ice, *Annals of Glaciology*, *4*, 253-259.

Stefan, J. (1891), Uber die Theorie der Eisbildung, insbesondere uber die Eisbildung im Polarmeere, *Annalen der Physik und Chemie*, *42*, 269-286.

Stepetz, J. M., T. F. Zagaeski, and R. F. Novello (1978), In-plane shear tests for composite materials, AMMRC TR78-30, Army Materials and Mechanics Research Centre, Watertown, Massachusetts.

Taylor, P. D., and D. L. Feltham (2004), A model of melt pond evolution on sea ice, *J. Geophys. Res.*, *109*, C12007, doi:10.1029/2004JC002361.

Terziev, F. S., A. N. Kosarev, and A. A. Aliev (1992), Hydrometerology and hydrochemistry of the seas, Vol. 6. The Caspian Sea, Issue 1, Hydrometeriological conditions, Gidrometeoizdat, St. Petersburg (in Russian).

Timco, G. W. (1980), The mechanical properties of saline-doped and carbamide (urea)-doped model ice, *Cold Reg. Sci. Technol.*, *3*, 45-46.

Timco, G. W., and R. M. W. Frederking (1990), Compressive strength of sea ice sheets, *Cold Reg. Sci. Technol.*, *17*, 227-240.

Timco, G. W., and R. M. W. Frederking (1996), A review of sea ice density, *Cold Reg. Sci. Technol.*, *24*, 1 - 6.

Timco, G. W., and W. F. Weeks (2010), A review of the engineering properties of sea ice, *Cold Reg. Sci. Technol.*, *60*, 107-129, doi:10.1016/j.coldregions.2009.10.003.

Timoshenko, S. (1941), Stresses in beams, in *Strength of Material: Part I (3rd edition)*, edited, pp. 92-136, Van Nostrand Reinhold, New York.

Toyota, T., T. Kawamura, K. I. Ohshima, H. Shimoda, and M. Wakatsuchi (2004), Thickness distribution, texture and stratigraphy, and a simple probabilistic model for dynamic thickening of sea ice in the southern Sea of Okhotsk *J. Geophys. Res.*, *109*, C06001, doi:10.1029/2003JC002090.

Toyota, T., S. Takatsuji, K. Tateyama, K. Naoki, and K. I. Oshima (2007), Properties of sea ice and overlying snow in the Southern Sea of Okhotsk, *Journal of Oceanography*, *63*, 393-411.

Tsinker, G. P. (1994), Marine structures in cold regions, in *Marine structures engineering - Specilized applications*, edited, Chapman and Hall, Internataional Thompson Publishing Inc., New York.

Tucker, W. B., A. J. Gow, and W. F. Weeks (1987), Physical properties of summer sea ice in the Fram straight, *J. Geophys. Res.*, *92*, 6787-6803.

Tuhkuri, J., and M. Lensu (1997), Ice tank tests on rafting of a broken ice field, Rep. M-218, Helsinki Univ. of Tech., Helsinki, Finland.

Tuhkuri, J., and M. Lensu (1998), Ice tank tests on ridging of non-uniform ice sheets, Rep. M-236, 130 pp, Helsinki Univ. of Technol., Espoo, Finland.

Tuhkuri, J., M. Lensu, and S. Saarinen (1999), Laboratory and field studies on mechanics of ice ridge formations, Proc. of 15th International Conference on Port and Ocean Engineering Under Arctic Conditions Helsinki Univ. of Technol., Espoo, Finland.

Tuhkuri, J., and M. Lensu (2002), Laboratory tests on ridging and rafting of ice sheets, *J. Geophys. Res.*, *107*(C9), 3125, doi:10.1029/2001JC000848.

Untersteiner, N. (1961), On the mass and heat budget of arctic sea ice, *Arch. Meteorol. Geophys. Bioklimatol.*, *12*(A), 151-182.

Untersteiner, N. (1964), Calculations of temperature regime and heat budget of sea ice in the central Arctic, *J. Geophys. Res.*, *69*(22), 4755-4766.

Untersteiner, N. (1968), Natural desalination and equilibrium salinity profile of perennial sea ice, *J. Geophys. Res.*, *73*, 1251-1257.

USGS (2008), Circum-Arctic resource appraisal: Estimates of undiscovered oil and gas north of the Arctic Circle, *U.S. Geological Survey Fact Sheet 2008-3049*, Available at http://pubs.usgs.gov/fs/2008/3049.

Vancoppenolle, M., C. M. Bitz, and T. Fichefet (2007), Summer landfast sea ice desalination at Point Barrow, Alaska: Modeling and observations, *J. Geophys. Res.*, *112*(C04022), doi:10.1029/2006JC003493.

Vancoppenolle, M., H. Goosse, A. Montety, T. Fichefet, B. Tremblay, and J. L. Tison (2010), Modeling brine and nutrient dynamics in Antarctic sea ice: The case of dissolved silica, *J. Geophys. Res.*, *115*(C02005), doi:10.1029/2009JC005369.

Veitch, B., P. Kujala, P. Keiley, and E. Lehmus (1991), Ice tank experiments on the thermodynamics of deformed ice, Report M-110, 46 pp, Laboratory of Naval Architecture and Marine Engineering, Helsinki University of Technology Espoo, Finland.

Vella, D., and J. S. Wettlaufer (2008), Explaining patterns formed by ice floe interactions, *J. Geophys. Res.*, *113*, C11011, doi:10.1029/2008JC004781.

Vincent, W. F. (1988), Sea ice ecosystems, in *Microbial Ecosystems of Antarctica*, edited, pp. 26-51, Cambridge University Press, Cambridge.

Wadhams, P. (2000), *Ice in the Ocean*, Gordon and Breach Science Publishers, Amsterdam.

Wang, A. T. (1979), Crystallographic studies and strength tests of field ice in the Alaskan Beaufort Sea, Proc. of POAC79, Trondheim, Norway.

Wang, A. T. (1981), Uniaxial compression testing of Arctic sea ice, in *6th Int. Conf. POAC*, edited by B. Michel, pp. 346-355, Quebec City, PQ, Canada.

Wang, A. T., J. P. Poplin, and C. E. Heuer (1994), Hydrocarbon production concepts for dynamic annual sea ice regions, *Hydrotechnical Construction*, *28*(8), 472-492.

Wang, Y., and N. Azuma (1999), A new automated ice-fabric analyzer which uses image-analysis techniques, *J. of Glaciol.*, *29*, 155-162.

Weast, R. C. (1971), *Handbook of chemistry and physics*, Fifty-second ed., Cleveland, OH, Chemical Rubber Co.

Weeks, W. F., and D. L. Anderson (1958), Sea ice thrust structures, *J. Glaciol.*, *3*(23), 173-175.

Weeks, W. F., and A. Kovacs (1970), On pressure ridges, CRREL Rep. IR505, 59 pp, U.S. Army Cold Regions Res. and Eng. Lab., Hanover, N. H.

Weeks, W. F., and S. F. Ackley (1986), The growth, structure and properties of sea ice, in *The geophysics of sea ice*, edited by N. Untersteiner, pp. 9 - 164, Martinus Nijhoff Publ. , Dordrecht (NATO ASI B146).

Wettalufer, J. S., M. G. Worster, and H. E. Huppert (2000), Solidification of leads: Theory, experiments and field observations, *J. Geophys. Res.*, *105*(C1), 1123-1134.

Wettlaufer, J. S. (1991), Heat flux at the ice-ocean interface, *J. Geophys. Res.*, *96*, 7215-7236.

Wettlaufer, J. S., M. G. Worster, and H. E. Huppert (1997a), The phase evolution of young sea ice, *Geophys. Res. Lett.*, *24*(10), 1251-1254.

Wettlaufer, J. S., M. G. Worster, and H. E. Huppert (1997b), Natural convection during solidification of an alloy from above with application to the evolution of sea ice, *J. Fluid. Mech.*, *344*, 291-316.

Wettlaufer, J. S., M. G. Worster, and H. E. Huppert (2000), Solidification of leads: Theory, experiments and field observations, *J. Geophys. Res.*, *105*(C1), 1123-1134.

Whitman, W. G. (1926), Elimination of salt from sea water ice, *Am. J. Sci. Ser.*, *211*, 126-132.

Wilkinson, J. P. (2009), Ice tank experiments highlights changes in sea ice types, *Eos*, *90*(10), 81-82.

Woods, A. W. (1992), Melting and dissolving, *Journal of Fluid Mechanics*, *239*, 429-448, doi:10.1017/S0022112092004476.

Worby, A. P., M. O. Jefferies, W. F. Weeks, K. Morris, and R. Jana (1996), The thickness distribution of sea ice and snow cover during the late winter in the Bellingshausen and Amundsen Seas, Antarctica, *J. Geophys. Res.*, *101*, 28,441 - 428, 445.

Worster, M. G. (1986), Solidification of an alloy from a cooled boundary, *J. Fluid. Mech.*, *167*, 481-501.

Worster, M. G. (1992), The dynmics of mushy layers, in *Interactive Dynamics of Convection and Solidification*, edited by S. H. Davis et al., pp. 113-138, Kluwer Academic, Dortrecht, Netherlands.

Worster, M. G. (1997), Convection in mushy layers, *Ann. Rev. Fluid Mech.*, *29*, 91-122.

Worster, M. G., and J. S. Wettlaufer (1997), Natural convection, solute trapping and channel formation during solidification of saltwater, *J. Phys. Chem.*, *101*, 6132-6136.

Worster, M. G. (2000), Solidification of fluids, in *Perspectives in Fluid Mechanics*, edited by G. K. Batchelor et al., pp. 393-446, Cambridge Univ. Press, Cambridge, U. K.

Zhijun, L., P. Wanwei, Z. Tao, L. Ming, and G. Shugang (1995), Effect of porosity on the uniaxial compressive strenght of ice in Liaodong Gulf, Proc. of 10th Int. Symp. on Okhotsk Sea, Sea Ice & Peoples, Mombetsu, Hokkaido.

Zubov, N. N. (1945), L'dy Arktiki [Arctic Ice]. Izdatel'stvo Glavsermorputi, Moscow. (Engl. Transl. 1963 by U. S. Naval Oceanogr. Off. and Am. Meteorol. Soc., San Diego, Calif.)